Combined Wet Milling Crystallisation Methods for Particle Engineering

A thesis presented for the degree of
Doctor of Philosophy
in the Faculty of Science
of the University of Strathclyde
by

Bilal Ahmed

Strathclyde Institute for Pharmacy and Biomedical Sciences

October 2019

Declaration of Author Rights

This thesis is the result of the author's original research. It has been composed by the author and has not been previously submitted for examination which has led to the award of a degree.

Signed:

Date:

Acknowledgments

My sincere thanks to Professor Alastair Florence for his supervision, support and giving me the distinct privilege to work with him. His enthusiastic and meticulous attention to detail has been pivotal for the progression of my research for which I am grateful for. I would like to thank the EPSRC and the Doctoral Training Centre in Continuous Manufacturing and Crystallisation for funding this work. I am also thankful to Dr Thomas Vetter and Dr Daniel Markl for their diligent examination of this thesis.

Thanks to my second supervisor Professor Jan Sefcik for his guidance and assistance as well as members of the Florence research group, namely Dr Cameron Brown, Dr Humera Siddique, Vishal Raval and Dr Thomas McGlone. Their mentorship, kindness and allowing me to work with them on several collaborative projects is appreciated. I am very grateful to Dr Okpeafoh Stephen Agimelen for his considerable help and discussions throughout my research as well as Dr Vaclav Svoboda and Dr Javier Cardona for their collaborative efforts and contributions made to this thesis. Further thanks to the CMAC National Facility namely Dr Deborah Bowering and Dr Monika Warzecha for their instrument support. I am also appreciative to my fellow peers, friends and DTC cohort for their unwavering support, humour and accompanying each other during long research nights over the years.

Special thanks to Dr Charles Papageorgiou, Dr Yihui Yang, Dr Justin Quon for their hospitality and Dr Ian Houson for giving me the opportunity to carry out a 3-month industrial placement at Takeda Pharmaceuticals in Boston, USA. I benefited a great deal working with the team at Takeda which led to contributions made to this thesis.

Most importantly, I am deeply indebted to my family for their immeasurable love, endless support, encouragement and patience to whom without, the completion of this thesis would not be possible. I will always be grateful to Iqra and Ribal and my beloved parents.

And finally, the validity of my gratitude can only be verified through acknowledgement at the One from whom originates All Knowledge, to whom be All Praises.

Abstract

Recent advances in pharmaceutical manufacturing for consistent supply of medicines with the required physical properties has emphasised the need for robust crystallisation processes which is a critical separation and purification technique. Mechanical milling is employed post crystallisation as an offline unit operation usually in a separate dry solids processing facility for adjusting the particle size and shape attributes of crystalline products for downstream processing. An emerging and increasingly applied technology is high shear wet milling in crystalline slurries for inline size and shape modification during particle formation. This potentially avoids the need for multiple crystallisation trials and offline milling saving time, costs and powder handling. Similarly, sonication is a powerful particle engineering tool through immersing ultrasound probes directly in solution.

This PhD project is focused on the investigation and process integration of wet milling and indirect ultrasound for enhancing crystallisation processes and engineering particle attributes. The experimental study combined a cooling and isothermal crystallisation (seeded & unseeded) process with wet milling and indirect sonication. Results from the combined method provides the ability to modify and selectively achieve a range of product outcomes including particle sizes with tight spans, equant shapes and low surface energies as well as increased nucleation rates.

High shear from wet milling is also implemented as a seeding protocol configured to a mixed-suspension mixed-product removal continuous crystalliser which proved to be an adequate seed generation strategy.

Deploying accurate quantitative analysis of size and shape attributes for solid particles is further explored. A multi-sensor measurement approach was employed using inline sensors, computational tools and offline techniques. The performance of these tools were vigorously tested for strengths and limitations which was proven to be beneficial for characterising the breakage of crystalline materials as well as overall process understanding and opportunities for process control.

For my Mother and Father.

Contents

List of Figures

List of Tables

List of Abbreviations

API	Active Pharmaceutical Ingredient
BET	Brunauer, Emmett and Teller equation
CE	Circle Equivalent Diameter
CLD	Chord Length Distribution
CSTR	Continuous Stirred Tank Reactor
CQA	Critical Quality Attributes
DMSO	Dimethyl Sulfoxide
ESI	Electronic Supplementary Information
FBRM	Focused Beam Reflectance Measurement
FDA	Food & Drug Administration
FFC	Flow Function Coefficient
FID	Flame Ionisation Detection
ATR-FTIR	Attenuated Total Reflectance Fourier Transform Infrared Spectroscopy
HCL	Hydrochloride
HSWM	High Shear Wet Mill / Milling
HPLC	High-Performance Liquid Chromatography
iGC-SEA	Inverse Gas Chromatography Surface Energy Analyser
MSMPR	Mixed-Suspension Mixed-Product Removal
MSZW	Metastable Zone Width
MeOH	Methanol
PAT	Process Analytical Technology
PBM	Population Balance Model
PDF	Probability Density Function
PFR	Plug Flow Reactor
PLS	Principle Least Squares Regression
PSD	Particle Size Distribution
PSE	Process Systems Enterprise
PVM	Particle Vision Measurement
RSWM	Rotor-Stator Wet Mill / Milling
SA	Surface Area
SEM	Scanning Electron Microscope
STC	Stirred-Tank Crystalliser
SWMCL	Square Weighted Mean Chord Length Distribution
UPLC	Ultra-Performance Liquid Chromatography
WMSC	Wet Milling Seeded Crystallisation (combined)
WMC	Wet Milling Crystallisation (unseeded, combined)
WMC-MSMPR	Wet Milling Crystallisation Mixed-Suspension Mixed-Product Removal Crystalliser

Nomenclature

a	standard activity of the solution phase	[-]
a^*	standard activity of the crystalline phase	[-]
$\mathrm{A_{cr}}$	area of collision on rotor tooth	[m]
c	solution concentration	[-]
c^*	equilibrium solution concentration	[-]
dE	differential energy	[-]
dL	change in a length dimension	[-]
D_r	outer diameter of the rotor	[m]
E^*	energy dissipation rate	[-]
$E_{A.g}$	activation energy	[J/mol]
f_{sr}	shear frequency	[$\mathrm{s^{-1}}$]
g	order with respect to supersaturation	[-]
G	linear growth rate	[m/s]
ΔG	total free energy difference	[-]
ΔG_{crit}	critical free energy difference	[-]
ΔG_s	surface excess free energy	[-]
ΔG_v	volume excess free energy	[-]
H	height of rotor tooth	[m]
J	number of nuclei formed per unit time per unit volume	[#/s.$\mathrm{m^3}$]
k_b	nucleation rate constant	[-]
k_g	growth rate constant	[-]
N_A	avogadro's number	[-]
$\widehat{N}_{CLD}$	estimated number of images from CLD inversion algorithm	[-]
$\widehat{N}_{IMG}$	estimated number of images from PVM image analysis	[-]
n/n_m	number of moles adsorbed onto the monolayer sub-coverage	[Mol $\mathrm{g^{-1}}$]
N_R	number of outer teeth located on rotor tooth	[-]
N_s	number of outer teeth located on stator tooth	[-]
N_{ST}	number of slurry turnovers	[-]
$P_{display}$	power displayed as amplitude on ultrasound display unit	[%]
P_{output}	power output dissipated across ultrasound flow-cell	[KW / $\mathrm{m^2}$]
P_0	saturated solvent vapor pressure, in pascals	[torr]
$\dot{Q}$	volumetric flow rate through wet mill	[$\mathrm{m^3 s^{-1}}$]
R	gas constant	[J $\mathrm{mol^{-1}}$ $\mathrm{K^{-1}}$]
r_c	nucleus radius	[-]

S	supersaturation	[-]
S_r	tip speed	[m/s]
τ	residence time	[s or min]
$\Delta\mu$	difference in chemical potential	[KJ/ Kmol]
μ_0	standard potential	[-]
V_R^0	net retention volume	[ml/g]
W_r	width of rotor tooth	[m]
Υ_{SV}^d	dispersive surface energy	[mJ/m^2]
$\dot{\Upsilon}$	shear rate	[s^{-1}]
φ_r	relative weighting factor	[-]
σ	relative supersaturation	[-]
ω	angular rotational speed	[s^{-1}]

List of publications and presentations arising from this work

Publications

BROWN, C. J., MCGLONE, T., YERDELEN, S., SRIRAMBHATLA, V., MABBOTT, F., GURUNG, R., L. BRIUGLIA, M., **AHMED, B**., POLYZOIS, H., MCGINTY, J., PERCIBALLI, F., FYSIKOPOULOS, D., MACFHIONNGHAILE, P., SIDDIQUE, H., RAVAL, V., HARRINGTON, T. S., VASSILEIOU, A. D., ROBERTSON, M., PRASAD, E., JOHNSTON, A., JOHNSTON, B., NORDON, A., SRAI, J. S., HALBERT, G., TER HORST, J. H., PRICE, C. J., RIELLY, C. D., SEFCIK, J. & FLORENCE, A. J. 2018. Enabling precision manufacturing of active pharmaceutical ingredients: workflow for seeded cooling continuous crystallisations. *Molecular Systems Design & Engineering*. 3, 518-549. https://doi.org/10.106/j.ces.2018.06.067

AGIMELEN, O. S., SVOBODA, V., **AHMED, B**., CARDONA, J., DZIEWIERZ, J., BROWN, C. J., MCGLONE, T., CLEARY, A., TACHTATZIS, C., MICHIE, C., FLORENCE, A. J., ANDONOVIC, I., MULHOLLAND, A. J. & SEFCIK, J. 2018. Multi-sensor inline measurements of crystal size and shape distributions during high shear wet milling of crystal slurries. *Advanced Powder Technology*, 29, 2987-2995. https://doi.org/10.106/j.ces.2014.11.015

AHMED, B., BROWN, C. J., MCGLONE, T., BOWERING, D. L., SEFCIK, J. & FLORENCE, A. J. 2019. Engineering of Acetaminophen Particle Attributes Using a Wet Milling Crystallisation Platform. *International Journal of Pharmaceutics*. 554, 201-211. https://doi.org/10.1016/j.ijpharm.2018.10.073

Presentations

AHMED, B. 2016. Lab-scale Platform for Control of Particle Attributes: Seed Production via Media Milling. *ETH Zurich Crystal Shape Engineering Summer School*, Switzerland, Poster Presentation.

AHMED, B. 2016. Application of Inline Wet Media Milling Strategy Towards Particle Property Control. *45th Annual BACG Conference*, University of Leeds, Leeds UK, Oral Presentation.

AHMED, B. 2017. Continuous Seeding Strategy Design for Continuous Crystallisation. *ISIC 20, 20th International Symposium on Industrial Crystallisation*, Dublin Ireland, Poster Presentation.

AHMED, B. 2018. Monitoring API Crystal Breakage in Wet Milling Using Inline Imaging and Chord Length Distribution Measurements. *8th World Congress on Particle Technology*, Florida, Orlando US, Oral Presentation.

Chapter 1

Introduction

1. Introduction

Particle engineering of active pharmaceutical ingredients (API) is an increasingly studied area of research & development (Ticehurst and Marziano, 2015). During drug substance manufacturing, particle formation typically originates from crystallisation which is a critical multiphase unit operation for the purification and separation of APIs (Jones, 2002). It is estimated over 90% of pharmaceuticals including aerosols, capsules and tablets are isolated in their crystalline form (Beckmann, 2013).

The key physical properties produced from crystallisation such as particle size, shape, polymorphic form, enantiomer and purity all have considerable influence on a drug product's manufacturability, stability and performance in patients (Leane et al., 2018). It is therefore imperative that these properties are well defined and well controlled as they affect a drug's bioavailability, shelf-life and to effectively formulate the API into a finished drug product (Cote and Sirota, 2010). Particle size is an important performance related attribute which often requires tight control and monitoring during drug development (Schorsch et al., 2012). However, achieving control over the particle size is not necessarily achieved at the point of API crystallisation and isolation. Often, a milling step is required (Figure 1.1) to reduce and deliver small particle sizes for the manufacture of solid oral dosage forms for APIs with low aqueous solubility or to generate seed material for controlling crystallisation.

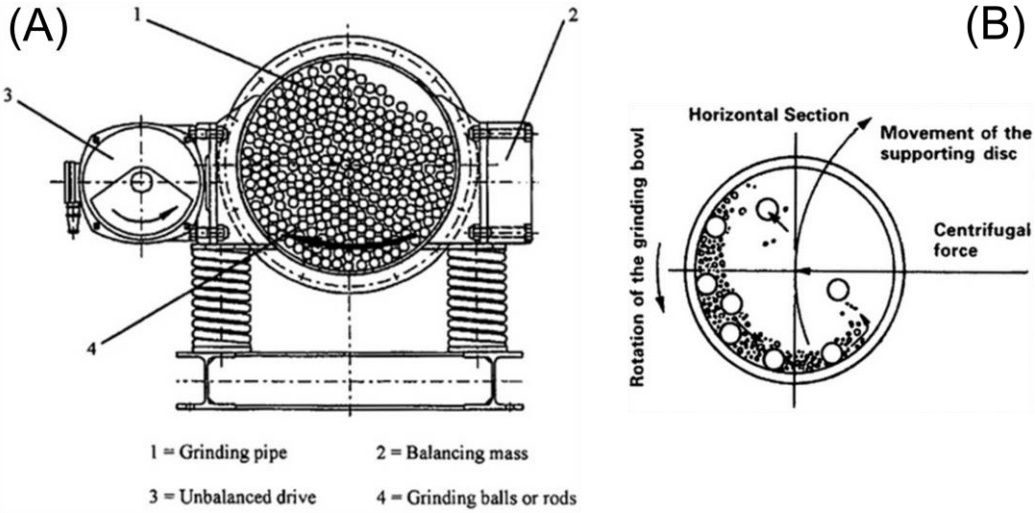

Figure 1.1 Diagram showing view of an eccentric dry vibration mill (A) and movements of working parts and balls in a planetary ball (B) which are frequently used in the pharmaceutical industry (Baláž, 2008).

However, dry milled material poses several issues for instance, a large number of fines, off-spec particle size distributions (PSD), agglomerated particles and undesired solid state transformations such as polymorphic change as a result of high energy input (Kougoulos et al., 2011). It has also been shown that the cost of dry milling can be more than the entire drug product formulation process (Variankaval et al., 2008).

In comparison, clearly therefore it is of interest to explore strategies that avoid the need for dry milling. Mechanical manipulation using wet milling has shown to be an appealing alternative for size control. If applied for particle size reduction, wet milling eliminates the need for separate offline dry milling and reduces the number of unit operations, costs and steps required in the manufacturing process. Also, the incorporation of wet milling with crystallisation allows for multipurpose functionality such as

particle size & shape manipulation, seed generation, accelerating the rate of crystallisation kinetics, mixing, de-agglomeration and presents an overall more flexible approach to particle engineering (Burcham et al., 2009). Wet mills can also be operated as continuous devices which is a highly promising feature in the continuous manufacturing of pharmaceuticals (Badman and Trout, 2015, Chatterjee, 2012, Kleinebudde et al., 2017). As drug structures become larger, costlier and more complex, crystallising directly to target requirements with strict manufacturing specifications is challenging and demanding. Hence, using particle engineering tools such as rotor-stator mixers (Burcham et al., 2009), ultrasound (Price, 2017) and static mixers (Jiang et al., 2014) can provide an additional means for crystallisation process control to achieve desirable outcomes such as faster filtration and drying rates and improved powder flow behaviour (Durak et al., 2018).

This thesis aims to investigate the impact of rotor-stator and indirect ultrasound devices on crystallisation processes. They are used as particle engineering tools for size reduction, shape control, accelerating the rate of nucleation and continuous seed generation on chosen model compounds. The advantages of process integration and multi-sensor analysis by combining high shear wet milling during crystallisation and for breakage on crystalline materials is studied (chapter 4 to 6). Furthermore, an industrial case-study (chapter 7) applying an indirect ultrasound platform is evaluated for control and tailoring of API particle attributes.

1.1. Milling

It is often convenient in industrial crystallisation to produce large crystals for ease of filtration. However, small particle sizes (< 50 μm) are preferred for manufacturing of solid oral dose forms as they possess high surface areas which improves inhalation and dissolution rates of poorly soluble compounds (Burcham et al., 2009). Mechanical milling (dry) is used not only for size reduction but also for problematic particle habits such as high aspect ratio needles to improve filtration and handling of the powder form and formulate (Variankaval et al., 2008). In theory, milling breaks up particles along the longest axis, reducing needle length whilst preserving width. A list of milling techniques commonly used in pharmaceutical manufacturing is shown (Table 1.1).

Table 1.1 Comparison of achievable particle size ranges from different milling technologies (Burcham et al., 2009).

	Hammer mill	Universal & pin mill	Jet mill	Jet mills internal classifier	Media mills	Toothed rotor-stator	Colloid mill
State & size (μm)	Dry	Dry	Dry	Dry	Wet	Wet	Wet
Very fine (50-150)	Yes	Yes	No	Yes	No	Yes	Yes
Super fine (10-50)	Yes	Yes	Yes	Yes	Yes	Yes	Yes
Ultra-fine (<10)	No	Yes	Yes	Yes	Yes	No	Yes
Colloidal (<1)	No	No	No	Yes	Yes	No	Yes

1.1.1. Size Reduction during Milling

Particle size reduction is defined as the mechanical breakdown of solids into smaller particles without changing their state of aggregation (Bernotat and Schönert, 2000). Many products undergo size reduction processes such as foods, pigments, ceramics, sugar, flour and spices (Bernotat and Schönert, 2000). For organic crystalline materials, the extent of size reduction can depend on the equipment type, loading conditions, milling residence time and intensity as well as the structural and mechanical properties of the compound. Mechanical properties include particle hardness, abrasiveness, toughness, brittleness, stress and elasticity (Zhou and Qiu, 2010). Ultimately, the applied force through impact, compression, shear or attrition influences size reduction (Baláž, 2008).

In a crystal lattice comprised of a regular structure, molecular ions are positioned and balanced through attractive and repulsive forces determined by intermolecular forces (Born and Lande, 1981). This leads to an arrangement in a crystal lattice of oppositely charged molecules in equilibrium at a free energy minimum. When a form of mechanical stress is applied to the crystal, the original positioning and orientation of molecules held in equilibrium positioning can change to new positions of higher free energy (Baláž, 2008). At certain stress levels, thermodynamics then compels the molecules to return to their original arrangement of lowest free energy resulting in returning elastic forces which counter

balances the applied stress (Zhou and Qiu, 2010). Therefore the crystal shape is recovered when the state of stress ceases.

A stress-strain curve can be plotted (Figure 1.2) for assessing particle behaviour under applied stress. Within Hooke's law which depicts a linear relationship between stress (σ) and strain (ε), the deformation of a solid body is reversible and is referred to as the elastic deformation region. The elasticity of a material can be measured by Young's modulus (E) through tensile experiments where it is defined as the proportionality coefficient between the tensile stress and strain ($\sigma = \varepsilon Y$) (Zhou and Qiu, 2010). When crystals of non-brittle nature are exposed to disruptive forces from high energy milling, these forces can exceed the elastic region (elastic limit or yield stress) and enter into an irreversible phase known as plastic deformation (Figure 1.2). Fracturing of crystals occurs only then beyond the plastic deformation phase which is marked as "Non-brittle fracture" as shown in Figure 1.2.

For brittle materials of a fragile nature, no elastic deformation is displayed. Fracturing of crystals occurs when the imposed stress exceeds the elastic limit (Figure 1.2). Materials that fracture or break are attributed to the energetics and the initial distribution and propagation of cracks (Baláž, 2008). Several studies have outlined the theory of crack formation and propagation in literature (Smekal, 1922, Rumpf, 1962).

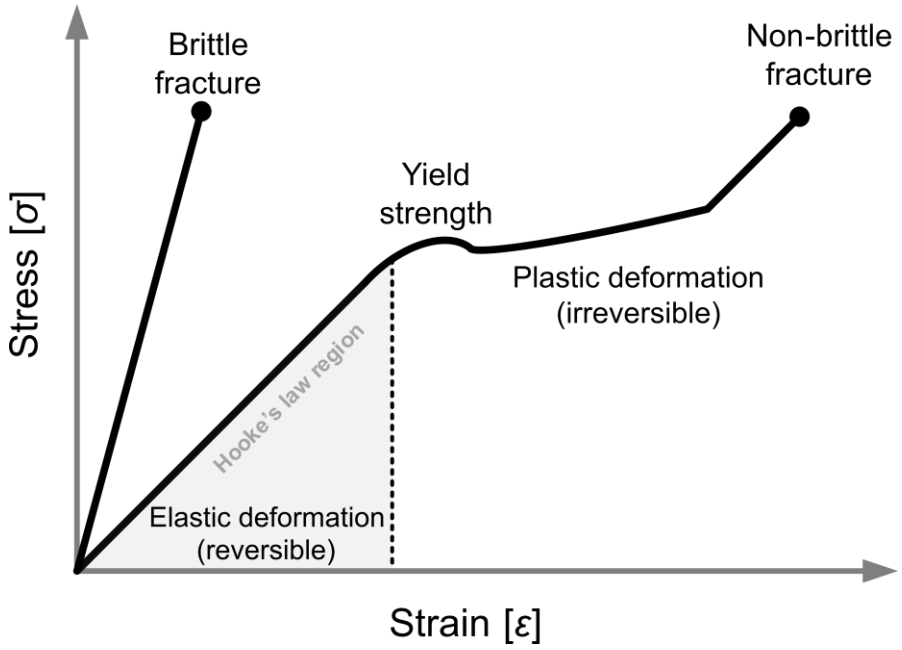

Figure 1.2 A stress-strain curve illustrating Hooke's law for materials under applied stress from mechanical force. Hooke's law states the force needed to extend or compress a spring by some distance is proportional to that distance (Zhou and Qiu, 2010).

Knowledge of breakage mechanisms and predicting the optimal energy input required for size reduction processes is important. This may avoid overmilled conditions of a final product thus avoiding detrimental effects such as potential disruption to the crystallinity (Luciani et al., 2015). To account for the energy input required from mechanical action, Kick, Rittinger and Bond derived empirical laws from a differential equation (Eqn 1.1) which assumed the energy required to produce a change dL in a particle of a size dimension L is a simple power function of L as shown (Hukki, 1961):

$$dE/dL = KL^n \qquad \text{Eqn 1.1}$$

Here, dE represents the differential energy required, dL is the change in a typical dimension; L is the magnitude of a typical length dimension and K, n are constants. The differential equation (Eqn 1.1) has been partially used for different industrial milling processes (Hukki, 1961, Juhász and Opoczky, 1990). It has also been applied for describing the fracturing of APIs through wet milling which is discussed later (Engstrom et al., 2013).

1.1.2. Wet Milling

Wet milling in a suspension medium is of great interest to the pharmaceutical industry as it can eliminate the need for an isolated size reduction processing step. This saves considerable time, cost, space and chemical exposure encountered with traditional offline dry mills (Kougoulos et al., 2011). They can be integrated as part of the crystallisation-isolation sequence which allows for greater flexibility in crystallisation process development and manipulating quality attributes (Harter et al., 2013). The importance of wet milling should also result in no yield loss, require no handling of the dry material and can be performed in such a way that crystal form changes can be avoided. A common practice is to directly wet mill (~ 1 – 2 hr) a crystallised suspension for imparting particle size reduction (Figure 1.3), de-agglomeration or shape modification (Cote and Sirota, 2010). An example of wet milling impacting on the type 2 diabetic drug metformin HCL is shown which demonstrates size reduction and shape modification to the crystalline material (Figure 1.3).

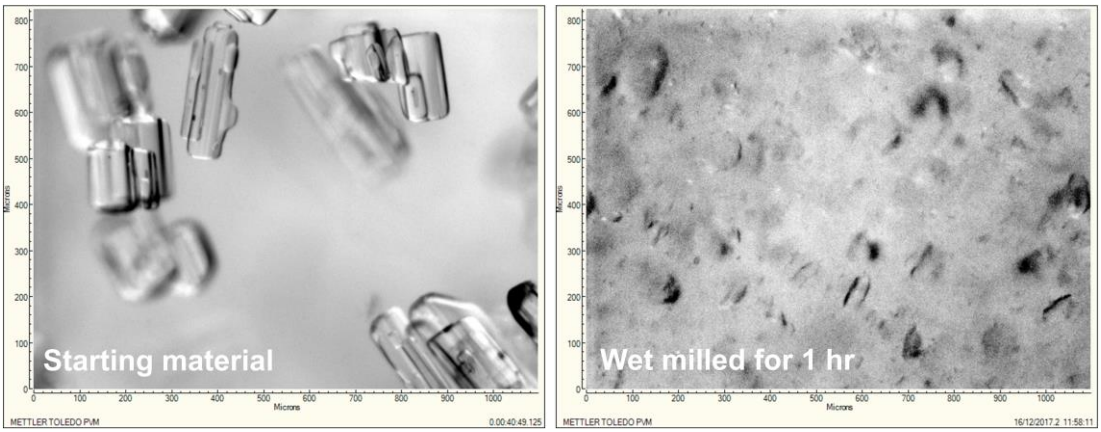

Figure 1.3 Images of metformin HCL particles which reduced from an average size of 1647 μm (start) to 71.50 μm (1 hr) during wet milling. The images were generated from own experimental work.

Wet mills are typically configured in a recycle-loop mode with the crystallisation vessel or a subsequent vessel which involves continuous recirculation of the suspension (Figure 1.4). This combined system has received significant interest and ongoing efforts which are later discussed and reviewed (section 1.4.1). The majority of wet mills can be operated in both batch and continuous processing modes. They can also be configured through a single-pass route which involves continuously passing the feed solution / suspension through one or more mills (Figure 1.4). Amongst the most commonly used wet mills for particle engineering of APIs are colloid mills, media mills and toothed rotor-stator mills (Table 1.1) as well as in situ homogenisers and ultrasound probes.

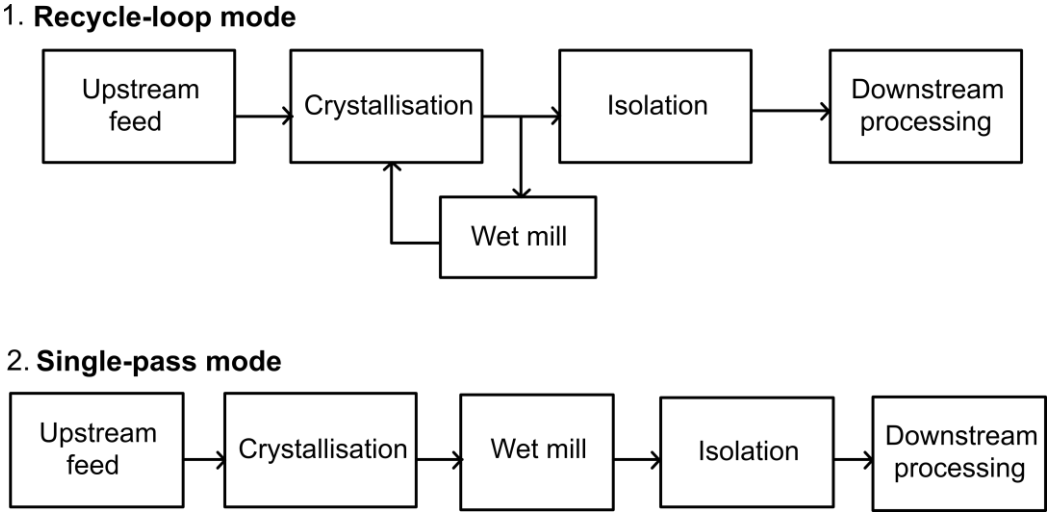

Figure 1.4 Processing routes for particle engineering of APIs through the recycle-loop and single-pass wet milling modes.

1.1.3. Rotor-Stator Devices

In processing industries, rotor-stator mixers are used as process intensive energy devices for accelerating homogenisation, dispersion, emulsification, wet milling, dissolution and mixing (Calabrese et al., 2002). Many of these devices consist of a high-speed rotor to a stator within the internal framework (Figure 1.5) where tip speeds of 50 m/s are achieved corresponding to high shear rates up to 100,000 s^{-1}. This leads to local high energy dissipation rates (1000 – 100 000 (W/kg or m^2/s^3)) as the kinetic energy generated by the rotor dissipates mainly inside the stator (Atiemo-Obeng and Calabrese, 2004). The energy dissipation across rotor-stator mixers have been reported to be up to three orders of magnitude higher than conventional stirred tanks (0.1 – 100 (W/kg or m^2/s^3)) (Zhang et al., 2012, Atiemo-Obeng and Calabrese, 2004). The key factors and characteristics for rotor-stator mixers are high speed, high shear and higher power as well as geometry.

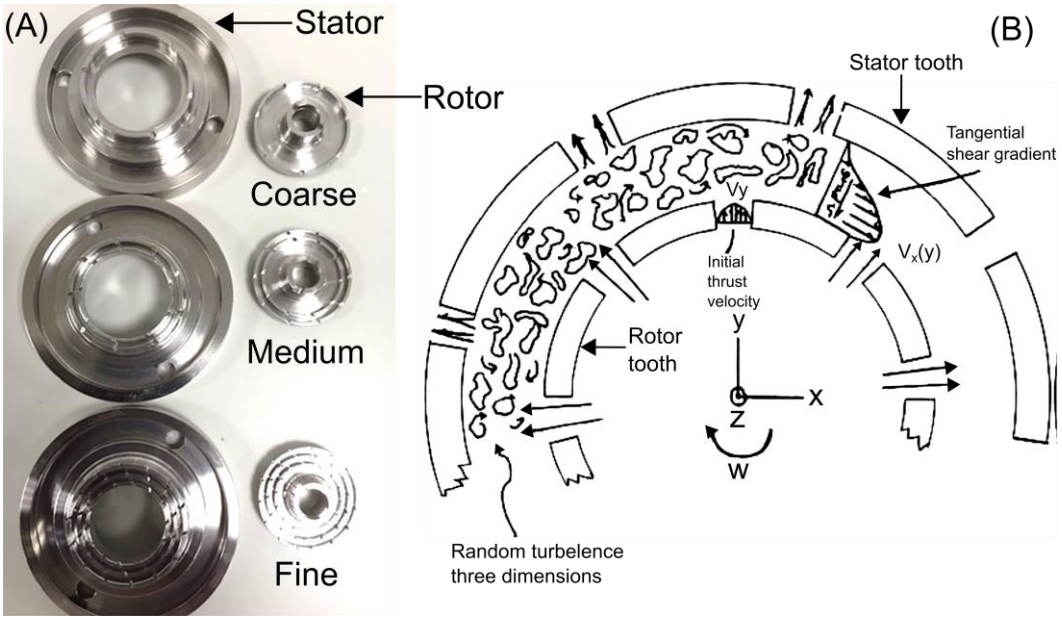

Figure 1.5 Image of rotor-stator modules (A) and schematic illustrating the hydrodynamics of a rotor-stator high shear mixing environment (B) (Atiemo-Obeng and Calabrese, 2004).

Newer high-shear mixers consisting of toothed rotor-stator wet mill (RSWM) devices are increasingly being employed for pharmaceutical processing (Harter et al., 2013). They consist of a spinning rotor with a fixed concentric stator with the number of teeth rotor rows (1 to 3) spread across the inner and outer diameter of the rotor and stator pair with a small gap in between (Figure 1.5). This gap can be changed across different equipment configurations (coarse, medium, fine).

The reduction in particle size is reported to occur from extreme high shear stresses (10^4 Pa) (Bałdyga et al., 2008, Luciani et al., 2015) and turbulence created between the alignment of the rotor and stator teeth during slurry flow (Figure 1.5). The mixing regime within a rotor-stator has been extensively analysed and modelled through computational fluid dynamics

(CFD) for emulsification (solid-liquid & liquid-liquid) applications which has shown the turbulence kinetic energy (m^2 / s^2) to dissipate rapidly (Atiemo-Obeng and Calabrese, 2004). However, there is limited information on the flow patterns, energy dissipation and different stator geometries during high shear wet milling of pharmaceutical molecules (Zhang et al., 2012). Yang (Yang, 2011) investigated wet milling of sucrose and mannitol using a Silverson L4R inline rotor-stator mixer. It was concluded the turbulent flow in the high shear mixer was complicated especially close to the mixing head and therefore the flow may not be completely isotopic. Thus, a Reynolds Stress Model and large eddy simulation through CFD is recommended to explain and describe the turbulent flow (Yang, 2011).

1.1.4. Breakage Mechanisms

The exact mechanism for particle breakage within the rotor-stator framework is yet to be concluded for crystalline materials. It has been suggested that in addition to fluid forces through shearing, particle-particle collisions and particle-wall (rotor-stator) collisions are dominant mechanical processes (Engstrom et al., 2013). Rotor-stator wet milling of crystalline suspensions has shown mass fracture and attrition as the two governing mechanisms for particle size reduction (Figure 1.6) (Hogg, 1999, Lee et al., 2004). Mass fracture is defined as the fragmentation of the parent crystal which produces two or more child particles of small sizes < 30 μm. This occurs during the early stages of wet

milling as the total stress being exerted onto the particles immediately exceeds the maximum elastic strain energy that the particles can store without relaxing as displayed earlier from the stress-strain curve in Figure 1.2 (Lee et al., 2004). On the other hand, attrition is considered a degradation mechanism arising from the mechanical stress exceeding the critical energy at the local edges of particles where chipping can also occur (Luciani et al., 2015).

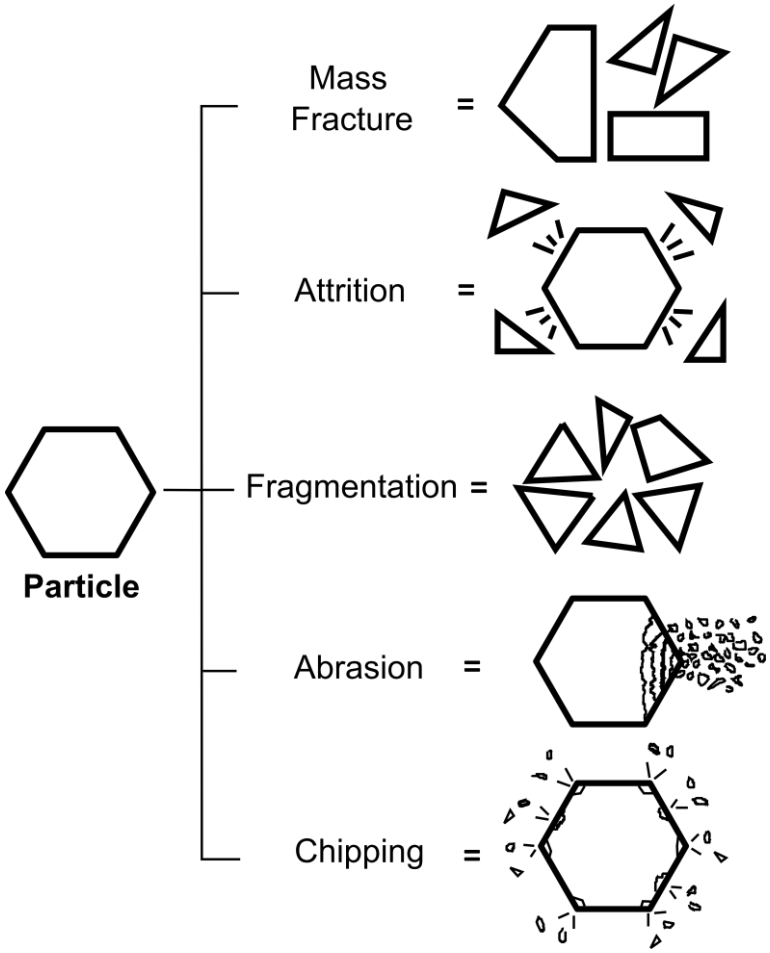

Figure 1.6 Sketch of breakage mechanisms that can potentially occur during various mechanical milling (dry & wet) and grinding processes of organic materials (Austin et al., 1976).

Population balance modelling (PBM) for estimation of breakage kinetics of wet milled materials is increasingly being studied. Austin et al (Austin et al., 1976) presented a model for quantifying the breakage rate and breakage distribution function in various types of mills (mainly dry) such as ball, vibration-ball, hammer, ball-race and shred-grinding processes. Although the model was built for ceramic materials, the breakage rate and distribution function was then adopted and demonstrated by Luciani et al (Luciani et al., 2015) for organic molecules. From the study, a mathematical model (first-order kinetics for breakage) through population balance modelling was built for describing the breakage of crystalline materials and the applicability of different scale-up factors to predict the milling performance. The outcomes of the model produced reasonable predictions with respect to the effect of changes in rotational speed, generator configuration and variability in the initial feed PSD (Luciani et al., 2015). Furthermore, Luciani (Luciani, 2018) constructed a master curve which correlated the relative critical particle size and relative cumulative energy imparted to particles for breakage analysis and particle size prediction. Interestingly, the master curve was shown to predict well for rotor-stator wet milling and other types of mill such as media and ball milling (Figure 1.7).

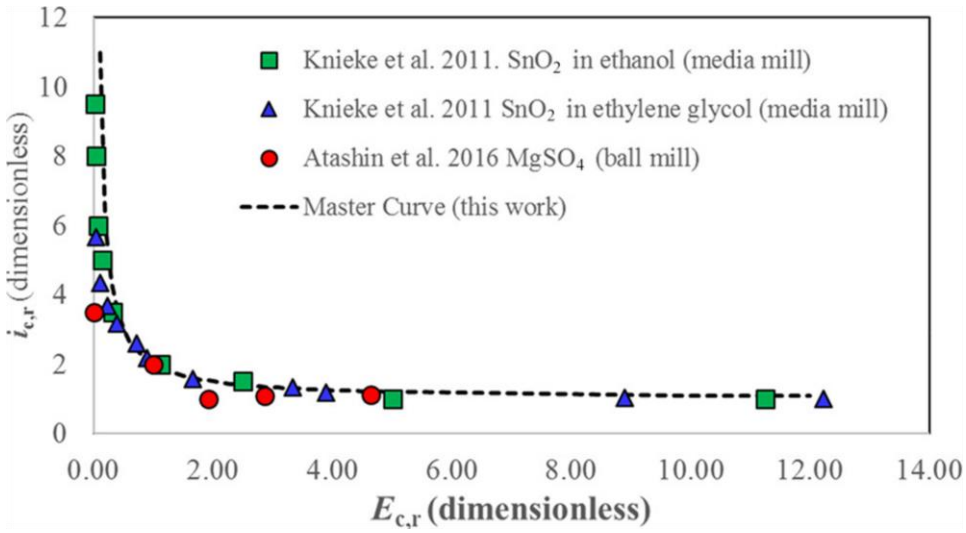

Figure 1.7 Normalised critical particle size vs normalised cumulative energy for different mills / materials. The dashed line corresponds to the master curve calculated for rotor-stator wet milling given by equation 12 in the reported source (Luciani, 2018).

The significance of different scale-up factors for predicting milling performance is often calculated. This includes, tip speed (S_r), shear rate (Υ) and shear frequency (f_s) = s^{-1}. Tip speed (S_r) = m / s is calculated from:

$$S_r = \pi D_r \omega \qquad \text{Eqn 1.2}$$

(D_r) = m is the outer diameter of the rotor and (ω) = s^{-1} is the angular (rotation) speed of the rotor. The shear rate (Υ) = s^{-1} can then be calculated as a function of tip speed and rotor-stator gap thickness (h) = m:

$$\Upsilon = \frac{S_r}{h} \qquad \text{Eqn 1.3}$$

To consider the different number of rotor-stator teeth used, the shear frequency (f_s) = s^{-1} can be determined:

$$f_s = N_r N_s \omega \qquad \text{Eqn 1.4}$$

Here, the number of teeth summed over all the rows on the rotor teeth ($N_r = \#$) and over all the rows on the stator teeth ($N_s = \#$) are included. The shear frequency (f_s) allows for different rotor-stator teeth pair configurations to be compared on a normalised basis from lab scale to pilot plant mill scale whereas using tip speed alone, information on the mill configuration is lost. This was shown to provide essential process understanding at lab-scale which resulted in rapid development of a robust process that was successfully scaled to 40 kg batches in pilot plant (Lo et al., 2012).

1.2. Crystallisation

Crystallisation has widespread use in healthcare products, electronic devices, dyes, pigments, foodstuffs, fertilizers, bulk and fine chemicals and medicines (Jones, 2002). Well-known products include salt, sugar, diamond, sodium carbonate and zeolite crystals (Jones, 2002). In pharmaceutical drug manufacturing, multiple crystallisation unit operations are often required during chemical development as it is a critical separation and purification technique resulting in a solid-liquid mixture. Control of crystallisation with optimal properties is therefore important to ensure the quality of the administered pharmaceutical drug.

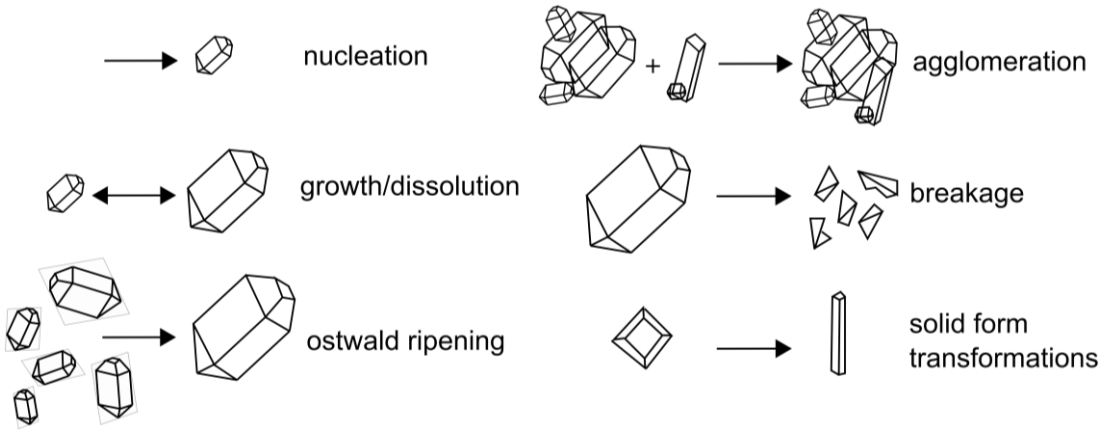

Figure 1.8 Various crystallisation mechanisms that can occur during process development (Mazzotti et al., 2015).

However, a range of crystallisation mechanisms typically occur which can have a considerable effect on downstream processing (Figure 1.8). For example, a wide particle size distribution may cause slow filtration rates and inefficient drying which can be a major bottleneck to the entire manufacturing process development (Kim et al., 2005).

1.2.1. Crystallisation Mechanisms

Nucleation is a stochastic event which involves "birth" of small nuclei followed by growth of these nuclei into larger crystals within a supersaturated solution (Myerson, 2002). Nucleation occurs under the influence of supersaturation to allow the system to reach equilibrium in solution which requires a change of free energy and must precede an activation barrier (Gibbs, 1928). For crystallisation process development, determining the phase diagram is important as it outlines the solubility of an API in a given solvent composition. The solubility of an API is the maximum concentration that exists at equilibrium for a solid and liquid

phase for a given set of temperatures and pressures which is often displayed as a solubility line or curve (Figure 1.9) (Jones, 2002).

To access the formation of crystals, a supersaturated phase must be reached above the solubility curve (Figure 1.9). Supersaturation is defined as the driving force for crystallisation and is given by the change in chemical potential ($\Delta\mu$). The chemical potential ($\Delta\mu$) describes the difference between the liquid phase (μ_L) and the solid crystalline phase (μ_C). For a saturated solution which is in equilibrium with the solid solute, the liquid phase (μ_L) and solid crystalline phase (μ_C) are equal and therefore the chemical potential is zero. When the solution is supersaturated, the chemical potential is expressed in terms of standard potential (μ_0) and the standard activity (a) (Davey and Garside, 2006):

$$\Delta\mu = \mu_0 + RT \ln a \qquad \text{Eqn 1.5}$$

Here, the gas constant (R) = 8.134 J mol^{-1} K^{-1} and temperature (T) = K are included. Equation 1.5 is rearranged to:

$$\frac{\Delta\mu}{RT} = \ln\left(\frac{a}{a^*}\right) = \ln S \qquad \text{Eqn 1.6}$$

Where the standard activity of the solution phase (a) and the standard activity of the crystalline phase (a^*) are included. The supersaturation is the so called supersaturation ratio which is expressed as follows:

$$S = \frac{c}{c^*} \qquad \text{Eqn 1.7}$$

Equation 1.7 includes the solution concentration (c) and the equilibrium solution concentration (c^*) at a constant temperature and pressure. The supersaturation is also commonly expressed as the relative supersaturation (σ) for an ideal solution whereby the activity is independent of concentration and c / c^* ≈ 1:

$$\sigma = \frac{c - c^*}{c} \qquad \text{Eqn 1.8}$$

A certain degree of supersaturation is required before spontaneous nucleation occurs at an appreciable rate and is observed within a finite time interval. The extent of this supersaturation is referred to as the metastable zone limit (Barrett and Glennon, 2002). Hence, measuring the metastable zone width (MSZW) from the solubility profile becomes important as regions for nucleation-dominated and growth-dominated crystallisation can be identified in the phase diagram (Figure 1.9). Supersaturation generation can be achieved by different crystallisation methods such as cooling (Brown and Ni, 2012), anti-solvent addition (Svoboda et al., 2017), evaporative (Warzecha et al., 2017) and through reactions (McGinty, 2017, Jiang and Ni, 2019). Cooling crystallisation is the most commonly employed method in industrial crystallisation (Myerson, 2002).

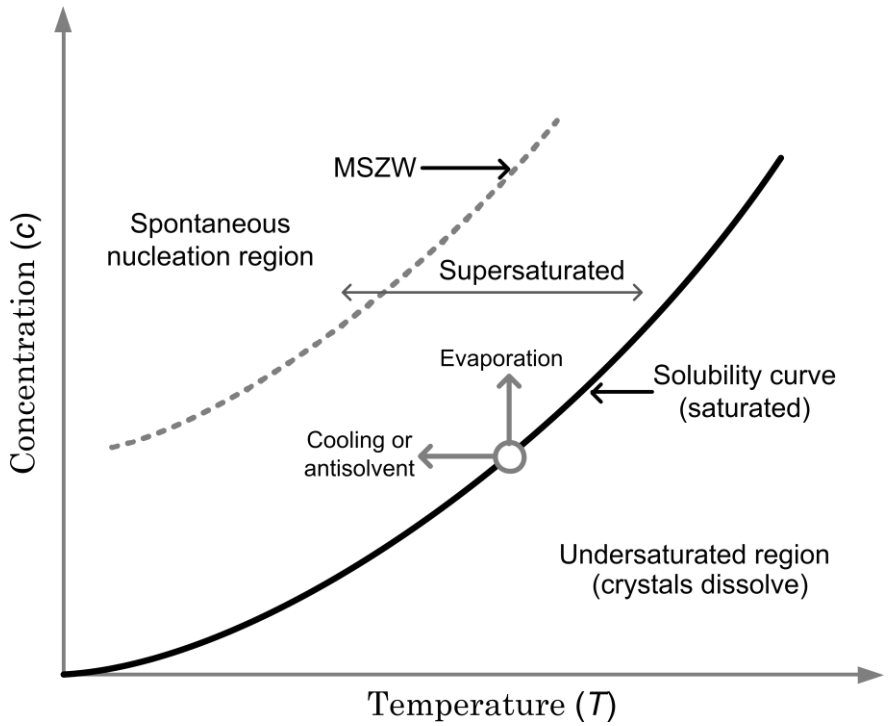

Figure 1.9 Example of a solubility represented as a solid 'black' line and metastable zone width shown as a dashed 'grey' line profile for crystallisation process development (Jones, 2002).

1.2.1.1. Primary Nucleation

Nucleation can be divided into two-types; primary and secondary nucleation where primary is classified as homogeneous or heterogeneous nucleation. Homogeneous nucleation occurs without the presence of any surfaces, whereas heterogeneous nucleation is induced through the presence of non-crystalline surfaces which provides adsorption for solute molecules and reduces the free energy barrier for nucleation (Erdemir et al., 2009).

A number of theories (classical, non-classical, two-step) have described the origins of homogenous nucleation (Vekilov, 2010). The classical nucleation theory (CNT) involves the clustering and aggregation of molecules or ions

to a critical size (nuclei) with an associated total free energy difference (ΔG) for its formation and growth (Figure 1.10). Typically, the critical nuclei are well below the detection limit and therefore in accordance with the CNT theory, a nucleus is a particle with a size:

$$^{d}/_{dL}\ (\Delta G) = 0 \qquad \text{Eqn 1.9}$$

Above the critical nucleus size, the total free energy difference (ΔG) is defined between a small solid solute particle and the solute in solution which includes the sum of free energy required to create a surface excess free energy (ΔG_s) and the volume excess free energy (ΔG_V) (Davey and Garside, 2006, Mullin, 1997):

$$\Delta G = \Delta G_v + \Delta G_s \qquad \text{Eqn 1.10}$$

The summation involves the free energy of volume (ΔG_V) outweighing the free energy of the surface (ΔG_s) of the cluster. This corresponds to the critical free energy difference, ΔG_{crit} and associated nucleus radius (r_c) showing the minimum size a cluster must achieve to remain stable and grow which leads to a decrease in free energy (Figure 1.10). Hence, clusters of sizes less than the associated nucleus radius (r_c) will dissolve. Evidently, from the free energy diagram (Figure 1.10), it is assumed from the CNT theory that at constant temperature and supersaturation, a decrease in concentration is minimal upon formation of the critical nucleus.

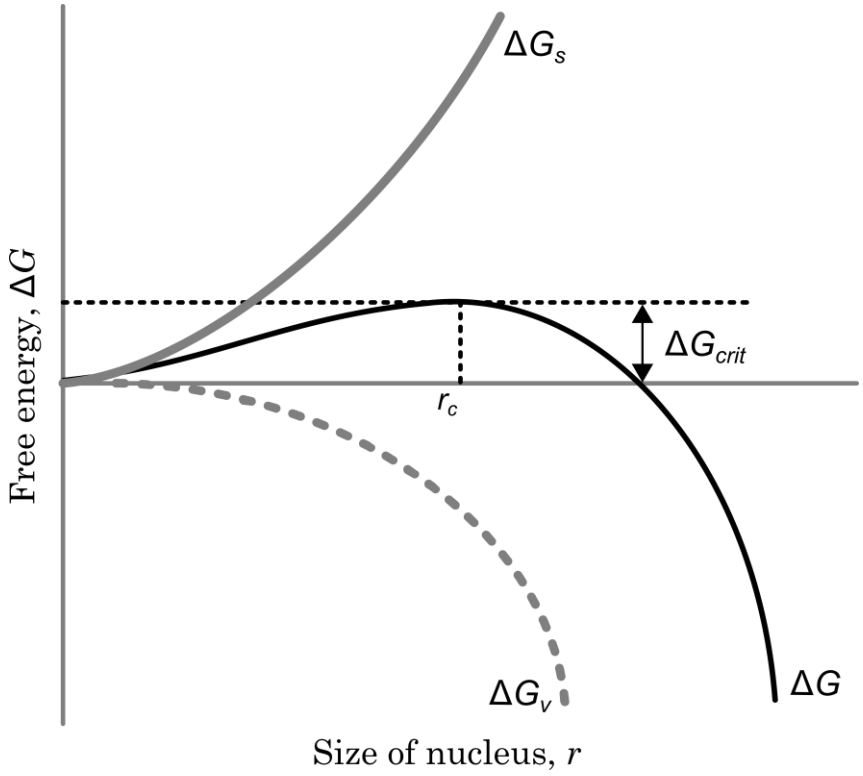

Figure 1.10 Free energy diagram for nucleation (Erdemir et al., 2009).

However, both the height of the barrier and the ΔG_{crit} value decrease with increasing supersaturation with the barrier eventually becoming small enough for nucleation to become spontaneous (Davey and Garside, 2006). The rate of nucleation, J, i.e., the number of nuclei can be expressed in the form of the Arrhenius reaction equation:

$$J = A \exp(-{}^{\Delta G}/_{\boldsymbol{k}T}) \qquad \text{Eqn 1.11}$$

Where the number of nuclei formed per unit time per unit volume (J) = # / s.m^3, rate constant (A) = # / s.m^3, Boltzmann constant ($\boldsymbol{k}$) = 1.3805 x 10^{-23} J / K and temperature (T) = K are expressed.

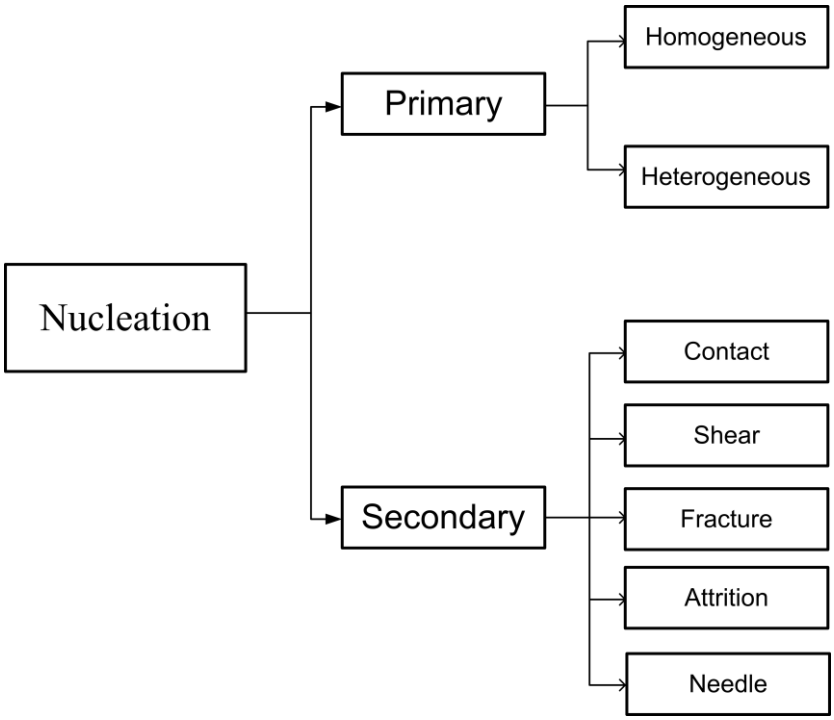

Figure 1.11 Classification system for primary and secondary nucleation mechanisms (Jones, 2002).

1.2.1.2. Secondary Nucleation

Secondary nucleation occurs in the presence of crystals and usually results from the introduction of 'seed' crystals in the supersaturated solution (Agrawal and Paterson, 2015). Widely debated in literature, a variety of secondary nucleation mechanisms can occur (Figure 1.11). These range from contact with other crystals or crystalliser parts, shear from fluid flow / turbulence or crystal-impeller impact, fracture due to crystal-crystal or crystal-wall impact, attrition from fluid flow, crystal-crystal, crystal-impeller and crystal-wall impact (Davey and Garside, 2006). These mechanisms can have a considerable impact on the rate of secondary nucleation kinetics and the obtained crystal size and size distribution. To

describe the overall rate process of secondary nucleation, equation 1.12 can be used (Davey and Garside, 2006):

$$B = k_b M_T^J N^k \Delta c^b \qquad \text{Eqn 1.12}$$

Where the secondary nucleation rate (B), stirrer speed (N) = a.u, concentration of crystals in solution (M_T), specified function of the vessel geometry (k_b), supersaturation (c) and exponents (J, k and b) are parameters determined by the particular assumptions of the model (Davey and Garside, 2006). In crystallisation process development, applying a secondary nucleation mechanistic model is important as it can assist in the estimation of nucleation rates from small scale experiments to commercial scale plants (Garside and Davey, 1980, Briuglia et al., 2018, Steendam et al., 2018).

1.2.1.3. Crystal Growth

The growth crystals of visible size occurs after nucleation which determines the final particle size, shape and purity. Several theories have outlined crystal growth mechanisms which have focused on the propagation of steps on the crystal surface either by two-dimensional nucleation or by the screw dislocation of the BCF theory (Myerson, 2002). However, the majority of industrial crystallisations and mass transfer processes correlate data to the diffusion-reaction layer model.

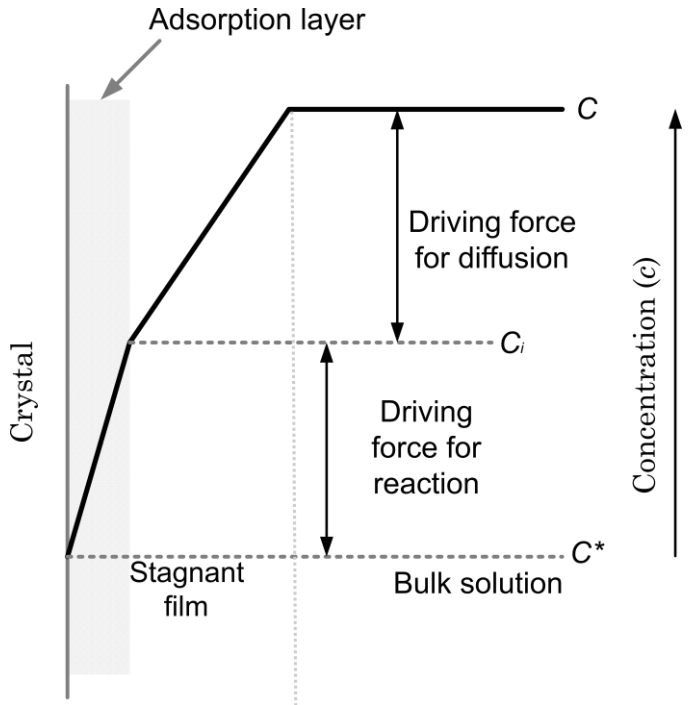

Figure 1.12 Crystallisation driving forces during crystal growth (Mullin, 1997). C, C_i, C^* represent the bulk, crystal-liquid interface and equilibrium solubility. The stagnant film is often denoted as δ which indicates the degree of thickness.

This is a simple model which outlines the diffusion of solute from the crystal-liquid interface through a stagnant film which is then incorporated into the crystal leading to a concentration decrease at the crystal-liquid interface (Figure 1.12). Detailed descriptions of the diffusion-reaction layer model from the works of Noyes and Whitney (1897), Nernst (1964), Berthoud (1912) and Valeton (1924) is reported (Mullin, 1997). As a crystal is comprised of various faces, these faces can possess individual growth rates leading to particles of different morphologies such as spherical, needles and platelets. Typically, crystal growth can be expressed as a

linear growth rate (G) = m / s where L is the characteristic dimension that is increasing:

$$G = \frac{dL}{dt} \qquad \text{Eqn 1.13}$$

Equation 1.13 can be extended to include the overall driving force and temperature effects:

$$G = A\, exp\left(\frac{-E_G}{RT}\right)\,(S-1)^g \qquad \text{Eqn 1.14}$$

Where, the constant (A), activation energy (E_G) = kJ / mol and order of growth (g) are included. The crystallisation kinetics of nucleation and growth can then be correlated with supersaturation using empirical expressions of the form:

$$B = k_b \Delta c^b \qquad \text{Eqn 1.15}$$

$$G = k_g \Delta c^g \qquad \text{Eqn 1.16}$$

Here, nucleation rate constant (k_b) = m / s, nucleation order (b) and growth rate constant (k_g) = m / s are shown. Determination of crystal growth rates can then be used to inform crystallisation process development.

1.2.1.3.1. Estimation of Growth Rates

Measuring crystal growth rates have relied on growth of a single seed crystal where direct measurement of the change in mass or size of a crystal (or crystals) at a fixed temperature and supersaturation is obtained. Several repeats at different temperatures and supersaturations can then determine kinetic parameters by fitting to a power law model (Myerson, 2002). Various single crystal growth measurements and procedures are known (Botsaris and Denk Jr, 1970, Clontz et al., 1972).

In crystallisation processes where many crystals are growing in bulk suspension, crystal growth rates can be estimated from batch isothermal experiments. The rate of desupersaturation along with the initial mass and size of the seed and final product crystals is used to estimate growth rates which is widely implemented for process design and modelling purposes (Mitchell et al., 2011, Garside, 1982, Qiu and Rasmuson, 1994, Vetter et al., 2013, Myerson and Ginde, 2002, Pérez-Calvo et al., 2016, Vetter et al., 2011).

1.2.1.4. Materials Balance

The reactors used in crystallisation processes usually include batch stirred reactors, continuous stirred tank (CSTR) or plug flow reactors (PFR). Calculating the material balance for an individual reactant or product is essential for process understanding (Figure 1.13).

accumultation of moles in element per unit time	=	moles entering element per unit time	-	moles leaving element per unit time	-	moles dissapearing due to reaction per unit time
(1)		(2)		(3)		(4)

Figure 1.13 A typical material balance used for chemical reactors.

In batch processing, there is no addition or removal of products during the reaction (Figure 1.14, (A)). Therefore, terms 2 and 3 will equal zero and when operating at steady-state, term 1 is zero. For a CSTR, the process has a continuous supply of feed material whilst products are continually being removed (Figure 1.14, (B)). Likewise to batch which assumes perfect mixing, there are no concentration or temperature gradients within the reactor. A plug flow reactor is a type of tubular reactor whereby feed material is continuously supplied to the reactor and products are continually removed (Figure 1.14, (C)). The velocity profile in a plug flow reactor is uniform over any cross-section normal to the direction of the fluid motion thus in a plug flow crystalliser, the assumption is that there is perfect radial mixing but no axial mixing.

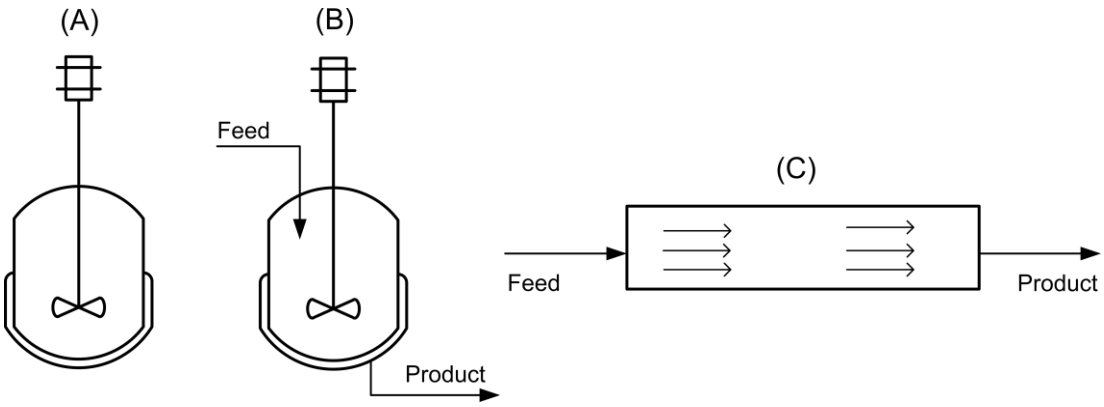

Figure 1.14 Sketch of a batch reactor (A), continuous stirred tank reactor (B) and a plug flow reactor (C) which are used for crystallisation processes.

1.2.1.4.1. The Population Balance

Knowledge of crystallisation mechanisms (Figure 1.8) along with the three conservation laws (mass, energy and crystal population) can generate population balance models (Mersmann, 2001). PBMs are important as they can establish clear and quantitative relationships between variables and characterise key components of a crystallisation process such as nucleation and growth rates (Randolph and Larson, 1988, Randolph and Larson, 1962). They are particularly useful for batch and continuous crystallisers for modelling of PSDs. However, in the case of a continuous crystalliser, PBMs with only growth and nucleation terms yields an analytical expression for the PSD (Randolph and Larson, 1962). Consider the equation for a well-mixed mixed-suspension mixed-product removal (MSMPR) crystalliser:

$$n = n^{\circ}\exp(-\frac{L}{G\tau}) \qquad \text{Eqn 1.17}$$

Where the population density (n°) at L = 0 (i.e., the nuclei), linear crystal growth rate (G) and the residence time in the crystalliser (τ) is shown (Tung et al., 2009). Plotting ln n versus L will then result in a straight line with slope ($1/G\tau$) (Figure 1.15, (B)). As the growth rate can now be determined, the intercept n° is converted to the nucleation rate ($B^{\circ} = n^{\circ}G$) which can possess other variants. However, a few assumptions are made.

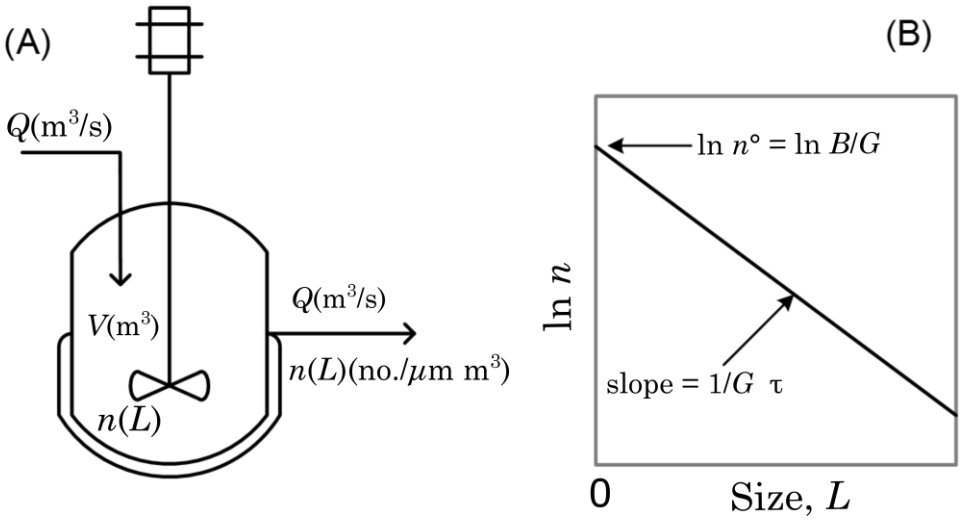

Figure 1.15 Schematic of an MSMPR crystalliser with a volume V (m^3) fed with solution at a volumetric rate Q (m^3/s) (A). Upon nucleation and growth, the population density of particles $n(L)$ are represented which have the same crystal size distribution as in the product stream (A). Equation 1.17 is graphically presented in the semi-logarithmic form which predicts the number density to decay exponentially with size at a rate determined by the growth rate and the mean residence time (B) (Davey and Garside, 2006).

For instance; the process is assumed to be at steady state, no presence of crystals in the initial feed stream, all crystals are of the same shape and characterised by a chosen linear dimension L, no attrition occurs and crystal growth rate is independent of the crystal size. These assumptions may not be fulfilled for many organic molecular crystallisations as has been reported in detail elsewhere (Randolph and Larson, 1988, Tung et al., 2009). Recent efforts have also attempted to describe particle shape evolution in MSMPR crystallisers using morphological population balance models (Ramkrishna and Singh, 2014).

1.2.2. Seeding Crystallisation

A well-controlled crystallisation process can be achieved through the addition of seed crystals of the desired crystal form. The ideal seeding conditions (in terms of supersaturation, temperature, agitation) would be to minimise both primary and secondary nucleation whilst conserving the number of crystals during crystal growth within the MSZW (Mullin, 1997). This helps to ensure consistent product attributes (size, shape, form) and process efficiency. To promote the growth of large uniform crystal sizes, a range of seeding parameters should be controlled. These include varying the initial seed size distribution, mass loading (1 – 10 %), form, addition point and addition rate which can all have a considerable effect on the crystallisation trajectory and final product quality (Aamir et al., 2010, Beckmann, 2000).

The generation of seeds is usually sourced through dry milling of the raw supplied material (vendor) or recrystallised material. Milled seeds can then be divided into different particle size fractions through a sieve shaker. For cooling crystallisation, small seed sizes < 10 μm are preferred as this provides high surface areas (typically > 5 m^2 / g) for early stages of growth and targeting a uniform particle size distribution (Ward et al., 2006, Brown et al., 2018). It is recommended to prepare and charge seeds to the reactor as a slurry suspension rather than dry seed handling and addition (Cote and Sirota, 2010).

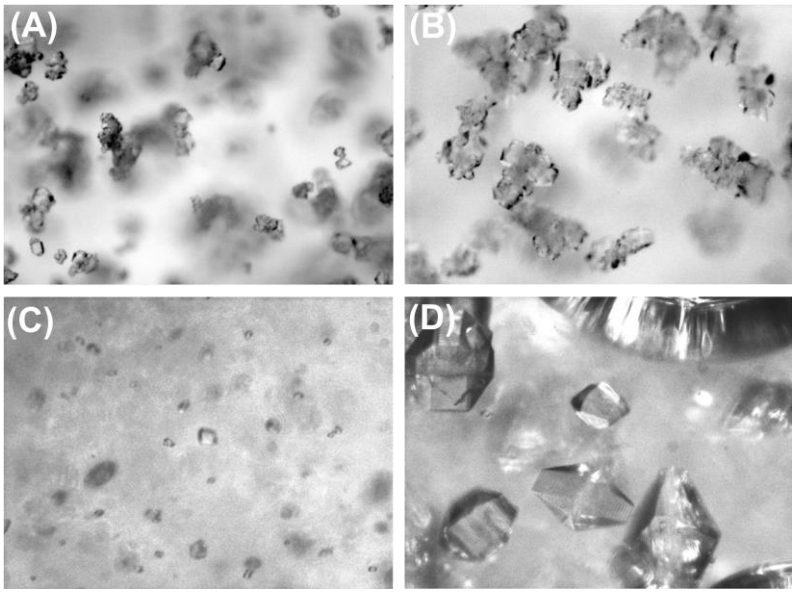

Figure 1.16 In situ particle images during a crystallisation showing the impact of seed input (A & C) on the product output (B & D) for acetaminophen. A cooling crystallisation was implemented for both experiments. The images were generated from own experimental work.

For instance, consider the impact of seed preparation and addition on the crystallisation of acetaminophen (Figure 1.16). Here, agglomerated seeds prepared through dry milling and sieving and dry addition (Figure 1.16, (A)) crystallised to agglomerated product crystals (Figure 1.16, (B)). Alternatively, seeds generated and added as a slurry suspension through wet milling (Figure 1.16, (C)), crystallised to large uniform and well-faceted product crystals (D). During a cooling crystallisation process, the cooling rate is a key parameter to consider when designing the crystallisation (Figure 1.17). To deliver an optimal process for growth, implementing supersaturation control through a determined concentration-temperature profile is the ideal strategy as this can avoid any undesired and uncontrolled nucleation or fouling events (Figure 1.17, (C – D)).

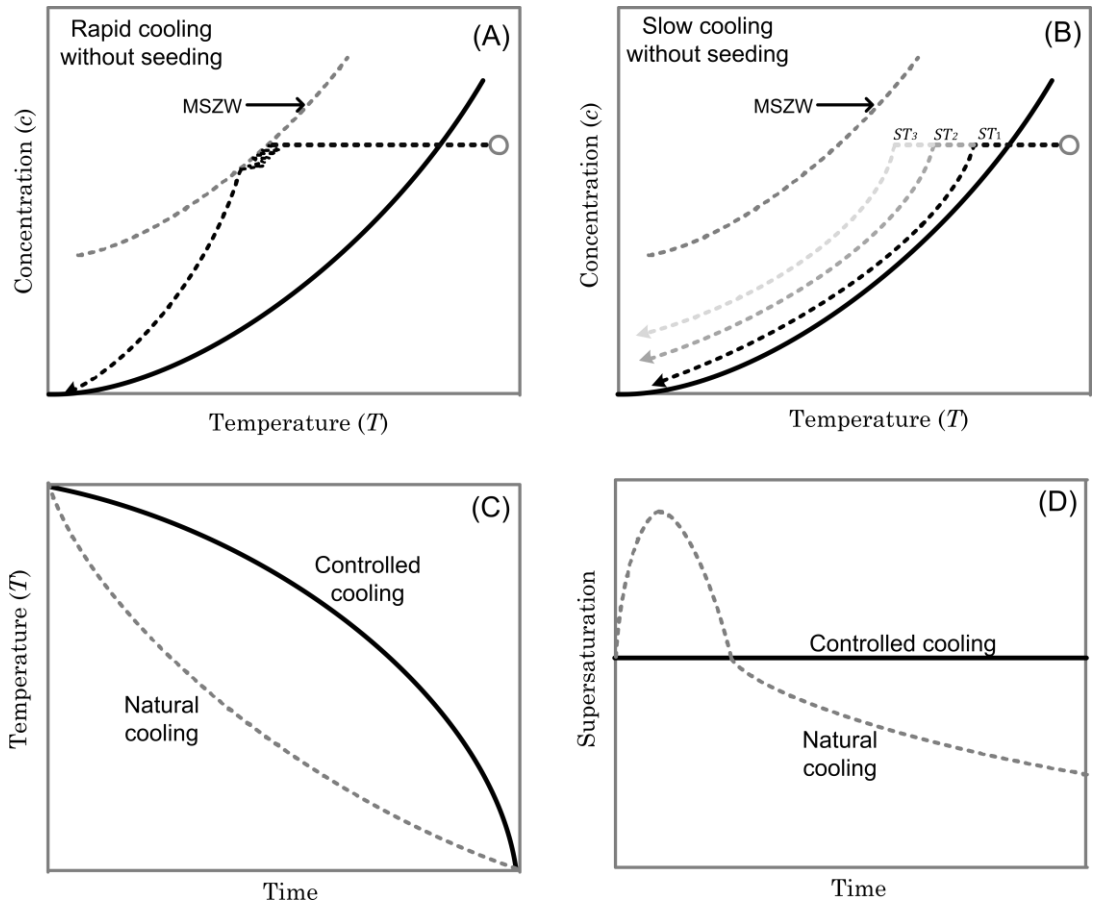

Figure 1.17 Seeding and cooling profiles for a cooling crystallisation (Jones, 2002). Solid 'black' lines represent the solubility and MSZW (annotated) as a 'grey' dashed line (A - B). Rapid cooling without seeding supersedes the MSZW boundary leading to uncontrolled primary nucleation (A) whereas seed addition at different and higher temperatures ($ST_{1\text{-}3}$) followed by a slow cooling profile leads to controlled crystallisation (B). The impact of controlled cooling versus natural cooling can also effect supersaturation generation and consumption (C – D).

There is also considerable work being done on model-based and direct design approaches for cooling crystallisation such as direct-nucleation control (DNC) controlled by process analytical technology which has been applied to unseeded crystallisations (Abu Bakar et al., 2009, Saleemi et al., 2012, Nagy and Braatz, 2012).

1.2.3. Continuous Manufacturing of Pharmaceuticals

There is increased interest in continuous manufacturing for pharmaceuticals as it can present numerous advantages over traditional batch manufacturing methods. These include better product quality, reduced variability, processing times and cost and increased process flexibility (Badman and Trout, 2015, Kleinebudde et al., 2017). The drive for continuous processing has placed great emphasis on leading industry manufacturers and research institutes for creating and exploring more modular processing environments. For example, continuous-flow technologies and single-use systems provides substantial inventory reduction and supply chain benefits as the demand for small-molecule manufacturing increases (Kuehn, 2018). A study by Grand View Research expects small-molecule APIs to account for the largest share of the pharmaceutical market, rising to $239.8 billion by 2025 (Challener, 2018).

Small-volume continuous manufacturing for delivering APIs on-demand and end-to-end integration of all unit operations from drug substance to drug product offers the biggest benefits, flexibility and cost effectiveness for regulatory agencies (Cole et al., 2017, Mascia et al., 2013, Srai et al., 2015). Eli Lilly demonstrated small-volume continuous manufacturing for API production using eight continuous unit operations including extractors, evaporators, crystallisers and filters during drug substance manufacturing (Cole et al., 2017).

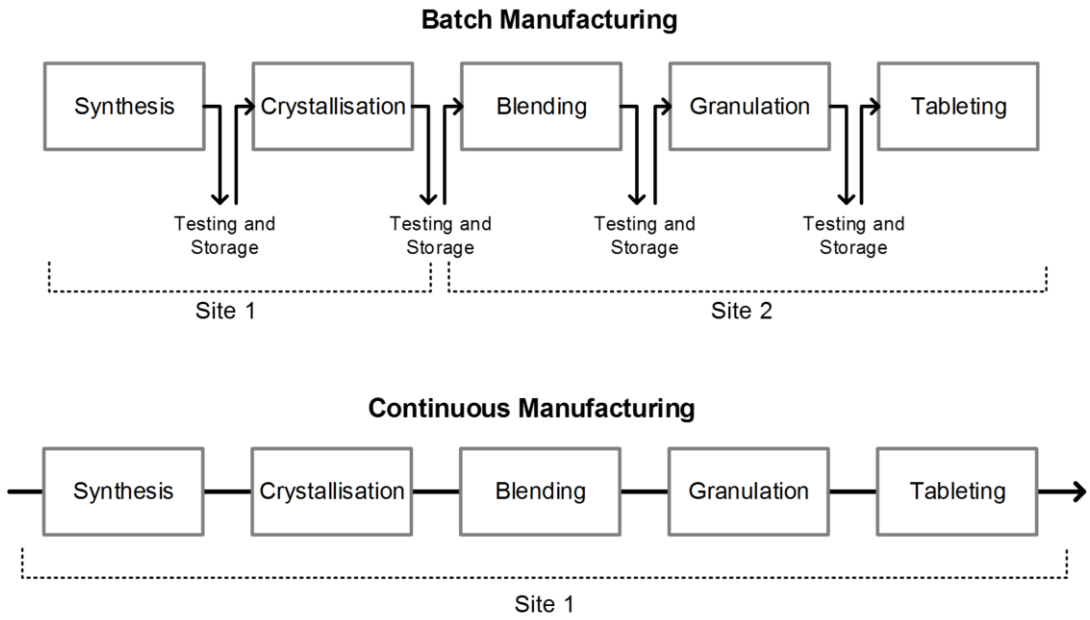

Figure 1.18 Batch manufacturing involves discrete and separate steps in which production stops between steps, so samples can be tested for quality offline. Pharmaceuticals made using continuous manufacturing are moved nonstop within a single facility, eliminating hold times between steps. (Kuehn, 2018).

The multistep continuous-flow CGMP process produced 24 kilograms (3 kg per day) of the cancer drug prexasertib monolactate which was suitable for use in human clinical trials (Cole et al., 2017). Recently, the U.S. Food and Drug Administration (FDA) approved Orkambi (lumacaftor / ivacaftor), which is a new cystic fibrosis drug using continuous drug product manufacturing methods, specifically direct compression at Vertex pharmaceuticals (Nasr et al., 2017). In 2016, the U.S. FDA also approved Janssen Pharmaceuticals, Inc., switch in the production method from batch to continuous drug product manufacturing for the existing product, Prezidarunasta (Nasr et al., 2017). So although the portfolio of produced drugs through continuous manufacturing methods is still relatively small,

these examples represent a significant step in integrating continuous manufacturing into commercial pharmaceutical production.

The interest in continuous manufacturing has also led to the establishment of research initiatives between academia and industry. These include the Novartis-MIT Center (U.S), EPSRC Future Manufacturing Research Hub in Continuous Manufacturing and Advanced Crystallisation (CMAC, U.K) and Center for Structured Organic Particulate Systems (C-SOPS, U.S).

1.2.3.1. Continuous Crystallisation

As part of this change, there is a need to design and implement continuous unit operations. Continuous crystallisation is therefore of interest and has been demonstrated across a range of processing technologies, compounds and reactor types such as single and multiple-stage continuous stirred reactors (Wood et al., 2019, Baxendale et al., 2015). Other crystallisation reactors for continuous processing include oscillatory baffled reactors (Lawton et al., 2009, McGlone et al., 2015, Briggs et al., 2015), segmented flow (Robertson et al., 2016, Jiang et al., 2014) and static mixers (Baxendale et al., 2015).

Key advantages of continuous crystallisation over batch include reduced process start-up and time to reach steady-state (Powell et al., 2015), high yields and purity (Quon et al., 2012, Wong et al., 2012), enhanced control of the physical properties of the crystalline product (Alvarez et al., 2011, Vetter et al., 2014) and scale-up or scale-out which can be achieved with

less effort and risk (Zhao et al., 2014). However, there are certain points which should be taken into consideration when selecting conditions for continuous crystallisation in particular when complex phenomena such as secondary nucleation, attrition, fouling, encrustation or agglomeration can significantly complicate the process as well as equipment design (Brown et al., 2017).

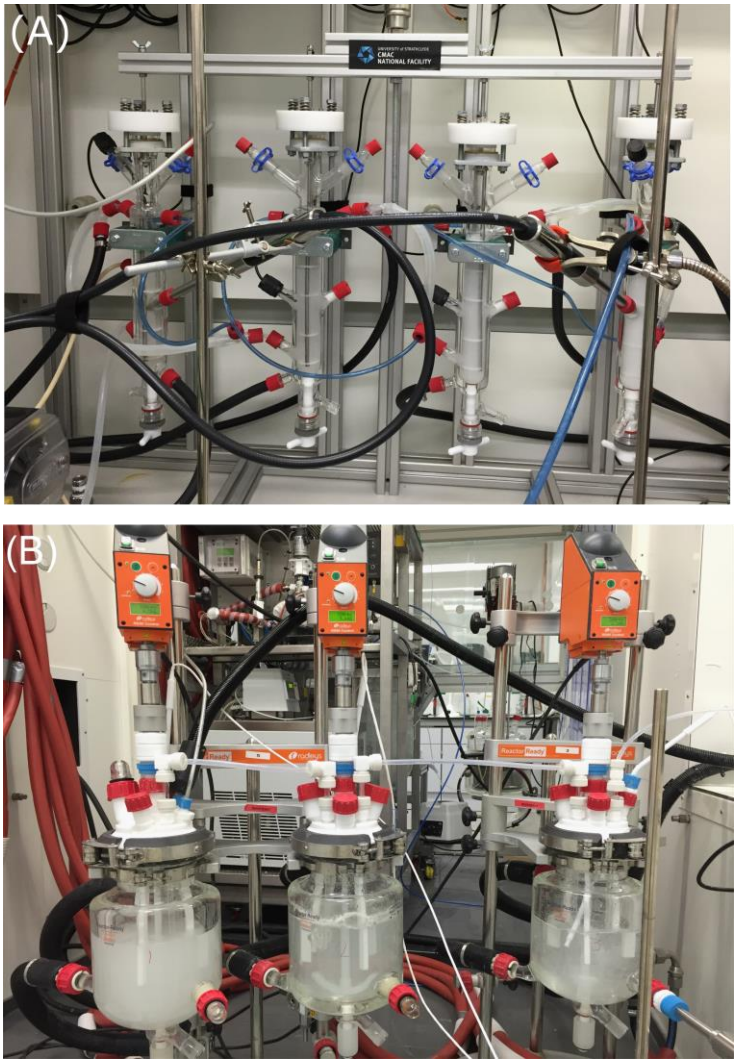

Figure 1.19 Images of continuous crystallisation platforms; moving baffle oscillatory baffled crystalliser (A) and a mixed-suspension mixed-product removal crystalliser (B).

1.3. Particle Attributes

In particle manufacturing, tracking and controlling physical attributes of the constituent particles is necessary for drug product development and process understanding (Ticehurst and Marziano, 2015). Particle attributes including size, shape and surface areas that are impacted by crystallisation can show impact on manufacturability, oral bioavailability and dosage forms (Leane et al., 2018). The demand for tight particle attribute control become increasingly important when low-solubility compounds are required for drug formulators as particle size can be used to improve API dissolution in the gut (Variankaval et al., 2008). As mechanical milling processes such as high shear wet milling are frequently being employed, establishing the influence of process-induced disorder to changes in API attributes is important which is summarised in Figure 1.20.

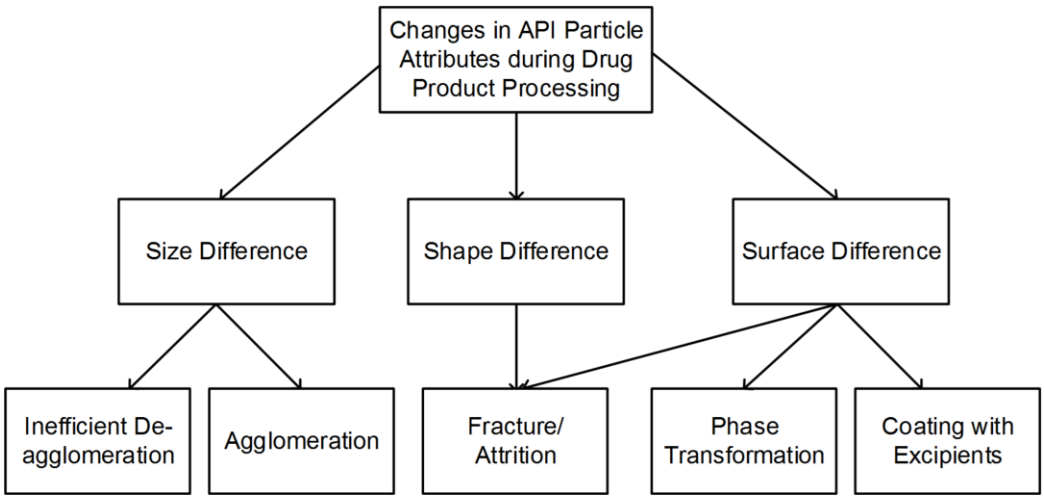

Figure 1.20 Establishing key attribute relationships undergoing particle engineering processes (Ticehurst and Marziano, 2015).

1.3.1. Particle Size and Size Distribution

Particle size is an important attribute monitored in pharmaceutical manufacturing and is critical to an API's processing behaviour during downstream unit operations (Bauer, 2009). For example, small particle sizes driven by bioavailability considerations are in conflict with desired physical attributes for good flow properties and other linked parameters such as segregation, compactability and surface adhesion. These outcomes can all have an influence on the selection criteria for downstream processing either through direct compression, roller compaction, wet granulation or other technologies for conversion of the powder to a tablet core / filled capsule (Leane et al., 2015, Leane et al., 2018).

When interpreting the particle size distribution, it is ultimately the shape of the individual particles which defines the interpretation as particles are usually discretised and measured according to a certain length, width or circle equivalent diameter (Bauer, 2009). As particles are 3-dimensional objects, it is difficult to solely rely upon a single dimension for characterising particle size (Schorsch et al., 2014). Terms such as "equivalent spheres" or "circle equivalent diameter" are used to describe the particle size (Bauer, 2009, Malvern, 2012).

Bulk samples produced from unit operations such as crystallisation and milling can contain distributions of many particle sizes and shapes (rods, needles, plates, cubes, flakes etc.,) therefore the use of statistical means (mode, median and mean) for analysis becomes necessary.

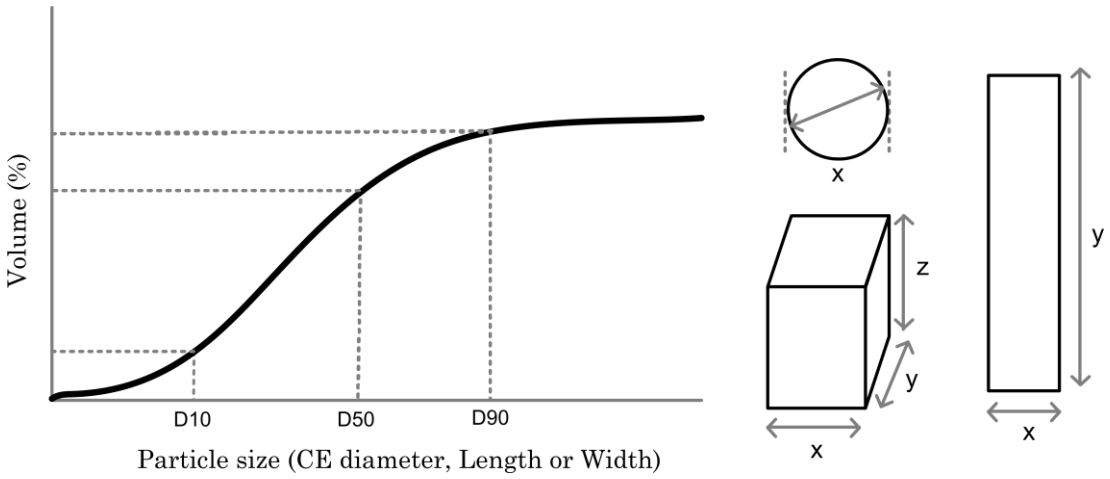

Figure 1.21 Measurement of particle size and size distribution with statistical analysis (Malvern, 2012). D50 is a commonly used notation as it represents the median above the diameter where half of the particle population lies below.

Often quoted, the volume moment mean D [4, 3] reflects the size of those particles which constitute the bulk of the sample volume whereas the surface area moment D [3, 2] is most sensitive to the presence of fine particles in the size distribution (Malvern, 2012). The particle size distribution width is also quantified by D10, D50 and D90 on the x-axis as shown from a cumulative curve (Figure 1.21).

1.3.2. Particle Shape

Spherical and compact particle shapes are largely favoured to long needles (high aspect ratio) for improving downstream processing such as filtration rates (Ottoboni et al., 2019). In crystallisation, the obtained particle shape is linked to the symmetry of the internal crystal structure and packing of a solid in a unit cell (Mullin, 1997). It is therefore important to understand

the intermolecular interaction framework comprising a particulate material. The crystal shape can then be predicted using well established methods based on crystal structure such as Bravais-Friedel-Donnay-Harker (BFDH) (Davey and Garside, 2006). However, as crystallisation is a relatively complex phenomena, there are several external factors including supersaturation, temperature, solvent selection, additive or impurity concentration which may contribute to the actual shape produced.

1.3.3. Particle Surfaces

Whilst careful selection of crystallisation parameters and operating policies can be used to generate well-faceted crystals of the desired size and shape, pharmaceutical crystals are anisotropic in nature (Shah et al., 2015). This can be attributed to the low symmetry of the molecular packing and the growth mechanisms (screw dislocations, kinks, disorder, steps, impurities etc.,) as well as impact from high energy intensive unit operations.

Characterisation and measurement of surface properties such as surface areas, energies and heterogeneity is important in order to understand how surface chemistry and performance is affected by unit operations such as mechanical milling (Figure 1.22) (R Williams, 2015). Ho (Ho et al., 2012) investigated surface characterisation techniques (iGC-SEA & DIA), particle shape and attachment energy predictions as essential tools for understanding and explaining the underlying fracture behaviour of crystalline solids.

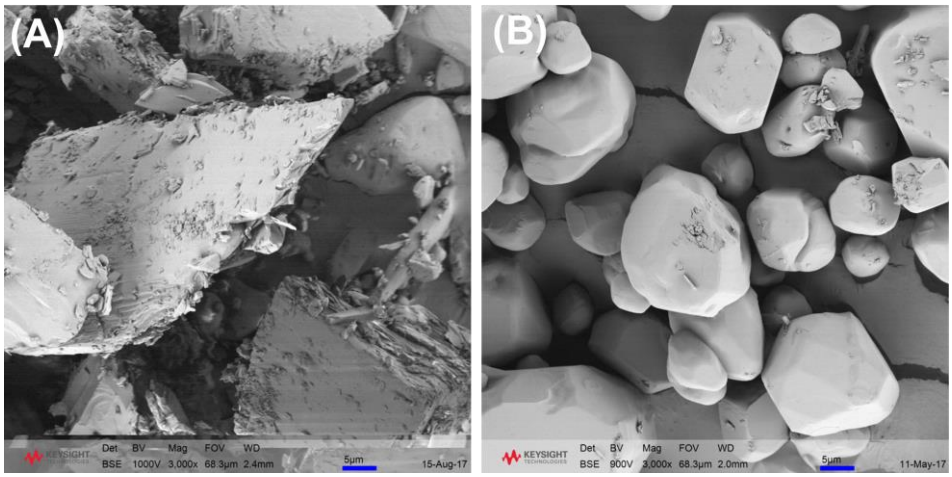

Figure 1.22 Surface images obtained from an SEM microscope displaying raw acetaminophen as supplied by vendor (A) and recrystallised & wet milled material (B). The images were generated from own experimental work.

Additional studies have shown differences in surface energies of milled pharmaceutical powders such as salbutamol-sulphate, *dl*-propranolol hydrochloride and α-lactose monohydrate to influence powder flowability and blending performance (Ticehurst and Marziano, 2015).

1.3.4. Particle Characterisation Techniques

There are several techniques for particle size measurements. These can include the use of a sieve of a known pore size allowing certain size fractions to be obtained and indirect techniques as they measure particles passing through detectors of various kinds; X-ray diffraction, light scattering, X-ray absorption, laser diffraction and image analysis (Bauer, 2009, Malvern, 2012, Schorsch et al., 2014). Particle shape is usually analysed by image analysis such as microscopy and scanning electron microscope (SEM) whereas atomic force microscopy (AFM),

contact angle and inverse gas chromatography (iGC-SEA) are used for surface property analysis (R Williams, 2015).

Offline measurements are widely used and relied upon for analysing product attributes. This involves manual sampling with analysis in a centralised laboratory. Alternative measurement modes such as At-line, True on-line and inline methods are increasingly being used (Table 1.2). Process analytical technology (PAT) is appealing and beneficial as it can be used inline for real-time analysis during a crystallisation process and thus potentially mitigate the need for offline analysis and sampling (Bakeev, 2010, Wu et al., 2014). The application of PAT has also led to detecting the onset of various crystallisation phenomena such as polymorphic transformations (Simone et al., 2014b) and improving the purity and particle size distribution (Simone et al., 2015). As such, common PAT tools include ATR-FTIR, FBRM and PVM which is described in section 3.2.1.

Table 1.2 Different measurement modes employed for crystallisation process development.

Measurement Mode	Definition
Off-line	Manual sampling with analysis in a centralised laboratory
At-line	Manual sampling with analysis next to process
True on-line	Some of the sample passes through the analyser
In-line	No sampling, PAT probe inserted into reactor or pipe

1.4. Particle Engineering: Wet Milling Applications

Process intensification is applied to continuous manufacturing of pharmaceuticals and is defined as any chemical engineering development that leads to a substantially smaller, cleaner, safer and more energy efficient technology (Stankiewicz and Moulijn, 2000). A key driver for the adoption of wet milling is the opportunity to combine multiple unit operations into a single intensified process.

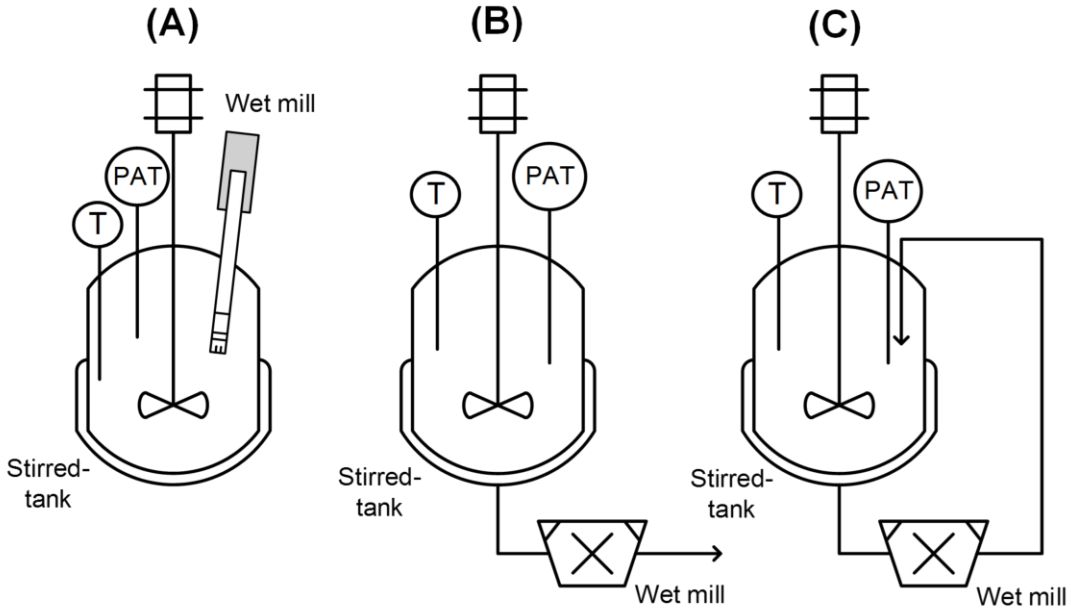

Figure 1.23 Sketch of intensified process configurations combining wet milling with stirred-tank reactors. An immersion (in situ) wet mill mode inserted through the top of the stirred-tank (A); single-pass mode which involves feeding the suspension from the stirred-tank directly through the wet mill once (B); recycle-loop mode whereby the suspension is recycled multiple-times through the wet mill and back into the stirred-tank (C). The majority of wet mills are all based on a rotor-stator principle. Temperature (T) and PAT probes are usually inserted for process monitoring (Luciani et al., 2015, Acevedo et al., 2017).

The development of these approaches are then utilised to perform various particle engineering tasks such as inline size and shape modification therefore reducing the number of unit operations (i.e., dry mills) required in pharmaceutical manufacturing.

1.4.1. Recycle-Loop Mode

The recycle-loop wet mill mode is a relatively easy to use process with broad applicability in particle engineering (Figure 1.23). This section will review current wet milling trends for scale-up, size reduction, shape manipulation, seed generation and polymorph control.

1.4.1.1. Scale-up

Kamahara et al., (Kamahara et al., 2007) employed a semi-batch crystallisation process coupled with a rotor-stator wet mill to overcome uncontrolled local mixing and scalability issues encountered in a stirred-tank crystalliser. The aim was to generate and control fine particles through controlled secondary nucleation from high shear wet milling (160 & 600 W / kg) during crystallisation. The process was successfully scaled-up from 1 L to 1000 L pilot scale production by keeping the rotor tip speed (m / s) constant. Engstrom et al., (Engstrom et al., 2013) offered an improved scaling approach by introducing an energy dissipation rate (E^*) model for predicting particle size against energy input in wet milling across process conditions and scales (lab and pilot plant).

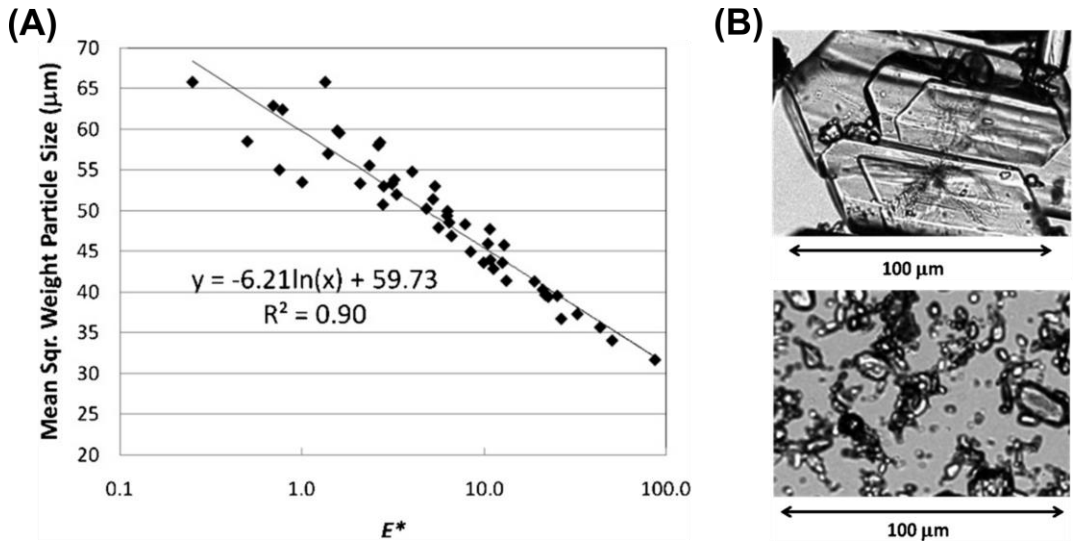

Figure 1.24 Comparison of particle size (FBRM) to normalised energy dissipation rate (E^*) on a logarithmic scale for the investigated API (A) (Engstrom et al., 2013). The data points plotted include experiments from all milling conditions tested for each module (coarse, medium, fine) as well as multiple data points along each particle size reduction curve (A). Image of particles after batch cooling crystallisation (top) followed by wet milling of the slurry at 20 – 25°C (bottom) displays particle size reduction.

The model expands on tip speed (m / s) and shear frequency (f_{sr}) (as described in section 1.1.3) as the number of slurry recycles, teeth configuration (coarse, medium, fine) and slurry residence time are included. Overall, the improved approach correlated API particle size to energy input (1 - 32.3 (a.u)) as shown (Figure 1.24). Scaling-up of API size reduction using a Quadro Ytron rotor-stator wet mill has also been reported elsewhere (Harter et al., 2013).

1.4.1.2. Size Reduction

Isothermal wet milling of crystalline suspensions is usually employed post-crystallisation for reducing and normalising the particle size

distribution. An earlier study by Kougoulos et al., (Kougoulos et al., 2011) compared the impact of conventional cooling crystallisation, sonocrystallisation, hammer milling and wet milling on the content uniformity and stability of mannitol. The optimisation of high shear wet milling (Silverson) imparted sufficient size reduction for the desired target PSD of 50 and 130 μm (D_v50) to produce an acceptable drug product formulation and performance.

Liu et al., (Liu et al., 2012) investigated wet milling of ibuprofen which observed size reduction from 70 to 33 μm (D_v50) whilst simultaneously altering the particle shape from needles to hexagonal crystals. Surprisingly, the powder flow function coefficient (FFC) which is used as an index for flow assessment showed wet milled product to be between 2 and 4 which falls into the cohesive powder range (Rahman, 2009) and was similar to commercial ibuprofen. Different lactose mass content (%) comprising of lactose I (FFC 3.1 = cohesive flow) and lactose II (FFC 14 = easy flow) were then used as binary mixtures with milled and commercial ibuprofen to increase the FFC (Figure 1.25). However, it was concluded as a result of isothermal wet milling the smaller particle size and possible change to surface morphology reduced powder flowability. Readers are also referred to the follow-up study by Liu et al., (Liu et al., 2013) whereby the complex relationship between ibuprofen particle properties (size and shape) on particle compressibility (yield stress) and compactability (tablet tensile strength) is demonstrated.

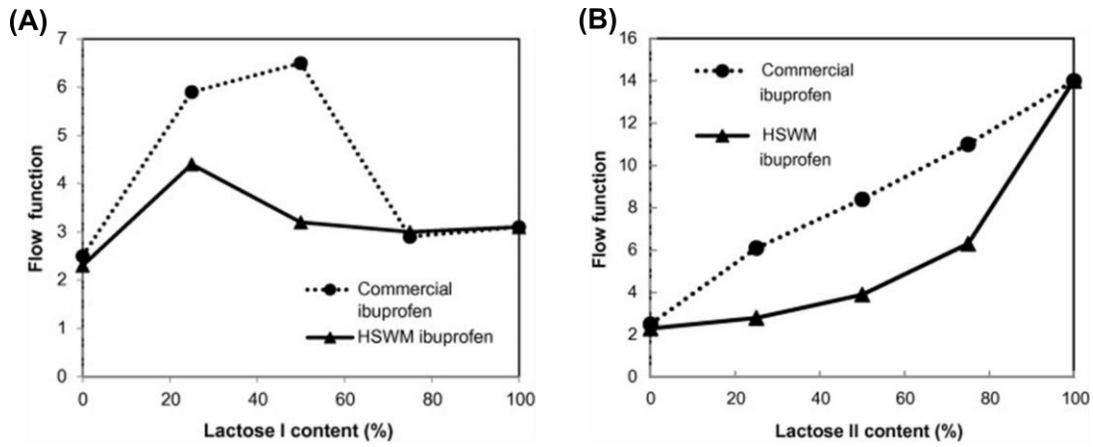

Figure 1.25 Flow function of binary mixtures versus lactose I & II content. Lactose I content had a similar particle size to high shear wet milled ibuprofen (A). Lactose II content of a larger particle size than Lactose I content (B) (Liu et al., 2012).

1.4.1.3. Shape Manipulation

During size reduction, particles are likely to undergo shape alteration when long aspect ratio crystals (i.e., needle-like) serve as the starting material. A promising approach to shape modification is by combining the number of recycle-passes through a wet mill with subsequent temperature cycling. Wilson et al., (Wilson et al., 2018) investigated this strategy as a practical means for tuning the length and width of an API. The experimental methodology is detailed in Figure 1.26 which produced more equant particle shapes. As a result, this greatly improved the powder handling properties including bulk density (0.37 g / ml), FFC (2.3 to 5.3) and overall powder processing as demonstrated by roller compaction (Wilson et al., 2018).

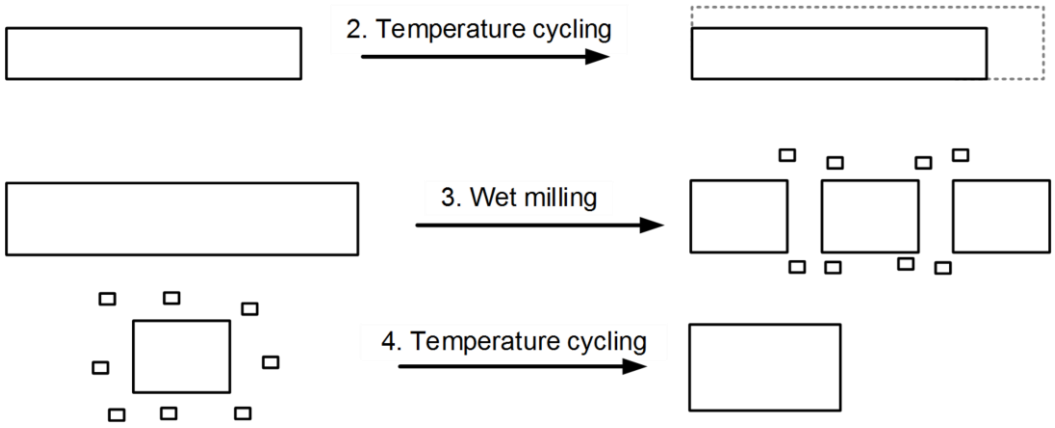

Figure 1.26 Schematic showing the proposed crystal size and shape manipulation mechanism (Wilson et al., 2018). Step 1: Material was crystallised by cooling from a saturated solution in the presence of seed to produce needle-like particles, step 2: Temperature cycling of crystallised starting material from step 1 which increases needle length and width whilst reducing the fine particle fraction, step 3: Wet milling (recycle-loop mode) which results in a decrease in needle length primarily and finally step 4: Additional temperature cycling which increases needle length and width whilst reducing the fine particle fraction (generated from wet milling). A milling speed of 16000 rpm was selected which reduced the particle length from 58.4 to 27.7 μm (D_v50).

Shape modification of β L-glutamic acid (needle-like) has also been performed through a novel 3-stage cycling process consisting of crystallisation, milling and dissolution stages (Salvatori and Mazzotti, 2018). To identify the optimal conditions required in each stage for equant product shapes, an extensive experimental campaign along with process simulations (previously published (Salvatori and Mazzotti, 2017)) was conducted. It was found, employing a large number of temperature cycles > 4, selecting mild milling conditions from 5000 to 12000 rpm and ensuring

40% mass dissolution was in fact, enough to dissolve the fines whilst constricting nucleation. These were concluded as the required operating conditions for consistently producing a compact particle morphology.

1.4.1.4. Seed Generation

Rotor-stator wet milling can be used as a continuous seed generation device which is beneficial for crystallisation processes. Yang et al., (Yang et al., 2015) applied the wet mill as a downstream nucleation device for continuous crystallisation of acetaminophen. Analysis of start-up, yield index and size distribution (CLD) on an MSMPRC was investigated (Figure 1.27). It was shown, the mill operated as a continuous size reduction tool due to controlled secondary nucleation and breakage mechanisms when compared to the reference MSMPRC experiment (without wet milling) as seen in Figure 1.27, (B).

The practical ease of incorporating the recycle-loop mode was further demonstrated on a 3-stage MSMPR for a seeded cooling crystallisation of acetaminophen (Brown et al., 2018). The number of continuously generated seeds allowed for the crystallisable product mass to be targeted and optimised via an integrated flowsheet product in gCRYSTAL 4.2.0 where secondary nucleation kinetics were modelled explicitly.

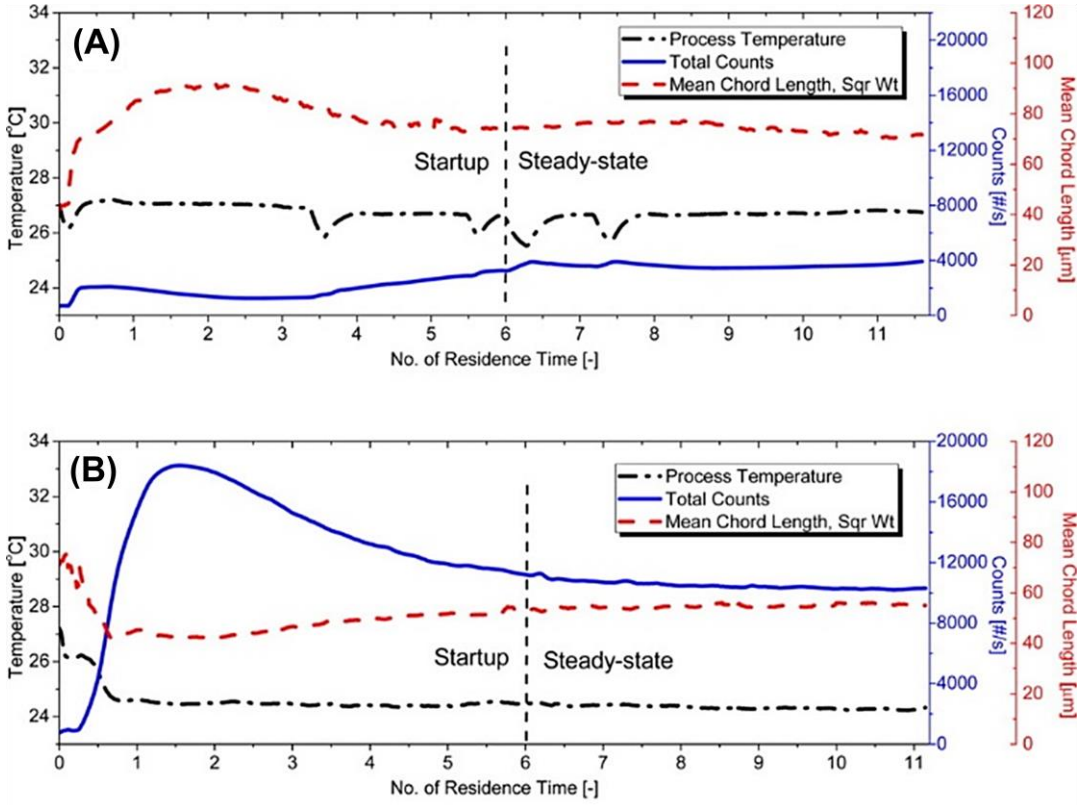

Figure 1.27 Process temperature, real-time FBRM total counts and square weighted mean chord length (SWMCL) in the MSMPRC. Profile trends for the continuous crystallisation without wet milling coupled which achieved a SWMCL of 71 μm is shown (A). The effect of wet milling coupled via the downstream recycle-loop mode with continuous crystallisation which achieved a smaller SWMCL of 55 μm is also shown (B). Both experiments consisted of a startup duration of 6 residence times (Yang et al., 2015).

1.4.1.5. Polymorphic Control

An emerging area of interest is in the application of high shear for aiding in the separation of conglomerate forming chiral molecules (Köllges and Vetter, 2017, Köllges and Vetter, 2018) as well as polymorphic control and selection (Köllges and Vetter, 2019, Li et al., 2019). Köllges and Vetter (Köllges and Vetter, 2019) demonstrated the impact of wet milling on the polymorphic composition of L-glutamic acid (LGA) during continuous crystallisation (Figure 1.28). The influence of wet milling produced the stable β polymorph of LGA at operating conditions (feed concentration, crystalliser temperature and residence time) when compared to the metastable α polymorph which formed without wet milling (Figure 1.29). It was concluded, mild milling conditions (3000 rpm) induced sufficient crystal breakage on LGA leading to increased surface area and thus provided the ability to steer towards the stable polymorph (Figure 1.29).

A follow-up publication on predicting the polymorphic outcome of LGA in the presence of wet milling has also been reported (Li et al., 2019). By deploying a similar continuous crystallisation process (Figure 1.28), the desired operating spaces for the single-stage MSMPR was identified which allowed the right polymorph to be reliably obtained in addition to the required size, solute recovery and productivity. This was achieved from parametric analysis through constructing a dimensionless population balance equation, details of which are explicitly outlined in the article (Li et al., 2019).

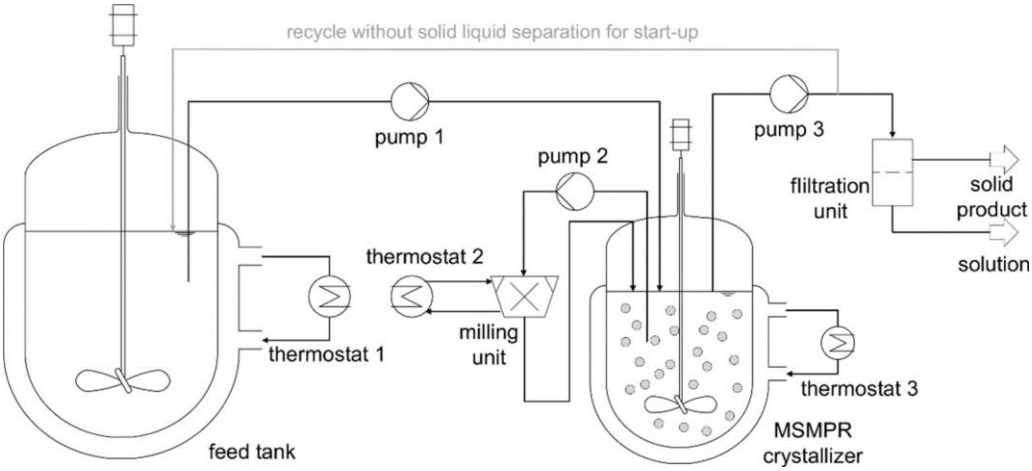

Figure 1.28 Schematic representation of the continuous crystallisation setup (Köllges and Vetter, 2019). The MSMPR unit is equipped with the rotor-stator wet mill via the recycle-loop mode.

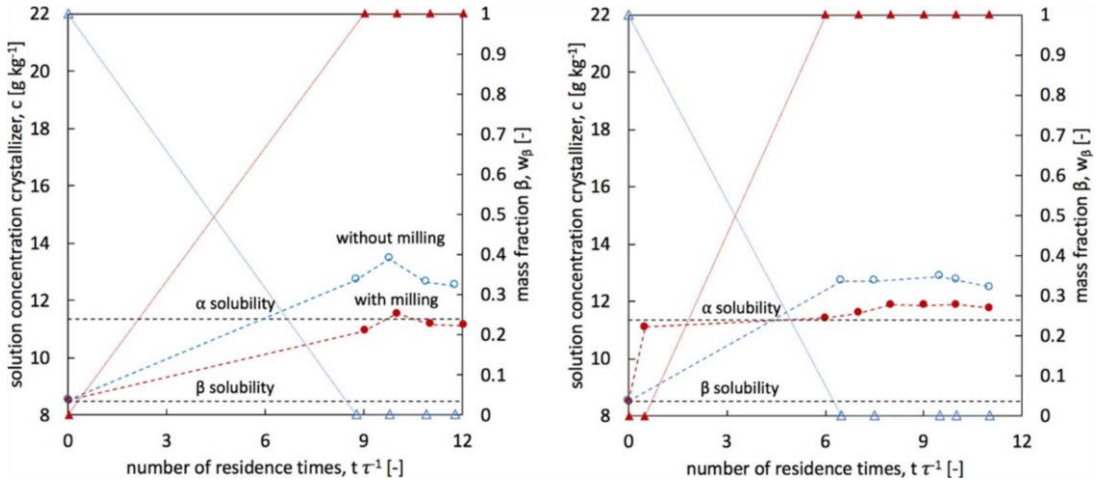

Figure 1.29 Profile trends showing solution concentration and mass fraction of the β polymorph for experiments conducted at a residence time τ = 2 h (Köllges and Vetter, 2019): (left) startup of 4_β and 8_α at c_{in} = 20 g kg^{-1}; (right) startup of 12_β and 16_α at c_{in} = 30 g kg^{-1}. The results of the α-seeded are drawn in red and those of the β–seeded in blue. Solution concentrations without and with milling are drawn as open circles (○) and filled circles (●). The mass fractions of the β polymorph are given on the right vertical axis and are drawn for without and with milling as open triangle s (Δ) and solid triangles (▲). Lines have been drawn to guide the eye.

1.4.1.6. Summary

Clearly, implementing wet milling for particle engineering has found widespread use and interest in several areas. A summary of the reviewed applications from the recycle-loop mode is shown (Figure 1.30). Whilst numerous overlaps can be drawn between each of the applications, the diagram merely looks to show the common trends in crystallisation process development when utilising wet milling via the recycle-loop mode.

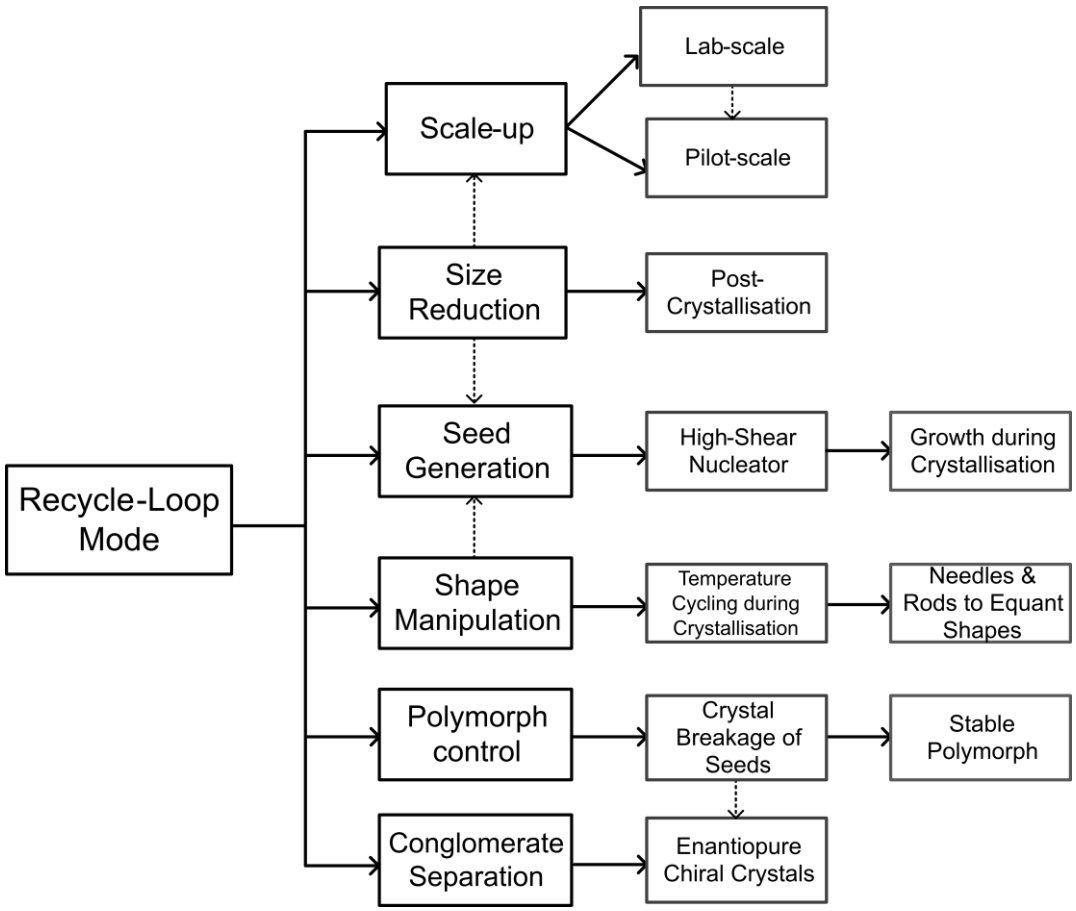

Figure 1.30 The diagram provides an overview on the current (scale-up & size reduction) and emerging (seed generation, shape manipulation, polymorph control and conglomerate separation) areas of interest via wet milling in pharmaceutical manufacturing.

1.4.2. Ultrasound for Particle Engineering

Ultrasound technology is a common particle engineering tool and is used for inducing nucleation at low supersaturations and manipulating the particle size and shape (Sander et al., 2014). Ultrasound transmission in a liquid solution occurs through acoustic cavitation via sound waves. During propagation, these sound waves exert alternating phases of compression and rarefaction (expansion) (Figure 1.31). The intensity of these phases is related to the amplitude of the wave expressed in microns of displacement of the vibrations at the source of the sound which is proportional to the power delivered (Price, 2017).

This gives rise to bubbles during rarefaction which shrink during the compression phase and then expand again during subsequent rarefaction phases (stable cavitation). As the amplitude of the sound waves increase, the pressure reduction during the rarefaction phase becomes large enough to allow bubbles of solvent vapour to form in solution (Price, 2017). Ultimately, the cavitation effect gives rise to the formation, growth and implosive collapse of bubbles in liquid (Figure 1.31). As a result, intense local heating (~5000 K), high pressures (~1000 atm) and large heating & cooling rates (> 10^9 K / s) are generated (Mason et al., 2005, Suslick, 1990). This rapid cooling generates a highly localised supersaturation which triggers nucleation and has been shown for roxithromycin (Guo et al., 2005) *p*-Aminobenzoic acid (Gracin et al., 2005), lactose (Siddique et al., 2015) and potassium sulphate (Lyczko et al., 2002).

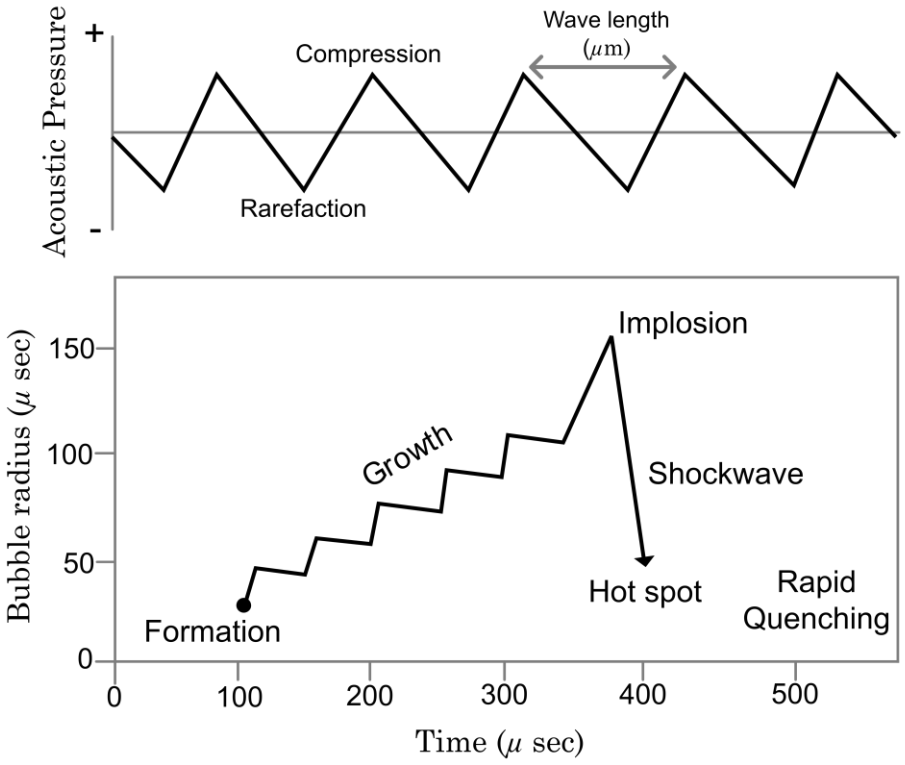

Figure 1.31. Mechanisms arising from ultrasound propagation through a liquid solution showing growth and destruction of a cavitation bubble (Devarakonda et al., 2003).

For crystallisation processes, ultrasound probe horns are usually immersed in direct contact with the process solution through a stirred-tank which directly transfers acoustic energy to the system consisting of several hundred W cm^{-2} (Figure 1.32). Through careful process design and optimisation of conditions i.e., power output (kW / m^2) and ultrasonic duration, this has the potential to affect almost all of the processes in crystallisation as summarised in Figure 1.33 (Price, 2017). In addition to crystallisation, the versatility of ultrasound has uses in emulsification, dispersing, cell disruption and disintegration (Mason et al., 2005).

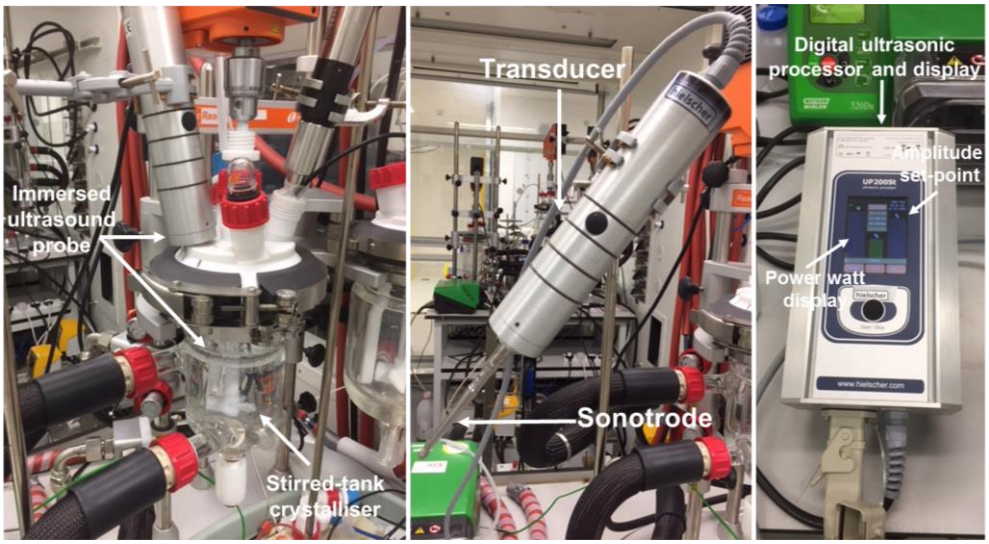

Figure 1.32 Laboratory setup of batch crystallisation integrated with an immersed ultrasound probe horn in direct contact with a liquid solution. The ultrasound device displayed is an UP200St (Hielscher, 200W 26kHz) probe.

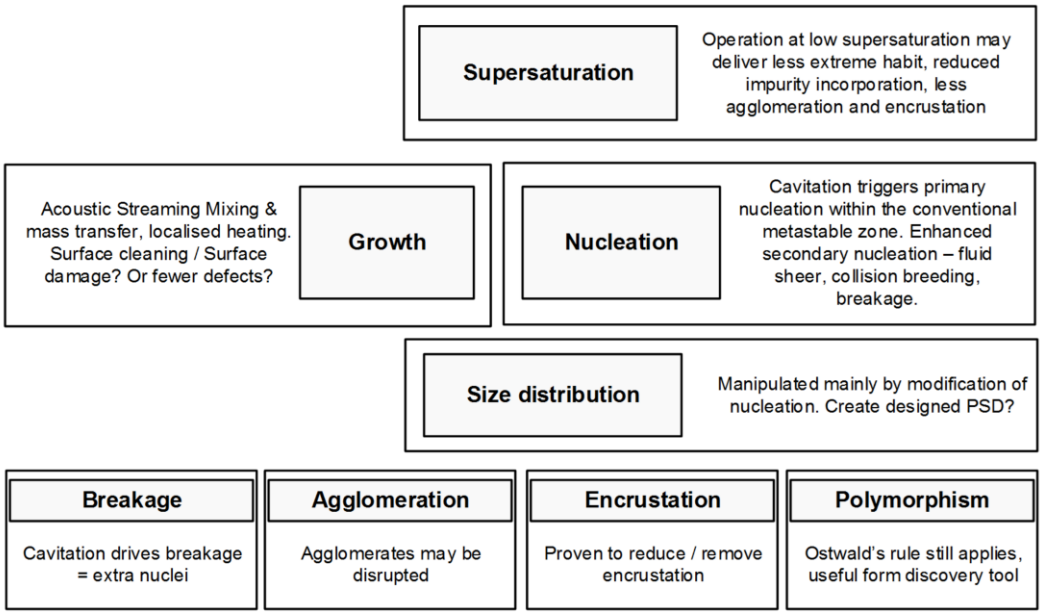

Figure 1.33 Crystallisation processes which may be subject to modification by insonation. These effects are independent as supersaturation drives both growth and nucleation which together control the size distribution. This is further influenced by breakage, agglomeration, encrustation and the polymorphic form (Price, 2017).

Chapter 2

Aims & Objectives

2. Aims & Objectives

2.1. Aims

The overarching aim of this research is to investigate particle engineering strategies through the direct combination of wet milling with crystallisation processes equipped with multi-sensor measurements comprised of inline, offline and computational tools. High shear rotor-stator and indirect ultrasound devices are incorporated and applied for enhanced control and tailoring of particle attributes. The relationship between process parameters and product attributes is of central importance as well as evaluating the practical ease of integration and performance through semi-continuous and continuous crystallisation approaches. Overall, this work aims to explore the application of particle engineering as an effective and alternative route for manipulating particle properties during pharmaceutical processing.

2.2. Objectives

In the first part of this work in chapter 4, the objective is to outline the effect of process conditions and wet mill configuration on product attributes of acetaminophen in 2-propanol. This will involve a recirculation mode using a rotor-stator device coupled to a stirred-tank crystalliser. A combined seeded cooling crystallisation and wet milling process with interchangeable rotor-stator teeth and rotation speeds is then deployed with further decoupling experiments. Real-time FBRM & PVM monitoring sensors and a computational tool for converting chord length distribution

(CLD) from FBRM to particle size distribution (PSD) inline is explored across selected conditions. Advanced offline characterisation via image analysis and inverse gas chromatography are utilised for quantifying isolated product attributes including the surface chemistry (energies). In addition, the energy dissipation rate model (E^*) developed by Engstrom et al., (Engstrom et al., 2013) for predicting particle size performance in rotor-stator wet milling is tested.

The objective of chapter 5 is to provide a practical approach to continuous seed generation using high shear from a rotor-stator device for cooling crystallisation of acetaminophen in 3-methyl-1-butanol. Initial work will entail generating an optimal cooling profile for growth using an inline ATR-FTIR sensor. A combined unseeded cooling crystallisation and wet milling mechanism with supersaturation feedback-control including fixed rotor-stator teeth and rotation speed is then performed. This is aimed at showing the impact of high shear on nucleation and maintaining constant supersaturation with inline sensors (FBRM & PVM) during cooling. Scale-up flexibility is then further assessed from the combined methodology across different batch crystalliser scales (1 L & 10 L).

In the second part, a continuous MSMPR process composed of 3-stages is investigated for targeting a defined particle size and size distribution. The process will consist of the optimal cooling profile for delivering a growth-dominated process. At the same time, high shear wet milling will be operated on a single-stage MSMPR for continuous seed generation and

direct seed slurry transfer using pneumatic pressure to the subsequent reactor stages for growth during cooling.

Chapter 6 evaluates the performance, strengths and limitations of using multi-sensor measurement modes through inline PAT (FBRM & PVM), computational tools (CLD to PSD conversion & imaging) and offline techniques (imaging). The effect of crystallisation is decoupled and a breakage only process using the recirculation mode is explored by sequential ramping phases through increasing the wet mill rotation speed. Crystalline materials subjected through this process are acetaminophen, metformin HCL and benzoic acid all of which exhibit different morphologies and mechanical properties. The objective is then to critically assess and analyse modifications to solid particles from size and shape distributions during high shear wet milling of crystalline slurries. Discussions surrounding accurate characterisation and sensitivity to different particle systems by using the multi-sensor approach will be reviewed.

In chapter 7, a proof-of-concept industrial case-study using indirect sonication is investigated. A flow-cell of confined volume (3.9 ml) with an attached indirect ultrasound is configured to a stirred-tank reactor through the combined method. Two API systems will be selected at supersaturation values which are slow to nucleate without seeding. The rate of desupersaturation at constant isothermal temperatures with continuous ultrasound pulsing (indirectly) is studied. The intensity of ultrasound

power input is varied with additional control experiments for decoupling and determining the process mechanisms. Overall, the influence of indirect ultrasound on nucleation rates and particle size and shape attributes will be analysed using FBRM (particle counts & CLD), HPLC & UPLC (concentration), microscopy (imaging) and process modelling tools. A key objective of this work is to further asses the feasibility of the indirect ultrasound strategy on maintaining constant temperature control over long periods of continuous operation and as a potential nucleator for seed generation.

Chapter 3

Materials & Methods

3. Materials & Methods

3.1. Materials

Acetaminophen (> 99.5%, CAS: 103-90-2) was purchased from Sigma-Aldrich and 2-propanol (reagent grade, > 95%) was sourced from Fisher-Scientific (Loughborough, UK) which were used from chapters 4 to 6. For chapter 5, 3-methyl-1-butanol (reagent grade, > 95%) purchased from Sigma-Aldrich was used. Metformin hydrochloride (CAS: 1115-70-4) was purchased from Molekula, benzoic acid (> 99.5%, CAS: 65-85-0) and surfactant TWEEN® 20 (CAS: 9005-64-5) were both purchased from Sigma-Aldrich (Dorset, UK) and were all used in chapter 6.

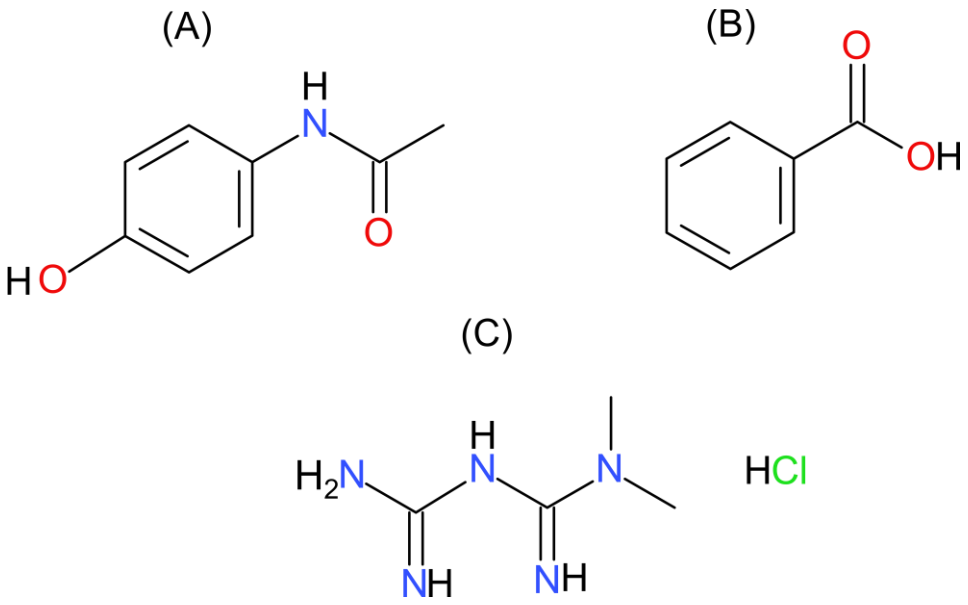

Figure 3.1 Chemical structures displayed for acetaminophen (A), benzoic acid (B) and metformin hydrochloride (C).

For the industrial case-study (chapter 7), APIs TAK-438 and TAK-117 both synthesised at Takeda Pharmaceuticals Ltd (Boston, USA) were used in methanol (HPLC grade, > 99.5%) and DMSO (reagent grade, > 99.5%) which were purchased from Fisher-Scientific. An in-house purification system was used to source water for all experimental chapters.

3.2. Methods

3.2.1. Inline Measurements

3.2.1.1. Attenuated Total Reflectance - Fourier Transform Infrared (ATR-FTIR) Spectroscopy

The use of spectroscopy through inline means has shown to be an essential technique for monitoring chemical entities in crystallisation of pharmaceutical molecules. This occurs through infrared light sourced from a fourier transform infrared spectrometer (FTIR) being absorbed at specific frequencies which is related to the vibrational bond energies of the functional groups present in the molecule. ATR-FTIR spectroscopy is a versatile tool and is based on the presence of an evanescent field in an optically rarer medium (the sample) in contact with an optically denser medium (the crystal) within which radiation is propagated due to internal reflection (Figure 3.2).

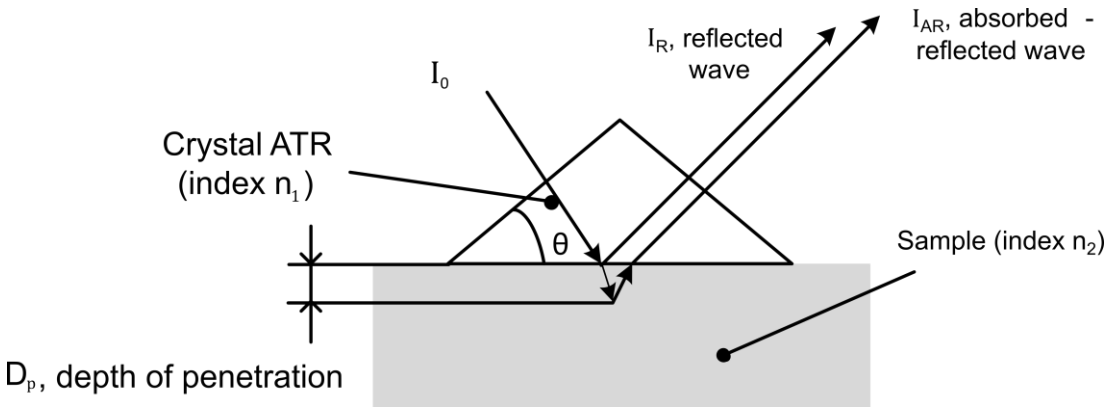

Figure 3.2 Principle of the ATR FTIR sensor (Lewiner et al., 2001).

The depth of penetration (D_p) of the evanescent wave from the infrared beam is small and therefore the interaction of this field is limited to the solution phase allowing measurement of the solute concentration in the slurry without being disturbed by the solid particles (Lewiner et al., 2001). The depth of penetration can be measured as follows:

$$D_p = \frac{\lambda}{2\pi n_1[sin^2\theta - (n_2/n_1)^2]^{1/2}} \quad \text{Eqn 3.1}$$

Where the wavelength of the incident radiation (λ), refractive indices of the crystal (n_1) and of the solution (n_2) and the angle of incidence (θ) of the propagating radiation are expressed. Hence, an ATR-FTIR inline probe is useful for crystallisation process monitoring as the ATR element is inherently a surface measurement technique and does not depend on scattering in the presence of particles, bubbles or dispersed droplets.

A Mettler Toledo ReactIR ™ 15m probe (Leicester, UK) for recording of the IR spectra was used for acetaminophen in 3-methyl-1-butanol (Chapter 5). The spectrometer is coupled to an ATR probe comprising a diamond crystal

and silver halide fibre optics. This is a probe based analytical technique in which the analysis is based on the mid-IR region (650 – 4000 cm^{-1}). An air background was acquired prior to immersion of the probe in the crystallisation solution. The sample spectrum was typically acquired every 15 s comprising of 50 scans with a resolution of 8 cm^{-1}. To enable real-time monitoring of solute concentration and supersaturation, the calibration method and the multivariate calibration model obtained by GRAMS V9 / AI ™ (Thermo Fisher Scientific, Renfrew, UK) pre-processing software is explained in section 3.2.3.1.

3.2.1.2. Focused Beam Reflectance Measurement (FBRM) Laser-Backscattering

Focused beam reflectance measurement (FBRM) provides real-time measurements through a highly focused laser beam which is projected through a sapphire window. The beam rapidly scans in a circular motion through a set of rotating optics at a fixed velocity (2 m / s) across any particle flowing through the window's field of view (Barrett and Glennon, 1999). As the beam scans across a particle or particle structure, light is scattered in all directions with the light that scatters back to the probe used to measure a chord length of the particle i.e., the distance between two points on the edge of a particle. With a high scanning speed, thousands of chords are counted per second producing a chord length distribution (CLD) over the range from 0.8 to 1000 μm (Barrett and Glennon, 1999). The CLD is related to the size and shape of particles in a slurry however

does not provide a direct PSD measurement (Kail et al., 2007). Furthermore, the FBRM sensor records the lengths of the chords for a pre-set duration after which the CLD is reported.

A Mettler Toledo FBRM G400 probe (Leicester, UK) was used for all experimental chapters with the macro view as the chord selected model.

3.2.1.3. Particle Vision and Measurement (PVM)

Particle vision and measurement (PVM) is a high resolution inline video microscope that visualises particles and particle mechanisms when inserted into a slurry suspension. The PVM sensor captures images of particles using size independent laser beams to which images recorded via light scattering backwards are captured on a CCD array which are then transferred to a camera (Barrett and Glennon, 1999). The PVM images give an indication to the observed size and shape of particles captured and usually require further image processing methods to extract quantitative particle size and shape information (Deneau and Steele, 2005, De Anda et al., 2005, Braatz, 2002).

A Mettler Toledo PVM V819 probe (Leicester, UK) was used from chapters 4 to 6 which captures greyscale images with an image resolution of 1360 x 1024 pixels and a pixel size of 0.8 μm equipped with an online image acquisition software.

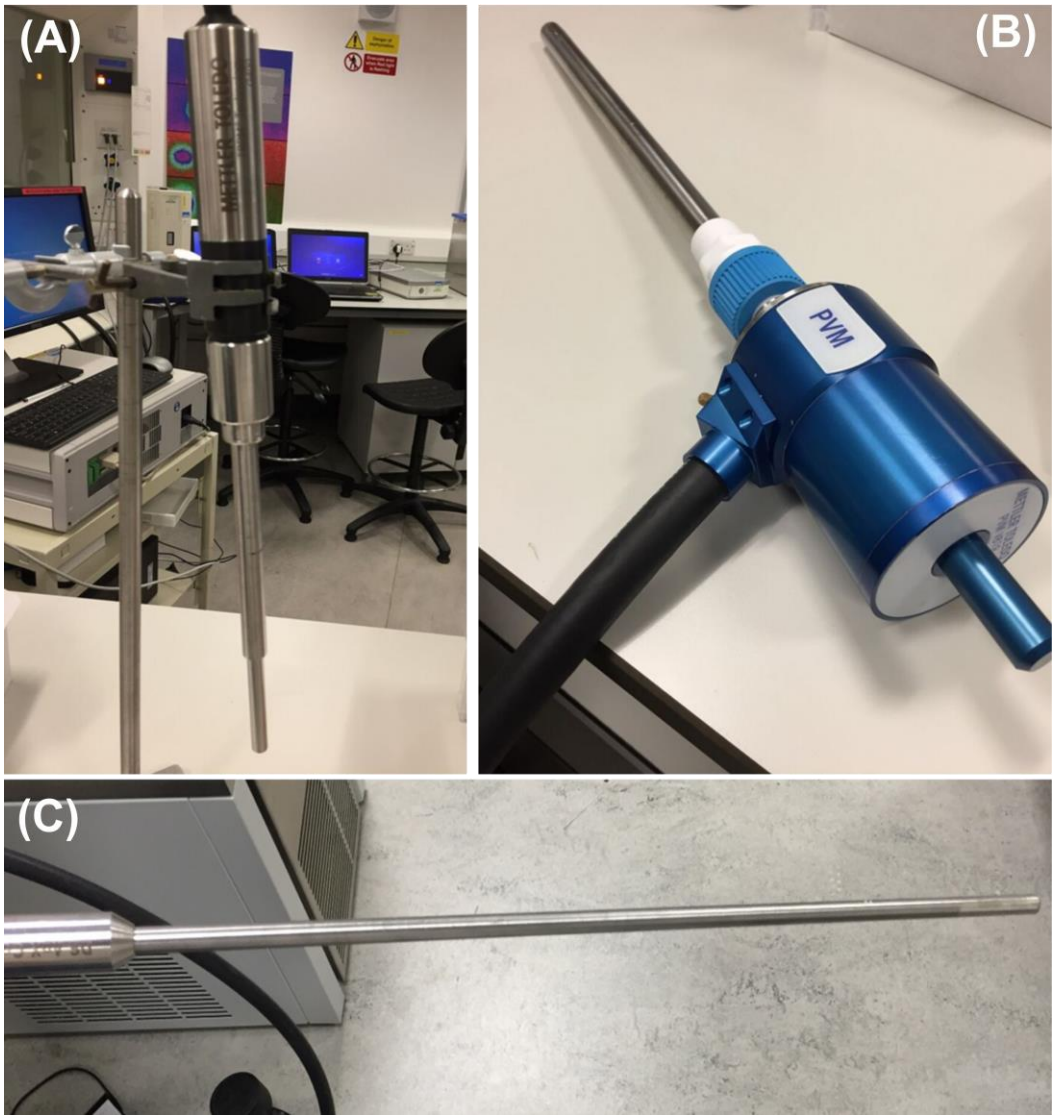

Figure 3.3 Inline measurement techniques; FBRM (A), PVM (B) and ATR-FTIR (C) which are suitable for immersing in liquid mediums and continuous monitoring.

3.2.2. Offline Measurements

3.2.2.1. Malvern Morphologi G3

For offline particle size and shape analysis, a Malvern Morphologi G3 (Malvern Instruments Ltd, Malvern, UK) was used which is an automated image analysis technique. The data is collected as a 2-dimensional

projection from scanned 3-dimensional particles (sample). This allows the circle equivalent (CE) diameter to be determined as the diameter of a circle is calculated with an equal area to the projected area of the scanned particle (Malvern, 2012). For individual scanning of particles, the instrument uses compressed air to aid in dispersion of particles onto a glass plate with automated microscopy.

Samples were prepared using a high energy dry dispersion unit requiring 5 - 11 mm^3 of recrystallised material with a 10x magnification in the size range of 0.5 – 1000 μm. Particle properties were then measured as responses ranging from volume weighted circle equivalent diameter [4, 3] μm with D_v10, D_v50 & D_v90 statistics calculated as well as shape analysis (aspect ratio & circularity) of the milled compound. Aspect ratio is defined as the ratio of the width to the length of the particle with values ranging from 0 to 1. For example, a rod would typically have a low aspect ratio whereas a spherical particle would have a high aspect ratio. Circularity is the ratio of the perimeter of a circle with the same area as the particle divided by the perimeter of the actual particle image. Values range from 0 to 1 where a perfect circle would have a circularity of 1 while an irregular object will have a value closer to 0.

Offline particle size distribution data was further processed to give a density distribution on the ordinate axes; a probability density distribution (PSD) was plotted against volume weighted circle equivalent diameter

[4, 3] μm to give a final offline particle size distribution. The instrument was used from chapters 4 to 6.

3.2.2.2. Malvern Mastersizer 2000

The mastersizer can determine the particle size offline using laser diffraction. The particle size distribution is measured by the angular variation in intensity of light scattered as a laser beam passes through a dispersed particulate sample (Malvern, 2012). The angular scattering intensity data is then analysed to calculate the size of the particles responsible for creating the scattering pattern through the Mie theory of light scattering (Malvern, 2012). The particle size is reported as a volume equivalent sphere diameter.

The mastersizer (Malvern Instruments Ltd, Malvern, UK) was equipped with a wet dispersion unit (Hydro 2000s) which circulated the sample through a cell located within an optical unit used for all particle size measurements. A manual measurement was undertaken for each sample. A dispersion unit speed of 1500 rpm, ultrasound 0 – 20%, sample measurement time of 10 s, 5 to 15% obscuration limit and three measurement cycles were carried out. Samples were added dropwise to the wet dispersion unit to generate the desired obscuration. Offline particle size distribution data was then exported as raw files. The mastersizer instrument was used for the industrial case-study chapter 7.

3.2.2.3. Microscopy

Microscopy allows the observation of individual particles whilst measuring their size, shape and composition whereby the particles can then be viewed directly in an optical microscope or by projection. Different optical lenses, magnifications along with various illumination (bright field, dark field etc.) settings can be used. For sample preparation, dry particles were dispersed onto a microscope slide where a digital stereomicroscope connected to a computer was used for sample viewing and analysis. The microscope could be operated both in reflectance and in transmittance mode. Microscopy was used for the industrial case-study chapter 7.

3.2.2.4. Scanning Electron Microscope (SEM)

Scanning electron microscope scans highly focused electron beams over a surface to create images. The electrons in the beams interact with the sample producing various signals that can be used to obtain information about the surface topography and composition of the particulate material. SEM images of obtained samples were recorded in backscattered mode at a beam voltage of 900 V using a U9320B Field Emission Scanning Electron Microscope (Keysight, Santa Rosa CA, USA). Sample preparation involved mounting the samples on aluminium stubs using a carbon tape and coating with a 10 nm gold layer using an EM ACE 200 sputter-coater (Leica Inc., Germany). SEM images were acquired for experimental chapters 4 & 5.

3.2.2.5. Inverse Gas Chromatography Surface Energy Analyser (iGC-SEA)

Inverse gas chromatography (IGC) provides quantitative understanding on the surface thermodynamic properties of powders. It is based on a vapor adsorption method through solid-gas interactions and is a widely used technique for determining the dispersive component of the surface energy (γ_{SV}^{d}). Measurements by IGC are normally conducted at very low solute concentrations (infinite dilution) which results in a single numerical value of γ_{SV}^{d} for homogenous materials and thus exhibits Henry's Law adsorption behaviour (Ylä-Maïhaïniemi et al., 2008). However, many complex particulate solids display heterogeneity such as organic crystalline materials and can be demonstrated by nonlinear isotherms obtained at low solute surface coverages. Therefore, a single value for γ_{SV}^{d} is in these cases an upper limit estimate and is not necessarily representative of the whole surface (Heng et al., 2006). Rather, it is preferred a surface energy distribution profile is obtained as this can provide valuable insights into the effect processing conditions on product surface properties.

IGC is the inverse use of a conventional gas chromatography (GC) where an unknown solid sample is packed in a column and known dispersive alkane vapor probes (non-polar) are injected via an inert carrier gas such as methane. The retention time of the probe molecules is recorded by the GC detector to which the retention volume and partitioning co-efficient for the solid-vapor interaction can then be determined.

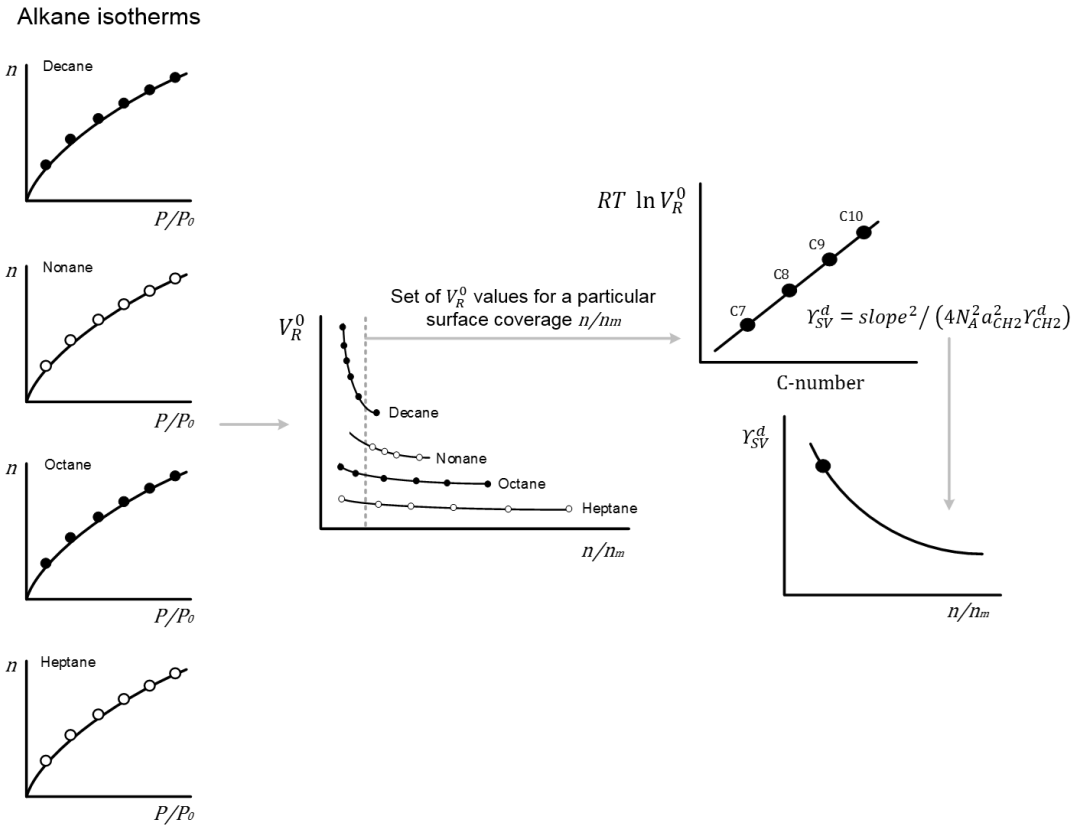

Figure 3.4 Schematic diagram of the experimental isostere method for determining the dispersive surface energy distribution profile (Y_{SV}^d) (Ylaï-Maïhaïniemi et al., 2008).

This allows for a distribution of Y_{SV}^d to be obtained through conducting a series of finite concentration IGC measurements (Figure 3.4). In the peak maximum isotherm determination method which is the time of the maximum Flame Ionisation Detection (FID) signal, each experimental value for the net retention volume provides one datum point of the adsorption isotherm. Firstly, IGC requires the specific surface area to determine the surface energy, especially as this can depend on surface coverages. The specific surface area for the solid sample is based on the use of the Brunauer, Emmett, Teller (BET) adsorption model. The BET method

traditionally uses nitrogen sorption (Livingston, 1949) or krypton (Beebe et al., 1945) for surface areas below 0.5 m^2 g^{-1} where the nitrogen technique has shown limitations such as extreme high vacuum conditions at low temperatures (77 k) (Legras et al., 2015). This may completely dry out most pharmaceutical hydrates and cause fragile crystals to collapse under these conditions leading to different properties and surface areas. An alternative and preferred technique is IGC for BET determination from using one of the alkane isotherms. For instance, the linearised BET equation is applicable on isotherms type II and IV only (Figure 3.4), where there is a formation of a monolayer followed by multi-layers:

$$\frac{P}{n(P_0 - P)} = \frac{C - 1}{n_m C}\left(\frac{P}{P_0}\right) + \frac{1}{n_m C} \qquad \text{Eqn 3.2}$$

Here, the solvent partial pressure in the gas phase (P) = Torr, saturated solvent vapor pressure (P_0) = Torr, amount of gas adsorbed (n) = Mol g^{-1}, the monolayer capacity (n_m) = Mol g^{-1} and the BET constant (C) are shown. The BET equation fits the isotherm (type II or IV) over a specific range of equilibrium pressures (P / P_0) usually for $0.05 < P / P_0 < 0.35$ (Legras et al., 2015). The monolayer capacity (n_m) can be determined from the slope and intercept of the linearised BET equation fitted to the isotherm. The specific surface area (S_{BET}) = m^2 g^{-1} is expressed as:

$$S_{BET} = aN_A n_m \qquad \text{Eqn 3.3}$$

Where the molecular cross-sectional area of (a) of a solute molecule, Avogadro's number (N_A) and the monolayer capacity (n_m) = Mol g^{-1} are included. Since n_m and a are known, the specific surface area (S_{BET}) can be calculated.

For surface energy measurements, the net retention volume (V_R^0) which is a fundamental surface thermodynamic property of the solid-vapor interaction process is calculated from:

$$V_R^0 = \frac{j}{m} F (t_R - t_0) \frac{T}{273.15} \quad \text{Eqn 3.4}$$

Here, column temperature (T) = Kelvin, K, carrier gas exit flow rate (F) at standard temperature and pressure (STP), retention time for the adsorbing probe (t_R), mobile phase hold-up time (t_0), sample mass in the packed column (m) and the James-Martin correction (j) which corrects the retention for the pressure drop along the column bed are shown (Heng et al., 2006). As the molecular mass of the injected vapor probe molecules increases as a result of increasing hydrocarbon chain lengths (octane, nonane, decane etc.), the propensity of the solute species to interact with the sample surface also increases and is thus able to probe higher energy sites via adsorption.

With the known monolayer capacity for each alkane, the surface coverage (n/n_m) at each measured solute concentration can be calculated from the amount desorbed (n). Illustrated in Figure 3.4, the net retention volume of each alkane injection at a particular surface coverage (n/n_m) allows the

dispersive surface energy (γ_{SV}^{d}) to be calculated from the slope of the alkane reference line when the term $RT \ln V_R^0$ is plotted against the carbon numbers of the alkane probe molecule by using the Dorris-Gray approach. Further details on deriving the dispersive surface energy through the Dorris-Gray and Schultz approaches are reported (Schultz et al., 1987, Dorris and Gray, 1980, Ylä-Maïhäniemi et al., 2008).

An iGC-SEA (Surface Measurement Systems Ltd, London, UK) system was used for surface energy and Brunauer, Emmett, Teller (BET) specific surface area analysis. Acetaminophen powder (~ 800 mg) from the milled product was packed into an iGC glass column (3000 x 4 mm ID) with silanised glass wool inserted at each end. Duplicate columns were prepared for all samples. Helium was used as the inert carrier gas at a flow rate of 10.0 standard cubic centimetre per minute for all injections and methane was the reference gas to determine the dead time, which represents the time necessary for a molecule to travel across the column without any interaction. First the BET specific surface area was calculated ($P/n[P_0 - P]$) for each sample using octane as the adsorbate and each target fractional surface coverage (n/n_m) assigned between the minimum and maximum surface coverage (0.05 to 0.35) which depends on the sample mass. Then, a series of purely dispersive *n*-alkane vapour probes all of high purity, HPLC-grade solvents (undecane, decane, nonane and octane) were injected at different concentrations and a target fractional coverage area from 0.005 to 0.2. The retention time was determined by a Flame Ionisation

Detector (FID). This allowed the dispersive component (γd) at a given surface coverage (n/n_m) to be determined for all the samples using the net retention volume ($\ln V_R^0$) at specified target coverage by the peak maximum parameter. Using all non-polar solvents, the surface heterogeneity of the samples was determined by calculating the dispersive surface energy (γ_{SV}^d) of acetaminophen according to the Dorris-Gray peak max method using the surface measurement systems advanced analysis software (V.1.4.2) (Kondor et al., 2015, Doris and Gray, 1980). The IGC instrument was used for chapter 4.

3.2.2.6. High-Performance Liquid Chromatography (HPLC)

HPLC is a form of column chromatography that passes through a sample mixture or analyte in a solvent (known as the mobile phase) at high pressures through a column with the chromatographic packing material (stationary phase). Depending on the chemical structure of the analyte, the molecules are retarded while passing in the stationary phase. The specific intermolecular interactions between the molecules of a sample and the packing material define their time. Therefore, different constituents of a sample are eluted at different times. From this, HPLC is able to separate out compounds within the sample due to their physical properties. The instrument consists of five main parts, auto-sampler, the degasser and pump, the column compartment and the UV detector which recognises the analytes after leaving the column whereby the signals are converted and

recorded by a data management system (computer software) and then shown in a chromatogram.

It is a widely used analytical technique for measuring the analyte concentration in pharmaceutical analysis as it can provide very accurate results for multiple components using simple linear calibration models based on the peak area of each component (Yang et al., 2016b). This can be done through preparing a single external standard, calibration curve or internal standard which are all simple when compared to building a spectroscopy calibration method as the chromatographic peak area is typically a linear function of analyte concentration. Ultra-performance liquid chromatography (UPLC) is also a common technique for online monitoring of analyte concentration. Whilst the operating principles are the same to HPLC, UPLC offers improved resolution and sensitivity, lower solvent consumption and analysis times of only a few minutes (Yang et al., 2016b, Swartz, 2005). A HPLC instrument (Agilent 1100 Series, Santa Clara CA, USA) and UPLC (Acquity, Waters, Milford MA, USA) was used for all concentration measurements in the industrial case-study chapter 7.

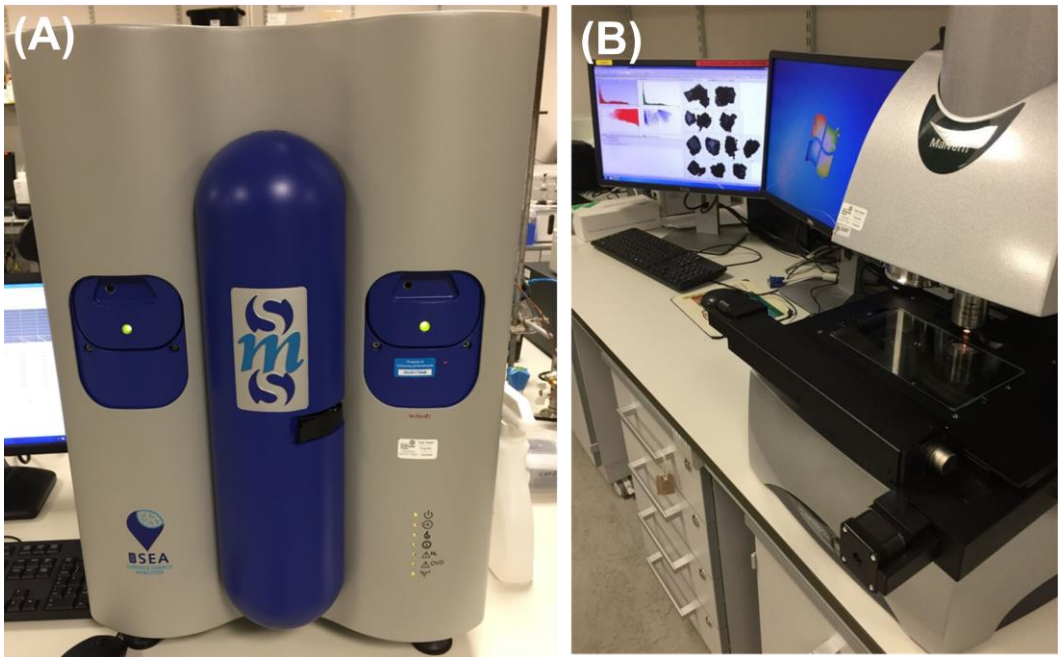

Figure 3.5 Images of offline measurement techniques used; Inverse Gas Chromatography (A) and Malvern Morphologi G3 (B).

3.2.3. Software Tools

3.2.3.1. Calibration Development and Model

Measurement of solute concentration for acetaminophen in 3-methyl-1-butanol (chapter 5) requires construction of a calibration model which relates the ATR-FTIR spectral response to the dependant variable. For development of a calibration model which is to be employed across a range of temperatures, it is necessary to remove the effects of temperature from the spectra or to include such effects in the model (Gracin et al., 2002). The choice of the calibration model type is dependent on the complexity of the spectra for example, if the solute spectrum overlaps with that of the solvent, the use of a multivariate regression model such as partial least

squares (PLS) is likely to be required (Billot et al., 2010, Kadam et al., 2011, Simone et al., 2014a). Several calibration procedures using ATR-FTIR for measurement of concentration and supersaturation have been reported (Dunuwila, 1997, Dunuwila and Berglund, 1997, Cao et al., 1999).

For the calibration experiments, a series of fixed concentrations of acetaminophen in 3-methyl-1-butanol solvent were prepared at *ca.* 105°C and transferred to an OptiMax™ workstation equipped with a Mettler Toledo ReactIR ™ 15m unit and FBRM G400 probe. A stepped cooling profile was completed using 15°C steps over the range from 105 to 0°C (Figure 3.6). Evaporation of solvent at high temperature was minimised by use of a reflux condenser. Six acetaminophen concentrations were included in the calibration set: 10, 50, 90, 125, 200, 275 g kg^{-1} solvent. Two further experiments were performed to validate the calibration model: 60 g kg^{-1} solvent at 20°C and 180 g kg^{-1} solvent at 65°C. All experiments were held at a constant temperature for a period of *ca.* 30 – 70 min. The onset of nucleation was detected by FBRM due to increase in shorter chord counts at which point the experiment is stopped as concentration begins to decrease. To measure the solubility curve, an acetaminophen-solvent slurry of 300 g per kg solvent was prepared and a stepped heating profile (5°C min^{-1} ramps and 60 min hold periods) was completed with excess solids present (confirmed by FBRM total counts) throughout to ensure a saturated supernatant.

All spectral data were processed using GRAMS™ V9 software which was also used to generate partial least squares (PLS) models via the GramsIQ add-on. PLS is a widely used technique in chemometrics, especially in the case where the number of independent variables is significantly larger than the number of data points and has found wide application in industrial crystallisation processes (Roberts et al., 2017) .

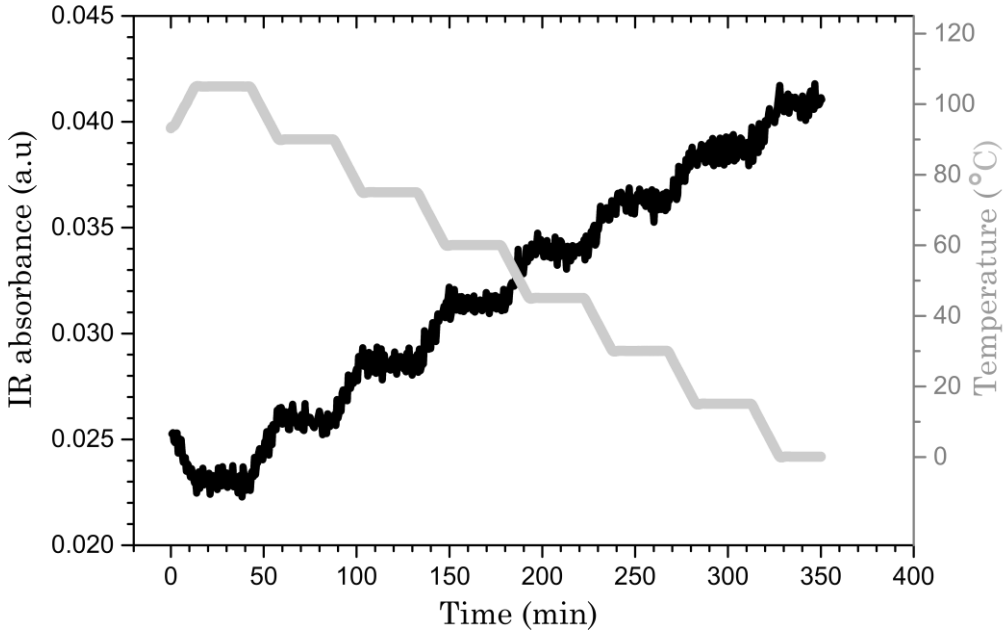

Figure 3.6 Example profile of a raw IR calibration dataset with a selected peak at 1670 cm^{-1} (carbonyl band) for acetaminophen in 3-methyl-1-butanol. The concentration for this experiment was 90 g kg^{-1} solvent which observed no nucleation and therefore the IR spectra (black line) was able to equilibrate at each temperature hold point (grey line).

Only those spectra that were acquired when the temperature had stabilised were used to construct the calibration model. For pre-processing, all spectra were baseline corrected and the 1700 - 800 cm^{-1} region was selected. Both the spectral and solute concentration data were mean centred prior to construction of the PLS model. The optimum PLS model was selected on the basis of the accuracy of the prediction obtained for the two validation experiments. The optimum calibration model employed 6 latent variables which consisted of an R^2 of 0.9997. This provided a reasonable fit as shown in Figure 3.7:

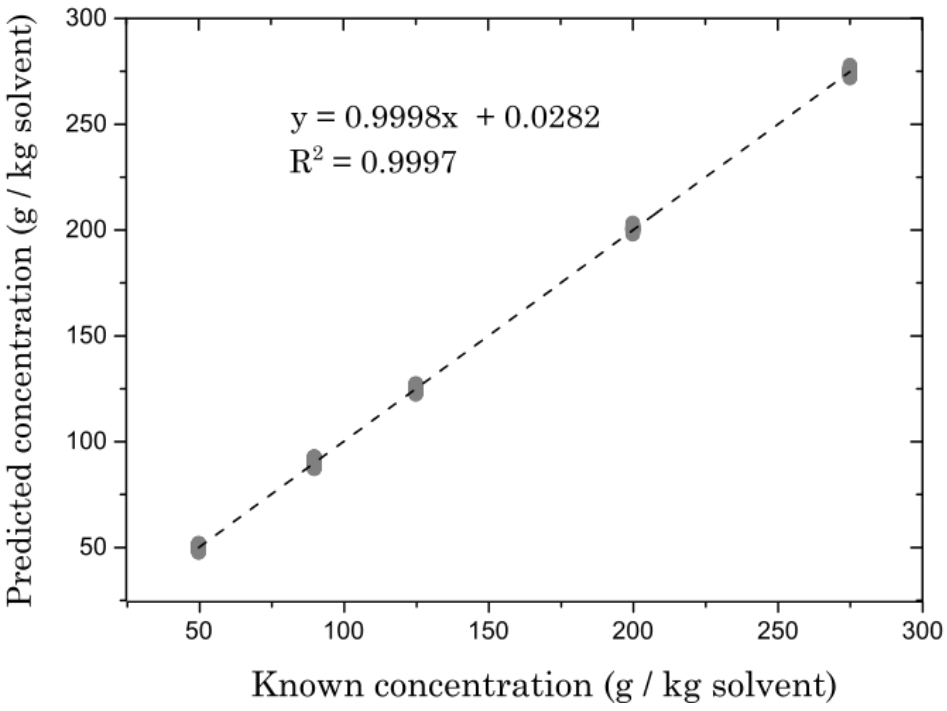

Figure 3.7 Calibration plot displaying known (actual) concentration vs predicted concentration for acetaminophen in 3-methyl-1-butanol.

The calibration model was then used to determine the solubility curve for acetaminophen in 3-methyl-1-butanol from IR spectra acquired when the temperature was constant during the hold periods. The predicted solute concentrations in the two validation experiments were 72 and 191 g kg^{-1} compared to the actual concentrations of 60 and 180 g kg^{-1} respectively. Although this gives an error of 6 to 20% (with the larger error present at lower concentrations), this was deemed to be adequate for the subsequent steps in the workflow approach for a seeded cooling crystallisation which is detailed in chapter 5.

3.2.3.2. gCRYSTAL Modelling Software

Population balance modelling (PBM) can be used for estimation of kinetic parameters for the various crystallisation mechanisms (nucleation, growth, agglomeration etc.,) occurring in a process. Several PBM implementations have been described and reported (Omar and Rohani, 2017) ranging from bespoke, freeware formulation implemented in MATLAB by MathWorks (Natick MA, USA) or commercial platforms such as gCRYSTAL by Process Systems Enterprise (PSE, London, UK) which are currently the most common.

For better process understanding, PBM and flowsheet simulations were employed in chapters 5 & 7 by implementing the gCRYSTAL 4.2.0 (PSE) software package. The software offers various particle size-change mechanisms and kinetics for characterisation of crystallisation processes as well as convenient toolboxes for parameter estimation.

To solve the numerical PBM equations in the software, a high resolution finite volume scheme with flux limiting function (HRFVS-FL) is integrated into the system which has been described elsewhere (Qamar and Warnecke, 2007, Qamar et al., 2009). The HRFVS-FL achieves similar accuracy compared to that obtained by the method of characteristics when solving crystallisation processes whereby supersaturation is modified with time but decreases the computational costs (Mesbah et al., 2011). This method divides the size domain for the discretisation of the PBM according to a geometrical grid which gives smaller step sizes at smaller crystal size thus improving the PSD resolution at initial times. The bounds and centre of each grid cell for a geometrical grid is computed through the following equations:

$$L_{i+\frac{1}{2}} = L_{min} + 2^{(i-N)/6}\,(L_{max} - L_{min}), \text{For } i = 1{:}N \qquad \text{Eqn 3.5}$$

$$L_i = \frac{L_{i+\frac{1}{2}} + L_{i-\frac{1}{2}}}{2} \; For\; i = 1{:}N \qquad \text{Eqn 3.6}$$

The purpose of process modelling in chapter 5 & 7 was for parameter estimation in order to fit the selected parameters such as concentration and PSD to measured experimental data. To this end, parameter estimation should be viewed as a fine tuning activity by rigorously adapting the parameter values in order to bring the model predictions into agreement with the experimental measurements. This requires configuring selected kinetic models together with the physical properties,

the solubility curve and model assumptions in the process flowsheet. Parameter estimation in gCRYSTAL 4.2.0 is based on the Maximum Likelihood formulation which provides simultaneous estimation of parameters in both the physical model of the process and the variance model of the measuring instruments i.e., the sensor which can be a constant variance, constant relative variance or heteroscedastic variance (combined both constant and relative variance). When solving a Maximum Likelihood Parameter Estimation problem, the software attempts to determine values for the uncertain physical and variance model parameters (θ), that maximise the probability that the mathematical model will predict the measurement values obtained from the experiments. Assuming independent, normally distributed measurement errors ($\varepsilon_{i,j,k}$) with zero means and standard deviations ($\sigma^{i,j,k}$), this maximum likelihood goal can be captured through the following objective function (ϕ):

$$\phi = \frac{NT}{2}\ln(2\pi) + \frac{1}{2} min_{\theta} \left\{ \sum_{i=1}^{NE} \sum_{j=1}^{NV_i} \sum_{k=1}^{NM_{ij}} \left[\ln\left(\sigma_{ijk}^2\right) + \frac{\left(\tilde{z}_{ijk} - z_{ijk}\right)^2}{\sigma_{ijk}^2} \right] \right\} \qquad \text{Eqn 3.7}$$

Here, the total number of measurements taken during all experiments (NT), the set of parameters to be estimated (θ) with acceptable values being subject to given lower and upper bounds ($\theta^l \leq \theta \leq \theta^u$), the number of experiments performed (NE), the number of variables (NV_i) measured in the i^{th} experiment, the number of measurements (NM_{ij}) of the j^{th} variable in the i^{th} experiment, the variance (σ_{ijk}^2) of the K^{th} measurement of variable j in i, $\tilde{z}_{ijk}$ the K^{th} measured value of variable j in experiment i and z_{ijk} the

K^{th} predicted value by the model of variable j in experiment i (Pérez-Calvo et al., 2016).

The overall maximum likelihood objective function may be split into a constant, a variance and a residual term (Eqn 3.7). Both the constant ($\frac{NT}{2}\ln(2\pi)$) and the variance term ($\ln\left(\sigma_{ijk}^2\right)$) are fixed for a given parameter estimation while the maximum likelihood function is minimised by minimising the residual term ($\frac{\left(\bar{z}_{ijk} - z_{ijk}\right)^2}{\sigma_{ijk}^2}$) (Pérez-Calvo et al., 2016).

The definition of the grid to solve the population balance equations as well as the selected variance of the experimental variables introduced in the objective function might modify the obtained values of the model parameters. Therefore, a preliminary study of the effect of these options on the parameter estimation is required to obtain a meaningful model. The lower bound, L_{min}, and the upper bound, L_{max}, of the size domain for both chapters 5 and 7 have been chosen to be 1 and 2000 μm to capture both the crystallisation phenomena taking place and the size of the crystals over the whole experimental time domain. The size domain has been divided into 100 grid cells. Other model assumptions are detailed in section 5.2.7 and 7.3.3 whereby experimental data was numerically fitted to the model framework equations to obtain the value of the kinetic model parameters.

3.2.3.3. CLD-Inversion App

A CLD-inversion App is deployed to estimate the inline particle size distribution (PSD) and particle aspect ratio from raw chord length distribution (CLD) data measured by a Mettler Toledo focused beam reflectance measurement (FBRM) sensor (Agimelen et al., 2015).

To deduce the actual PSD and particle shape (aspect ratio) from experimental CLD data, an inverse problem needs to be solved. Discretising both the CLD (which is already measured as a discrete distribution) and PSD followed by construction of an appropriate transformation matrix which relates these two distributions is the most common method (Kail et al., 2009, Wynn, 2003, Li and Wilkinson, 2005, Agimelen et al., 2015). The transformation matrix depends on the chosen size bins to discretise the two distributions and the corresponding size ranges in addition to the shape of the particles. The transformation matrix isn't usually known in advance and therefore needs to be estimated along with the corresponding PSD (discretised) so that the convolution of the transformation matrix with the PSD yields a CLD which agrees with the experimentally measured CLD (Agimelen et al., 2016). It is known, a combination of factors in a process produce the experimentally measured CLD which differs from the theoretically calculated CLD. For example, in addition to particle number and size, the particle shape, particle concentration, probe positioning and calibration, optical effects of the continuous and dispersed phase and other process parameters produce the

experimentally measured CLD as reported from several sources (Kail et al., 2007, Irizarry et al., 2017, Schoell et al., 2019).

Considering the discretisation method used in the inversion algorithm for calculating the PSD from a known CLD, a size range ($D_{\min}$ to $D_{\max}$) of particles used is firstly specified (Agimelen et al., 2015). $D_{\min}$ is the smallest particle size and $D_{\max}$ is the largest particle size in the population whereby the inversion algorithm automatically determines the best values for each size range. A number S of consecutive bins of the chord length histogram from the FBRM sensor are chosen. The bins make up a window of width S, where the width (or size) of a window is the number of bins contained within that window. The geometric mean of the first two bin boundaries of a window is taken as $D_{\min}$ and the geometric mean of the last two bin boundaries of a window is taken as $D_{\max}$. The procedure is illustrated in Figure 3.8 below:

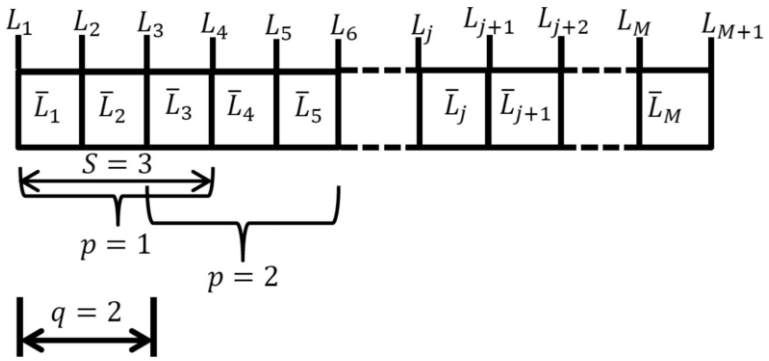

Figure 3.8 Pictorial representation of the bins and bin boundaries of the CLD histogram showing a window of size S, at the first two positions set by $p = 1$ and $p = 2$ shifted by q. The window is moved in such a way that some of the bins contained in the window at $p = 1$ overlap some of the bins of the window at $p = 2$ (Agimelen et al., 2015).

The boundaries of the chord length histogram are labelled as:

$$L_j, j = 1, 2, 3, \ldots\ldots, M + 1 \qquad \text{Eqn 3.8}$$

The characteristic chord length $\bar{L}_j$ of bin j is the geometric mean of the chord lengths of its boundaries:

$$\bar{L}_j = \sqrt{L_i} L_{j+1.} \qquad \text{Eqn 3.9}$$

Initially during the calculation, the first w bins of the chord length histogram are chosen, so that $S = w, D_{\min} = \bar{L}_1$ and $D_{\max} = \bar{L}_w$. After the first iteration (see steps 5 to 9 in the article (Agimelen et al., 2015)), a new set of bin boundaries are then selected. Whilst the new set of bin boundaries are made up of the same number of bins S as the previous set, it is shifted to the right of the previous set by an amount q. Hence, there are q bins between the beginning of the first set of bins and the beginning of the second set. The shift is made in such a way that the two sets of bins overlap each other. For example as shown in Figure 3.8, the window initially runs from bin boundary L_1 to bin boundary L_4. At this position, the window contains bins L_1 to L_3 so that the width of the window is $S = 3$. At the end of the first iteration, a new set of bins are chosen, this time starting from bin boundary L_3 and ending at bin boundary L_6 (Figure 3.8). The number of bins in the new set of bins (or window) is the same as before $S = 3$. Each window (or set of bins) is identified by its position index p. Therefore, the value of the first position index is $p = 1$ and the value of the second position index is $p = 2$. There are two bins between

the beginning of the window at $p = 1$ and beginning of the window $p = 2$ so that $q = 2 < S$. At the end of the second iteration, the window is shifted to the right again while maintaining fixed values of S and q. This process continues until the last bin boundary of the chord length histogram is reached (Agimelen et al., 2015).

Each time a set of bins are chosen, the values of $D_{\min}$ and $D_{\max}$ are calculated as:

$$D_{\min} = \bar{L}_1 \beta^{(p-1)q} \quad \text{Eqn 3.10}$$

$$D_{\max} = D_{\min} \beta^{(S-1)} \quad \text{Eqn 3.11}$$

Where $\beta = \bar{L}_{j+1} / \bar{L}_j$. The position index of the window takes values:

$$p = 1, 2, 3, \ldots, \left\lfloor \frac{M}{q} \right\rfloor \quad \text{Eqn 3.12}$$

Here, the floor function $\lfloor . \rfloor$ returns the values of the largest integer that is less than or equal to M/q. Once the values of $D_{\min}$ and $D_{\max}$ have been calculated from equations 3.10 & 3.11, the particle size bins are then constructed. The bin boundaries D_{i} of the particle size bins are calculated:

$$D_{\mathrm{i}} = D_{\min} \mu^{i-1}, \quad i = 1,2, \ldots, N+1 \quad \text{Eqn 3.13}$$

Where:

$$\mu = \left(\frac{D_{max}}{D_{min}} \right)^{1/N} \quad \text{Eqn 3.14}$$

N is the chosen number of particle size bins. The characteristic size of a particle size bin can then be calculated as:

$$\bar{D}_i = \sqrt{D_i D_{i+1}} \qquad \text{Eqn 3.15}$$

Once the characteristic particle sizes $[\bar{D}_1 \bar{D}_N]$ have been constructed, the transformation matrix $\tilde{\mathbf{A}}$ can then be performed (for a chosen aspect ratio). Equations used for building the transformation matrix are explicitly detailed in the article (Agimelen et al., 2015).

However, certain factors need to be considered with this approach for instance, there are a number of different matrices and PSDs whose convolutions give rise to the same CLD. Whilst the developed CLD-inversion App allows for a range of estimated particle sizes in a slurry in situ, the transformation matrix is constructed with a single aspect ratio for all particles. Hence, there is a possibility that the transformation matrix is constructed with inappropriate aspect ratio or that there is a wider range of aspect ratios present for particles in a bulk suspension of same or different sizes. It has been demonstrated, that it is still possible to calculate different CLDs all of which have good agreement with an experimentally measured CLD even though some of the transformation matrices were constructed at aspect ratios that were far from the shape of the particles described (Agimelen et al., 2015). However, equally it was shown that as the aspect ratio deviated further from the true shape of the particles, then the corresponding PSD becomes increasingly noisy. This

situation led to the introduction of a penalty function in order to eliminate unrealistic aspect ratios. Nonetheless, if there is a wide variation of aspect ratios of particles in slurry, introducing further constrains on the aspect ratio to reduce the search space and regularise the inverse algorithm would be useful (Agimelen et al., 2016).

The purpose of using the CLD-inversion App throughout this work is to investigate the effectiveness, accuracy and limitations for monitoring inline PSD during complex particle engineering processes such as a combined wet milling and crystallisation process. A key advantage of this computational tool is the ability to work without any pre-information regarding particle size or shape as the comprehensive algorithm searches for a global best solution to the inverse problem (Agimelen et al., 2015, Agimelen et al., 2016).

The App is accessed through a Graphical User Interface (GUI) where raw extracted experimental chord length distribution data (macro view, no weighted) in .csv from a Mettler Toledo FBRM G400 series probe is obtained. The PSD can then be estimated from the CLD by selecting either the “Whole File” or “Range” option. The “Range” option was chosen throughout this work where a desired range of CLD counts are selected at specified time intervals. For estimation of PSD and aspect ratio to proceed, the algorithm needs to know the range of aspect ratio to search in the format [min, max].

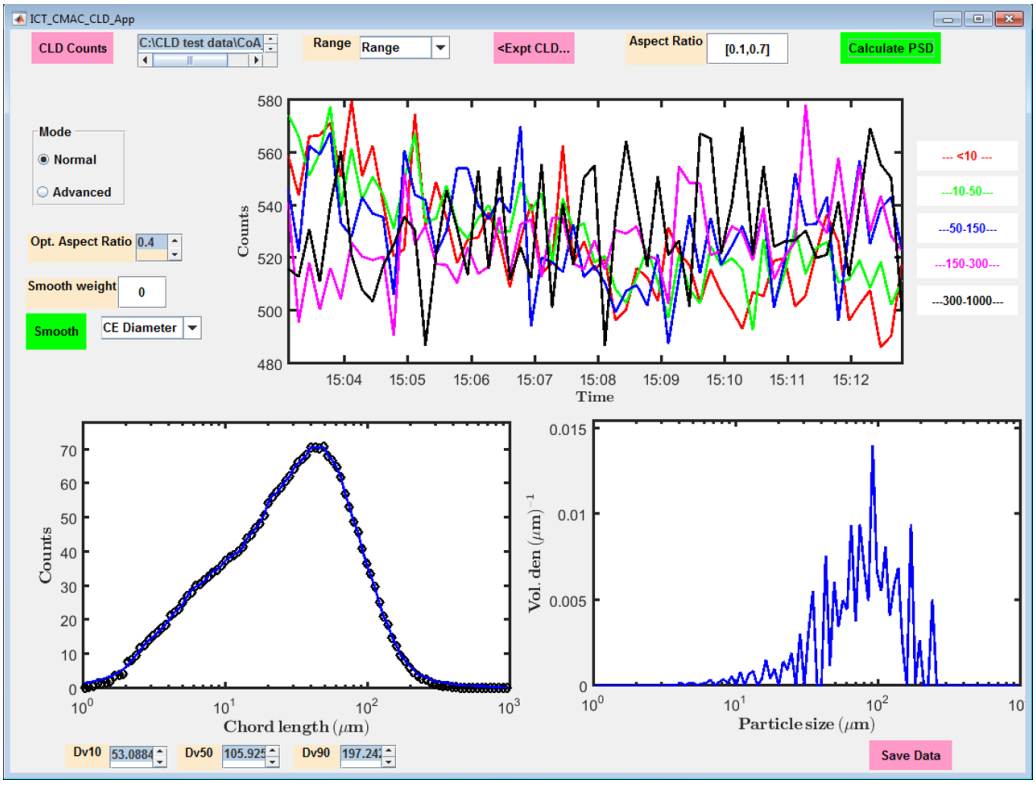

Figure 3.9 CLD-inversion app interface for PSD estimation from raw measured chord lengths captured by an FBRM sensor (Agimelen et al., 2018a).

The minimum aspect ratio that can be entered is 0.1 and the maximum is 1. The aspect ratio is defined as the ratio of width to length, hence needle-like particles would be close to 0.1. Upon entering the aspect ratio values, the PSD can now be calculated as shown from the example interface (Figure 3.9). The CLD-inversion algorithm was used from chapters 4 to 6.

3.2.3.4. Imaging App

An imaging software app was used which generates distributions of particle attributes (size and shape) from image analysis techniques (Cardona et al., 2018, Cardona and Tachtatzis, 2018). It incorporates a

focus evaluation step to extract meaningful quantitative size and shape information through rejection of out-of-focus particles (Cardona et al., 2018). The model simulates 2D projection of three-dimensional particles onto the focal plane and then computes the corresponding size and shape distribution. The inclusion of a focus classifier allows the user to apply this tool to both offline and inline imaging data. The sequential steps followed by the image analysis framework is shown (Figure 3.10).

The app was applied to collected images (.bmp files) from a Mettler-Toledo PVM V819 sensor for chapter 6 which produced quantitative information on particle size and shape (Figure 3.11).

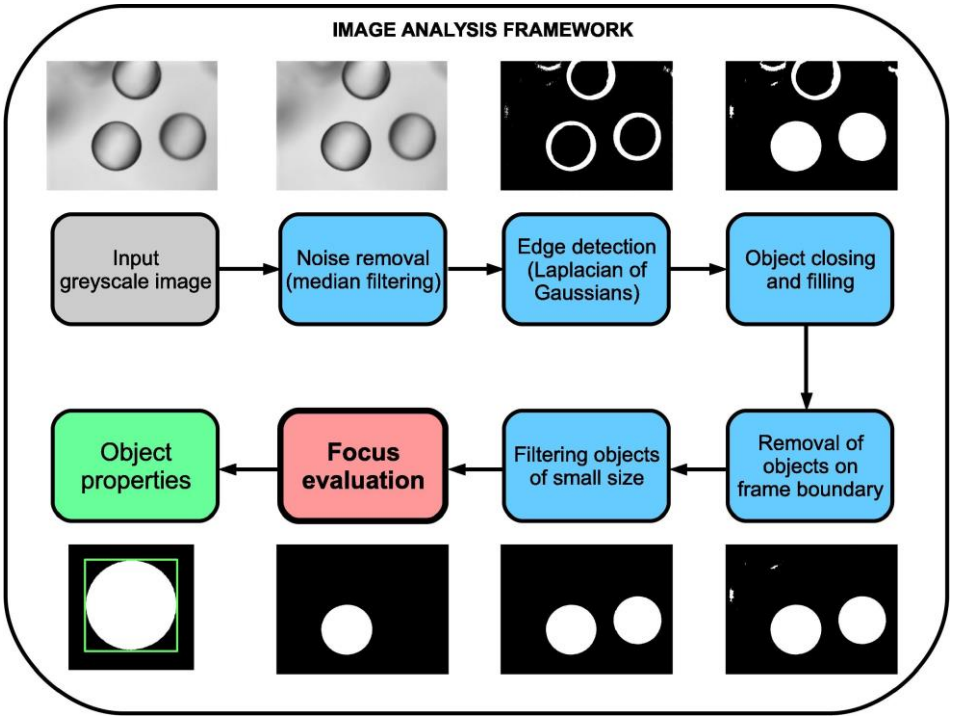

Figure 3.10 Diagram of the steps followed by the image analysis framework (Cardona et al., 2018).

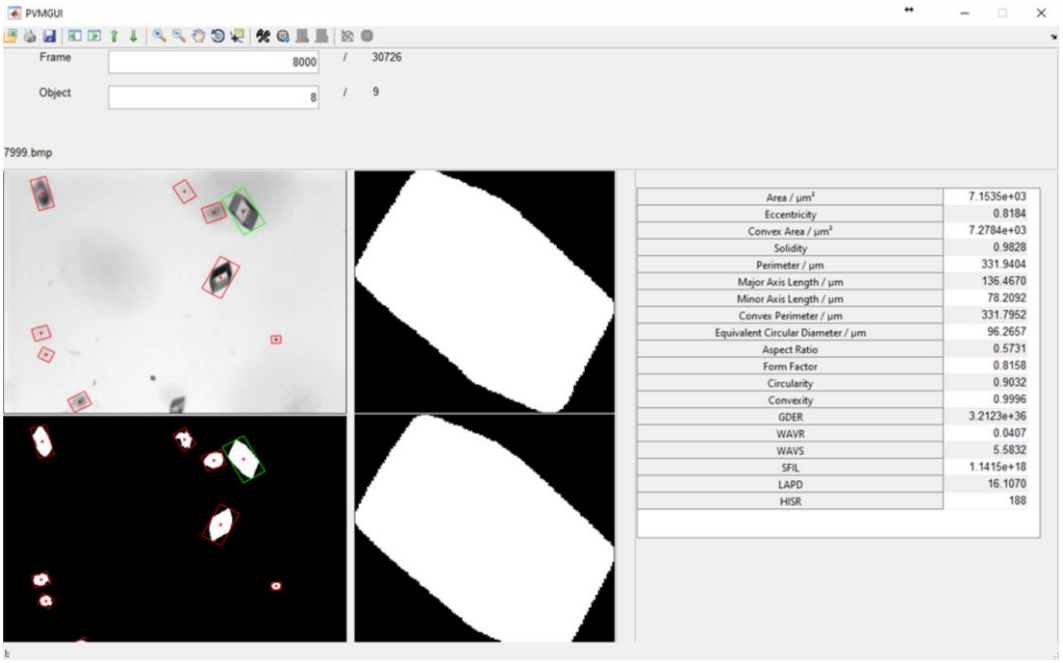

Figure 3.11 Imaging app interface (MATLAB, The MathWorks, Inc) for estimation of PSD and shape statistics from captured inline images (Cardona et al., 2018, Cardona and Tachtatzis, 2018).

Chapter 4

Engineering of Acetaminophen Particle Attributes Using a Wet Milling Crystallisation Platform

This chapter has been published as a journal article:

AHMED, B., BROWN, C. J., MCGLONE, T., BOWERING, D. L., SEFCIK, J. & FLORENCE, A. J. 2019. Engineering of Acetaminophen Particle Attributes Using a Wet Milling Crystallisation Platform. *International Journal of Pharmaceutics*. 554, 201-211.

4. Engineering of Acetaminophen Particle Attributes Using a Wet Milling Crystallisation Platform

4.1. Introduction

It is known that crystallisation is a widely used technique for purification and imparting control of the physical properties of molecular solids (chapter 1, 1.2). Within pharmaceutical manufacturing, an important goal is to design the required crystallisation process to deliver robust control over particle properties (form, purity, size, shape, surface, area and mechanical) to ensure consistent performance (Beckmann, 2013, Baxendale et al., 2015).

The integration of wet milling with crystallisation processes via process intensification has shown to be an attractive means for control of particle properties as reviewed in section 1.4. Importantly, it can be applied in a recirculation mode during crystallisation with integrated PAT showing controlled crystal size reduction in suspensions even with the occurrence of competing phenomena such as primary & secondary nucleation (Yang et al., 2016a), growth and multiple breakage mechanisms (Lee et al., 2004, Cote and Sirota, 2010). However, complete decoupling and analysis of mechanisms during combined wet milling crystallisation processes is yet to be extensively investigated. Furthermore, the impact of high shear wet milling process parameters on material surface properties such as surface energy distributions and surface areas in relation to particle size and shape is an area of interest (Luner et al., 2012).

In this study, an investigation of the relationship between process parameters and product attributes is presented for acetaminophen using a semi-continuous wet milling seeded cooling crystallisation process (WMSC) (Figure 4.1). Utilising a toothed rotor-stator wet mill, selected teeth configurations (coarse, medium, fine and multiple-stage) were operated from low to high rotation speeds (rpm). Constant inline PAT (process analytical technology) monitoring of chord length distributions (μm) with offline volume weighted circle equivalent diameter [4,3] μm, aspect ratio and circularity was assessed simultaneously at various milling turnovers.

Chord lengths (μm) were inverted to provide an estimation of inline particle size distribution (PSD) at specified milling times through an the inverse algorithm method (as described in chapter 3, 3.2.3.3) Agglomerated bimodal seeds which are commonly produced by standard offline seed generation techniques, was the input material to test for the overall robustness of the process to deliver narrowing and improvement to the particle size distribution throughout. This work to our knowledge is the first study to test this process as well as variability in wet milling teeth and speed (rpm) arrangement on material surface properties through measurement of surface areas and surface heterogeneity.

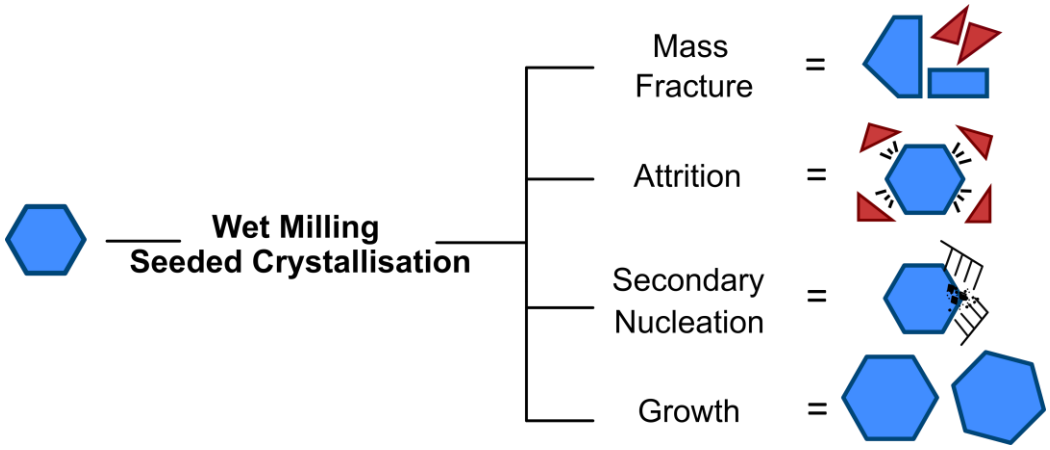

Figure 4.1 Schematic highlighting potential mechanisms involved when operating a wet milling seeded crystallisation (WMSC) process, adapted from (Engstrom et al., 2013). A de-agglomeration phase within the mass fracture mechanism can also occur when agglomerated input starting material is used.

4.2. Experimental Section

4.2.1. Materials and Methods

The model compound studied for this system was acetaminophen which is a widely known analgesic and antipyretic compound. The solvent 2-propanol and distilled water was used for all experiments. A Mettler Toledo OptiMax™ workstation consisting of a 1 L stirred tank crystalliser (STC) equipped with an in-line Hastelloy® Pt100 temperature sensor was used for all experiments with the system controlled and operated through the iControl v5.4 software (Figure 4.3). The following Mettler-Toledo inline process analytical technology tools used for each of the experiments were: FBRM probe (G400 series) for particle tracking and chord length distribution by laser back-scattering (iC FBRM V4.3) and a PVM V819 probe with online image acquisition software V8.3 included. An IKA

MagicLab (Module UTL) wet mill unit was used for the inline milling process. Mill outlet temperature was monitored on the IKA operating unit display. Rotation speeds were operated from 6000 to 18000 rpm, with varying teeth configurations investigated across coarse, medium and fine rotor-stator modules as well as a multiple-stage configuration incorporating all three (coarse, medium, fine). The temperature of the wet mill chamber was manually controlled during milling to match the temperature of the feed solution within 1°C throughout cooling.

4.2.2. Seed Preparation

Seed crystals of raw acetaminophen used for the experiments were prepared through an offline vibratory ball mill (Griffin & George) and sieved (Fritsch analysette 3 type sieve shaker, Northants, UK) approximately into the required size fraction; 25 - 63 μm. This fraction was used for all experiments.

4.2.3. Particle Size and Shape Characterisation

For offline sample analysis, a Malvern Morphologi G3 was used for both particle size and shape measurements. All milled acetaminophen was analysed for size and shape information to which the measurement details are outlined (chapter 3, 3.2.2.1). Both a high and low energy dispersion method was used for characterising the seed crystals.

4.2.4. Scanning Electron Microscope (SEM)

Samples were subjected to an SEM microscope for image analysis. Details of the method analysis is described (chapter 3, 3.2.2.4).

4.2.5. Surface Energy Characterisation

An iGC-SEA system was used for surface energy and Brunauer, Emmett, Teller (BET) specific surface area analysis for acetaminophen samples. The instrument setup and method details are outlined (chapter 3, 3.2.2.5). Each sample produced a standard error ranging from 0.2 to 2.2%. A detailed background review to deriving the surface energy descriptor can be found from numerous sources (R Williams, 2015, Kondor et al., 2015, Newell et al., 2001).

4.2.6. Wet Milling Seeded Crystallisation Process

A seeded cooling crystallisation process was selected using ca. 1.84% seed loading, solution starting concentration 179.6 g / 1000 g of 2-propanol and a constant cooling rate from 35°C to 10°C over 3 hours. The rationale for the selected conditions was to maximise crystal growth within the metastable zone width by adding low seed mass of high surface areas at high concentrations (Table 4.1 & Figure 4.2). A slow cooling profile was employed to promote growth and avoid any undesired nucleation events. To monitor the impact of wet milling mechanisms during cooling and its performance as a continuous device, the crystallisation was then operated whilst simultaneously wet milling the suspension under different rotor-stator teeth configurations and rotation speeds (rpm). Low to high speeds were utilised through the recirculation mode as illustrated in the experimental setup (Figure 4.3 & Figure 4.4).

A normalised energy dissipation rate (E^*) model for describing the energy imparted to particles for reduction in slurry which depends on the rotor speed, or tip speed as well as the slurry dynamics and wet mill geometry has been previously reported (Engstrom et al., 2013) for scale-up (section 1.4.1.1). The model was used for predicting the particle size for acetaminophen from the recycle-loop configuration under different milling configurations (number of teeth and rotation speed) which incorporated the rotor tip speed (S_r) = m/s and shear frequency (f_{sr}) = s^{-1} expressions:

$$E^* = \varphi_r \,.E_r \qquad \text{Eqn 4.1}$$

$$E_r = \frac{S_r^2}{S_{rb}^2} \qquad \text{Eqn 4.2}$$

$$\varphi_r = \frac{NR_O \,.NS_O \,.\omega}{NR_{Ob} \,.NS_{Ob} \,.\omega_b} \,.\frac{N_{ST} \,.\, N_G/\dot{Q}}{N_{STb} \,.\, N_{Gb}/\dot{Q}_b} \,.\frac{W_r \,.\, H_r}{W_{rb} \,.\, H_{rb}} \qquad \text{Eqn 4.3}$$

Here, the relative energy term (E_r) considers the kinetic energy of the wet mill rotor tooth impacting the particles in slurry and compares the kinetic energy of a given experiment to a reference experiment (b). The relative weighting factor (φ_r) accounts for critical inputs missing from the tip speed correlation by including the shear frequency (f_{sr}), residence time (τ) and relative area of collision on the rotor tooth (A_{cr}) = m. For shear frequency (f_{sr}), the number of outer teeth located on the rotor (NR_O) and stator (NS_O) tooth modules as well as the angular rotational speed (ω) = rpm were measured. Hence, the shear frequency expression expands on rotor tip speed as the outer diameter of the rotor tooth and angular rotation speed

are included. Residence time (τ) includes the number of slurry turnovers (N_{ST}), number of rotor and stator module generators (N_G) and the volumetric flow rate ($\dot{Q}$) = $m^3 s^{-1}$ through the wet mill. The width (W_r) = m and height (H_r) = m of the rotor tooth is also measured and included in the area of collision (A_{cr}) term. A more detailed description to the normalised energy dissipation rate (E^*) model is reported (Engstrom et al., 2013).

Table 4.1 Seed characterisation and conditions used for all experiments.

Seed mass (g)	2.24
Seed size (Dv50, μm)	30.49
Seeding supersaturation	1.18
Seeding concentration (g / 1000 g solvent)	182.60

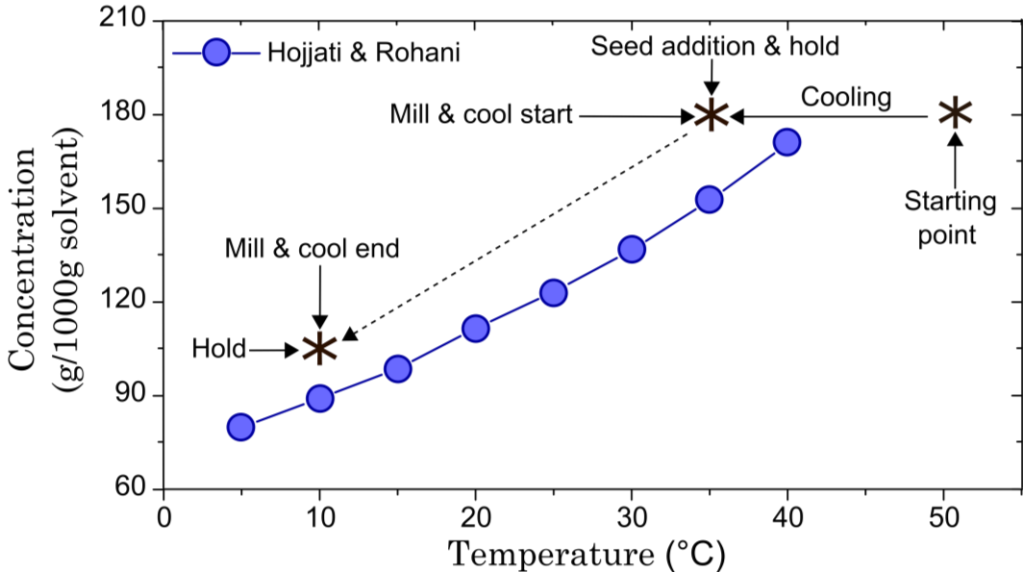

Figure 4.2 Temperature dependent solubility profile for acetaminophen in 2-propanol solvent (Hojjati and Rohani, 2006) with the experimental trajectory and key process step annotated. Seeding conditions are shown in Table 4.1.

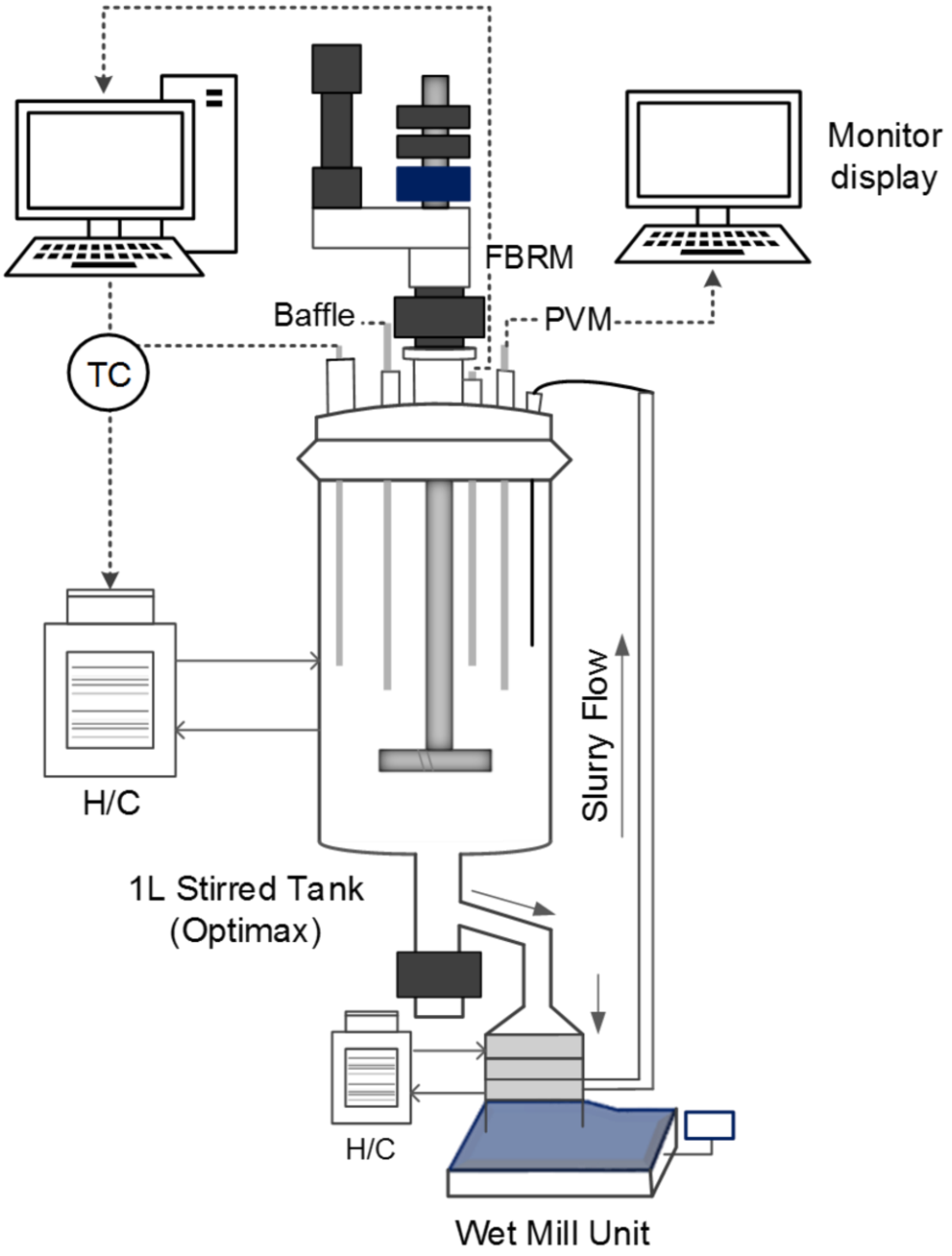

Figure 4.3 Experimental apparatus consisting of a baffled crystalliser vessel (OptiMax) with integrated rotor-stator wet mill through the recycle-loop mode. PAT (FBRM, PVM), temperature control and stirrer were controlled via iControl software.

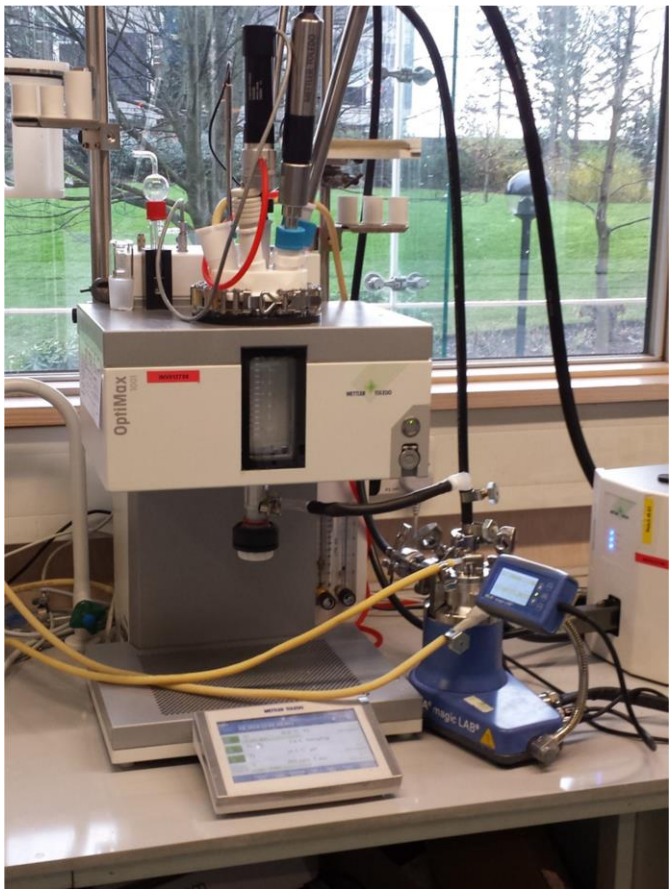

Figure 4.4 Image of the experimental apparatus.

Acetaminophen (120 g) was added to 2-propanol (669.5 g) within the OptiMax 1 litre vessel. FBRM and PVM were integrated within the vessel. The cooling profile was based on the temperature dependent solubility of acetaminophen in 2-propanol (Hojjati and Rohani, 2006). The solution was prepared by heating the mixture to 50°C over 15 min with the agitator set to 600 rpm. After a further 30 min the solution was then slowly cooled to 35°C over 15 min. Seed crystals (size fraction of 25 - 65 μm) were prepared in a separate flask and added to the vessel as a slurry suspension (2.24 g / 1.84%, Table 4.1). An additional 30 min hold period at 35°C was carried out to allow seed dispersion. A linear cooling profile (0.13°C / min)

over 3 hours was then implemented down to 10°C with wet milling occurring simultaneously during this cooling period. A further hold period from 30 min to 1 h at 10°C was carried out. The recrystallised product suspension was then filtered (90 mm mean diameter) using a Büchner funnel, washed with chilled distilled water and dried overnight (40°C) in a vacuum oven.

Experimental runs tested different rotor-stator configurations including the number of teeth (coarse, medium and fine) and rotation speeds (Table 4.2). The total number of outer teeth on the rotor and stator modules ranged from 13 to 61 which only considered the outer teeth. The E^* model considers the combination of generators within the mill setup to consist of one generator as additional generators simply increases the residence time in the wet mill chamber with the imparted energy being the same from one generator to the next.

Samples were taken for the majority of the experiments at different milling residence times (min) consisting of every 28 minutes as each set of conditions was dependent on the number of slurry turnovers (N_{ST}) and the volumetric flow rate ($\dot{Q}$) = L / min. As no separate pump was used in the recycle-loop to avoid process complexity, the mill rotation speed provided continuous recirculation of the suspension and can be selected to match the volume to pumping ratio (Figure 4.3 & Figure 4.4). The volumetric flow rate was calculated from a linear regression fit ($r^2 = 0.928$) for calibrated flow-rates as a function of variable rotation speeds (rpm) measured by

Engstrom et al., (Engstrom et al., 2013). Thus, a relatively high flow rate of 1.30 L / min was achieved for the selected 18000 rpm speed in comparison to 0.29 L / min at 6000 rpm. However, it would be desirable to conduct a set of own calibration tests to confirm the reported values especially if selecting a wider range of rotation speeds (rpm) which was not investigated in this chapter. For the decoupling experiments, a seeded cooling crystallisation experiment with no mill was carried out using the same concentration and cooling profile as well as seed mass and size. Two saturated (isothermal) wet milling experiments under the same process configurations were also operated at fixed temperature with no cooling implemented during milling (Table 4.3).

4.3. Results and Discussion

4.3.1. Particle Size and Shape Analysis

To control the behaviour of cooling crystallisation, seeding with existing crystals of the parent form allows greater reproducibility of the desired product attributes such as PSD (Aamir et al., 2010). However, often poor seed qualities such as bimodality and agglomerated seeds are commonly introduced into crystallisation processes making it difficult to control and deliver a monodisperse PSD of the final product. One method to overcome this is to integrate a wet mill to deliver tightening of the PSD over time and increase nucleation kinetics of slowly nucleating compounds as shown in Figure 4.5.

Table 4.2 Investigated parameters for the combined wet milling seeded crystallisation process.

Rotor-Stator Configuration	Total No of Teeth $NR_O + NS_O$	Rotation Speed, ω (rpm)	Flow Rate, $\dot{Q}$ (L / min)	Cooling Rate (°C / min)	Milling Residence Time (min)	Number of Slurry Turnovers, N_{ST}	Normalised Energy Dissipation Rate, E^*
Coarse	13	6000	0.29	0.13	28,56,84,112,140,168	8,16,24,33,41,49	0.04,0.15,0.33,0.59,0.93,1.33
Coarse	13	18000	1.30	0.13	28,56,84,112,140,168	36,73,109,145,182,218	1,2,3,4,5,6
Medium	19	6000	0.29	0.13	28,56,84,112,140,168	8,16,24,33,41,49	0.1,0.2,0.2,0.3,0.4,0.5
Medium	19	18000	1.30	0.13	28,56,84,112,140,168	36,73,109,145,182,218	2.14,4.29,6.43,8.57,10.71,12.86
Fine	29	6000	0.29	0.13	28,56,84,112,140,168	8,16,24,33,41,49	0.2,0.4,0.6,0.7,0.9,1.1
Fine	29	18000	1.30	0.13	28,56,84,112,140,168	36,73,109,145,182,218	5,10,15,20,25,30
Multiple-stage	61	18000	1.30	0.13	28,56,84,112,140,168	36,73,109,145,182,218	1,2,3,4,5,6

Table 4.3 Investigated parameters for saturated (isothermal) wet milling experiments at constant temperature.

Rotor-Stator Configuration	Total No of Teeth $NR_O + NS_O$	Rotation Speed, ω (rpm)	Flow Rate, $\dot{Q}$ (L / min)	Temperature (°C)	Concentration (g / 1000 g solvent)
Coarse	13	18000	1.3	15	97.80
Coarse	13	18000	1.3	35	151.57

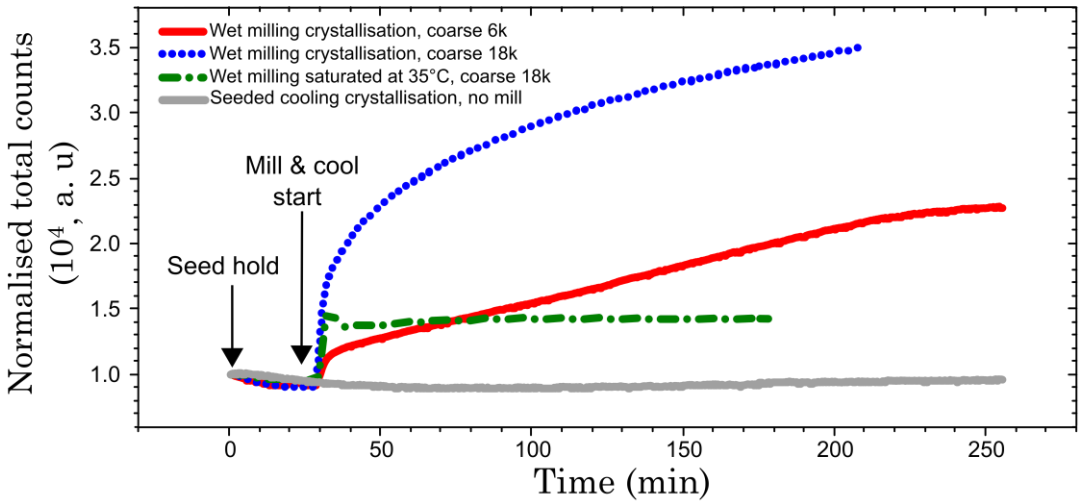

Figure 4.5 Total count profiles (inline) versus time for each of the experimental conditions.

4.3.1.1. Cooling Crystallisation, No Mill

From Figure 4.5, initial data captured via an FBRM sensor displays normalised total particle counts as a function of time from the conducted experiments. A seeded cooling crystallisation process without wet milling with the same seeding conditions and cooling profile was implemented. This was to observe the growth behaviour of acetaminophen in 2-propanol. For this experiment, total counts increase very slowly over time in contrast to other observed trends when wet milling is coupled (Figure 4.5). This indicates the crystallisation to be of a slow growing system with agglomeration occurring as observed from the PVM images (Figure 4.6). Ultimately, this results from agglomerated seeds introduced which leads to a broad final PSD (Figure 4.8, (B)). Therefore secondary nucleation, breakage or de-agglomeration is likely to be insignificant from this experiment.

4.3.1.2. Saturated 35°C, Coarse 18k rpm

The wet mill was now coupled to the stirred-tank with a seeded suspension being continuously recycled at constant temperature to decouple the effect of crystallisation. This was to primarily identify the mechanisms arising from wet milling only. For the saturated coarse 18k at constant temperature of 35°C had shown a significant impact on the total counts (Figure 4.5). Here, the dominant effect of mass fracture after mill start-up is clearly observed with de-agglomeration of the seed particles. This is shown from the effect of mill start which leads to an immediate sharp increase in total counts (5 - 10 min, Figure 4.5) resulting in rapid size reduction within 30 min of milling as further evident from the immediate shift from inline particle size distributions (Figure 4.7, (C)). The total counts then reached an almost steady value (Figure 4.5) for the remainder of the experiment as no additional mechanisms are believed to be occurring which can be further noticed from the matching inline PSD trends for 1 hr and end milling periods (Figure 4.7, (C)). Hence, no increase or decrease in particle size occurred. For this decoupling experiment, mass fracture and de-agglomeration are therefore predominant (Figure 4.6).

4.3.1.3. WMSC, Coarse 6k rpm & Coarse 18k rpm

Examining two selected WMSC at low and high rotation speeds (rpm) (Figure 4.5, coarse 6k & 18k) introduces additional mechanisms with the most significant being secondary nucleation. Total count trends and inverted chord length distributions (Figure 4.5, Figure 4.7, (A & B))

indicate that milling the suspension under supersaturated conditions during cooling gives rise to a significant reduction in mean particle size with an accompanying increase in the number of counts, largely due to mass fracture and de-agglomeration during the initial 30 min of mill start. This immediate breakage and de-agglomeration of the starting seed particles is simultaneously observed from the inline particle size distribution (μm) shift (Figure 4.7, (A & B)) and is clearly seen from the images captured by the PVM sensor (Figure 4.6). Total counts display sharp increases within 20 min of starting the mill after which they approach constant values (Figure 4.5). Larger counts decrease rapidly over time as a result of mass fracture due to interaction of the largest particles with the mill teeth. The gradual levelling of the total counts during the latter stages of milling is attributed to the completion of the initial mechanisms and depletion of larger particles remaining in the system, with fines generation still evident due to milling and secondary nucleation (Kamahara et al., 2007, Yang et al., 2015).

Interestingly during the WMSC process, mass fracture followed by fines generation whereby attrition of particles produces fines growing under the influence of supersaturation results in observed particles. During the saturated milling experiment at 35°C, mass fracture is followed by no detectable fines generation as the attrition mechanism is creating fines subsequently not growing to a point observable without the driving force of supersaturation (Agrawal and Paterson, 2015). However, from the

conducted experiments we observed initial occurrence of a mass fracture process from both the WMSC and saturated wet milling at constant temperature.

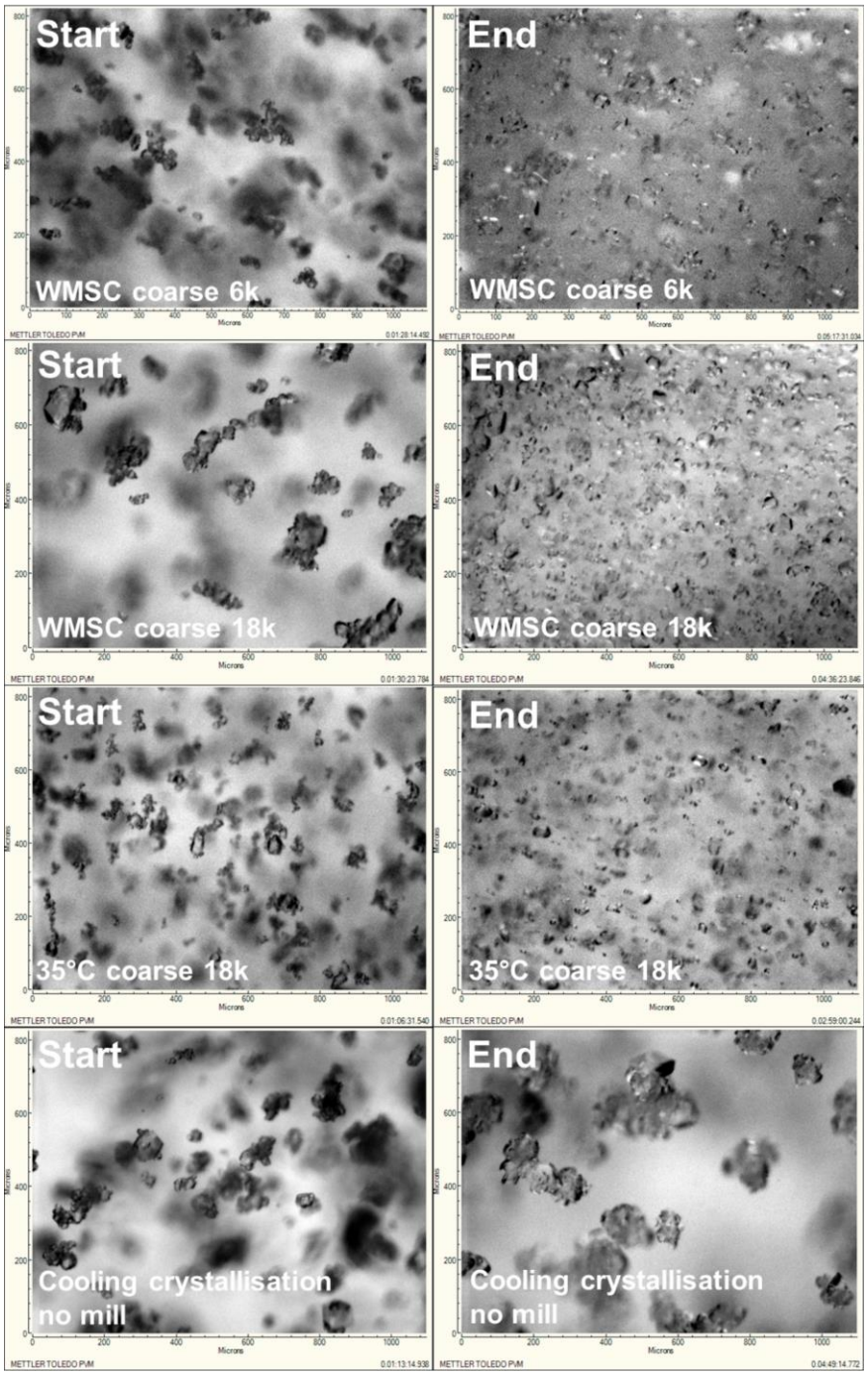

Figure 4.6 Inline images captured by a PVM sensor showing the suspended seed crystals at the start and end of each experimental run.

As a consequence, secondary nucleation arising from the driving force of supersaturation and attrition during the WMSC process is predominant during the latter stages of cooling with imaging showing the clear increase in particle population at the end of each experimental run as a result of the process (Figure 4.6). Similar trends were consistently seen when varying teeth configuration across the WMSC experiments (Table 4.2). Incorporation of inline FBRM and PVM sensors during a wet milling process thus serve as essential process monitoring tools (PAT) to identify and distinguish between coinciding mechanisms (Figure 4.1) occurring at specific time intervals during an experimental run (Cardona et al., 2018).

The CLD-inversion algorithm had successfully tracked inline particle size throughout the course of the experiments. For WMSC at coarse 6k & 18k and saturated (35°C) milling at 18k, a gradual shift in PSD from right to left is seen (Figure 4.7, (A – C)). Whilst tightening of the distribution occurs from the effect of wet milling, wider distributions were obtained for end mill & cool points (Figure 4.7, (A & B)). For instance, for WMSC coarse 18k (Figure 4.7, (B)), seed hold produced a span of 1.10 whereas at the end mill & cool point, 1.59 was achieved. Similarly, for saturated (35°C) milling at 18k (Figure 4.7, (C)), a span of 0.94 (seed hold) increased to 1.50 (end mill & cool). This was due to particle agglomeration in suspension during the end hold period without wet milling.

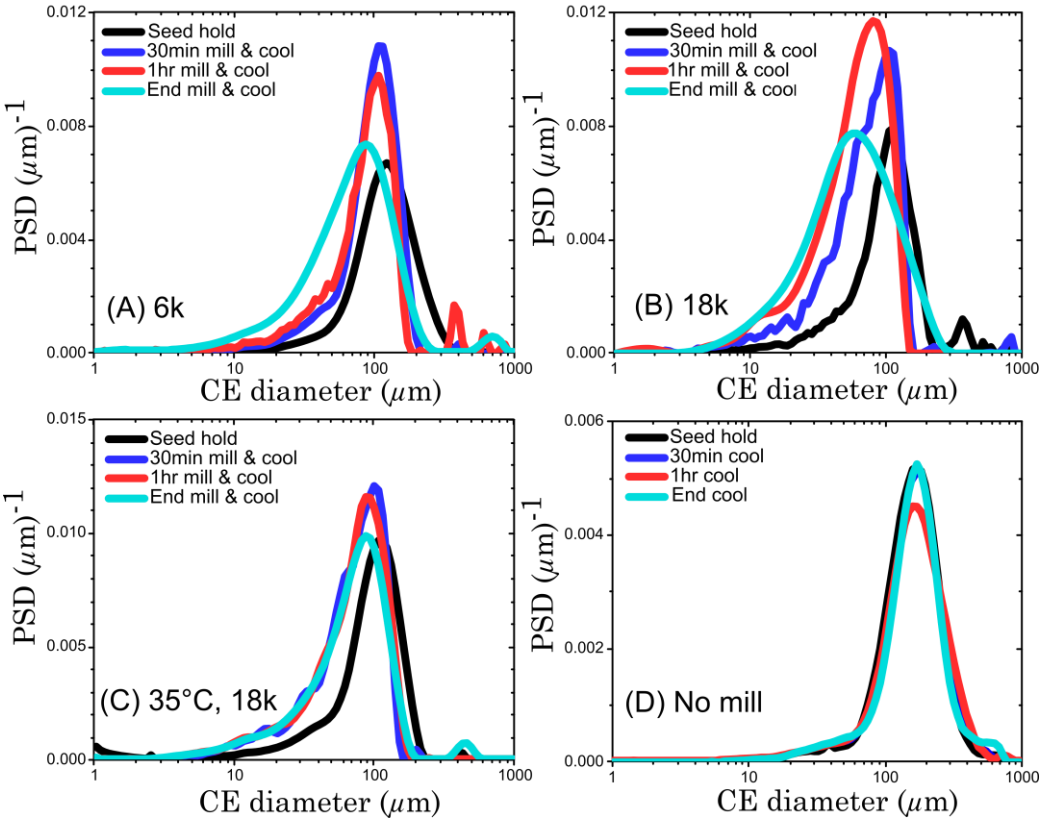

Figure 4.7 Changes in particle size distributions (PSDs) derived from FBRM measurements during the experimental runs. WMSC with 6k rpm (A); WMSC at 18k rpm (B); saturated (35°C) milling at 18k rpm (C) and cooling crystallisation with no milling (D).

A substantial advantage from inline wet milling is its ability to act as a continuous de-agglomerating tool whilst maintaining a narrow PSD. This is more evident from the breakage only experiments to which particles had reduced and remained narrow with a shorter end hold period (Figure 4.7, (C)). Without wet milling applied, a minimal shift in PSD from left to right occurs due to slow growth kinetics of acetaminophen in 2-propanol (Figure 4.7, (D)) and agglomerated seed input. A preliminary check was performed for quantitative analysis of growth kinetics. This

included a typical linear growth rate function (defined earlier in equation 1.13) which was adapted to include a number of particles term:

$$G = n \frac{dL}{dt} \qquad \text{Eqn 4.4}$$

Total counts from the FBRM sensor (Figure 4.5) were used an indicative measure for the number of particles (n). The change in particle size over time ($\frac{dL}{dt}$) by assuming theoretical growth of the seeds (Dv50 = 30.49) along with the product sizes of 90.2, 53.56 & 34.49 μm for the batch cooling crystallisation (no mill) and WMSC 6k & 18k experiments were included in equation 4.4. This resulted in growth rates of 1.89 (no mill), 2.74 (6k) & 3.15 μm / min (18k) which further illustrates reasonably slow growth kinetics for acetaminophen during desupersaturation without wet milling applied.

Collected offline particle sizes as a function of volume weighted circle equivalent diameter (μm) of end milled product emphasises the robustness of the process to deliver a consistent narrow PSD. This is more evident when using a higher rotation speed (rpm) than lower speeds (Figure 4.8, (A & B)). As rotor-stator teeth arrangement and rotation speed (rpm) are the two main governing factors of the wet mill, we identify rotation speed (rpm) as the main factor for targeting smaller particle size ranges with tighter spans as seen from the measured Dv50 values (Table 4.4). Furthermore, the energy dissipation rate model was examined to assess the effect of wet milling during crystallisation for size prediction.

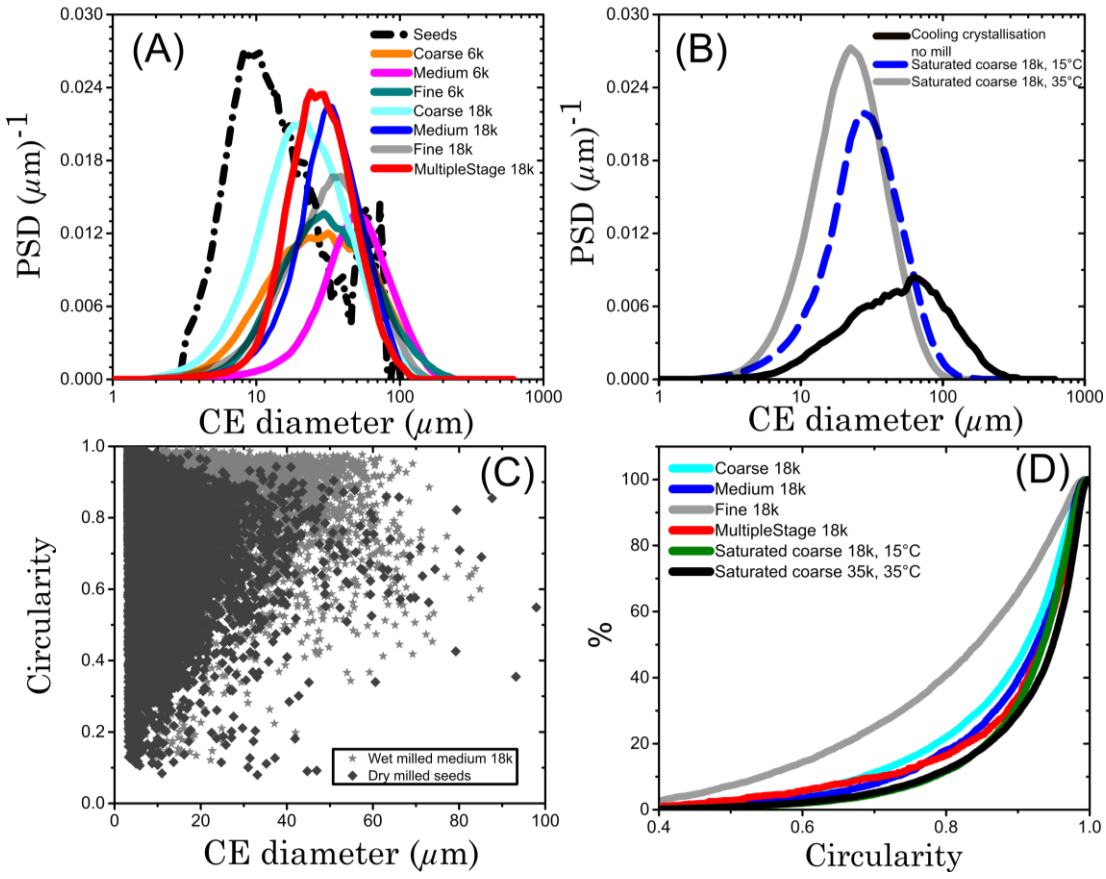

Figure 4.8 Offline particle size and shape from different experimental conditions. PSDs shown for runs (A) saturated with milling at fixed temperatures 15°C and 35°C (B) with no milling, and circularity measurements (C and D).

Maximum energy dissipated E^* values reached 6 for 18000 (rpm) compared to 1.33 for 6000 (rpm). The normalised energy dissipation rate E^* correlated well with mean square weighted CLD (μm) from FBRM measurements for individual experiments, however a breakdown in the correlation term occurred when incorporating all conducted experiments (Figure 4.9). The breakdown can be attributed to several reasons such as breakage, attrition, growth and secondary nucleation (Figure 4.1) all of which are not included in the mechanistic model.

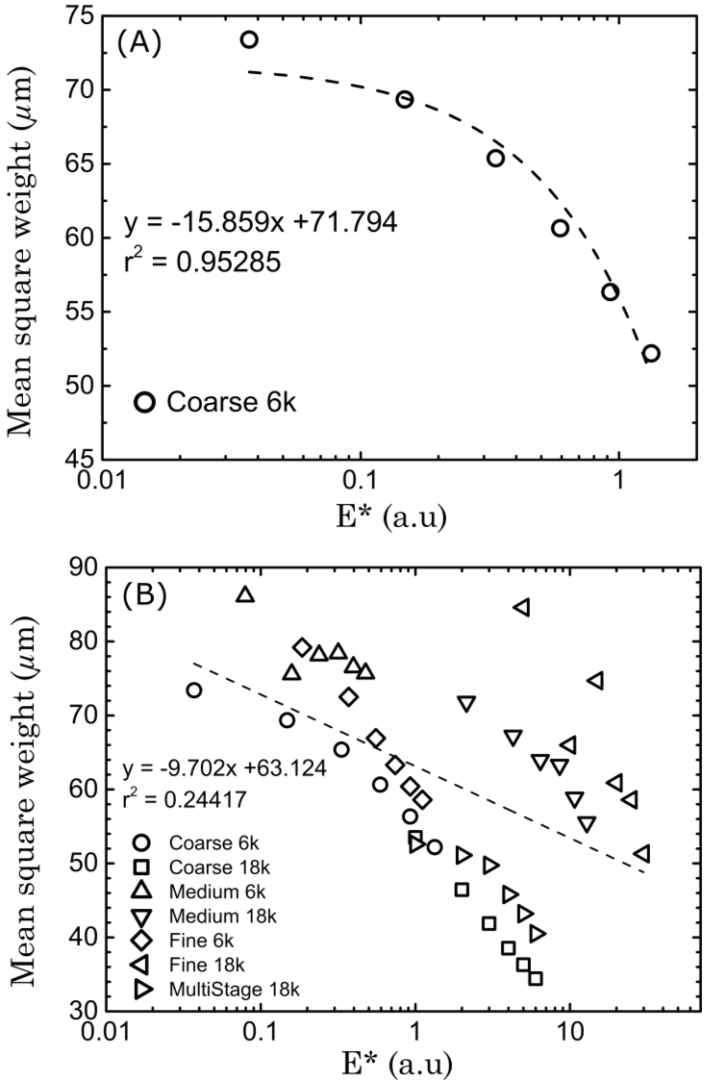

Figure 4.9 Logarithmic plots showing normalised energy dissipation vs mean square weighted CLD (μm) for a single coarse 6k experiment (A); and multiple configurations (B).

Selecting an accurate method for particle size characterisation, contribution of inner teeth to the overall energy dissipated and particle mechanical properties could be additional factors. Interestingly, the wet milling process was able to deliver narrow PSDs from a significantly skewed bimodal seed starting material under different rotor-stator teeth configurations specifically at higher rotation speeds (Figure 4.8).

The effect of wet milling on crystal shape is yet to receive wider attention in the literature, however coupling temperature-cycling with milling for modifying needle-like crystals is an emerging area of interest (Salvatori and Mazzotti, 2017, Wilson et al., 2018). Whilst dry milling can often produce irregular shaped particles, the WMSC process through varying teeth arrangement and rotation speed (rpm) has shown to deliver consistent circularity and aspect ratio values for acetaminophen. Both of these are important attributes in systems where flowability and filtration can be highly sensitive to any significant deviations. Mean particle circularity stays consistent from 0.83 to 0.91 with aspect ratios of 0.56 to 0.74 (Table 4.4). For majority of the milled samples increasing rotation speed (rpm) within the same teeth configuration had increased the circularity and aspect ratio. After the initial mass fracture process, during attrition and de-agglomeration, particles were considerably rounded off whilst colliding with more teeth present within the geometry.

Table 4.4 Offline particle size and circularity spans for the WMSC experiments.

Rotor-stator configuration	Rotation speed (rpm)	Dv50 (μm)	Size span	Circularity mean	Aspect ratio mean
Coarse	6000	53.56	1.46	0.86	0.65
Coarse	18000	33.49	1.57	0.90	0.69
Medium	6000	64.91	0.89	0.83	0.61
Medium	18000	41.49	0.78	0.89	0.67
Fine	6000	56.00	1.66	0.89	0.72
Fine	18000	47.81	1.10	0.83	0.56
Multiple-stage	18000	35.84	1.03	0.89	0.68
Coarse (15°C)	18000	37.70	1.03	0.90	0.71
Coarse (35°C)	18000	29.88	1.04	0.91	0.74

Hence, the controlled secondary nucleation phase after mass fracture shows that the competing processes were in equal states with particles still growing, healing & size reducing demonstrating simultaneous size and shape control whilst maintaining a high particle circularity from the WMSC process. This is further illustrated from the comparison of wet milled circularity from the seed material used indicating that due to the nature of dry milling, particles are largely irregular with greater surface roughening with a high presence of fines present (Figure 4.8, (C))

4.3.2. Surface Heterogeneity Analysis

Mechanical milling is believed to cause significant variation in particle surfaces as a result of breakage and overall intensity of the mill operation. As a consequence, this will lead to a significant change of an API's structural and chemical heterogeneity which in turn could pose difficulty during downstream processing (Ticehurst and Marziano, 2015). Therefore, investigating the consistency of particle surfaces between solid samples is important. In addition to particle size and shape analysis, surface energies from the combined method for acetaminophen under different teeth configuration, rotation speed (rpm) and of the dry milled as well as raw unmilled material is reported which has been unexplored in literature.

Surface areas through BET analysis show values in the range of 0.1 to 0.3 m^2 / g for the wet milled samples (Table 4.5). Operating at higher rotation speed (rpm) for each configuration resulted in smaller sizes and higher surface areas. However, the seed material generated via a dry ball mill yielded a much higher specific surface area than other samples (0.726 ± 0.0076 m^2 / g; Table 4.5). The dry milled seeds also show extensive fines, a range of aspect ratios and a large number of small agglomerated primary particles in comparison to the wet milled samples from the SEM images (Figure 4.10 & Figure 4.11) and raw unmilled acetaminophen as supplied from the vendor.

Table 4.5 Particle size, measured surface energy at starting surface coverage (0.005 n / n_m) and surface area values measured for the majority of the conducted experiments.

Rotor-stator configuration & speed (rpm)	Particle size, Dv50 (μm)	BET specific surface area (m^2/g)	Dispersive specific surface energy (mJ/m^2)
Coarse 6k	53.6	0.20 ± 0.004	42.9 ± 0.28
Coarse 18k	33.5	0.28 ± 0.001	41.5 ± 0.45
Medium 6k	64.9	0.10 ± 0.001	37.6 ± 2.19
Medium 18k	41.5	0.12 ± 0.006	50.2 ± 1.17
Fine 6k	56.0	0.11 ± 0.004	41.8 ± 0.27
Fine 18k	47.8	0.30 ± 0.004	42.9 ± 0.58
Multiple-stage 18k	35.8	0.12 ± 0.003	43.8 ± 0.16
Saturated coarse 18k 35°C	29.9	0.18 ± 0.004	43.0 ± 0.50
Dry milled seeds	30.5	0.73 ± 0.007	51.8 ± 0.57
Raw unmilled	75.8	0.29 ± 0.004	52.9 ± 0.37

In contrast for all wet milled samples, the number of fine particles has evidently reduced during the course of cooling and size reduction when compared to dry milling (Figure 4.10, (A – F)). The wet milled crystals show a range of morphological features between different teeth configurations (coarse, medium, fine, Figure 4.10 & Figure 4.11, (C – L)) which includes rounded, almost spherical particles (Figure 4.11, (I to J)) and evidence of particle breakage (Figure 4.10 & Figure 4.11, (F, K, L)) presumably due to particle-teeth collisions. Across the SEM data, the impact of breakage as well as growth can clearly be seen (Figure 4.10 & Figure 4.11, (C to L)).

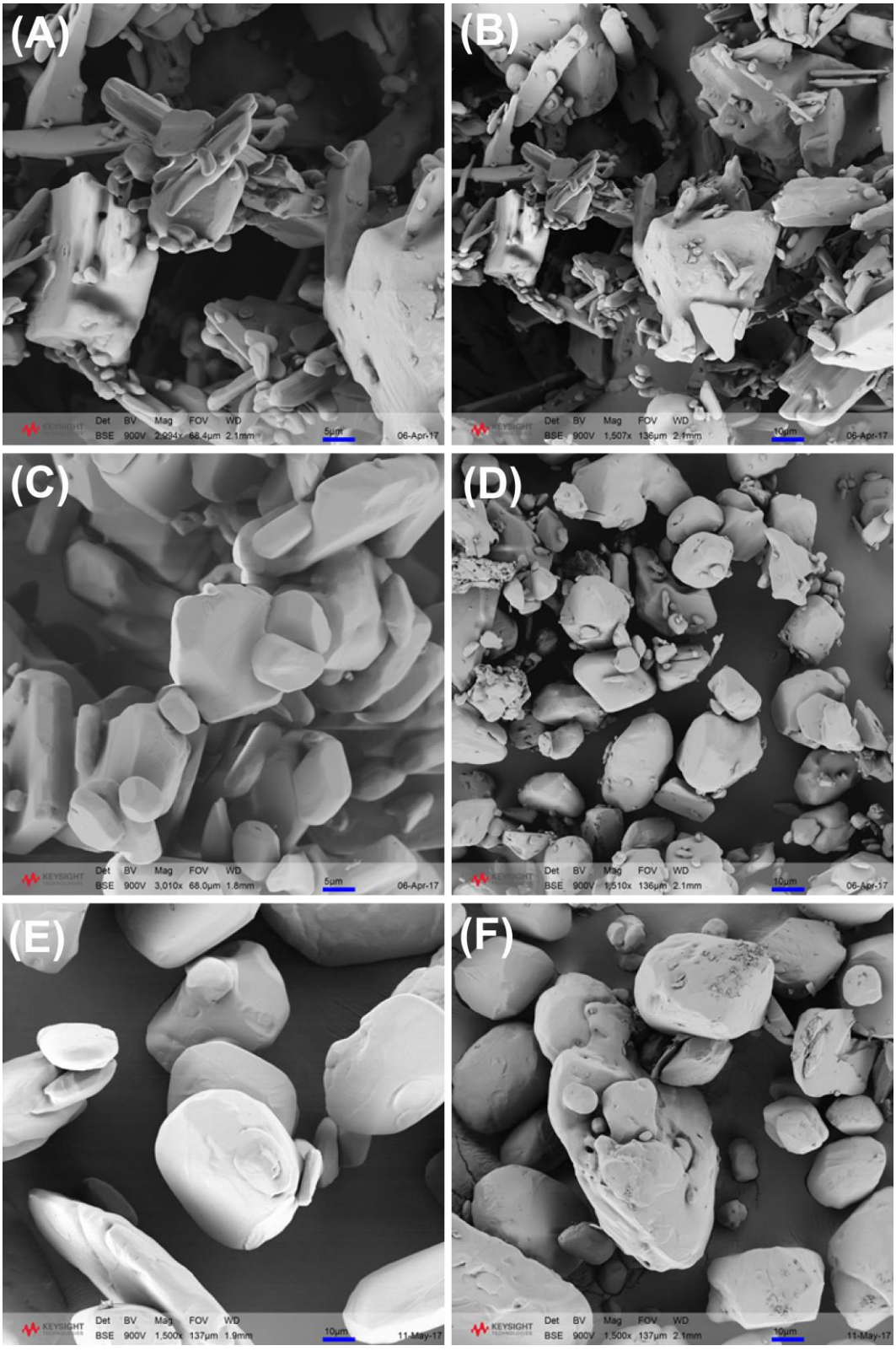

Figure 4.10 SEM images showing surface features of dry milled (A & B), WMSC coarse 6k (C) & 18k (D) and WMSC medium 6k (E) & 18k (F) crystals.

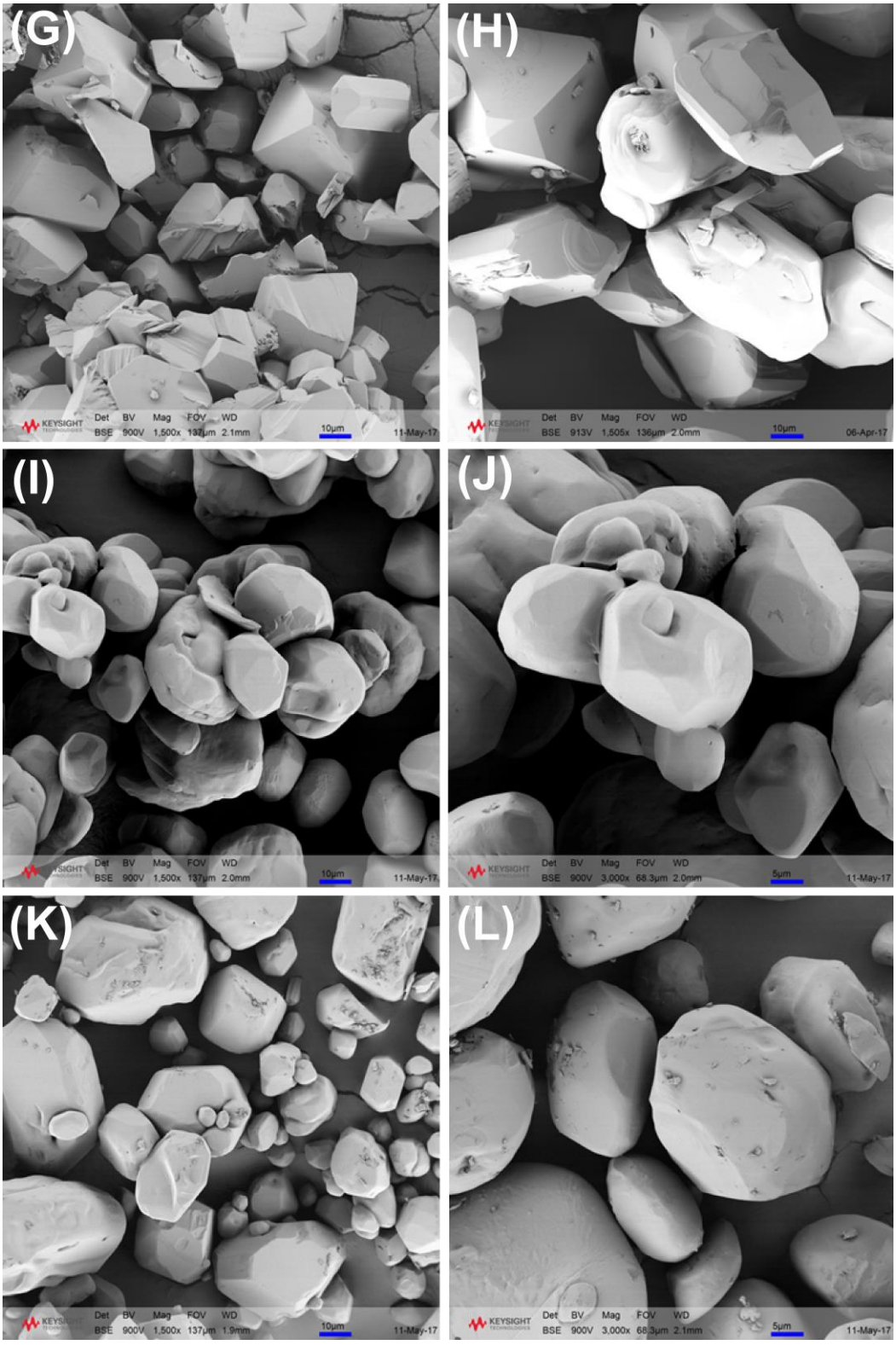

Figure 4.11 SEM images showing surface features of WMSC fine 6k (G) & 18k (k), WMSC multistage 6k (I) & 18k (J) and saturated (35°C) milling 18k (K – L) crystals.

Crystallised and wet milled samples from the different configurations exhibited maximum γ_S^d values between 37.6 and 50.2 mJ / m^2 when compared to the dry milled seed particles γ_S^d of 51.79 ± 0.57 mJ / m^2 and raw unmilled material of 52.90 ± 0.37 mJ / m^2 (Table 4.5). Whilst consistent γ_S^d values amongst the majority of wet milled samples with minimal variation was observed at the starting surface coverage of 0.05 n / n_m and irrespective of particle size (Table 4.5), analysing the surface heterogeneity profiles across low and high energy surface sites (0.05 to 0.9 n / n_m) displays variability in γ_S^d distributions from the measured samples (Figure 4.12, (A & B)). For the dry milled seed material, a considerably higher degree of heterogeneity from process induced disorder across surface coverage is seen from 51.79 ± 0.57 mJ / m^2 to a final value of 42.95 ± 0.38 mJ / m^2. This is considerably higher to all low & high wet milled samples with the exception of medium 18k and unmilled material (Figure 4.12, (A & B)). The area increment distribution of the seed is also relatively broad, emphasising the surface irregularity and distorted molecule orientation (Figure 4.12, (C & D)). This is consistent with the observation that this sample with the highest γ_S^d shows a greater propensity to agglomerate in comparison to the wet milled particles as increasing surface energy at low surface coverage leads to stronger cohesiveness between particles. Interestingly, the raw unmilled material displays a highly variable heterogeneous profile indicating surface irregularity in the bulk sample as

the surface energy has a starting value of 52.90 ± 0.37 mJ / m^2 (0.05 n / n_m) which rapidly decreases to a final value of 28.45 ± 0.74 mJ / m^2 (0.9 n / n_m).

At each rpm, the different wet mill teeth configurations yielded final particle sizes varying by approximately 20 μm. Reported studies such as Trowbridge et al (Trowbridge et al., 1998) showed a 20% increase in dry milled γ_S^d with a decrease in particle size from 30 to 10 μm. We have observed similar trends to a somewhat lesser extent from the majority of collected wet milled samples when increasing the rotation speed (rpm) between each rotor-stator configuration (Table 4.5). Medium 6k (19 total teeth), had a Dv50 of 64.91 μm and surface energy of 37.59 ± 2.12 mJ / m^2 whereas a medium 18k had a Dv50 of 41 μm and surface energy of 50.15 ± 1.17 mJ / m^2 (Table 4.5). The relatively high γ_S^d of medium 18k in comparison to other wet milled configurations was unexpected, showing more surface roughening from breakage and subsequently an increase in exposure of specific crystal planes with different surface chemistries (Figure 4.10, (F)). Fine 6k (29 total teeth) had a Dv50 of 56 μm and surface energy of 41.84 ± 0.27 mJ / m^2 , whereas fine 18k had a Dv50 of 47.81 μm and surface energy of 42.91 ± 0.58 mJ / m^2 (Table 4.5). The increase in heterogeneity profiles for fine 18k & multiple-stage 18k after 0.06 surface coverage could be attributed to other interactions occurring at the higher energy sites such as solvent effects (Figure 4.12, (B)).

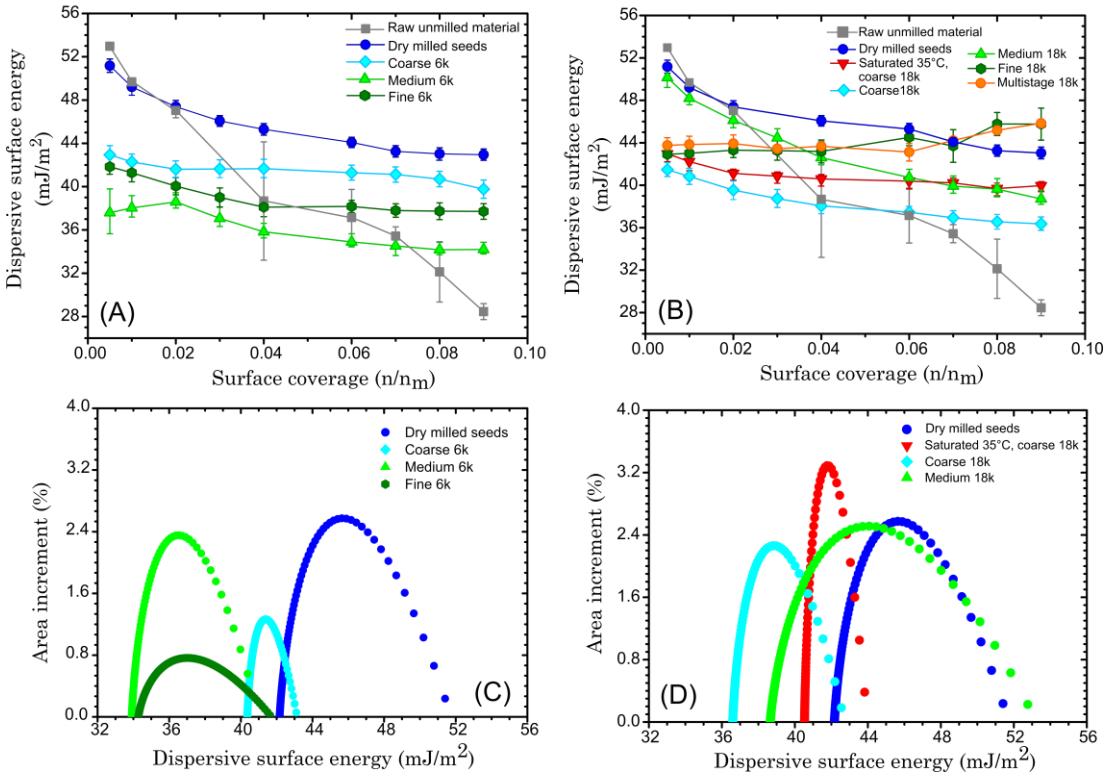

Figure 4.12 Surface heterogeneity profiles measured across different surface coverages (A and B) and area increment distributions (C and D).

Nevertheless, both samples maintained expected circular morphology with fine 6k & 18k showing well-faceted crystal faces (Figure 4.11, (G & H)). In addition to the coarse 6k, which possessed 13 total teeth, these wet milled configurations at low rotation speed (rpm) had fairly similar particle size ranges (53.56 μm, 64.91 μm, 56 μm; Table 4.5) but with clearly different absolute energy heterogeneity profiles across the full surface coverage (Figure 4.12, (A)). Altering between different rotor-stator teeth arrangement and speed (rpm) will subsequently lead to a different number of particle-teeth collisions and morphological features (Figure 4.10 & Figure 4.11) as the total number of teeth varies from 13 to 61 when increasing the rotation speed (6000 to 18000 (rpm)). When comparing the

reduction in γ_S^d as surface coverage is increased, for low rotation speed (rpm) the percentage decrease ranged from 7.4 to 9.0% whereas for high rotation speed (rpm) including the decoupled experiment at 35°C and dry milled seed, values ranged from 6.9 to 22% (Figure 4.12, (A & B)). This indicates that the number and direction of crystal faces and functional groups exposed varies when increasing or decreasing the number of teeth, rpm and consequently energy dissipated (0.04 - 30). Heng et al (Heng et al., 2006) reports that during a milling process, crystals of acetaminophen fracture along their weakest attachment energy resulting in the dominant exposure of the crystal facet (010) determined by contact angle measurements with the surface chemistry of the facet being hydrophobic.

In agreement with literature, for this process it would be reasonable to assume the immediate exposure of the crystal facet (010) is dominant upon mass fracture. However, crystal face indexing measured at different wet milling configurations and turnovers is out with the scope of this work. Furthermore, along with measuring particle size distribution spans, a heterogeneity profile constitutes an energy landscape of the material surface. To represent the heterogeneity of the samples in a more illustrative manner, the surface energy distributions are obtained by a point-by-point integration of the surface energy profiles, resulting in plots of dispersive surface energy versus percentage of surface (area increment), as shown (Figure 4.12, (C & D)). Area increment curves plotted alongside

surface energy distribution profiles show lower surface energy distributions are present for low rotation speeds (rpm) from areas 0 to 2.5% (Table 4.5) whereas for the WMSC and saturated coarse 18k configuration which has a tighter and smaller particle size distribution varies from areas 0 to 3.4% (Figure 4.12, (C)).

Interestingly, Luner et al (Luner et al., 2012) observed high shear wet milling for sucrose and succinic acid generated significantly higher surface energies than dry milling. In contrast, by combining wet milling during crystallisation had in fact, generated small uniform particle size distributions with lower surface energies, which is desirable for numerous crystallisation applications and downstream processing. It is also a method which is increasingly being applied for continuous seed generation as producing in situ slurry seed particles with small sizes, high surface areas and low surface energies has the potential to provide greater control and reproducibility for uniform crystal growth. This is subsequently investigated in chapter 5 as a seeding protocol for continuous crystallisation.

Although careful manipulation of wet mill parameters for targeting size and shape can be achieved, the heterogeneous nature of particle surfaces that can be obtained from a combined wet milling and crystallisation method as a result of changing teeth configuration is reported. This work starts to address the limited predictive capabilities for achieving specific surface area and energy attributes from wet mill devices. This would

enable greater control for seed generation and size reduction processes for specific attributes (Ticehurst and Marziano, 2015).

4.4. Summary

The effect of process parameters of a WMSC process have been presented on three physical particle attributes of acetaminophen namely, particle size, shape and surface energy. Crystal sizes in the range of 30 - 60 μm with narrow particle size distributions (span = 0.78 – 1.66) and crystal shape control (e.g. circularity 0.80 - 0.98) have been selectively achieved through tuning of the principle wet mill parameters, rotation speed and teeth configuration. The combination of advanced inline CLD to PSD conversion with simultaneous offline imaging analysis was an effective means to measure and track key changes to PSD and shape during the dynamic wet milling processes. The WMSC experiments generated acetaminophen particles with surface energies in the range of 37 – 50 mJ / m^{-2} achieved from different teeth configurations.

The combination of wet milling and crystallisation yielded lower surface energies than reported elsewhere (Luner et al., 2012) due to the surface healing driven by the crystal growth process. The heterogeneity of surface sites was impacted by increasing the number of teeth more than rotation speed. This is important as minimising heterogeneity can potentially improve manufacturability in downstream processing. Ultimately, selecting a high rotation speed with lower teeth proved to be desirable for engineering particle attributes.

The robust and flexible nature of a WMSC strategy has the potential to serve as a smart particle engineering toolbox for future API manufacturing demands where the properties can be selectively manipulated for chosen processing performance characteristics. In order to deploy this method routinely, work is progressing to develop an integrated workflow for process design to complement what has been shown elsewhere for continuous crystallisation (Brown et al., 2018).

Chapter 5

Implementing High Shear Wet Milling as a Continuous Seed Generation Platform

---

Part of this chapter has been published in a collaborative journal article:

BROWN, C. J., MCGLONE, T., YERDELEN, S., SRIRAMBHATLA, V., MABBOTT, F., GURUNG, R., L. BRIUGLIA, M., **AHMED, B**., POLYZOIS, H., MCGINTY, J., PERCIBALLI, F., FYSIKOPOULOS, D., MACFHIONNGHAILE, P., SIDDIQUE, H., RAVAL, V., HARRINGTON, T. S., VASSILEIOU, A. D., ROBERTSON, M., PRASAD, E., JOHNSTON, A., JOHNSTON, B., NORDON, A., SRAI, J. S., HALBERT, G., TER HORST, J. H., PRICE, C. J., RIELLY, C. D., SEFCIK, J. & FLORENCE, A. J. 2018. Enabling precision manufacturing of active pharmaceutical ingredients: workflow for seeded cooling continuous crystallisations. *Molecular Systems Design & Engineering*. 3, 518-549.

5. Implementing High Shear Wet Milling as a Continuous Seed Generation Platform

5.1. Introduction

In bulk cooling crystallisation processes, a terminal wet milling step is increasingly favoured over dry milling to size reduce a seeded suspension for generating a wet slurry seed bed (Cote and Sirota, 2010). The seed slurry is then capable of being subjected to a batch or continuous crystallisation platform for controlled growth and producing a monodispersed PSD. Interestingly, it was shown (chapter 4) that in fact, combining a high shear rotor-stator wet mill with a seeded cooling crystallisation process enhanced crystallisation kinetics (i.e., secondary nucleation) whilst engineering desired particle attributes (size, shape, surface energy). However, the majority of seeded cooling crystallisations including the combined WMSC approach require the availability of pre-existing seed material of different particle sizes which are usually sourced from external means such as multiple crystallisations, sieving or offline dry milling.

Rotor-stator wet milling exerts considerably high shear rates (400,000 s^{-1}), and forces (10^4 Pa) which are directly transferred from the high-speed spinning rotor-stator motion to the processing solution. Previous studies have shown controlled shear to induce nucleation from other devices such as Taylor-Couette on butyl paraben (Liu and Rasmuson, 2013) and glycine (Forsyth et al., 2014, Forsyth et al., 2015) (Figure 5.1).

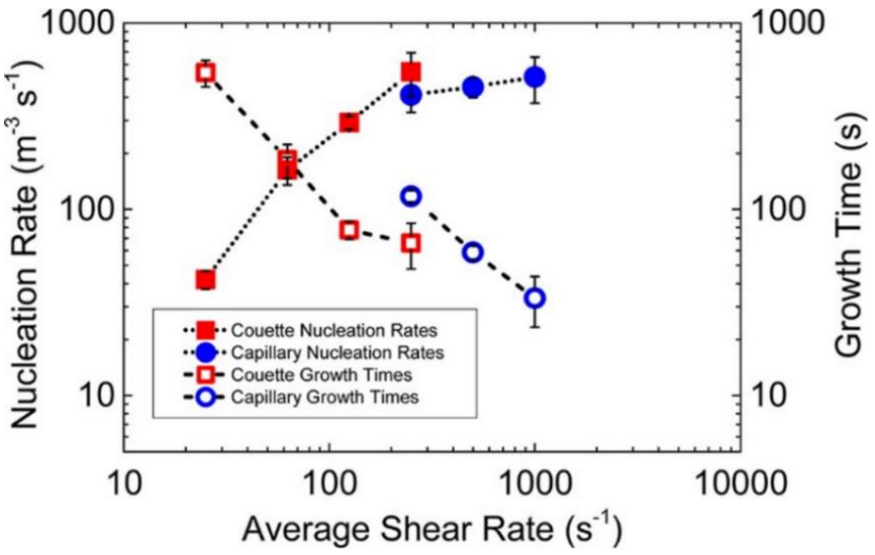

Figure 5.1 The influence of increasing average shear rate from well-controlled fluid shear devices (Taylor-Couette & Capillary) on the nucleation rate J and growth times t_g for glycine (Forsyth et al., 2014).

These have shown to exhibit average shear rates of 10 – 1000 s^{-1} (including stirred tank reactors) which is 2 – 3 orders of magnitude lower than rotor-stator wet mills (≤ 400,000 s^{-1}). As there is an increasing demand for more modular and flexible unit operations in continuous manufacturing of pharmaceuticals, the integration of nucleator devices with continuous crystallisers such as stirred-tank reactors can offer several benefits. For instance, a substantial reduction in nucleation time for compounds possessing wide MSZWs can reduce the process start-up and time to reach steady-state period. This can then be used to deliver a continuous supply of seeds for growth which as a result, potentially removes the need for external seed generation, characterisation, addition and dispersion.

This study evaluates the combined wet milling crystallisation (WMC) method as a seeding platform for continuous crystallisation. Acetaminophen in 3-methyl-1-butanol is used which possesses an average MSZW of 28.7°C ± 0.8 without seeding. In the first part of this work, the effect of high shear from rotor-stator wet milling coupled to an unseeded recycled solution during batch cooling crystallisation is investigated. The process incorporates a constant supersaturation feedback-control mechanism using an inline ATR-FTIR sensor during crystallisation and milling. Scalability of the combined method is then assessed across a 1 L & 10 L crystalliser whereby the wet mill's process adaptability and efficiency for rapidly accelerating nucleation and maintaining tight particle attributes (size & shape distributions, span) is presented.

In the latter part of this work, the combined WMC method is then integrated on a 3-stage MSMPR for employing a continuously seeded crystallisation process. The process intensified configuration provides in situ generated seeds from the WMC stage which is directly transferred as a continuous seed stream to stages 1 and 2 for growth only (Figure 5.2 & Figure 5.5). The performance and influence of this seeding protocol on process handling and operation as well as product attributes is evaluated. A key benefit of this study shows how alternative seed generation methods such as high shear wet milling devices can be readily deployed on-demand for continuous production of seeds in contrast to relying on traditional offline seed generation techniques in pharmaceutical manufacturing.

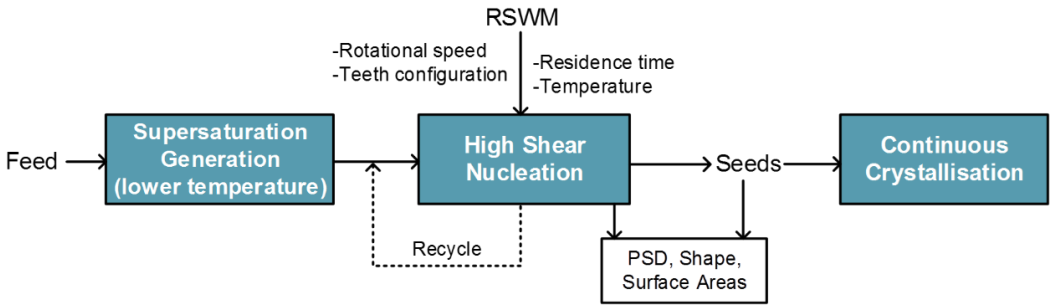

Figure 5.2 Flow diagram showing the integration of high shear wet milling via the recycle-loop mode for continuous seed generation coupled to a continuous crystalliser.

For all experimental campaigns, a toothed rotor-stator wet mill with selected single fine teeth configuration was operated at 15000 rotation speed (rpm). Constant inline PAT sensors were used for real-time analysis of inline particle counts and CLDs (μm) as well as concentration determination and particle imaging. Offline volume weighted circle equivalent diameter D [4, 3] (μm), aspect ratio and circularity were analysed for particle size and shape distributions. Product particles were also characterised for surface imaging to provide an insight into the influence of high shear wet milling on product particle surfaces.

Furthermore, this work contributes to the development of a multidisciplinary collaborative novel systems-based workflow approach for continuous seeded cooling crystallisation of active pharmaceutical ingredients (Brown et al., 2018). The devised workflow provides a rapid and systematic assessment of common crystallisation phenomena such as nucleation, breakage / attrition, fouling, agglomeration, etc., that can occur in addition to crystal growth. Knowledge and control of these mechanisms

can then allow for a holistic design and operation of a continuous crystallisation process with optimised and desired particle properties. The focal point of this chapter is to demonstrate that high shear generated in a rotor-stator wet mill environment is a practical and robust means for seed generation and particle attribute control. This work is integrated from stage 6 to 7 of the workflow as a proof-of-concept continuous crystallisation which applies the same continuously seeded crystallisation process for the developed acetaminophen in 3-methyl-1-butanol system.

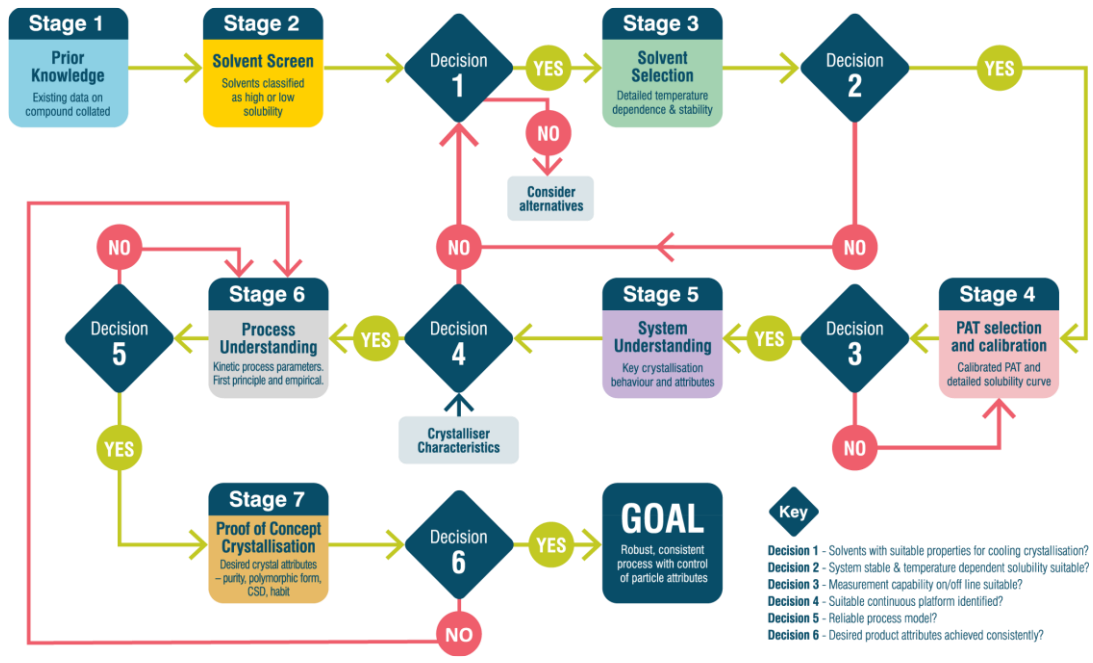

Figure 5.3 A systematic workflow for development of a seeded continuous crystallisation (Brown et al., 2018). Stage 6 and 7 are the focus of this chapter.

5.2. Experimental Section

5.2.1. Materials and Method

Acetaminophen (> 99.5%, CAS: 103-90-2) and 3-methyl-1-butanol (reagent grade, > 95%) were both purchased from Sigma-Aldrich and diethyl ether (reagent grade, > 95%) was purchased from Fisher-Scientific Ltd.

A Mettler Toledo OptiMax™ workstation consisted of a 1 L temperature-controlled stirred tank crystalliser (STC) equipped with an inline Hastelloy® Pt100 temperature sensor and a four-pitched blade agitator (600 rpm) was used. PAT probes; FBRM (G400 series), PVM V819 and ReactIR 15m (described in chapter 3, 3.2.1) were used for process monitoring (Figure 5.4). The process conditions of temperature and stirring speed of the slurry in the workstation were controlled using the iControl v5.2 software from Mettler Toledo.

For scale-up experiments, a 10 L (Microinnova Engineering GmBH, Austria) temperature-controlled stirred tank crystalliser (STC) equipped with an inline PTFE Pt100 temperature sensor and four-pitched blade agitator (600 rpm) was used. FBRM (G400 series) and PVM V819 probes were integrated, no ReactIR 15m probe was used. All wet milling incorporated experiments consisted of a lab-scale IKA MagicLab (Module UTL) rotor-stator wet mill unit configured through the recycle-loop mode. No pump was used for recycling. Mill outlet temperature was monitored on the IKA operating unit display with selected rotation speeds of 15000 and 26000 rpm with a single fine teeth configuration.

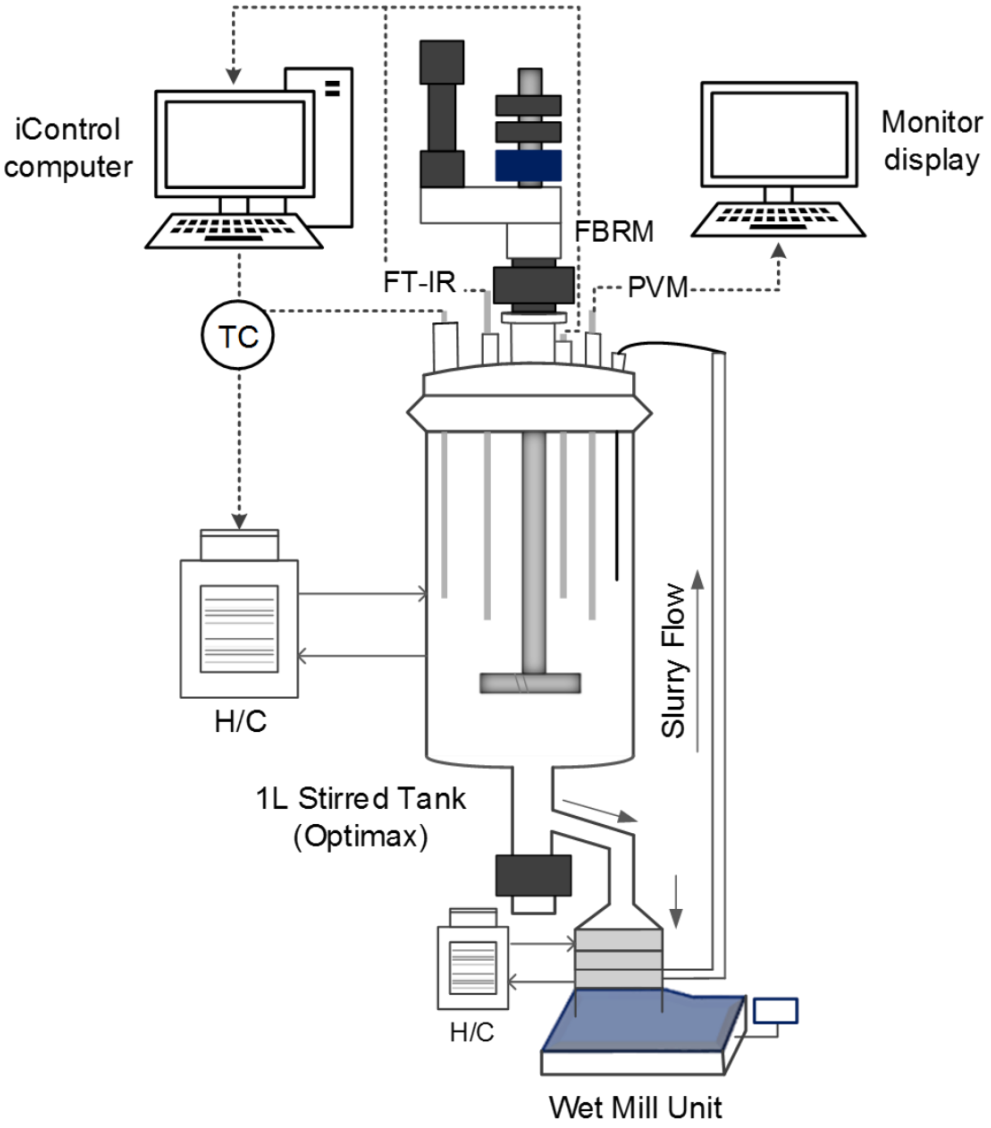

Figure 5.4 Experimental apparatus consisting of a 1 L baffled stirred tank crystalliser vessel (OptiMax) with an integrated rotor-stator wet mill unit via the recycle-loop mode. PAT sensors (FBRM, PVM, ATR-FTIR), temperature and stirrer were controlled via the iControl software. The iControl was also used with FBRM and ATR-FTIR probes for data synching, tracking and supersaturation feedback-control as described in section 5.2.6. The 10 L scale experiments consisted of a baffled stirred tank vessel with a similar wet milling recycle-loop mode.

The continuous WMC-MSMPR experiments were comprised of a Microinnova Engineering GmBH miniflow plant acting as a feed unit (combining thermostat (Lauda, Proline 855), a delivery pump with feedback-control from a Coriolis mass flow meter (Siemens), three 2 L glass reaction vessels (Radleys) each with a working volume of 1.5 L, three thermostat circulators (Lauda 420), an IKA MagicLab rotor-stator wet mill (Module UTL) operated at 15000 rpm with single fine teeth configuration and two lab filter dryers (Powder Systems Ltd, Maxi Lab) (Figure 5.5). Process monitoring was achieved through the mass flow meter, Pt100 probe, FBRM (G400 series) in all crystallisation vessels and a ReactIR 15m in the 2nd stage (Figure 5.5 & Figure 5.6). Continuous material transfer between crystallisation stages was maintained through the application of positive pressure (N_2 at 0.1 bar) to the first stage. Agitation in all crystallisation stages was provided by retreat curve impeller (PTFE) operated at 600 rpm and aided by three equally spaced baffles.

5.2.2. Seed Preparation

Seed crystals of raw acetaminophen were prepared (50 g) using an offline vibratory ball mill (Griffin & George) which was milled for 1.30 hr and sieved (Fritsch analysette 3 type) approximately into the required size fraction; 40 - 65 μm & 90 – 125 μm. The dry seed fraction was used only for preliminary batch experiments without wet milling coupled as described in section 5.2.6.

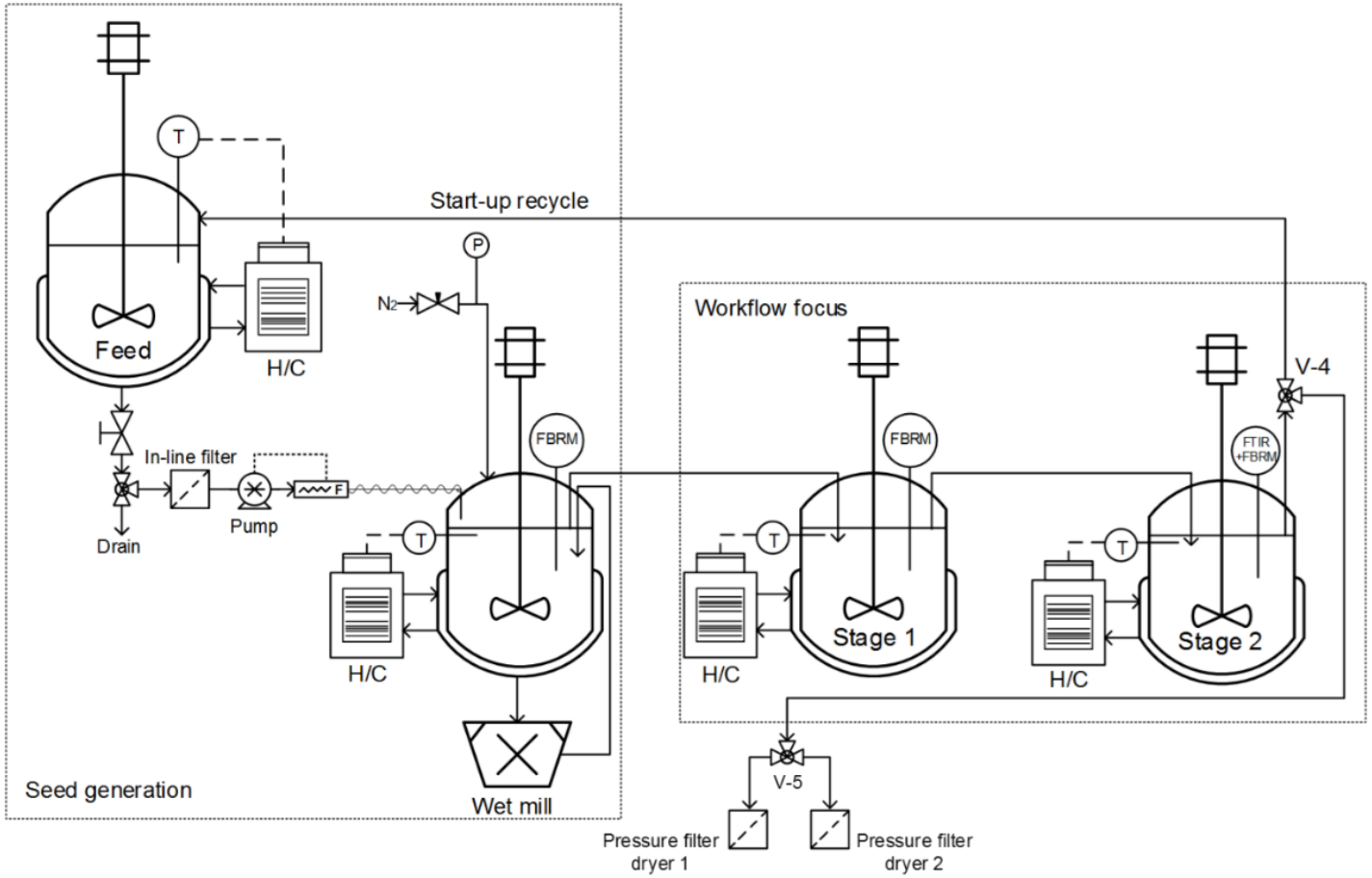

Figure 5.5 Process and instrumentation diagram for the continuously seeded crystallisation (WMC-MSMPR) configuration carried out (Brown et al., 2018).

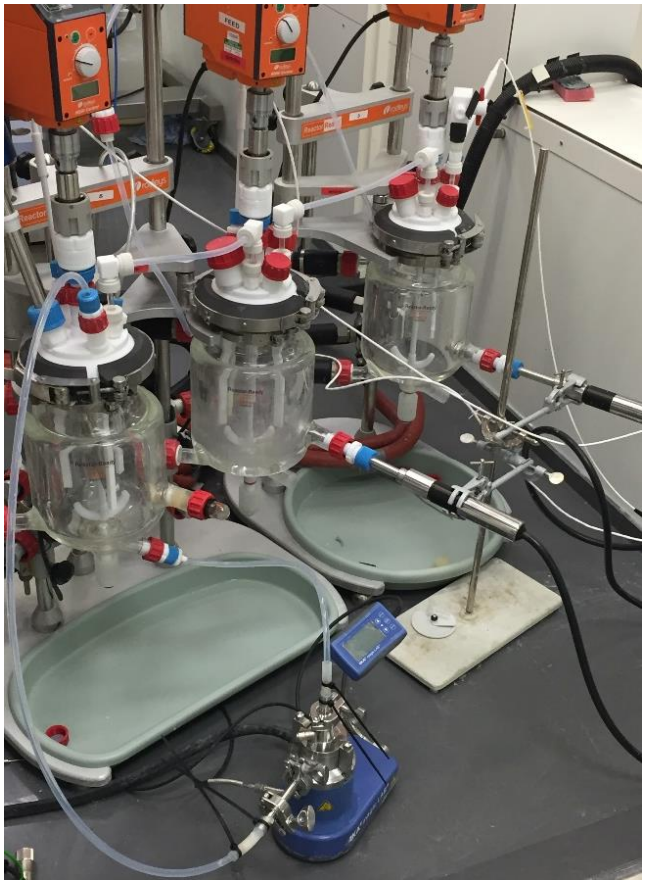

Figure 5.6 Image of the WMC-MSMPR equipment setup used.

5.2.3. Particle Size and Shape Characterisation

All samples were analysed for size and shape information using the Malvern Morphologi G3 (described in chapter 3, 3.2.2.1).

5.2.4. Scanning Electron Microscope (SEM)

Samples were subjected to an SEM microscope for shape and surface image analysis. Details of the method are described (chapter 3, 3.2.2.4).

5.2.5. gCRYSTAL Modelling Software

The gCRYSTAL 4.2.0 commercial modelling and simulation platform developed by Process Systems Enterprise Ltd was used to build a

population balance model for a quantitative estimation of crystallisation kinetics from the initial batch experiments without wet milling coupled. Parameter estimation, model testing and validation runs were carried out using the methods described in section 5.2.7.

5.2.6. Experimental Procedure: Parameter Estimation

For process understanding of acetaminophen in 3-methyl-1-butanol, a series of seeded cooling crystallisation experiments under constant supersaturation control without wet milling were performed. The aim of this was to provide an initial estimate of the kinetic parameters describing crystal growth in bulk suspension. The cooling profiles for all experiments were based on the temperature dependant solubility of acetaminophen in 3-methyl-1-butanol (Figure 5.7) with the calibration and experimental procedure described in section 3.2.3.1.

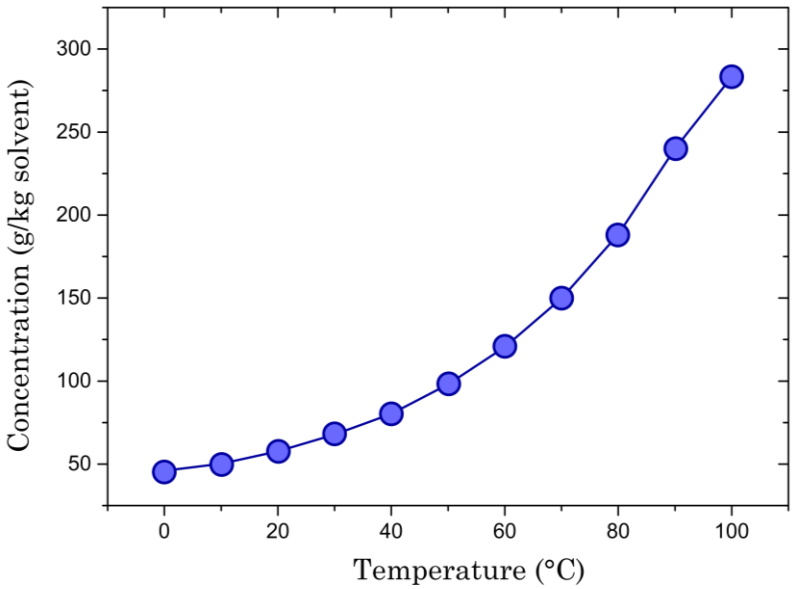

Figure 5.7 Temperature dependant solubility of acetaminophen in 3-methyl-1-butanol solvent.

To calibrate the ATR-FTIR sensor signal for enabling accurate supersaturation control during cooling crystallisation, a calibration-free approach is taken. This approach encompasses a closed-loop concentration-control method which allows supersaturation to be controlled at a constant level using ATR-FTIR (Grön et al., 2003, Barrett et al., 2010). A characteristic peak height, specific to the solute of interest is tracked directly at any given temperature. The peak height corresponding to the saturation solution at the same temperature is also measured so that the supersaturation at any point in the reactor is given in terms of the difference in peak height (Barrett et al., 2010). For instance:

$$C_{ij} = C_i(\mathrm{T}_j) \qquad \text{Eqn 5.1}$$

Where at any temperature (T_j) and the concentration of a given solute (i) is a function of the characteristic peak height. The solubility can be expressed in a similar form:

$$C_{ij}^{*} = C_i^{*}(T_j) \qquad \text{Eqn 5.2}$$

Therefore the supersaturation is given by:

$$\Delta C_{ij} = C_{ij} - C_{ij}^{*} \qquad \text{Eqn 5.3}$$

At any given temperature, the supersaturation will be directly proportional to the difference in peak height at that temperature. To implement constant supersaturation during cooling, the control condition requires

equivalent concentration and solubility gradients with respect to temperature. Therefore, pre-information in terms of solute peak and temperature should be collected first through applying low heating rates.

Acetaminophen (111g) was added to 3-methyl-1-butanol (600g) within the OptiMax workstation with fixed agitation at 600 rpm. FBRM and ReactIR sensors were integrated in the vessel. The solution was then cooled to 5°C at the fastest possible rate and held at 5°C for 2 h to allow for solid / liquid equilibrium. The solution was followed by heating to 85°C over a 16 h period with a further hold period of 2 h. This step enables the IR absorbance of a saturated solution as a function of temperatures to be determined as shown in Figure 5.8.

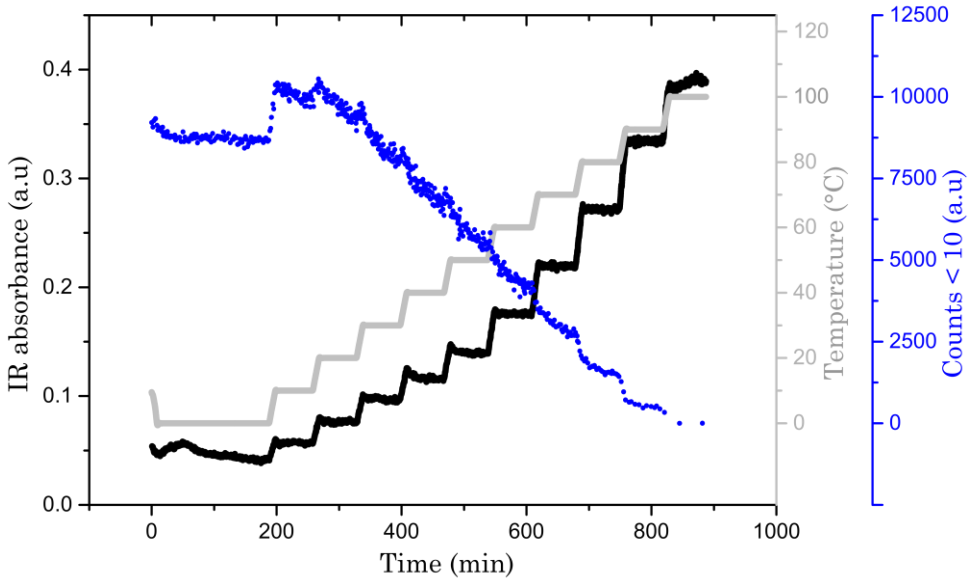

Figure 5.8 Raw IR (black line) with a selected peak height at 1670 cm^{-1} (carbonyl band), temperature (grey line) and FBRM fine chord counts < 10 (a.u, blue line) for acetaminophen in 3-methyl-1-butanol. FBRM counts show a decreasing trend over time indicating the onset of dissolution.

Upon collection of the IR dataset along with temperature, the solubility (c^*) is expressed as a second-order polynomial as a function of temperature where constants (a_c, b_c & c_c) are obtained:

$$c^* = a_c T^2 + b_c \mathrm{T} + c_c \qquad \text{Eqn 5.4}$$

Thus, by plotting temperature vs peak height (1670 cm^{-1}) an expression was generated:

$$\mathrm{y} = -766.13x^2 + 605.13\mathrm{x} - 23.72 \qquad \text{Eqn 5.5}$$

This expression was inserted in the iControl v5.2 (Mettler Toledo) user interface specifically within the "setpoint controlled by expression" task when designing the cooling program. The "x" values of the polynomial expression (equation 5.5) denote the selected IR peak height which is 1670 cm^{-1} with an additional temperature offset value for the desired supersaturation.

The experiment was then started by cooling the solution to 80°C minus a temperature offset (either 5°C or 8°C for S = 1.08 and 1.20, respectively to operate within the MSZW). Once this temperature was reached, the required seed mass was charged as dry seed into the vessel and the supersaturation control was then started using the setpoint expression in iControl (user defined trends) which was determined from the second order polynomial fit by plotting temperature vs peak height (1670 cm^{-1}), 5°C was set as the lower bound for the temperature.

Seeds were prepared by sieving of ball milled commercial acetaminophen. Two seed sizes, with D_v50 of 40 μm and 100 μm were used in addition to two seed loadings, M_{seed} of 0.019 and 0.036. On completion of experiments, the contents of the vessel were filtered and the cake was washed twice using two cake volumes of chilled diethyl ether. The wet cake was then transferred to a vacuum oven (40°C) for drying.

5.2.7. Estimation of Growth Kinetics

To estimate the growth kinetics of acetaminophen in 3-methyl-1-butanol from the constant supersaturation control experiments, physical properties such as molecular weight, density, solubility, etc., were configured in the global specifications module within the gCRYSTAL 4.2.0 user interface (Figure 5.9). A model of the Optimax vessel was then built in gCRYSTAL 4.2.0 using an MSMPR unit operation configured in batch mode (Figure 5.9) to represent the experimental batch stirred-tank crystalliser. The MSMPR unit configured in the flowsheet, models the crystallisation slurry by means of a well-mixed single compartment which assumes that the mixing time is much lower than the time scales of nucleation, growth and agglomeration (Schöll et al., 2007). Under this assumption, the energy dissipation from the stirrer can be averaged over the whole crystalliser and hence the mechanism for the particle formation can be assumed to be independent on the position within the crystalliser (Marchisio et al., 2006, Vicum et al., 2004). Other assumptions state that the liquid and solid

phases in the bulk are in thermal and mechanical equilibrium, that is, same temperature and pressure.

Time invariant controls for the model included mass of crystals in the slurry and solution composition which was retrieved from experimental concentration profiles from the IR probe. PSD data from the Malvern Morphologi G3 (imaging) for the initial seed input and product output was used for the PSD location parameter (characterisation of the model distribution) and PSD standard deviation. Temperature profiles (TC) were input as piecewise linear with three control intervals which were approximated from the supersaturation control experiments.

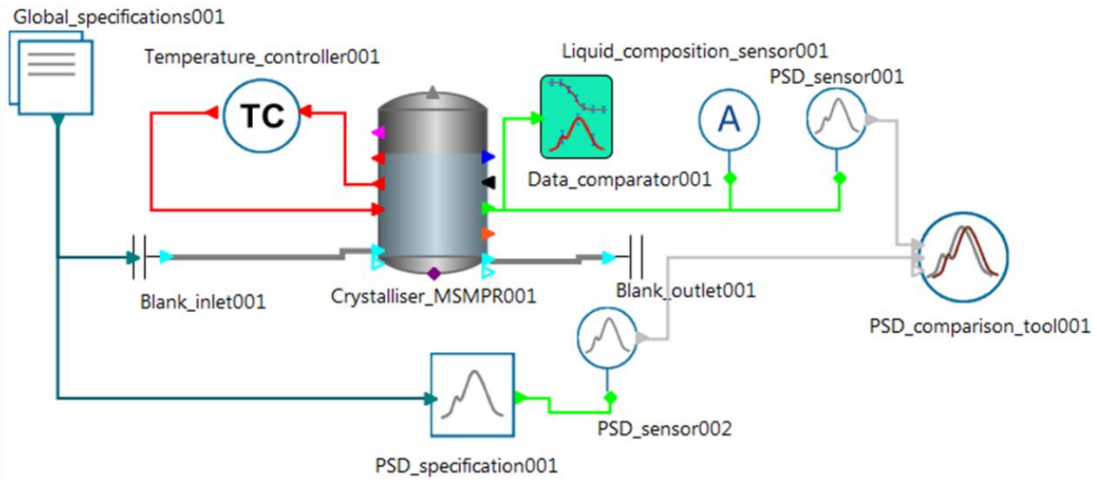

Figure 5.9 Schematic of flowsheet model used to describe the seeded batch crystallisation of acetaminophen in 3-methyl-1-butanol solution and for parameter estimation of growth kinetics. Typical experimental inputs include process temperature profile (TC), solution concentration (A), particle size measurements (PSD sensor) with selected kinetic models and operating conditions in the crystalliser MSMPR unit. A PSD comparison tool is also used to compare the experimental and model PSD.

The growth kinetic parameters to be estimated were selected as the power law kinetics (equation 5.6) with the driving force expressed as the relative supersaturation (equation 5.7):

$$G = K_g \, exp\left(\frac{E_{A,g}}{RT}\right) \sigma^g \qquad \text{Eq 5.6}$$

$$c^* = \frac{C - C(T_{sat})}{C(T_{sat})} \qquad \text{Eq 5.7}$$

Here, the growth rate constant (k_g) = m/s, activation energy ($E_{A,g,}$) = J/mol and order with respect to supersaturation (g) for a power law relationship is given. It was assumed that no nucleation took place within the seeded batch experiments and therefore the activation energy was set to zero as a constant priori for model simplicity. After model development, the supersaturation control experiments were imported into the gCRYSTAL folder of "Experiments > Performed," where the concentration profile by ReactIR and quantified by the previously developed calibration model (3.2.3.1), temperature and PSD (measured at the batch end) were saved. On the successful inputs of the batch experimental data, a group of kinetic parameters (Table 5.3) could be estimated using the "Parameter Estimations" tool in the software. Several multiple tries of initial guesses for lower and upper bounds for the crystallisation kinetic parameters were usually necessary to obtain a good agreement between model predictions and experimental measurements.

5.2.8. Experimental Procedure: Implementing Wet Milling

To implement high shear wet milling as a potential nucleator and seeding protocol for the continuous crystallisation experiments, the combined wet milling and crystallisation (WMC) process was operated without seeding and applied to a 1 L and 10 L crystalliser scale for initial tests. The cooling trajectory (77.3 - 15°C) was based on the temperature profile generated from the parameter estimation (batch) experiments (described in 5.2.6.) whereby growth kinetics were extracted and modelled. The aim of these experiments was to assess the feasibility of the wet mill to accelerate nucleation kinetics when applied at high temperatures (77.3°C) at moderate supersaturations (S = 1.17) whilst operating within the metastable zone width during the cooling profile.

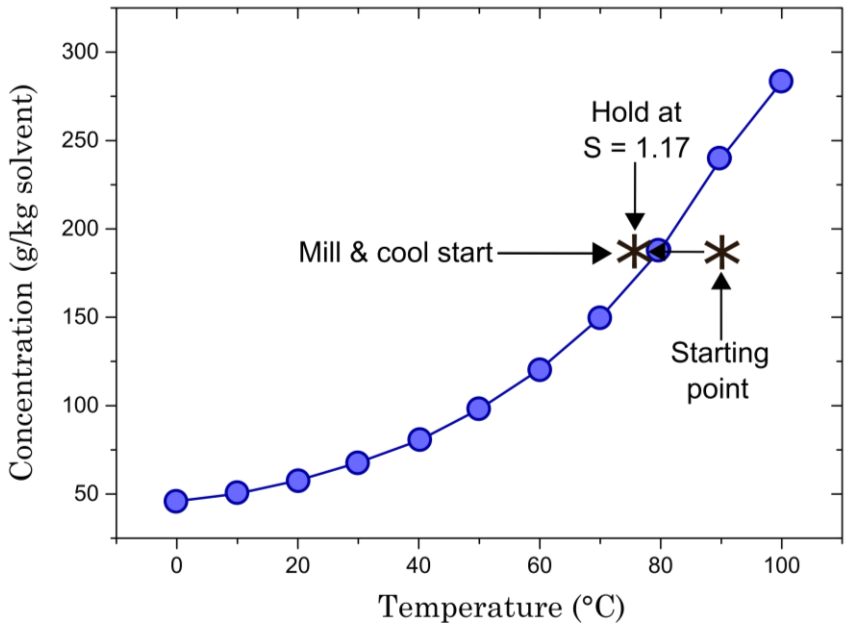

Figure 5.10 Temperature dependant solubility profile of acetaminophen in 3-methy-1-butanol solvent. Annotated wet milling cool and start points are shown during the unseeded crystallisation process.

Table 5.1 Investigated parameters for the WMC experiments operated at constant supersaturation of 1.17. Scale indicates crystalliser vessel, $\dot{Q}$ = volumetric flow rate, S_r = tip speed, Υ_{av} = average shear rate and E^* = energy dissipation are calculated from the rotor-stator configuration.

Scale (L)	C (g/kg)	Rotor-stator config	Total teeth $NR_O + NS_O$	Rotational speed ω (rpm)	$\dot{Q}$ (L/min)	S_r (m/s)	Υ_{av} (s^{-1})	E^*
1	188	Fine	29	15000	1.05	24	240000	2.9
10	188	Fine	29	15000	1.05	24	240000	2.9

5.2.8.1. 1 L Crystalliser Scale

Acetaminophen (111g) was added to 3-methyl-1-butanol (600g) within the OptiMax workstation. FBRM, PVM and ReactIR were integrated into the vessel. The feed solution was prepared by heating the mixture to 90°C over 15 min to achieve dissolution with agitation fixed at 600 rpm. Upon dissolution, the solution was held for 30 min to ensure the presence of no particles. The solution was then cooled over 15 min to 77.3°C with a further 15 min hold period once the target temperature was reached. The solution was simultaneously cooled and wet milled (fine, 15000 rpm) over 2.30 hrs. The cooling trajectory followed the supersaturation feedback-control mechanism applied through the absorbance-temperature model via the ATR-FTIR sensor (as detailed in section 5.2.6). A supersaturation of 1.17 was maintained throughout the experiment. Once the end temperature (15°C) was reached, the contents of the vessel were drained and filtered (90 mm mean diameter) using a Büchner funnel with the cake washed

twice with 2 cake volumes of chilled diethyl ether. The wet cake was then transferred to a vacuum oven (40°C) for drying.

5.2.8.2. 10 L Crystalliser Scale

Acetaminophen (1.29 kg) was added to 3-methyl-1-butanol (6.82 kg) in a 10 L vessel. FBRM and PVM integrated into the vessel with agitation fixed at 600 rpm. The experimental procedure followed a similar method to the 1 L crystalliser scale. However, as no ReactIR probe was inserted in the vessel, the temperature profile for maintaining constant supersaturation was determined from the 1 L experiments and manually added to the input temperature profile in the heater-chiller (Lauda 420) unit. Upon experiment end, the contents of the vessel were drained with filtration performed in a pressure filter dryer (Powder Systems Ltd, Maxi Lab). The filter cake was washed three times with two cake volumes of diethyl ether with agitation between washes to maximise removal of 3-methyl-1-butanol. Drying was performed under vacuum at 40°C for 3 h.

5.2.9. Experimental Procedure: Continuous Seed Generation

The experimental procedure involved preparing 25 L of feed solution in the feed vessel at a concentration of 188 g per kg solvent of acetaminophen in 3-methyl-1-butanol. The solution was heated to 90°C and maintained at this temperature until complete dissolution had occurred. During this period, trace heating (set point of 100°C) on the pipework and associated components (in-line filter, pump and mass flow meter) from the feed vessel to the first crystallisation vessel was commenced. This was important as it

prevented pre-nucleation from the feed to the first crystallisation stage. The crystalliser thermostats for each stage were set to their required temperatures of; 77.3°C, 50°C and 20°C respectively informed from batch parameter estimation experiments. Product valve, V-4 (Figure 5.5) was set to recycle back to the feed vessel. Each vessel was initially empty and un-pressurised.

Start-up was performed by transferring the feed solution at 100 g / min^{-1} (controlled by mass flow meter and pump) into the seed generation stage (first crystallisation stage (Figure 5.5)). Once this stage was approximately 50% full, wet milling through the recycling mode was started. Filling of the vessel continued until the 100% level (1.5 L) was reached at which point positive pressure was applied to enable material transfer to the crystallisation stages 1 and 2. Once stage 2 reached its maximum level, material was transferred back to the feed vessel via a 3-way valve (Figure 5.5). The recycle configuration allowed for the cascade to reach steady state without consuming material. Once a steady state was achieved, as indicated by the chord lengths (μm) via FBRM sensor showing a minimum variance for 2 residence times, product valve V-4 was turned to start product collection in the pair of pressure filter driers (Powder Systems Ltd, Maxi Lab) operating in duty and stand-by mode (Figure 5.5).

Table 5.2 Investigated conditions for the WMC-MSMPR experiments.

Process conditions	Value
Feed concentration (g/kg)	188
Stage temperatures (°C)	77.3, 50, 20
Mass flow rate (g/min)	100
Steady-state (min)	35
Total mean residence time (min)	45
Rotor-stator configuration	Fine
Total no of teeth, $NR_O + NS_O$	29
Rotational speed, ω (rpm)	15000

Filtration was performed once 10 L of product suspension was collected. The filter cake was washed three times with two cake volumes of diethyl ether with low speed agitation between washes to maximise removal of 3-methyl-1-butanol. Drying was performed under vacuum at 40°C for 3 h.

5.3. Results and Discussion

The following section will discuss results obtained for estimation of growth kinetics followed by implementing high shear wet milling as a nucleator.

5.3.1. Growth Behaviour

For concentration determination, the selected functional group which was monitored for acetaminophen in 3-methyl-1-butanol was the carboxylic acid group attached to an amide group (RHN-C=O). Collection of raw inline IR spectra was then processed through the GRAMS™ software using a previously developed calibration model described in section 3.2.3.1.

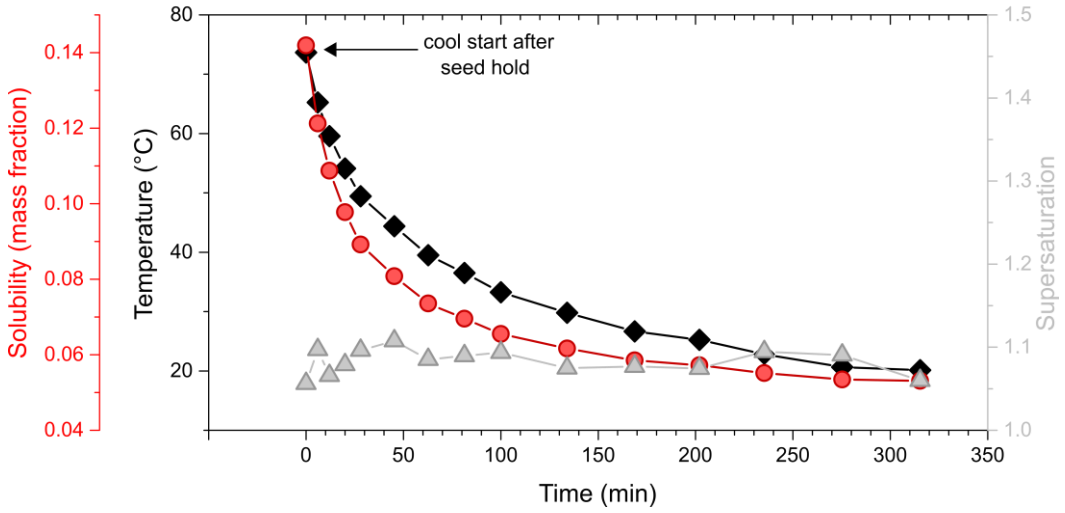

Figure 5.11 Maintained supersaturation (S = 1.08) control profile over time is shown for a 1 L batch parameter estimation experiment without wet milling coupled (section 5.2.6).

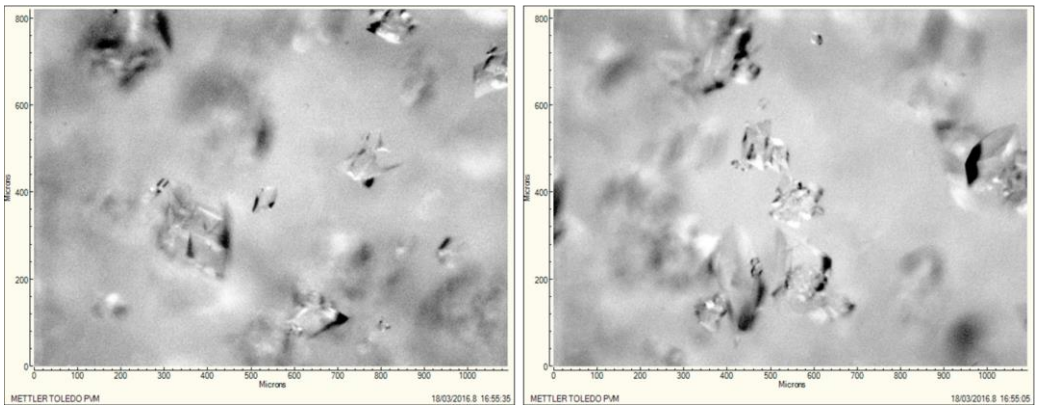

Figure 5.12 Inline particle images (final product) captured from a PVM sensor for the constant supersaturation control experiment (S = 1.08).

As shown in Figure 5.11, employing constant supersaturation displayed a well-maintained and a well-behaved crystallisation. This was observed throughout cooling without any supersaturation fluctuations or undesired nucleation events (fines) (Figure 5.11). Images collected from the PVM sensor show as large-dispersed crystals in bulk suspension with minimal aggregation (Figure 5.12).

5.3.2. Modelling of Growth Behaviour

The predicted concentration profiles generated from the two fitting experiments are shown (Figure 5.13, (A)) which were used to estimate the growth kinetic parameters (Table 5.3). Figure 5.13 highlights that good fits were achieved as is reflected in the weighted residual being significantly less than 95% χ^2 (Table 5.3). To validate the selected growth parameters (Eqn 5.1 & 5.2) and the mechanistic assumptions, the predicted and experimental PSDs for the product particles were compared with further additional validation experiments which consisted of simple linear cooling crystallisations from 78 to 5°C (Figure 5.13, (B)).

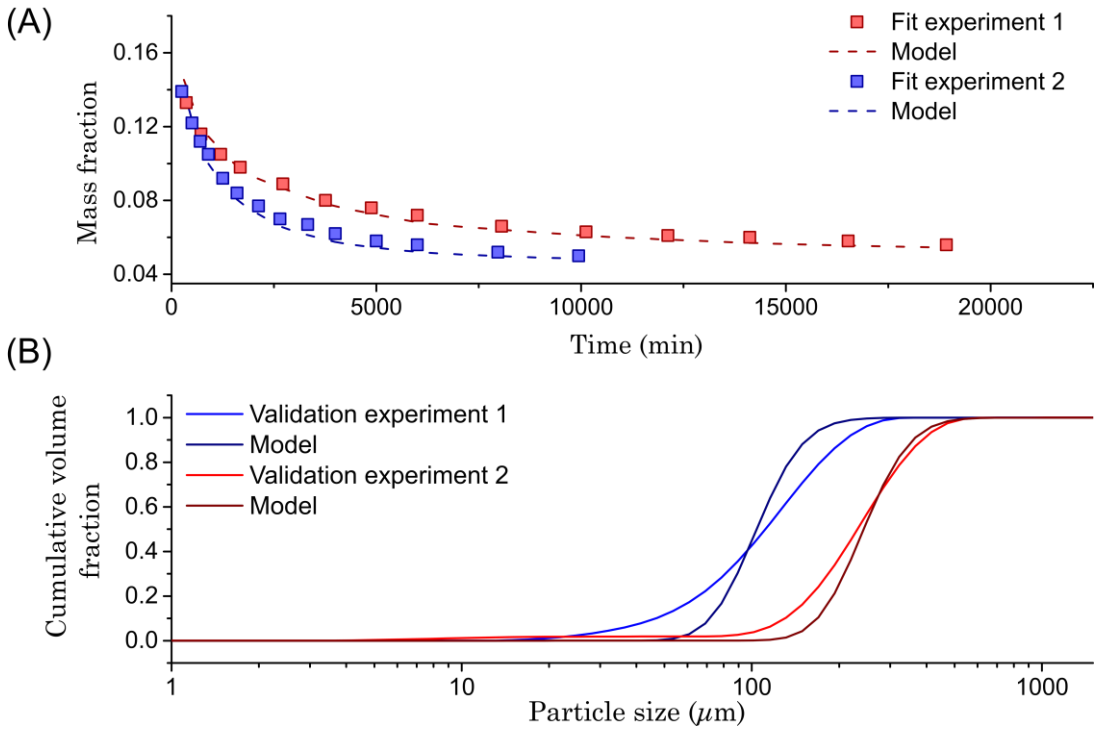

Figure 5.13 Comparison of experimental and model concentration profiles (A) and product particle size distribution (B) for the 1 L batch parameter estimation experiments (Brown et al., 2018).

Table 5.3 Estimated growth parameters (Brown et al., 2018)

Model parameter	Value	Units	Confidence Interval (95%)	Standard Deviation
Activation energy, $E_{A,g}$	0	J mol^{-1}		
Growth rate constant, K_g	3.64 x 10^{-4}	m s^{-1}	0.00571900	0.00278200
Order with respect to supersaturation, g	4.127		7.20500	3.50500
Weighted residual	2.616			
χ^2 value (95%)	38.885			

There is generally good agreement between the D_v50 results, indicating that the growth parameters accurately represent the system. However, the experimental PSDs do show more small particles in the distribution than is predicted (Figure 5.13, (B)). This may be due to attrition, secondary nucleation or breakage taking place in the process or that particle breakage is induced by the particle sizing method. However, these model deviations were judged acceptable in light of the selected target specification and the growth model was sufficiently accurate. (Rashid et al., 2017).

Where required, further investigations to determine additional kinetic parameters could be undertaken and various approaches have been described elsewhere (Pérez-Calvo et al., 2016). Based on the validated kinetic parameters from the growth-only model achieved by the initial batch parameter estimation experiments, several continuous crystalliser configurations were evaluated computationally. This involved scoping and selecting a suitable number of MSMPR stages (1, 2 or 3) for productivity, practical control and efficiency. As the cooling profile generated from

constant supersaturation experiments (batch) was to be applied during continuous crystallisation, a single stage was discounted as the stage temperature required to maintain supersaturation below the levels for primary or secondary nucleation would lead to low crystallisation productivity (see Figure 9 in the workflow article (Brown et al., 2018). A 2 stage and greater configuration displayed little increase in productivity whilst increasing the configuration and control complexity. Thus, a compromise was met with a 2 stage configuration. Further details on the D-optimal linear experimental design with constraints in the model which consisted of the factors (stage temperatures, stage volume and net flow rate) and responses (PSD, span, product volume fraction of crystals and stage supersaturation) is reported (Brown et al., 2018).

5.3.3. Analysis of Implementing Wet Milling

Prior to implementing the growth-model for a seeded cooling crystallisation process, a key focus of this work is to develop a practical seed generation strategy. Informed from previous work (chapter 4), rotor-stator wet milling through the recycle-loop mode (Figure 5.4) was applied to trigger nucleation which potentially, could be transferred as a direct seed stream to subsequent MSMPR stages for growth during cooling. Upon investigating the WMC method on a 1 L and 10 L crystalliser, it would be reasonable to assume the wet mill would also be able to nucleate a solution when coupled to a 2 L crystalliser which is the configured volume scale for each continuous MSMPR stage.

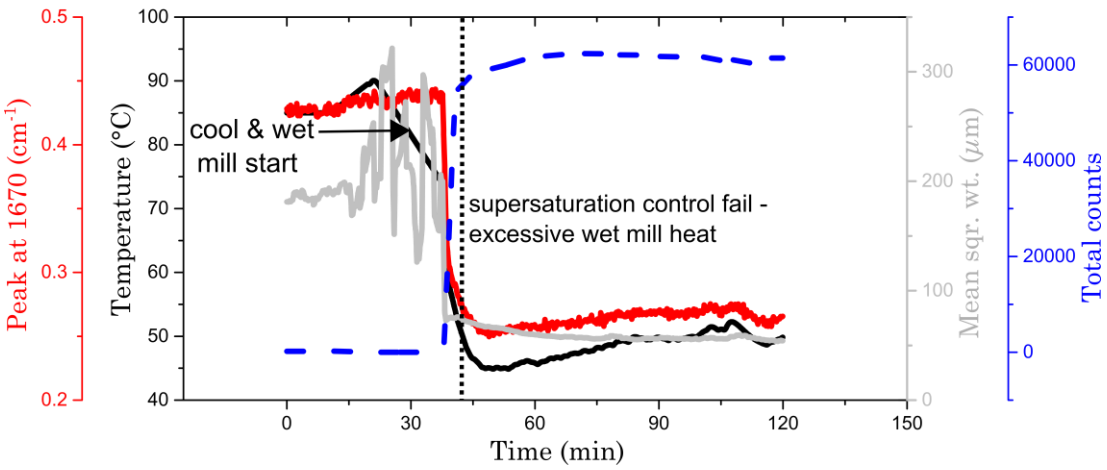

Figure 5.14 Inline profiles for a combined wet milling crystallisation experiment with supersaturation feedback-control consisting of a 1 L crystalliser scale. Selected IR peak height, supersaturation, temperature, mean square weight and total count trends are shown. The wet mill is configured with a multiple-stage (coarse + medium + fine) at 26k.

Initially, a multiple-stage rotor-stator configuration was chosen on the basis for exerting maximum shear (S_r = 40.8 m / s & Υ_{av} = 415000 s^{-1}) at high rotation speeds (26000 rpm) for the immediate induction of primary nucleation on starting milling. During the initial cooling phase (0 to 40 min), the monitored peak on the ATR-FTIR signal (1670 cm^{-1}) following the IR absorbance-temperature model (section 5.2.6) struggled to maintain constant supersaturation during the recirculation process (Figure 5.14). This was due to the excessive heat generation in the wet mill configured with a multiple-stage module at 26000 rpm. Therefore, this caused a large temperature offset in the feed vessel from wet milling heat generation leading to the supersaturation control failing to maintain the desired cooling profile over time (Figure 5.14). However, a sudden and rapid

increase in total counts within < 15 min of mill start upon cooling shows that the combined wet milling crystallisation strategy rapidly accelerated the total counts and hence the number of particles (< 30 min, ~ 50000 counts (a.u), Figure 5.14) when compared to the batch experiments (< 30 min, ~ 8000 counts (a.u), Figure 5.11). To overcome the heat generation issue from rotor-stator wet milling, the teeth configuration was changed to a single-stage fine configuration with a selected lower rotation speed (15000 rpm). Within the same experiment and conditions (1 L scale, (Figure 5.15)) upon dissolving the feed solution and reaching the supersaturation point, cooling and wet milling was started with the supersaturation feedback-control mechanism now functioning throughout the recycling process.

The selected fine teeth configuration at 15000 rpm with a rotor tip speed S_r of 23.6 m / s and average shear rate Υ_{av} of 240000 s^{-1}, increased the total counts upon immediate wet milling start (< 15 min, Figure 5.15). Overall, the selected configuration (fine, 15000 rpm) with constant supersaturation control proved successful in rapidly accelerating nucleation kinetics whilst maintaining a dispersed particle population (Figure 5.16) size and size distributions (D_v50 = 30.97 μm, span = 1.26, (Figure 5.17)) and particle shapes (mean aspect ratio = 0.687 & circularity = 0.91) as well as minimising excessive heat generation.

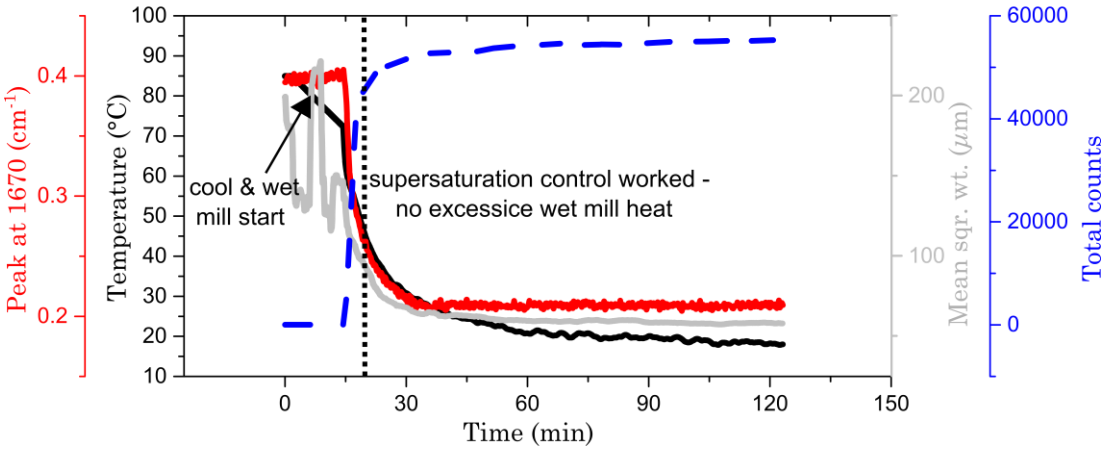

Figure 5.15 Inline profiles for a combined wet milling crystallisation strategy with supersaturation feedback-control for a 1 L crystalliser scale experiment. Inline selected IR peak, supersaturation, temperature, mean square weight and total count trends are shown. The wet mill was configured with a single-stage (fine) at 15k.

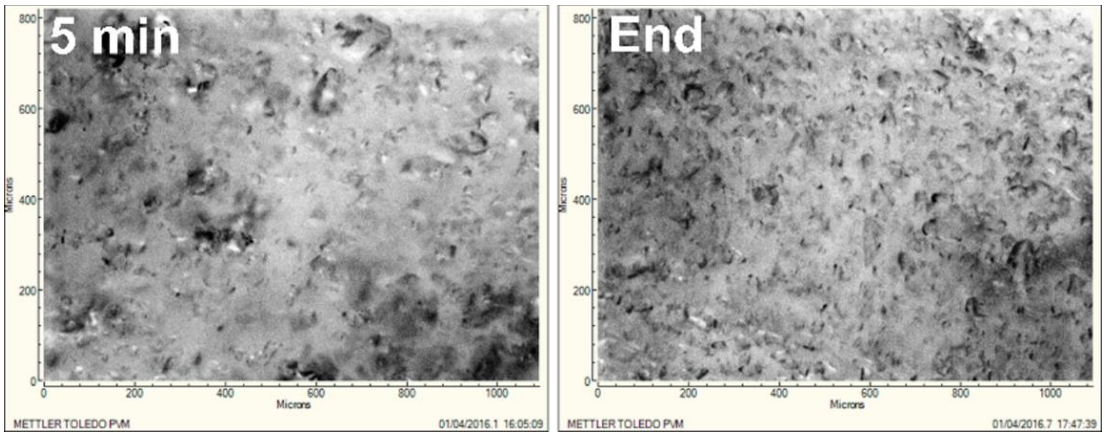

Figure 5.16 Inline particle images captured from a PVM sensor during the 1 L crystalliser scale experiment which consisted of a fine 15000 rpm rotor-stator configuration.

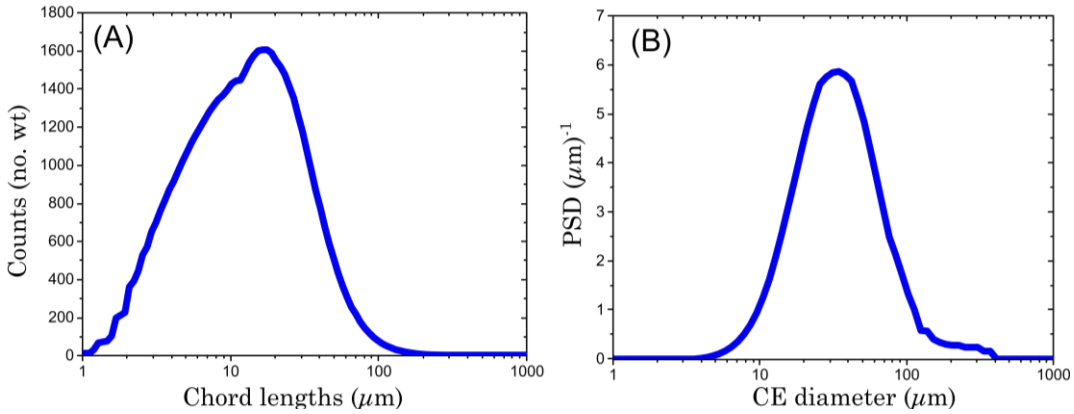

Figure 5.17 In situ chord lengths (A) and offline particle size distribution (B) both measured at experiment end for the 1 L crystalliser scale experiment which consisted of a fine 15000 rpm rotor-stator configuration.

5.3.4. Analysis of Implementing Wet Milling on Scale-up

Several experimental campaigns at the 10 L crystalliser scale demonstrated acceleration of nucleation using the combined strategy (Figure 5.18). An example inline profile from the FBRM sensor is shown (Figure 5.19). In common with Figure 5.15 upon cool and wet milling start, high shear accelerates nucleation as seen from both increasing count statistics (total and 50 – 150, Figure 5.19). Interestingly, whilst total counts continue to increase (40 to 80 min) followed by a levelling off phase (> 80 min), counts from 50 - 150 display a decrease (> 45 min) after the rapid nucleation burst (Figure 5.19). This indicates that as the particle population rapidly increases from 5 to 30 min due to the simultaneous high shear and cool effect, larger particles are seen to reduce over time (40 to 120 min).

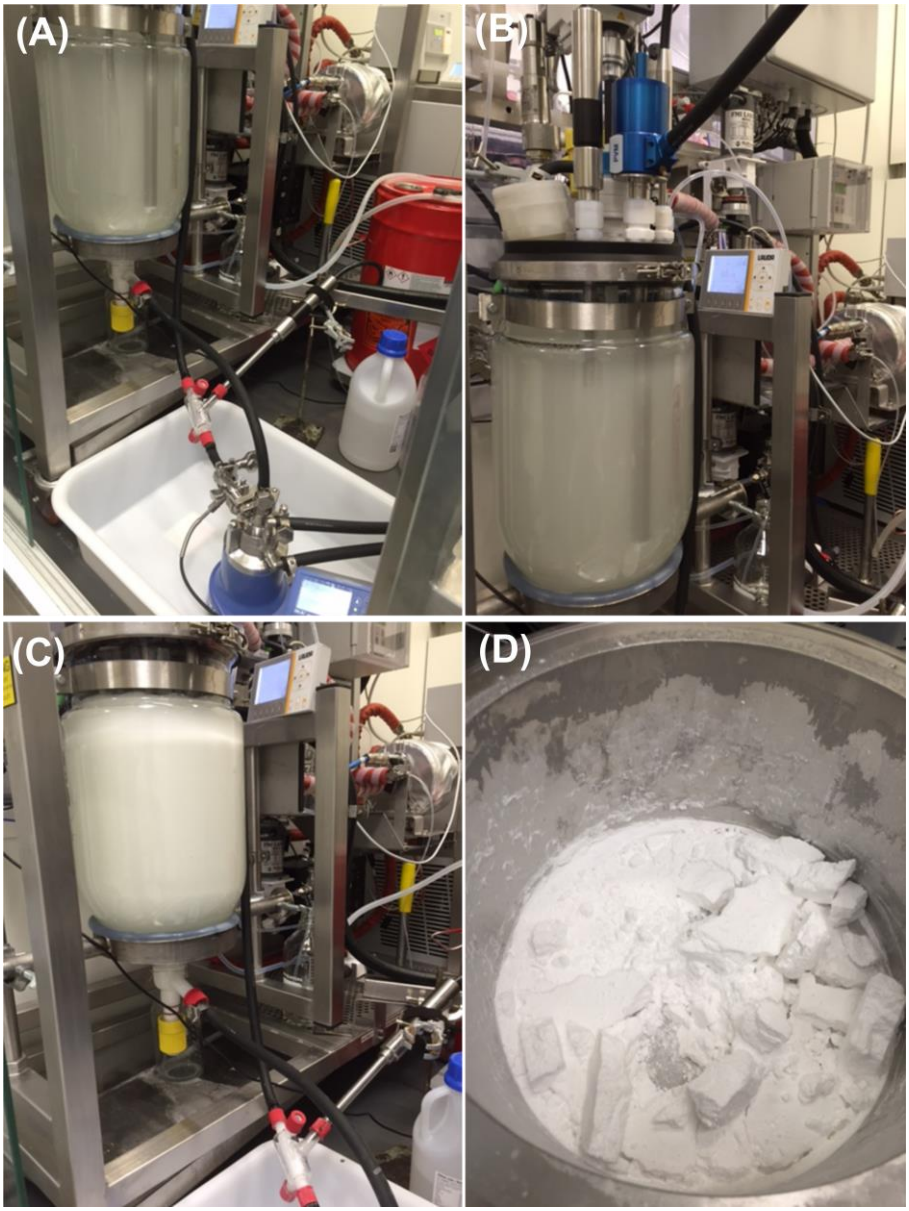

Figure 5.18 Laboratory images of a 10 L crystalliser scale. Wet milling applied in the recycle-loop (A) with a zoomed in image of integrated PAT sensors (FBRM & PVM) for process monitoring (B) upon 15 min of milling start. A flow-cell for direct FBRM measurements on the wet mill outlet was initially used (A) however, was quickly discarded for the remainder of the experiments due to clogging. Experimental end prior to isolation (C) and after isolation (filtration, washing, drying) yielded the dry solid product (D).

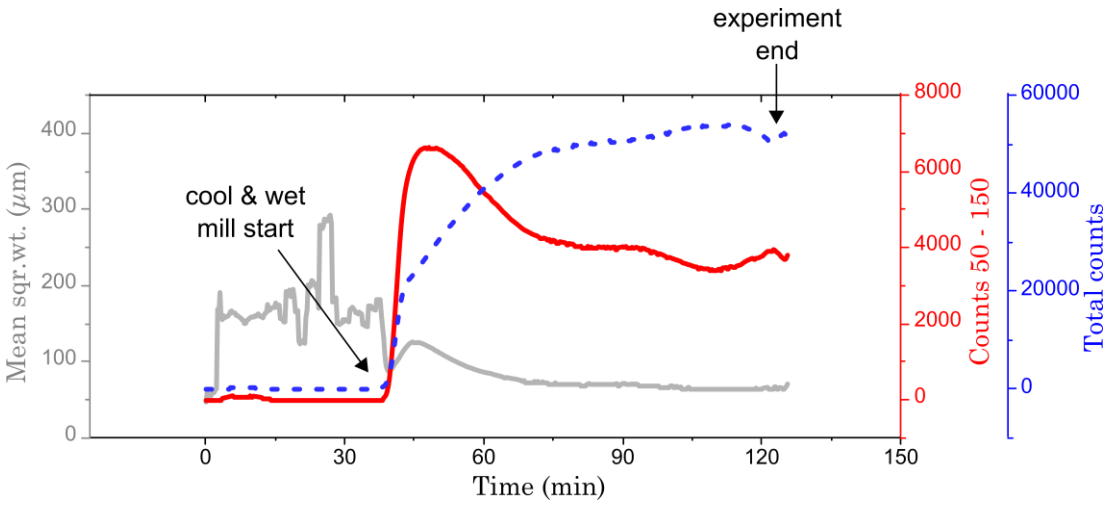

Figure 5.19 FBRM profile (inline) showing the impact of wet milling start on particle counts and mean square weight trends for the 10 L crystalliser scale experiment.

Further analysis of the tracked CLDs captured from an FBRM sensor for a single experiment displays a shift from right (62.91 μm) to left (33.66 μm) after 5 minutes of milling (Figure 5.20, (A)). This shift continues until the end of the experiment which is due to size reduction from continuous recycling of the particle suspension (Figure 5.20, (A)). Similar to the 1 L scale, the combined strategy applied to the 10 L crystalliser scale consistently generated monodisperse particle size and size distributions of less than < 50 μm with spans from 1.1 – 1.3 (Figure 5.20, (B)).

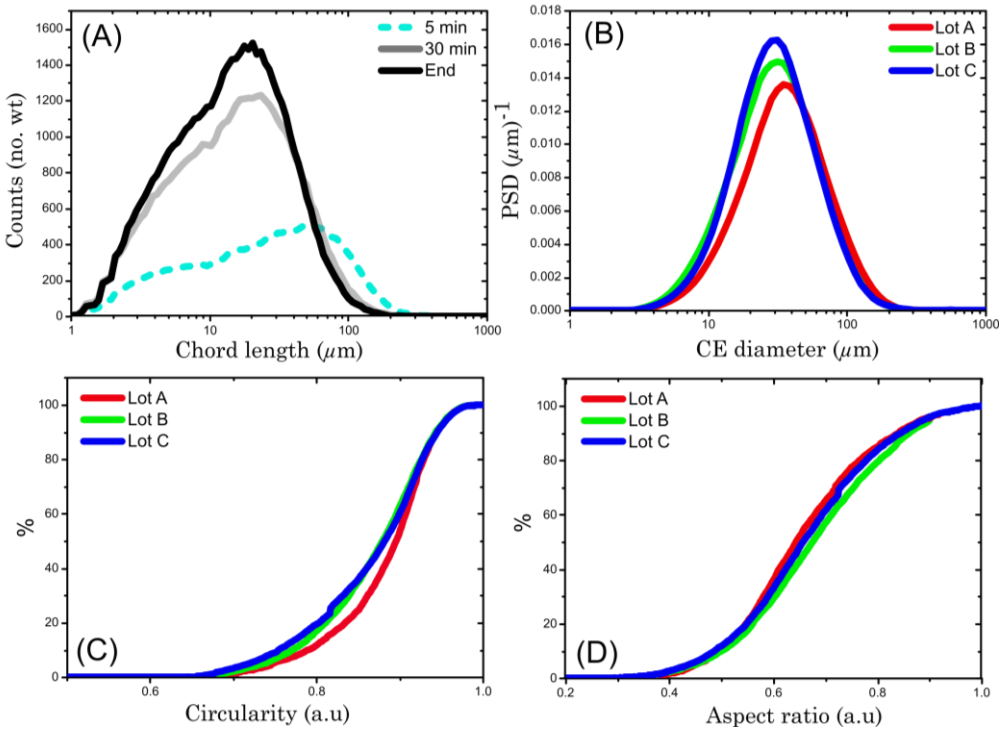

Figure 5.20 Chord lengths and particle size distributions (PSD) are shown for the 10 L crystalliser scale experiments. In situ raw CLDs tracked from 5 min to end are shown for a single experiment (LotA) (A). Offline product particle size distributions measured across several lots (A – C) and particle shape distributions are represented as undersize curves for circularity (C) and aspect ratio (D).

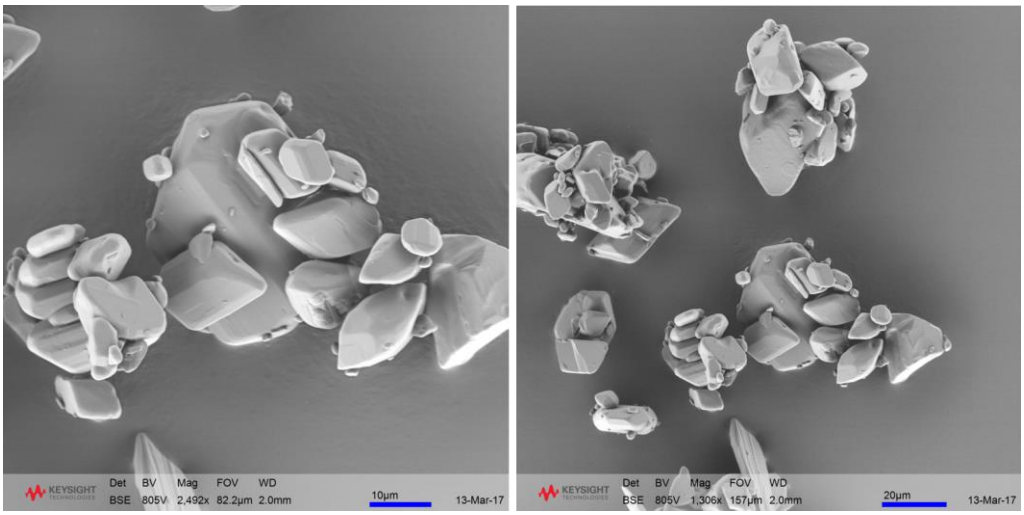

Figure 5.21 SEM images of product particles from the 10 L crystalliser scale experiments. The images shown are collected for Lot A.

The combined strategy produced equant particle shapes as seen from the final product particles consisting of a mean circularity of 0.85 and aspect ratio of 0.7 (Figure 5.20, (C & D)) as well as the SEM images (Figure 5.21). Low surface roughening on the product particles are also seen (Figure 5.21) which is attributed to the optimised cooling profile, from the 1 L batch parameter estimation experiments during crystallisation thus allowing surface healing from crystal growth. It is also noted, no undesired polymorphic transformations occurred for acetaminophen which remained monoclinic (Form 1, stable) across all high shear wet milling experiments (Table 5.1).

Rotor-stator wet milling when coupled to an unseeded cooling crystallisation acts as a high shear nucleator upon process start-up followed by subsequent milling which exerts particle size reduction. This is evident from real-time analysis captured via inline sensors (FBRM) across Figure 5.15 & Figure 5.20, (A). The mechanistic observation is also consistent with other reported studies such as immersion wet milling which was shown to act as a high shear nucleator first and then mill (Acevedo et al., 2017). Whilst this emphasises the complexity of the mechanisms occurring in the combined approach, inline PAT sensors are identified as critical components for process monitoring, control and understanding of the combined strategy.

5.3.4. Analysis of Continuous Seed Generation

The combined wet milling crystallisation strategy was now applied as the seed generation stage which was directly coupled to stages 1 and 2 in the MSMPR configuration (Figure 5.5 & Figure 5.22). The generation of seeds was achieved through a start-up procedure involving transfer of the feed solution (100 g min^{-1}) into the seed generation stage (Figure 5.5). Once the stage was approximately 50% full, the rotor-stator wet mill (fine 15000 rpm, Υ_{av} of 240000 s^{-1}) was switched on to trigger nucleation at 77.3°C.

Material transfer across the vessels (Figure 5.22) was then performed by applying positive pressure once the seed vessel reached 100% (1.5 L) full. Positive pressure for slurry transfer was selected as this reduces process complexity and potentially line blockages as no pumps were used between the stages. The cooling trajectory across the process setup followed the constant supersaturation profile determined from the 1 L batch parameter estimation experiments and was split across the seed stage and stages 1 & 2 (Figure 5.22).

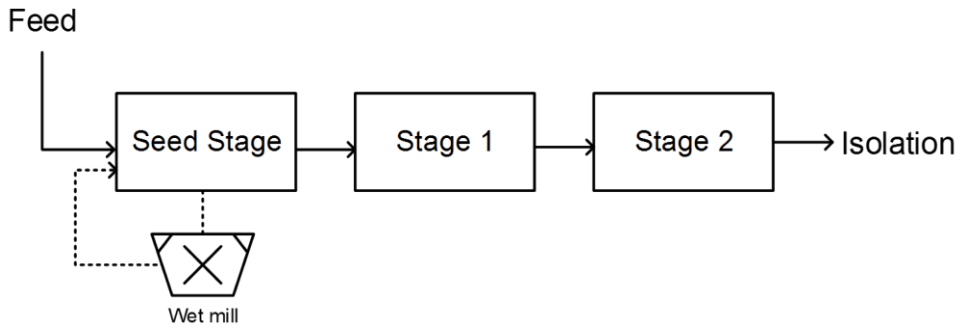

Figure 5.22 Flow-diagram showing the configured seed generation stage with the growth stages (1 & 2).

An example FBRM profile is shown (Figure 5.23, (A)) during one of the continuous crystallisation campaigns. This highlights the dynamics of the start-up period showing steady-state was not obtained until approximately 350 min. The operation in recycle of the whole process (after stage 2), continued until 440 min to ensure steady-state was obtained to which the process was then operated through the single-pass mode (Figure 5.23, (A)). The process trends remain relatively constant for the remaining 250 min of operation (time taken to deplete the feed vessel) which was directly collected for product isolation. With a total mean residence time (across all three crystallisers) of approximately 45 min (Table 5.2) this would indicate a requirement to operate for 6 to 7 residence times before steady-state was achieved. This is comparable to the generally accepted 7 to 10 residence times required for MSMPRs to reach steady-state (Ranodolph, 2012).

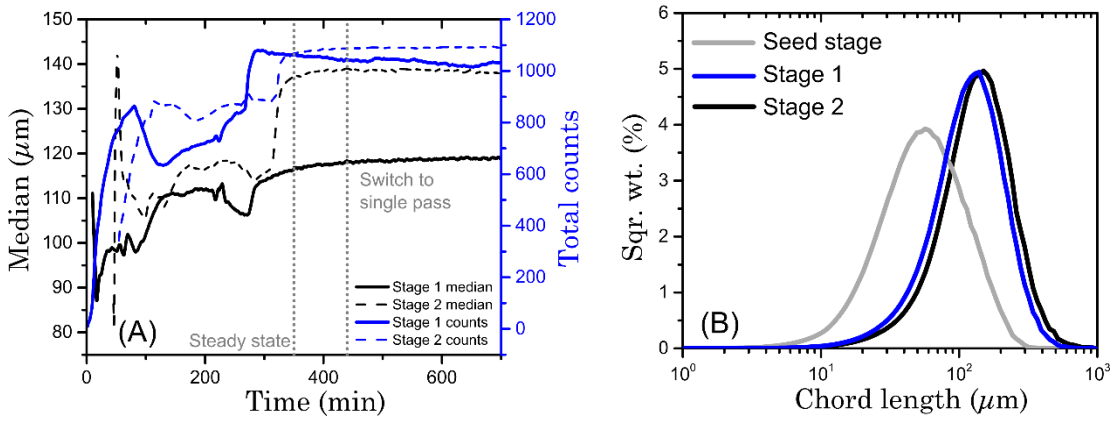

Figure 5.23 Example process trends from continuous crystallisation showing median (μm) and total counts over time (A) and chord length distributions (B) across each MSMPR stage (Brown et al., 2018).

The process trends further show an increase of approximately 20 μm in the median size between stages 1 and 2 at steady-state with narrow chord length distributions measured at the seed generation stage and growth stages (Figure 5.23, (B)).

The performance of the rotor-stator wet mill to continuously generate seeds via high shear and directly transfer as a seed slurry was a robust and practical approach. There was no significant clogging, fouling or encrustation across the stage transfer lines and within the vessels which ensured smooth running of the continuous process. Although the wet mill was continuously operated for long durations of the time (> 10 hr), leakage and blockages inside the wet mill were occasionally observed after 8 – 10 hours of operation. This could have been due to particle settling or entrapment inside the rotor-stator framework causing slurry accumulation over time inside the wet mill. However, these issues were solved relatively quickly and the desired particle size was achieved. An intermittent wet milling operation could be applied and investigated in future work to avoid leakage issues after long periods of process running.

Overall, the seed stage is the critical component of the continuous process as it controls the crystallisable mass and therefore the number of seeds that can be generated for growth. Future work could look to control the seed generation stage through varying wet mill process parameters (i.e., teeth & speed) for reducing the time to reach steady-state and targeting a defined PSD and shape from the two stage MSMPR.

Nevertheless, across the several filtered product lots from the experimental campaigns, an average target particle size of 112.0 μm (Dv50) with a standard deviation of 16.2 μm was met by first intent (Figure 5.24). The average span of the distributions was 1.66 with a standard deviation of 0.18.

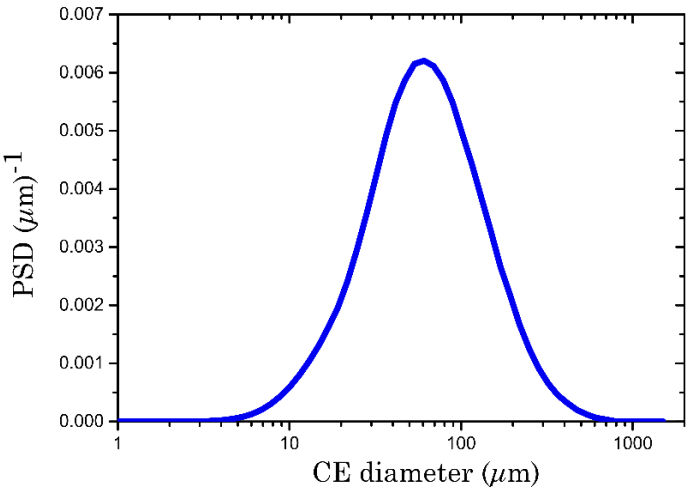

Figure 5.24 Average particle size distribution of 112.0 μm (Dv50) with a standard deviation of 16.2 μm was achieved from the continuous crystallisation campaigns.

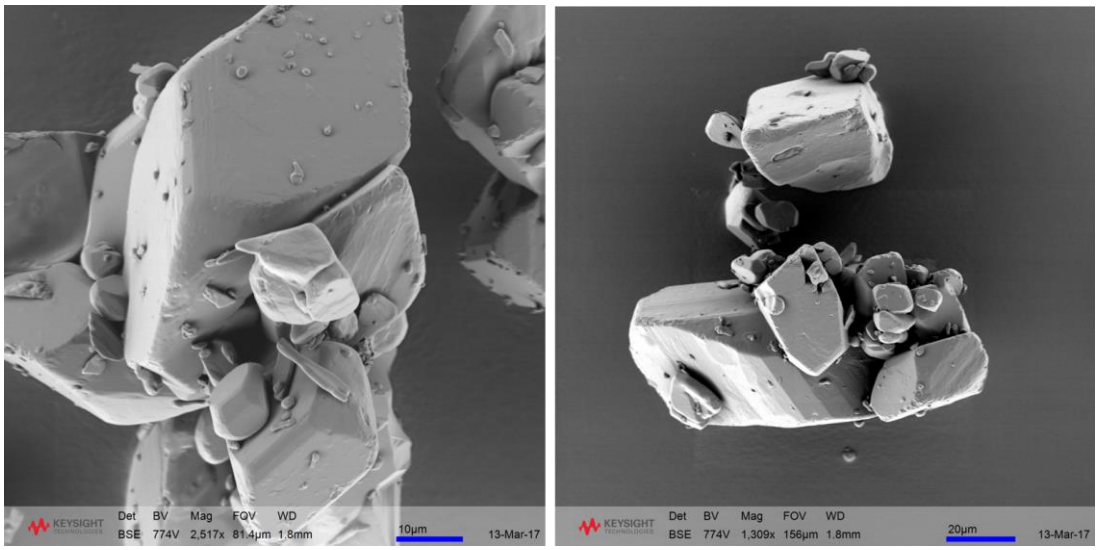

Figure 5.25 SEM images of final product particles generated from the continuous crystallisation campaigns.

The average circularity consisted of a mean 0.849 ± 0.013 suggesting product particles are of low aspect ratios which is also seen from the SEM images (Figure 5.25). Similar to the 1 L and 10 L combined WMC strategy, equant particle shapes were consistently produced from the WMC-MSMPR process which produced a larger particle size of 112.0 μm (Dv50) due to dedicated growth vessels (stages 1 & 2). Further process modelling work and results surrounding the continuous crystallisation campaigns with additional downstream unit operation tests on the product lots is reported in detail (Brown et al., 2018).

5.4. Summary

A combined wet milling crystallisation strategy has been presented for high shear nucleation across process scales (1 L, 2 L and 10 L) for acetaminophen. The experimental method and results allowed for the combination approach to be easily integrated and utilised as a continuous seeding platform which directly transferred a consistent seed stream for growth-only on an MSMPR process.

The combined wet milling crystallisation strategy accelerated nucleation during cooling (< 15 min) at moderate supersaturations (S = 1.17). It was evident from the selected wet mill configuration (fine teeth, 15000 rpm) substantial shear (Υ_{av} = 240000 s^{-1}) and energy dissipated (E^* = 2.9) from the rotor-stator framework triggered nucleation. Continuous recirculation of the suspension produced narrow size and size distributions of 30 – 55 μm with tight particle spans (1.1 – 1.4) as well as equant particle shapes (circularity = 0.85 – 0.91) across process scales. Interestingly, real-time analysis of process trends of chord lengths (μm), mean square weight (μm), particle counts and imaging via inline PAT sensors (FBRM & PVM) confirmed the wet mill to act as a nucleator first followed by milling causing particle size reduction through the WMC strategy.

A continuously seeded crystallisation process was investigated which makes use of the combined WMC method as a robust seed generation platform. This novel application continuously generated a seed slurry on-demand which was transferred to subsequent stages for crystal growth

informed through an optimal cooling profile. The process resulted in tight product attributes which was achieved by first-intent consisting of a particle size distribution of 112 μm and span of 1.66 amongst well-maintained particle shapes (circularity = 0.89).

The results of this study outline the capability to eliminate external seed generation through alternative particle engineering strategies. Adopting these strategies in the pharmaceutical industry is highly desirable for future continuous crystallisation process development specifically, as continuous manufacturing is increasingly being applied.

Chapter 6

Multi-Sensor Inline Measurement of Crystal Size and Shape Distributions during High Shear Wet Milling of Crystal Slurries

---

This chapter is a collaborative study which has been published as a journal article:

AGIMELEN, O. S., SVOBODA, V., **AHMED, B**., CARDONA, J., DZIEWIERZ, J., BROWN, C. J., MCGLONE, T., CLEARY, A., TACHTATZIS, C., MICHIE, C., FLORENCE, A. J., ANDONOVIC, I., MULHOLLAND, A. J. & SEFCIK, J. 2018. Multi-sensor inline measurements of crystal size and shape distributions during high shear wet milling of crystal slurries. *Advanced Powder Technology*, 29, 2987-2995.

6. Multi-Sensor Inline Measurements of Crystal Size and Shape Distributions during High Shear Wet Milling of Crystal Slurries

6.1. Introduction

The outcomes of a crystallisation process in terms of particle size and shape distributions are determined by a complex interplay of nucleation, growth, agglomeration and breakage which can vary widely from batch to batch or when input conditions or process parameters are changed. There are several approaches providing empirical control of particle size distributions (PSD) in crystallisation processes, such as seeding (to provide control over particle concentrations) and high shear wet milling (to provide control over particle size). A review of high shear wet milling as a size reduction technique has been described in detail elsewhere (section 1.4.1). Typically, for process monitoring by inline sensors, the focused beam reflectance measurement (FBRM) is widely employed (Heinrich and Ulrich, 2012) which provides a chord length distribution for particles in suspension. The CLD is related to the size and shape of the particles in suspension (Heinrich and Ulrich, 2012). The total counts of measured CLDs has been used as an indication for number of particles while the mean square weighted chord length has been used as an indication of particle size (Yang et al., 2015, Yang et al., 2016a, Yang et al., 2017).

Even though CLD counts are related to number of particles, it is not straight-forward to determine the actual number density of particles in a

slurry from CLD counts. Similarly, while CLD is related to the PSD, it does not provide an actual PSD of particles. This is because each particle with a given size and shape produces a unique chord length distribution (Heinrich and Ulrich, 2012) and these are then convoluted in an average weighted by a characteristic particle size to provide an overall CLD for the whole ensemble of particles of different sizes and shapes present in a slurry (Vaccaro et al., 2006, Mesbah et al., 2011).

Instead of using the mean square weighted chord length as an estimate for the mean particle size, it would be more realistic and accurate to use an actual PSD determined from inline measurements (Kail et al., 2007, Kempkes et al., 2008). For example, from transformation of CLD data (Agimelen et al., 2015, Agimelen et al., 2016) obtained inline or from analysis of inline images (Cardona et al., 2018). Hence, experimental wet milling studies could then benefit from the estimated particle size and shape distributions. Consider the case of needle-like particles undergoing wet milling, their length is likely to be reduced while their width would be much less affected. However, the most probable chord length for a needle-like particle is the width of the particle (Li and Wilkinson, 2005) and so the change in particle length may not be well reflected in the mean square weighted chord length. But this mean square weighted chord length is currently used an indication for particle size even when needle-like particles are involved (Yang et al., 2017). Furthermore, if the PSD is

estimated from data captured with inline instruments, there will be no need to sample the slurry for offline estimates of the PSD.

In this work, recently developed computational tools are implemented which comprise of the CLD-Inversion App (Agimelen et al., 2018a) and Imaging App (Cardona et al., 2018), in order to quantitatively investigate changes in PSD and particle shape during wet milling when the mill rotation speed is varied. In comparison to the combined wet milling crystallisation processes (chapter 4 & 5), the effect of crystallisation is decoupled and the impact of wet milling breakage-only is monitored on different crystalline materials which has not been explicitly demonstrated in the earlier chapters.

The PSDs are estimated separately from CLD and from imaging data obtained by the inline FBRM and particle vision and measurement (PVM) sensors, respectively. As the PSD is estimated from data captured by inline sensors, the computational tools enable us to monitor changes in particle properties during the wet milling in real-time. A new method for estimating the number of particles in slurries from the estimated volume based PSD from inline instruments is also introduced. Furthermore, inconsistencies arising between PSDs estimated from inline and offline instruments for the same wet milling process is analysed with limitations of inline sensors encountered during the study discussed.

6.2. Experimental Section

6.2.1. Materials and Method

The following materials were used in this work: acetaminophen (> 98% USP), benzoic acid (> 99.5%), and metformin hydrochloride (reagent grade). Acetaminophen and benzoic acid were purchased from Sigma-Aldrich and metformin hydrochloride was purchased from Molekula. The benzoic acid particles were suspended in distilled water obtained from an in-house purification system and the surfactant TWEEN 20 from Sigma-Aldrich was added to the benzoic acid slurry to ease dispersion of the particles and avoid foaming. Acetaminophen and metformin hydrochloride were suspended in 2-propanol (reagent grade, CAS: 67-63-0, Assay (GLC) > 99.5%) obtained from Fisher Scientific Ltd.

6.2.2. Experimental Setup

The experiments were conducted in the recycle-loop setup consisting of a Mettler Toledo OptiMax™ workstation, a Watson Marlow Du520 peristaltic pump and an IKA MagicLab (module UTL) rotor stator wet mill. The same OptiMax™ equipped with PAT as investigated in chapter 4 was used. A sketch of the setup is shown (Figure 6.1). The rubber tubing used in the flow loop had an inner diameter of 3.2 mm, the lengths of the pieces of tubing connecting the 1 L stirred tank to the peristaltic pump, the pump to the wet mill and the wet mill to the 1 L stirred tank were 94.5cm, 55 cm and 124 cm respectively. The internal volume of the wet mill was 30 ml. The peristaltic pump was operated at 50 rpm corresponding to a volumetric

flow rate of 350 ml / min. This then corresponds to a residence time of 5 s of the slurry in the wet mill. The temperature of the outlet of the wet mill was monitored with a thermometer attached to it. The outlet temperature was controlled to match the temperature of the inlet flow to the wet mill by means of a Lauda heater / chiller connected to the wet mill (Figure 6.1).

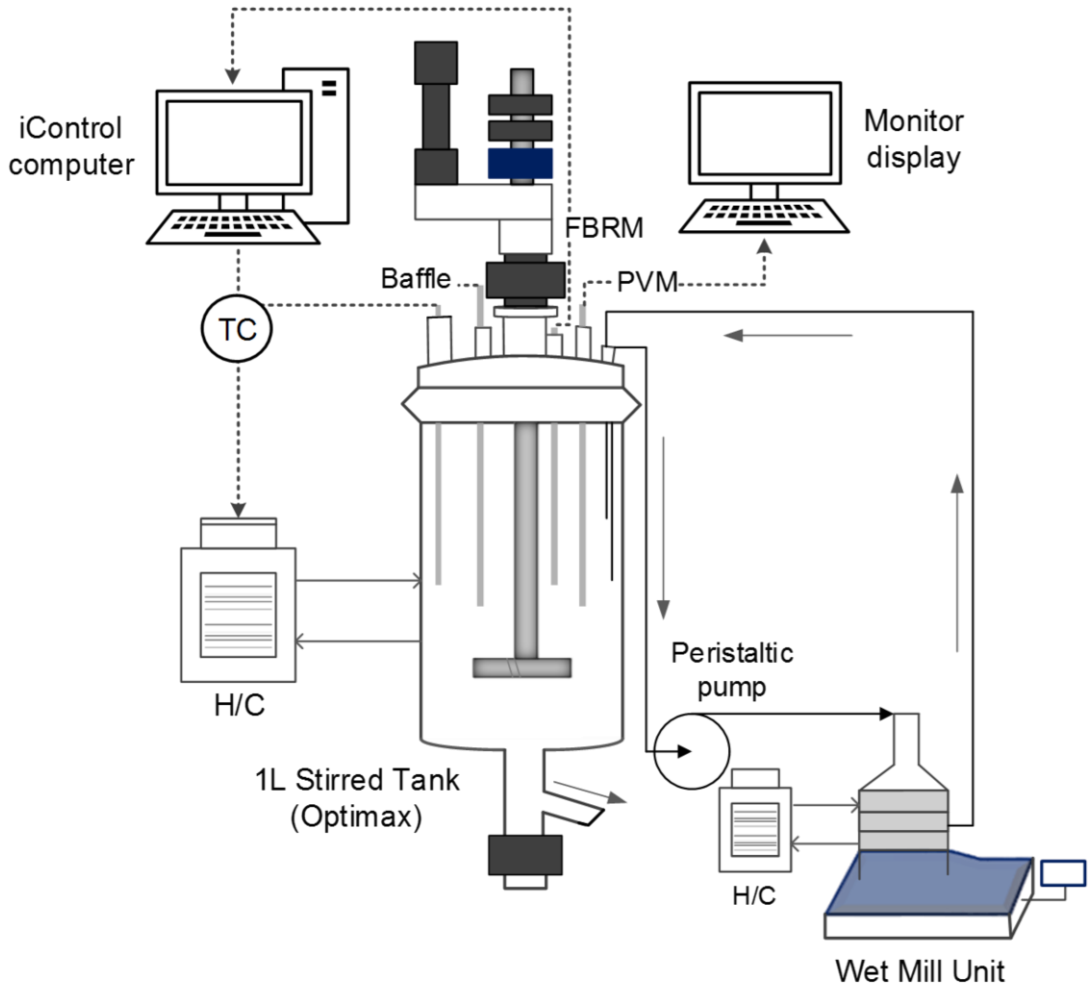

Figure 6.1 Sketch of the process setup used for the wet milling processes in this study.

The process conditions of temperature and stirring speed of the slurry in the Workstation were controlled using the iControl v5.2 software from Mettler Toledo.

Data related to the size and the shape of the particles in the wet milling processes was captured with the Mettler Toledo FBRM G400 series and PVM V819 sensors within the stirred-tank. Offline particle size and shape analyses were carried out using the Malvern Morphologi G3 instrument. A description for each of these techniques has been outlined earlier (chapter 3) and is further detailed from the following sources (Agimelen et al., 2015, Agimelen et al., 2016, Heinrich and Ulrich, 2012, Kail et al., 2007, Kail et al., 2009).

6.2.3. Experimental Procedure

The OptiMax vessel was charged with 900 ml of solvent at 25°C at the start of each experiment. A predetermined quantity of solid was then added, and heated to 40 - 50°C to dissolve. The solution was then cooled to 25°C over 20 min to saturate. Once the temperature had reached the setpoint value, a predetermined mass of solid powder was added to the saturated solution and allowed to equilibrate for 60 min. Before the addition of the powder, a sample of the original material (starting material) was initially analysed with the offline Morphologi instrument for size and shape information.

After the equilibration period (covering a period T_1), the peristaltic pump and wet mill were started simultaneously. The speed of the pump was maintained at 50 rpm throughout the experiments while that of the wet mill was initially set to 6000 rpm (for a duration T_2) after which it was increased in stages. At the next stage (with duration T_3) of the process, the speed of the wet mill was increased to 10,000 rpm, and subsequently to 14,000 rpm (for a duration T_4) and finally to 18,000 rpm (for a duration T_5). The temperature of the mill outlet was regulated manually by adjusting the heater chiller setpoint in order to maintain it at 25°C and prevent dissolution. The time intervals T_1 to T_5 varied from 30 – 90 min for each material.

At the end of the time interval T_5, the suspension was filtered and washed in a Büchner funnel. The same solvents which were used in the experiments for benzoic acid and metformin hydrochloride were used for washing each material at the end of their respective experiments, while acetaminophen was washed with chilled water. Each material had a low solubility in its respective wash solvent. The washed cakes obtained at the end of each wet milling process were then dried overnight in a vacuum oven. Samples of the milled product obtained at the end of each wet milling process were analysed for size and shape information using the offline Morphologi instrument.

6.2.3.1. Benzoic Acid

Benzoic acid particles were prepared by antisolvent crystallisation (after an initial dissolution of benzoic acid from Sigma-Aldrich) using a mixture of 70% - 30% ethanol - water mixture as solvent, and 20% - 80% ethanol - water mixture as antisolvent. A predetermined mass of antisolvent was added at a predetermined rate in order to obtain long needle shaped crystals. The particles were filtered and dried before being suspended in water for the milling experiment. The particles were suspended in water (saturated with benzoic acid) due to the low solubility of benzoic acid in water. However, due to poor wettability of benzoic acid in water, the surfactant TWEEN 20 was used at a concentration of 2 ml / L. The solid loading was 1.6% w / w.

6.2.3.2. Acetaminophen

Acetaminophen from Sigma-Aldrich was dissolved in 3-methyl-1-butanol after which prism like particles were obtained by cooling crystallisation. The particles obtained from the cooling crystallisation were then suspended in a saturated solution of acetaminophen in 2-propanol for the wet milling experiment. The solid loading was 4.2% w / w. Although the solubility of acetaminophen in 2-propanol is relatively high, the solvent was chosen to avoid agglomeration.

6.2.3.3. Metformin Hydrochloride

Metformin from Molekula was used directly as the particles were already rod-like. The particles were then suspended in a saturated solution of

metformin in 2-propanol (in which metformin has a low solubility and good dispersion) for the wet milling process. The solid loading was 3.5% w / w. The wet milling process for metformin was stopped at the stage T_4 (with the mill speed of 14,000 rpm as the particles were quickly broken in this case.

6.3. Data Analysis

As mentioned above, the starting material and the milled product for each material were analysed for size and shape information using the offline Morphologi G3 instrument. The CLD data acquired using the inline FBRM sensor (using the macro mode with no weighting) were analysed using a previously developed inversion algorithm (described earlier in section 3.2.3.3) which estimates corresponding particle size distribution and aspect ratio (assumed to be same for all particles). Similarly, the images captured using the inline PVM sensor were analysed using a previously developed image processing algorithm (described earlier in section 3.2.3.4) to obtain projections for particles captured in images and to provide the corresponding particle length and aspect ratio for each particle deemed to be in focus. Therefore, detailed size and shape distributions can be obtained, similar to those from offline measurements.

The method developed for estimating the number of particles from CLD ($\widehat{N}_{CLD}$) and images ($\widehat{N}_{IMG}$) by Agimelen (Agimelen et al., 2018b) produced during the wet milling process can be determined from an estimated volume based PSD for the particles in the suspension and solid loading

(which is constant during wet milling under saturated conditions). To estimate the number of particles, the particle length L is discretised and classified into N bins with the characteristic length $\bar{L_\iota} = \sqrt{L_i}L_{i+1}$ of bin i representing the length of particles in bin i, where L_i and L_{i+1} are the bin boundaries of bin i. The number of particles N_i in bin i is given as:

$$N_i = \frac{\tilde{m}_i M_0}{pV_i} \qquad \text{Eqn 6.1}$$

Here, the mass fraction of the particles in bin i ($\tilde{m}_i$), mass of the initially suspended particles (M_0) which is constant as there is no growth or dissolution, density of particles (p) and the volume of the particles in bin i (V_i) are included. Approximating the shape of all particles in bin with an ellipsoid of semi-major axis length $\bar{a_\iota} = \bar{L_\iota}/2$ and two equal semi-minor axis length $\bar{b_\iota} = \bar{r_i}\bar{a_i}$ where $\bar{r_i}$ is the mean aspect ratio of all the particles in bin i gives the volume of the particles in each bin i as $v_i = \pi\bar{r_i}^2\bar{L_i}^3/6$. Since all particles have the same density, the mass fraction of the particles in bin i can be replaced by their volume fraction $\tilde{v}_i$. Then the number of particles in bin i becomes:

$$N_i = \frac{6\tilde{v}_i M_0}{p\pi\bar{r_i}^2\bar{L_i}^3} \qquad \text{Eqn 6.2}$$

When the volume based PSD is estimated from the CLD inversion algorithm, the corresponding number of particles is obtained by summing over all bins as:

$$N_{CLD} = \sum_{i=1}^{N} N_i \qquad \text{Eqn 6.3}$$

As the slurry is initially allowed to equilibrate during the stage T_1 of each of the wet milling processes, the number of particles estimated at the stage T_1 will be taken as the base number of particles N_{CLD}^0. Then, the number of particles relative to the base number of particles $\widehat{N}_{CLD}$ is obtained from $\widehat{N}_{CLD} = N_{CLD}/N_{CLD}^0$.

In the case of image analysis, the mean number of objects per frame N_{IMG} is used as a measure of the number of particles. It is estimated by counting all objects which were detected and contained wholly within the image frames. This number of objects is then divided by the total number of frames to obtain N_{IMG}. Similar to the case of CLD, the number of particles estimated from images at T_1 will be taken as the base N_{IMG}^0. At the subsequent stages, the number of particles estimated from images relative to the base number of particles $\widehat{N}_{IMG}$ will be obtained from $\widehat{N}_{IMG} = N_{IMG}/N_{IMG}^0$.

6.4. Results and Discussion

The three particle analysis techniques employed in this work consistently showed particle breakage during wet milling progressing from the lowest to the highest mill rotation speed. However, the different techniques showed varying sensitivities as process conditions and particle size and shape distributions changed. Below, results for benzoic acid, metformin hydrochloride and acetaminophen is presented. Benzoic acid is primarily discussed in detail with respective limitations of the different techniques using results from all three systems also analysed.

6.4.1. Offline Analysis

The two-dimensional volume based probability density function (PDF) of particle length and aspect ratio estimated using offline imaging (Morphologi G3) for both the starting material and the final milled product for benzoic acid are shown in Figure 6.2 (A & B), respectively[1]. The data clearly show particle breakage as the broad peak between particle lengths 100 and 1000 microns and aspect ratios from 0.4 to 1 moves towards smaller lengths and higher aspect ratios (Figure 6.2, (A & B)). This is indicative of breakage of large elongated particles to much shorter, more isometric ones.

[1] The raw estimates of particle lengths and widths from the Morphologi instrument was extracted and analysed. In the volume based analysis, the particles were treated as ellipsoids of major axes lengths equal to the originally estimated particle lengths. The two minor axes were set equal to the originally estimated particle widths. This was to make the analysis consistent with those out on the inline PVM images and the particle representation in the CLD analysis.

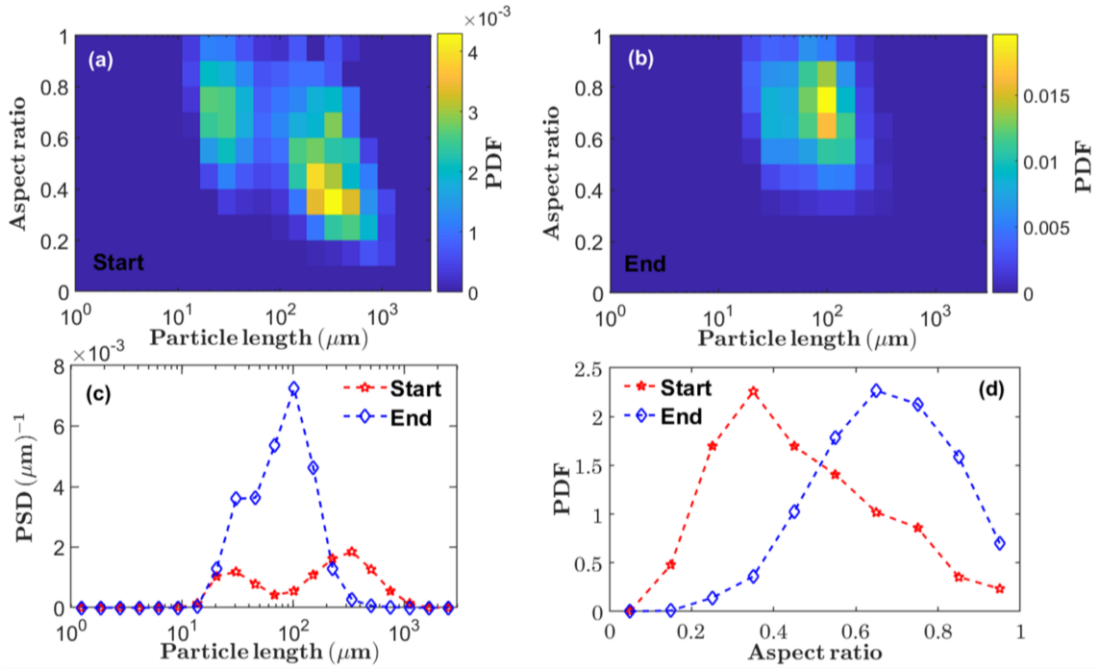

Figure 6.2 2D volume based probability density function (PDF) of particle length and aspect ratio for the starting material (a) and the final milled product (b) for benzoic acid from the offline Morphologi instrument. Corresponding 1D volume based particle length distributions (c) and 1D volume based aspect ratio distributions (d) of the starting material and the final milled product for benzoic acid. The number of particles contained in the measured PSD from the Morphologi instrument was 55787 for the starting material and 50000 for the final milled material.

In Figure 6.2 (C & D) one-dimensional projections of two-dimensional PDFs is shown, in terms of volume based particle length distributions and aspect ratio distribution for the starting material and the final milled product. Similar results were also obtained for acetaminophen and metformin (Figure 6.3 & Figure 6.4).

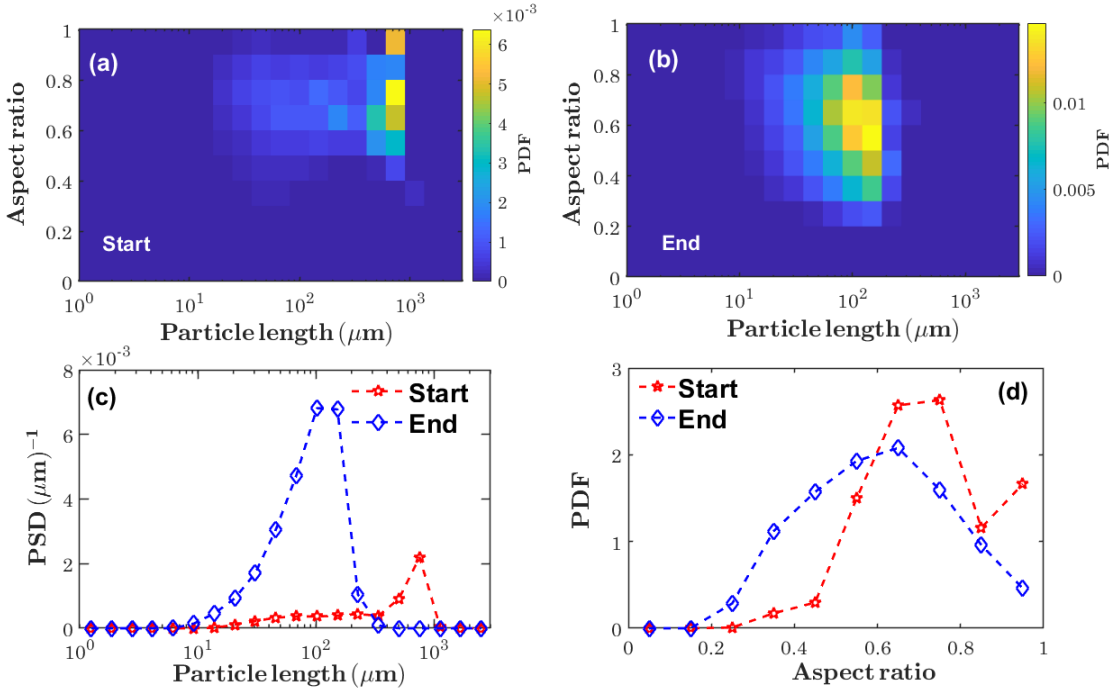

Figure 6.3 2D volume based probability density function (PDF) of particle length and aspect ratio for the starting material (a) and the final milled product (b) for acetaminophen from the offline Morphologi instrument. Corresponding 1D volume based particle length distributions (c) and 1D volume based aspect ratio distributions (d) of the starting material and the final milled product for acetaminophen. The number of particles contained in the measured PSD from the Morphologi instrument was 8428 for the starting material and 31050 for the final milled material.

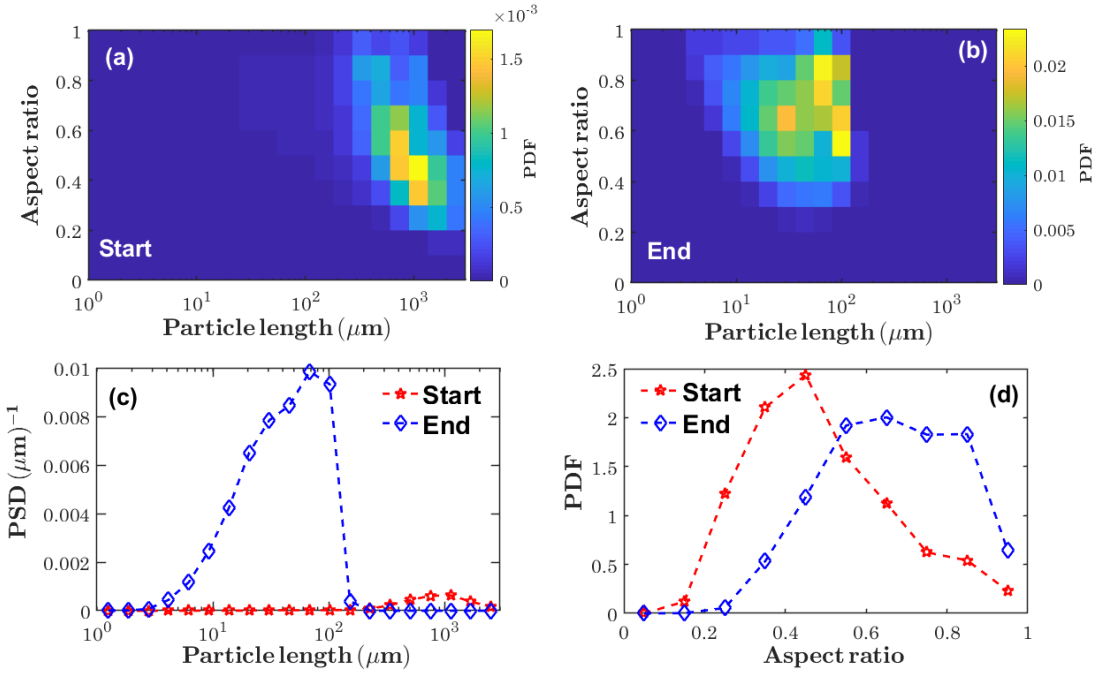

Figure 6.4 2D volume based probability density function (PDF) of particle length and aspect ratio for the starting material (a) and the final milled product (b) for metformin from the offline Morphologi instrument. Corresponding 1D volume based particle length distributions (c) and 1D volume based aspect ratio distributions (d) of the starting material and the final milled product for metformin. The number of particles contained in the measured PSD from the Morphologi instrument was 18737 for the starting material and 7401 for the final milled material.

6.4.2. Analysis of Inline CLD Data

The total CLD counts captured from the FBRM sensor at the different time intervals T_1 to T_5 during the wet milling of benzoic acid are shown by the solid line in Figure 6.5 (a). Each time interval (T_1 to T_5) corresponds to an increase in wet milling rotation speed. The estimated number of particles from the CLD data has been described in section 6.3.

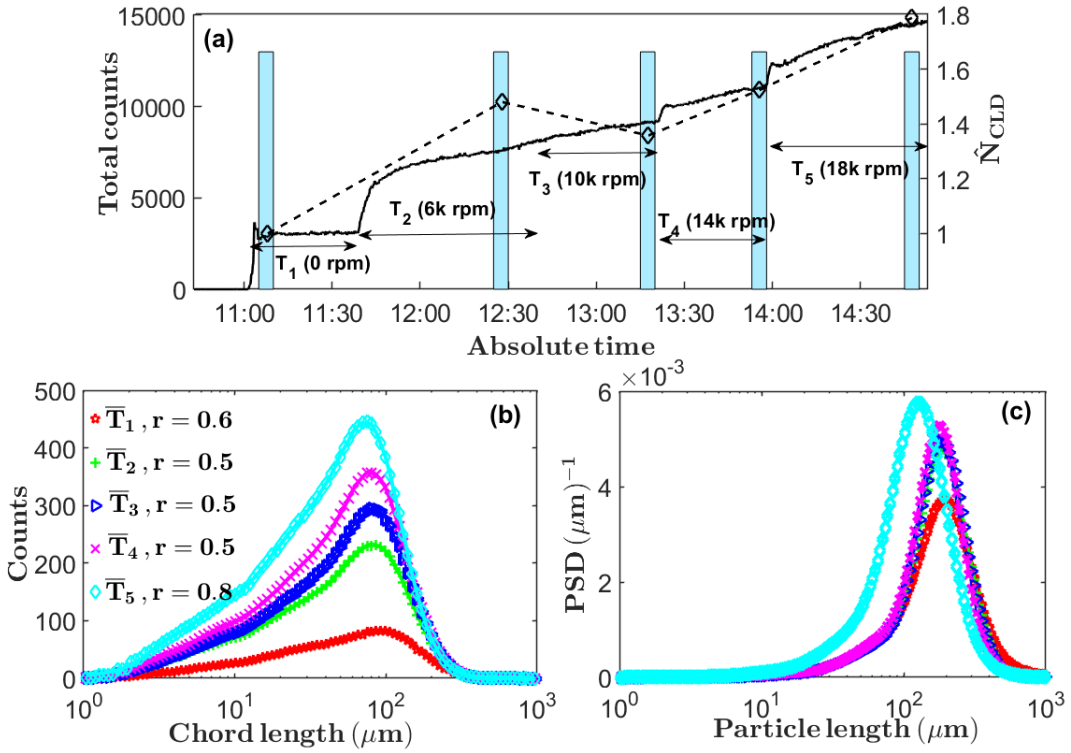

Figure 6.5 The total chord length counts for the benzoic acid sample during the wet milling stages covering the time intervals T_1 to T_5 are shown by the solid line in (a), while the symbols show the relative number of particles $\hat{N}_{CLD}$ for the same sample. The mean chord length distributions (CLDs) acquired in the 5 mins intervals $\bar{T}_1$ to $\bar{T}_5$ (shown by the vertical bars in (a)) within the time interval stages T_1 to T_5 are shown by the symbols in (b). The height of the vertical bars have no quantitative value and are all positioned as the same height at each time interval for consistency. The solid lines in (b) (with colours corresponding to the symbols) are the estimated CLDs at the aspect ratios r indicated in the (c). The estimated volume based PSDs from the CLDs shown in (b) at the aspect ratios indicated in (b) are shown in (c).

The increase in total chord counts over the wet milling stages T_1 to T_5 (Figure 6.5, (a)) clearly indicates breakage of particles during the process as the conditions were such that there was no nucleation or growth of particles. This breakage is also reflected in the increase in the relative

number of particles $\widehat{N}_{CLD}$ as shown by the symbols in Figure 6.5 (a). The mean CLD captured in 5 min time intervals ($\overline{T}_1$ to $\overline{T}_5$ shown by the vertical bars in Figure 6.5 (a)) within the time intervals T_1 to T_5 are shown by the symbols in Figure 6.5 (b).

Breakage of particles leads to an increase in the counts for smaller chord lengths of these CLDs over the time intervals $\overline{T}_1$ to $\overline{T}_5$ as the CLD acquisition time was fixed throughout the process. The solid lines (with the colours corresponding to the symbols) in Figure 6.5 (b) are the fitted CLDs obtained by solving the associated inverse problem. This involves searching for a PSD at different aspect ratios r (all particles are assumed to have the same mean aspect ratio) whose corresponding CLD gives the best fit to the measured CLD (Agimelen et al., 2015). In the case of Figure 6.5 (b), these best fits were obtained at r = 0.6 ($\overline{T}_1$), r = 0.5 ($\overline{T}_2$), r = 0.5 ($\overline{T}_3$), r = 0.5 ($\overline{T}_4$) and r = 0.8 ($\overline{T}_5$) as indicated in Figure 6.5 (b). In order to reduce the search space and regularise the inverse problem (described in section 3.2.3.3), experimental estimates of aspect ratio with reasonable bounds were achieved from the imaging instruments (PVM sensor and Morphologi). This information was then used to constrain the search for a representative aspect ratio during the wet milling processes.

The PSDs estimated from the CLDs (Figure 6.5, (b)) (at the best fit values of r) are shown in Figure 6.5 (c). The estimated PSDs (Figure 6.5, (c)) both show breakage of particles moving from T_1 to T_5. That is, the peaks of the

distributions shift to the left and both the right and left tails of the distributions shift to the left on moving from T_1 to T_5. Similar results were obtained from the analysis of CLD data for acetaminophen and metformin (Figure 6.6 & Figure 6.7).

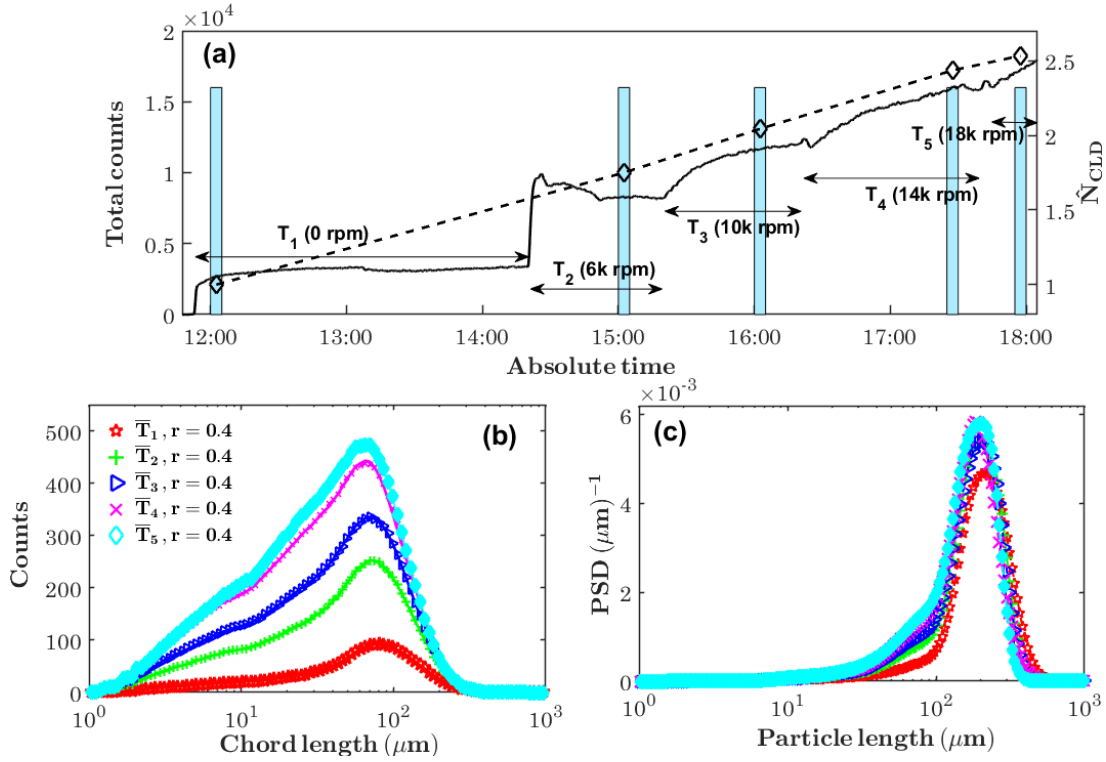

Figure 6.6 Total chord length counts and relative number of particles $\widehat{N}_{CLD}$ for the acetaminophen sample during the wet milling stages covering the time intervals T_1 to T_5 (a) and volume based data from CLD analysis (b & c) similar to Figure 6.5 is shown.

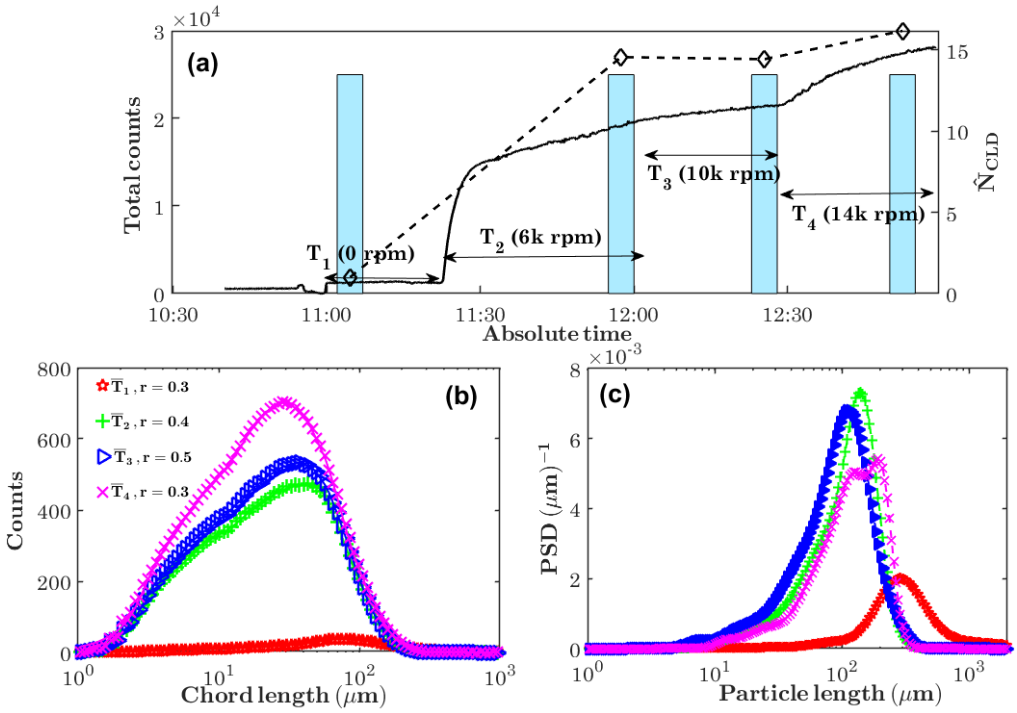

Figure 6.7 Total chord length counts and relative number of particles $\widehat{N}_{CLD}$ for the metformin sample during the wet milling stages covering the time intervals T_1 to T_5 (a) and volume based data from CLD analysis (b & c) similar to Figure 6.5 is shown.

6.4.3. Analysis of Inline PVM Images

Breakage of benzoic acid particles during wet milling is evident from inspecting inline PVM images. However, image analysis provides quantitative estimates of how particle size and shape distributions vary in response to changing mill rotation speed.

This can be clearly seen in the two dimensional probability density function of particle length and aspect ratio (Figure 6.8, (a)) obtained from the analysis of PVM images (moving from T_1 to T_5). It is noted that the particle length distribution obtained from PVM images has lower and upper cut-offs due to limitations of image size, resolution and subsequent image

processing. At the lower end, the cut-off is at a length of about 25 μm. This is because of the resolution of PVM images and a choice of a minimum pixel area required (here we used 576 μm^2, corresponding to length. 24 μm) by an image processing algorithm to distinguish between relevant objects and background image noise. Therefore all particles with smaller lengths were rejected by the image processing algorithm. Also, objects with lengths $\geq$ 500 μm tend to be undercounted by the image processing algorithm.

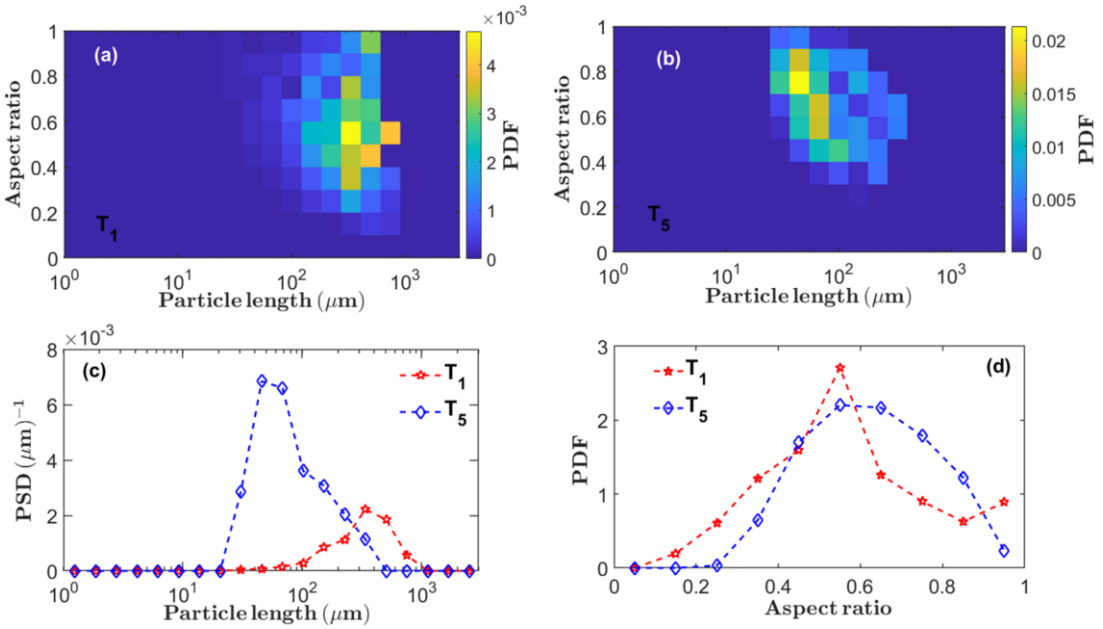

Figure 6.8 2D volume based probability density functions (PDFs) of particle length and aspect ratio estimated from images captured with inline PVM sensor during wet milling stages T_1 (a) and T_5 (b) for benzoic acid. The number of images captured and analysed at T_1 was 424 and 300 for T_5. Corresponding 1D volume based particle length distributions (c) and 1D volume based aspect ratio distributions (d) during wet milling stages T_1 and T_5 for benzoic acid. The number of particles contained in the measured PSD from the PVM sensor was 511 for T_1 and 821 for T_5.

This is because larger objects have a higher chance of touching the image frame so that most of them are rejected. Hence, the particle length estimates from PVM images are most reliable within the range from about 25 to about 500 μm.

6.4.4. Limitations of Particle Size Techniques

Wet milling of particle slurries from the three systems used in this work presented different challenges pertaining to particle sizing techniques and corresponding data analysis as discussed below.

6.4.4.1. Limitations of Offline Analysis

One of key limitations of particle sizing using offline imaging, such as the Morphologi G3 used in this work, is the change of state of the particles between the slurry and the dry powder used for analysis. In some cases, particles that were initially agglomerated before suspension could become de-agglomerated upon suspension and agitation. This is particularly obvious in the case of the acetaminophen starting material. The sample images from the offline instrument suggests the presence of agglomerates up to 1000 μm (Figure 6.9, (a)). Whereas, these large agglomerates seem to be missing in suspension as suggested by the sample images from the PVM sensor at T_1 (Figure 6.9, (b)). The presence of the large agglomerates in the starting material of acetaminophen leads to the peak close to 1000 μm in the estimated volume based PSD for acetaminophen obtained with the Morphologi instrument which is seen in Figure 6.10 (b).

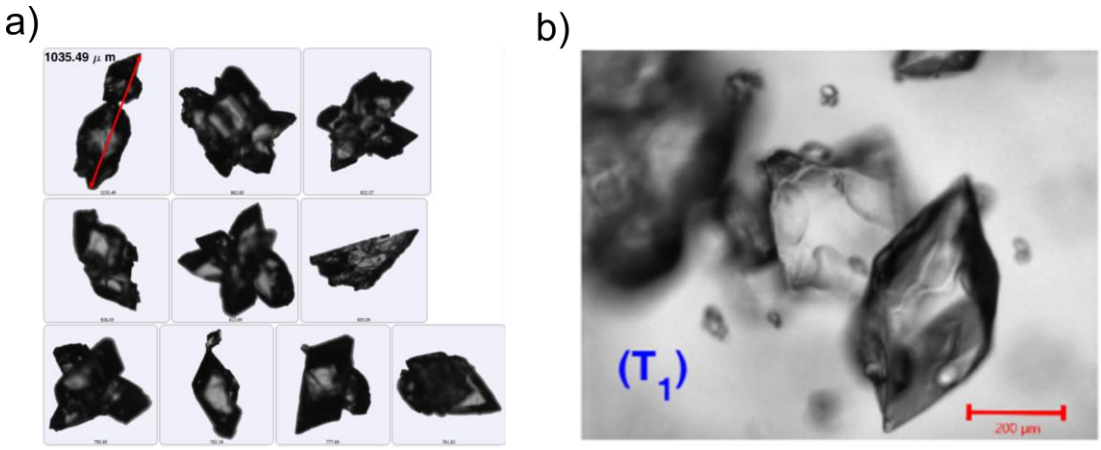

Figure 6.9 Sample starting material images for acetaminophen. a) image object collected via Morphologi G3 instrument with a length of 105.49 μm is indicated with the red arrow b) image collected at the start (T_1) using the inline PVM sensor.

Hence the peaks of the estimated volume based PSDs from CLD and PVM images at T_1 are shifted to the left of the corresponding estimate of the starting material of acetaminophen obtained from the offline Morphologi instrument (Figure 6.10, (b)). In some other cases, particles that were initially separated could become agglomerated upon filtration and drying for offline analysis. This is obvious in the case of the milled product of benzoic acid. The PVM images (Figure 6.11, (T_5)) of the benzoic acid sample suggests that the particles were mostly separated at T_5 whilst in suspension. However, a significant amount of them had become agglomerated upon filtering and drying before offline analysis with the Morphologi instrument, as seen in Figure 6.12.

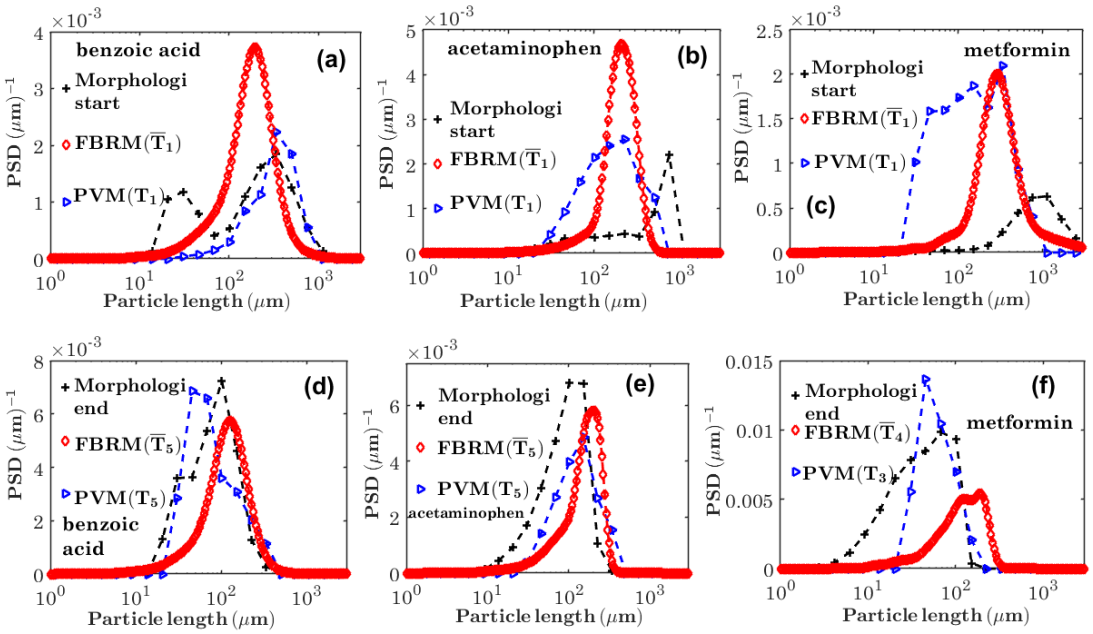

Figure 6.10 The volume based PSDs (a)-(c) estimated for the starting materials using data from the offline Morphologi instrument, CLD analysis $\overline{T}_1$, PVM image analysis at T_1, PVM image analysis at T_1, for each of the materials indicated. Similar estimates of the volume based PSDs at T_3, $\overline{T}_4$, $\overline{T}_5$, T_5, and for the milled products for each of the materials are shown in (d) – (f). The number of particles contained in the measured PSD for the starting material were 8428 (acetaminophen, (b)) and 18737 (metformin, (c)) from the Morphologi instrument. For the final milled material, the number of particles were 31050 (acetaminophen, (e)) and 7401 (metformin, (f)). From the PVM sensor, the number of images captured and analysed at T_1 for acetaminophen (b) was 361 and 150 for T_5 (e). The number of images captured and analysed at T_1 for metformin was 2103 (c) and 1899 for T_3 (f). From PVM image analysis, the number of particles contained in the measured PSD for T_1 were 1799 (acetaminophen, (b)) and 3540 (metformin). For acetaminophen at T_5 (e) the number of particles were 887 and for metformin at T_3 were 1007. The number of particles in the measured PSD from imaging for benzoic have been stated in Figure 6.2 & Figure 6.8.

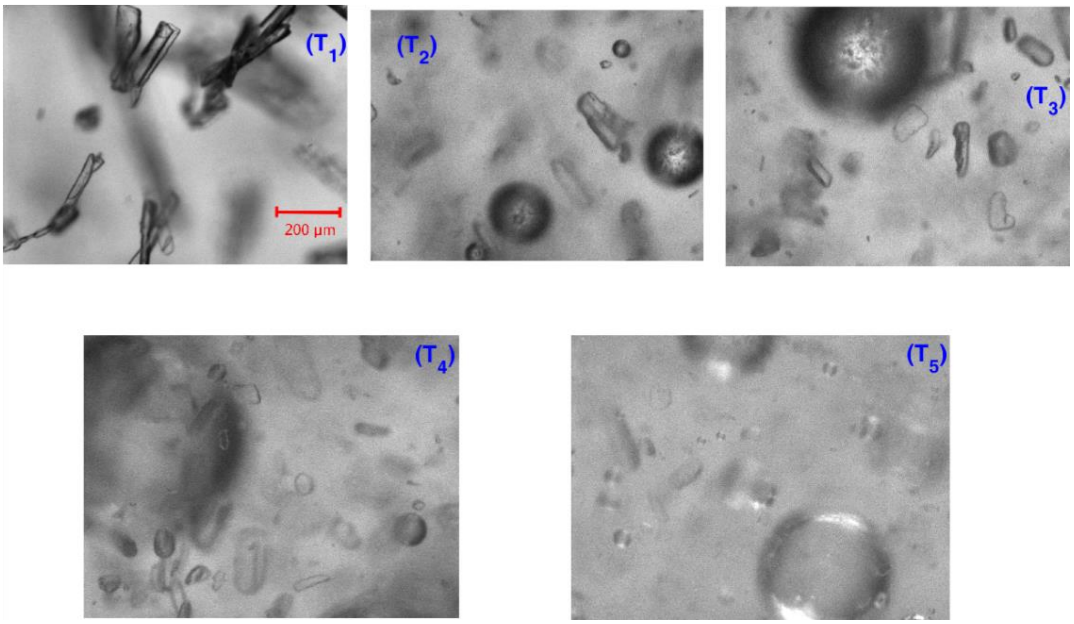

Figure 6.11 Some sample images collected using the inline PVM sensor during the wet milling of benzoic acid. The images were collected during the stages T_1 and T_5 of the process as indicated in the images.

Figure 6.12 Sample images obtained with the offline Morphologi instrument for the benzoic acid starting material. The object on the left indicated with the double red arrow has a length of 301.7 μm.

6.4.4.2. Limitations of CLD Analysis

The idealised CLD model (Li and Wilkinson, 2005) used in this work assumes that all particles lie on the focal plane of the laser spot of the FBRM instrument, and that the laser spot makes a straight chord on the particles. However, as the length dimensions of the particles become comparable to the diameter of the circular laser beam (the FBRM G400 used in this work has a diameter of 5.3 mm), the curvature of the chord becomes more pronounced and the relationship between the particle size and shape and the corresponding CLD becomes less accurate as the particle length increases.

This situation particularly arises in the case of the starting material of metformin in Figure 6.13. The sample image of the starting material of metformin (Figure 6.13, (a & b)) suggests the presence of particles of lengths $\approx$ 3000 μm. These lengths dimensions are not accurately represented in the CLD data, so that the peak of the volume based PSD estimated from CLD analysis at T_1 is shifted to the left of the corresponding estimate using the offline Morphologi instrument. This is seen in Figure 6.10 (c). There is also the possibility that some of these long rod-like particles were broken upon suspension and agitation, so that their contribution to the CLD data is reduced.

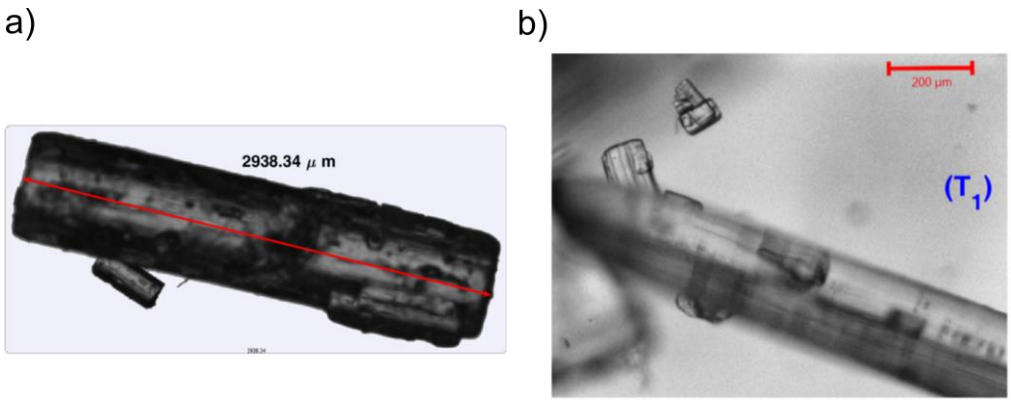

Figure 6.13 Sample starting material images for metformin HCL. a) image object collected via Morphologi G3 instrument with a length of 2938.34 μm is indicated with the red arrow b) image collected at the start (T_1) using the inline PVM sensor.

Another issue with CLD analysis is the situation where objects are transparent to the laser beam. There was a significant amount of bubbles produced during the wet milling of the benzoic acid sample, as seen in the PVM images (Figure 6.11) from T_2 to T_5. Even though these bubbles are not crystalline particles, they contribute to the chord count of the FBRM sensor. Because the bubbles are transparent to the laser beam, they lead to chord splitting (Heinrich and Ulrich, 2012, Kail et al., 2007) at their boundaries. This could lead to an artificially high count of shorter chords, and hence to an over estimation of fines in the estimated volume based PSD from CLD analysis.

The CLD modality is inherently biased towards larger particles (Agimelen et al., 2015). This leads to a situation whereby when there is a significant proportion of larger particles in a suspension. Therefore, the aspect ratio predicted from CLD analysis becomes biased towards that of the larger particles. This is clearly demonstrated in the case of metformin. Analysis of CLD data for metformin suggests an aspect ratio of r = 0.3 at both $\overline{T}_1$ and $\overline{T}_4$ as indicated in Figure 6.7 (b & c). The peak of the volume based 1D aspect ratio distribution (Figure 6.4) from Morphologi for metformin occurs at about 0.45 for the starting material. However, the corresponding estimate for the milled product shows a shoulder covering around 0.55 to 0.85. When this data is represented on a number basis (Figure 6.14), the peaks of the estimated 1D aspect ratio distribution from Morphologi for metformin almost coincide at 0.75.

This situation occurs because the metformin sample contains a significant amount of fines as seen in Figure 6.15. As the CLD modality is biased towards larger particles, which are more elongated in this case, the estimated aspect ratio of r = 0.3 at $\overline{T}_1$ is closer to the position of the peak of the 1D aspect ratio distribution from the Morphologi on volume basis rather than on number basis. This is because the smaller particles, which dominate the number based distribution, are more rounded than the larger particles.

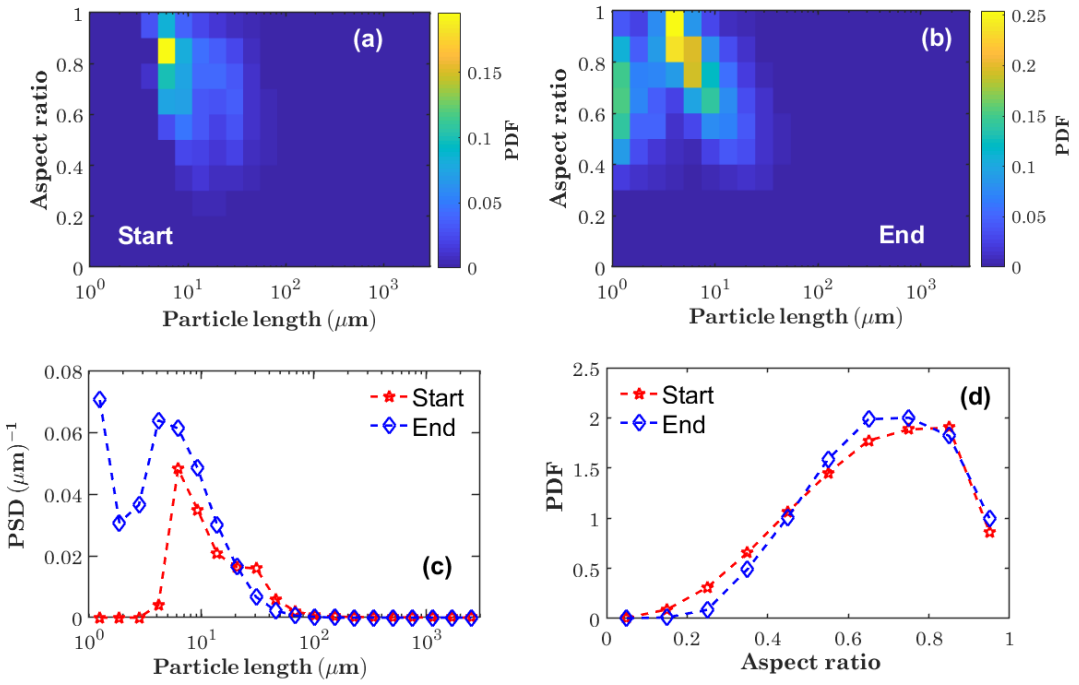

Figure 6.14 2D number based probability density function (PDF) of particle length and aspect ratio for the starting material (a) and the final milled product (b) for metformin from the offline Morphologi instrument. Corresponding 1D number based particle length distributions (c) and 1D number based aspect ratio distributions (d) of the starting material and the final milled product for metformin.

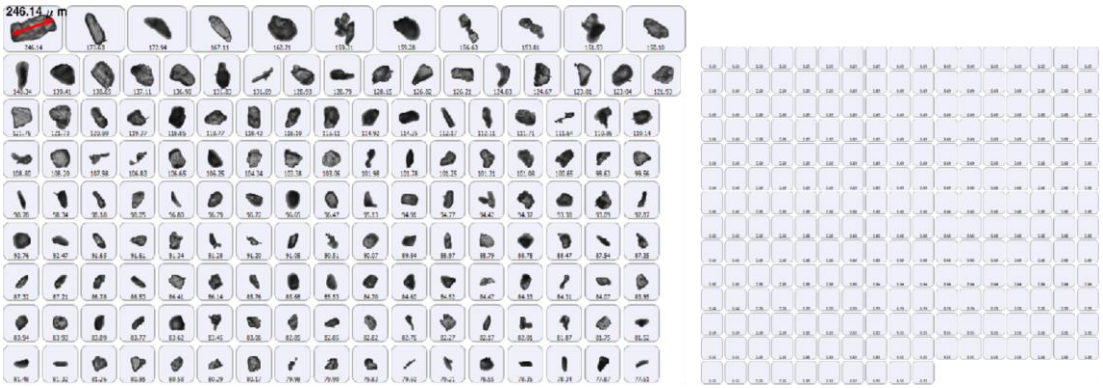

Figure 6.15 Some of the particles in the milled product (obtained with the offline Morphologi instrument) of metformin are shown in the images. The object indicated with the red double arrow has a length of 246.14 μm.

6.4.4.3. Limitations of Inline Image Analysis

Analysis of images captured with inline instruments such as the PVM comes with a number of challenges. One issue is objects not being in the focal plane of the camera (Cardona et al., 2018). Even though the image processing algorithm used in this work has a focus threshold, which allows objects captured out of focus to be rejected, some of these objects still get accepted when they just meet the criteria used for acceptance. Similarly, some objects are only captured partially in focus, so that only a part of the object's boundary will be detected. The size and shape of these objects captured out of focus or partially in focus are not well represented in the data. This situation contributes to the aspect ratios estimated for the three samples at both T_1 and T_5 extending up to 1, as seen in Figure 6.8 for benzoic acid, and in Figures 11 - 14 of the supplementary information (Agimelen et al., 2018b) for acetaminophen and metformin respectively. Another factor contributing to the aspect ratio distribution extending to 1 at both T_1 and T_5 is that the suspensions contained a significant amount of fines as seen in the PVM images (Figure 6.11 & Figure 6.17). These fines are mostly more rounded than the larger more elongated particles.

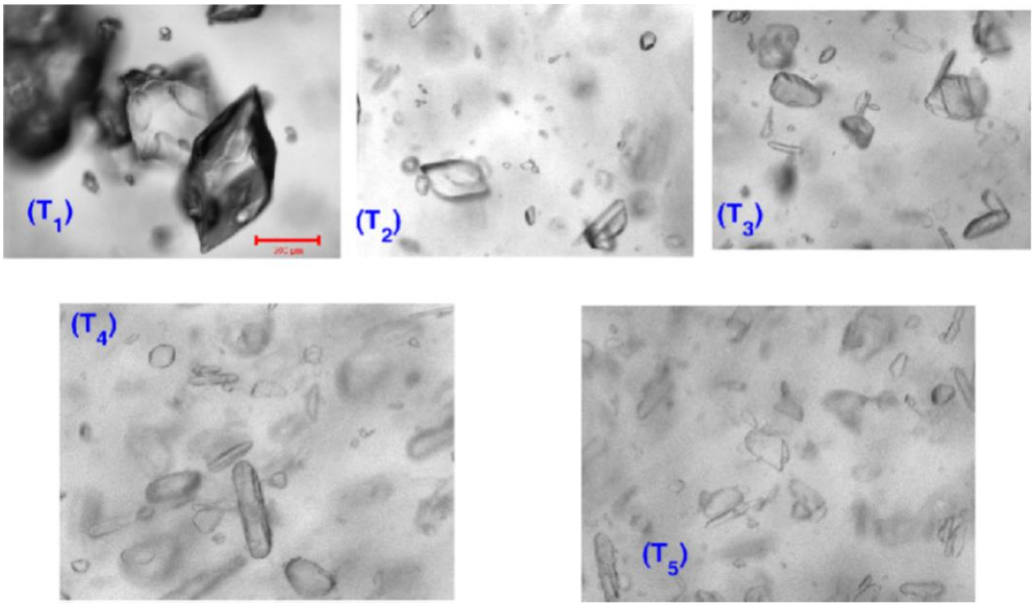

Figure 6.16 Some sample images collected using the inline PVM sensor during the wet milling of acetaminophen.

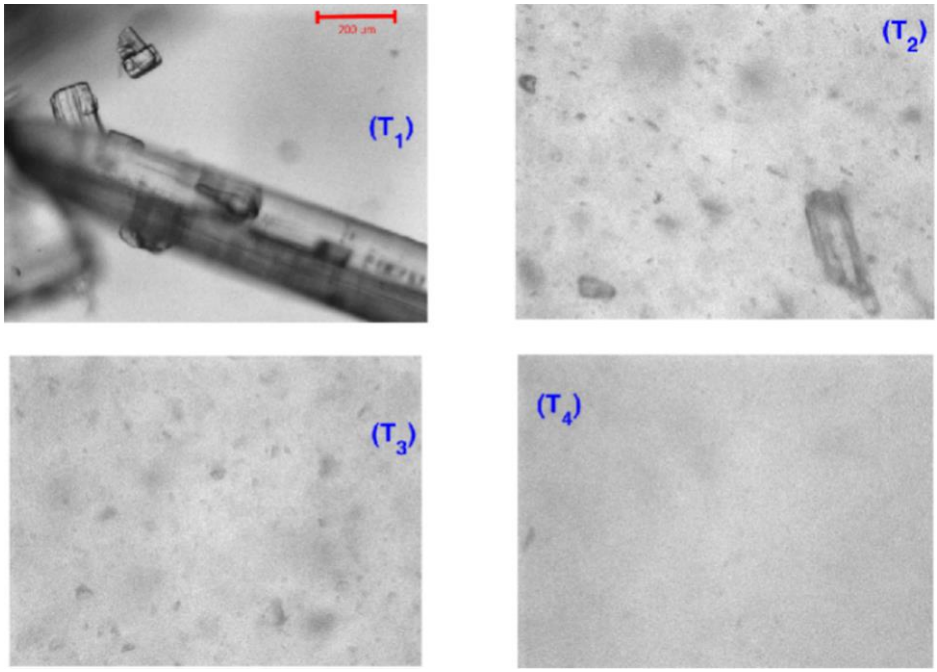

Figure 6.17 Sample images for metformin. The wet milling process for metformin was terminated at stage T_4 as the inline PVM images had almost become blank at the latter part of this stage.

Another limitation of image analysis is the case of objects touching the edge of the image frame. These objects are rejected from the analysis. This leads to a situation where the estimated PSD from image analysis is biased towards smaller particles when there is a significant amount of large particles touching the image frame. This effect is more pronounced in the case of metformin at T_1, where the estimated volume based PSD from PVM images is shifted to the left of the corresponding estimate of the starting material of metformin obtained with the offline Morphologi instrument (Figure 6.17). However, as mentioned earlier, it could also be that some of the long (with lengths $\approx$ 3000 μm) rod-like particles in the starting material of metformin may have broken to smaller particles upon suspension and agitation.

All images are affected by a resolution limit of the camera used, whereby small objects that are too close to the resolution limit are no longer distinguishable from the background noise of the image. As these objects are removed from the analysis, the fines could become under estimated if there is a significant amount of small particles in suspension. This is the reason all the particle sizes estimated from PVM images in this work have a cut-off close to 25 μm as seen Figure 6.8 & Figure 6.10.

This effect is even more pronounced in the case of metformin where it was virtually impossible to see objects in the PVM images at T_4 (Figure 6.17) where the captured images are virtually blank. Hence, analysis of images captured at T_4 for metformin was not done in this work. That is why the

volume based PSD for metformin (Figure 6.10, (f)) was estimated at T_3. This effect is also seen in the estimated relative mean number of objects per frame ($\widehat{N}_{IMG}$) in Figure 6.18.

As the wet milling progresses, the number of objects detectable in images reduces due to the reduction in particle sizes, hence the value of $\widehat{N}_{IMG}$ shows a small decrease after an initial increase. This is seen in the case of metformin shown in Figure 6.18 (c).

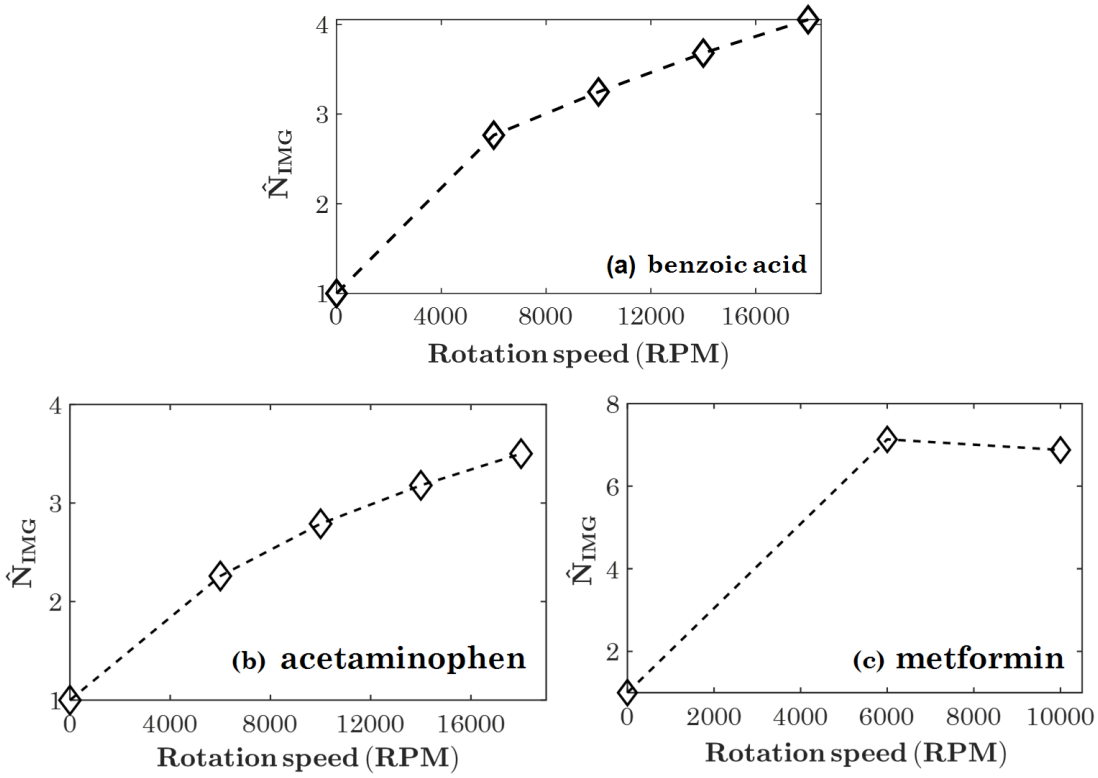

Figure 6.18 The relative number of objects per frame $\widehat{N}_{IMG}$ estimated from the images captured with the inline PVM instrument over time covering the period T_1 to T_5 for benzoic acid & acetaminophen and T_1 to T_3 for metformin are shown by the symbols.

6.4.5. Effect of Mill Rotation Speeds on Particle Size

The results shown in the previous sections show an overall decrease in particle size as a result of the wet milling. This decrease is reflected in all the PSDs estimated from CLD and both inline and offline images. The decrease in particle size and corresponding increase in particle number is also reflected in the estimated mean number of objects per frame $\widehat{\mathrm{N}}_{\mathrm{IMG}}$ (from inline images) as a function of rotation speed. This is shown in Figure 6.18. This is similar to the situation observed in $\widehat{\mathrm{N}}_{\mathrm{CLD}}$ in Figure 6.5 (a).

In order to accurately capture the increasing number of smaller particles as rotation speed increases, we counted all objects in images rather than just those in focus, as the number of objects detected in focus reduce with decreasing size near the resolution limit (which is around 25 μm here). Taking only objects in focus would lead to a reduction of the mean number of objects per frame, although this may eventually happen if particles become too small to be resolved by the camera.

In Figure 6.19 we can see the dependence of the volume weighted mean particle length D_{43} as a function of wet mill rotation speed, estimated from both CLD data and inline images, together with values from offline analysis estimated before and after milling. There is a good agreement between results from the two inline methods in all three cases (Figure 6.19) and between inline and offline measurements.

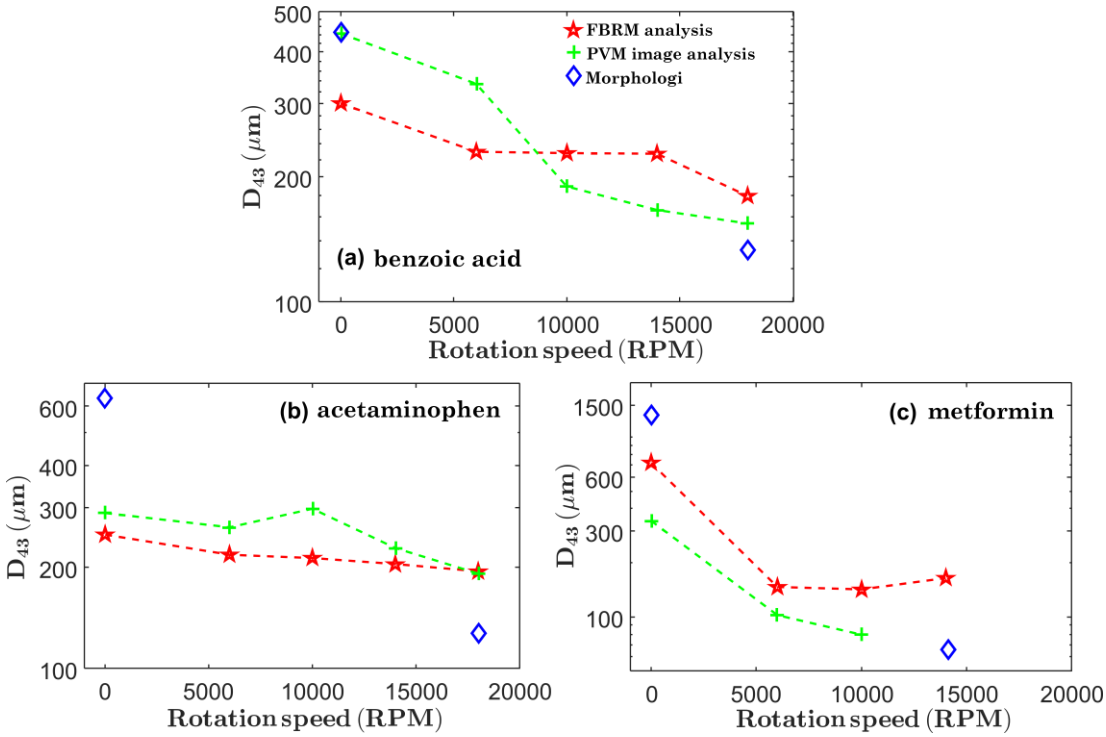

Figure 6.19 Estimated D_{43} values of particle length for the three materials using the three modalities as indicated. The estimates from the offline Morphologi instrument are added just for comparison as the particles were not in suspension during the measurement.

In the case of metformin, the estimated D_{43} value of the starting material obtained from Morphologi is more than double the corresponding values from inline CLD and PVM (Figure 6.19, (c)). This is because of the long rod-like particles of order 3000 μm in the starting material of metformin. These particles were out of the range of measurements of FBRM and PVM as discussed earlier.

A similar situation is seen with acetaminophen. The agglomerates present in the starting material of acetaminophen (Figure 6.9) causes the estimated D_{43} value of the starting material to be about double those of the

estimates from inline CLD and PVM images at 0 rpm (Figure 6.19, (b)). Furthermore, the estimated D_{43} value of the milled product of acetaminophen is about half the values estimated from inline CLD and PVM images. This could have been due to generation of fines during filtration and drying of the milled paracetamol.

Finally, we can also see that the mean particle size dependence on wet mill rotation speed between 6000 and 14000 rpm is relatively gradual for both benzoic acid and acetaminophen, while for metformin there is a very large decrease in the mean size after the lowest rotation speed (6000 rpm) is applied, followed by relatively little change afterwards. This indicates that material properties of crystals and solvents used are likely to play a significant role in performance of high shear wet mills in pharmaceutical manufacturing.

6.5. Summary

Recently developed computational tools were employed for estimating particle size and shape distributions from inline CLD and imaging data to study changes in particle size, shape and number in slurries during wet milling with variation in milling speed. The estimates from the inline instruments to corresponding estimates from offline analysis were also compared. The results show that these tools are suitable for obtaining quantitative estimates of particle size and shape distributions and number of particles in slurries. This is consistent with previous results (chapter 4). However, some inconsistencies were observed between estimates from

inline and offline measurements, and possible reasons for the discrepancies were discussed. The ability to capture changes in the quantitative particle attributes mentioned above show the promise that these tools hold for aiding modelling and control of crystallisation processes. The quantitative PSD and shape information obtained inline and in real time can be used to tune kinetic parameters in population balance models for crystallisation processes, accounting for time dependence of kinetic process parameters.

The results also reveal some of the challenges of estimating PSD from data captured with inline instruments. Inline imaging is limited to particles of certain minimum sizes due to camera resolution limits and out of focus rejection requirements for image processing algorithms. In addition, the PSD estimated by inline imaging becomes less representative as the sizes of the particles approach the size of the image frame. Similarly, the measured chord length from the FBRM sensor becomes less accurate as the length of needle-like particles approach the diameter of the circular trajectory of the FBRM laser spot. Also, CLD data could be affected by chords measured from bubbles present in the process. The CLD data could also become unrepresentative when there is significant chord splitting at the edges of the particles. Approaches for combining both CLD and imaging data in a multi-objective optimisation approach are being explored in further work in order to improve the robustness and accuracy of estimated PSD from inline CLD and imaging data.

Chapter 7

Industrial Case-Study. Demonstrating the Influence of an Indirect Ultrasound Strategy on Particle Size, Shape and Nucleation of APIs

This chapter is a result of an industrial placement held at Takeda Pharmaceuticals (Boston, USA) in collaboration with The University of Strathclyde (CMAC)

7. Demonstrating the Influence of an Indirect Ultrasound Strategy on Particle Size, Shape and Nucleation of APIs

7.1. Introduction

The application of ultrasound for particle engineering of pharmaceutical compounds has shown potential for accelerating nucleation kinetics (Ruecroft et al., 2005, Devarakonda et al., 2003), affecting breakage rates (Zeiger and Suslick, 2011) and achieving the de-agglomeration of particle suspensions (Cote and Sirota, 2010). To affect these mechanisms, acoustic energy generated from a horn in direct contact leads to cavitation in the process solution. However, this can also be achieved via indirect means for instance, transfer of ultrasound through an external medium. Ultimately, the application of ultrasound for process intensification can allow for particle attributes such as size and shape to be tailored to desired specifications which can improve downstream processing (Price, 2017). An overview of ultrasound principles & mechanisms for affecting crystallisation is discussed in chapter 1 (1.3.3).

7.1.1. Particle Size and Shape Control

Direct ultrasound application was demonstrated by Kim et al (Kim et al., 2003) for simultaneous size reduction and shape manipulation with subsequent temperature cycling for plate-like and needle-like habits which improved particulate processing (Figure 7.1). A recent study outlined the recommended operating modes for direct ultrasound either through continuous, single-pulse or multiple-pulse modes for PSD control

which was investigated on piracetam, acetaminophen and ibuprofen (Ramisetty and Rasmuson, 2018). The results highlighted that operating in multiple-pulses reduced energy consumption and generated smaller particle sizes with a narrower PSD in comparison to continuous and single-pulse modes (Ramisetty and Rasmuson, 2018). Further implementation of a direct ultrasound probe horn in "flow" for continuous generation of seed particles for batch and continuous crystallisation processes has also been shown useful for product attribute control (Siddique et al., 2015, Cote and Sirota, 2010).

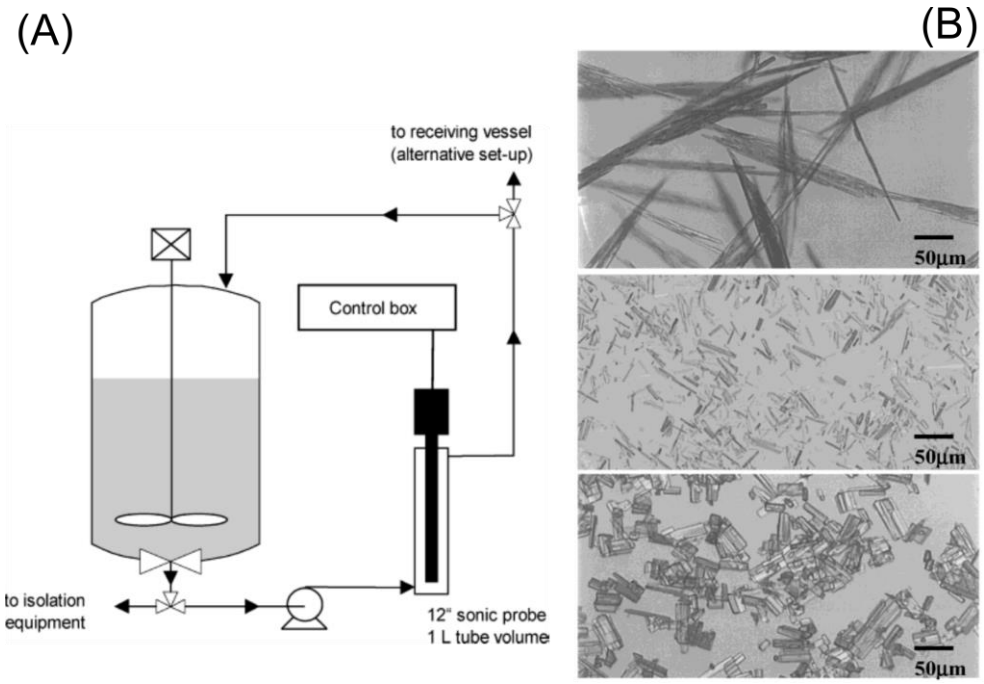

Figure 7.1 Schematic of inline sonication (direct) setup in a recycle scale-up process (A). Needle-like crystals of a BMS compound as crystallised (top); the particle length of the needles were reduced by application of ultrasound in the crystal slurry (middle); subsequent series of temperature cycling and ultrasonic treatment produced "brick-like" morphology (bottom) (B) (Kim et al., 2003).

7.1.2. Limitations of Direct Ultrasound

The insertion of an ultrasound probe horn in direct contact with a liquid medium is most commonly used however has well reported limitations (Sander et al., 2014). The most common issue being surface erosion leading to particle shedding which can affect the drug substance quality through incorporation of particulate metal impurities (Price, 2017). Substantial temperature deviations due to heating effects from the probe horn can also occur when inducing compression and rarefaction of the liquid medium through ultrasonic propagation (Zhang et al., 2015). For example, the multiple-pulse method employed from Ramisetty & Rasmuson (Ramisetty and Rasmuson, 2018) generated a temperature increase of 1.8°C / min each time when pulsing was applied with an input power of 144 W / kg. Although improved product attributes were obtained, frequent temperature increases during crystallisation processes can lead to unwanted impact such as dissolution of crystals. Other issues can include excessive noise in the vicinity of health and safety implications and the rapid dissipation of energy transferred per unit volume which leads to inconsistent distribution of power in the processed sample (Sander et al., 2014, Ruecroft et al., 2005, Capelo-Martínez, 2009).

To avoid the limitations arising from direct contact of an ultrasound probe with a liquid medium, alternative approaches through indirect ultrasound transfer have been described for crystallisation process development.

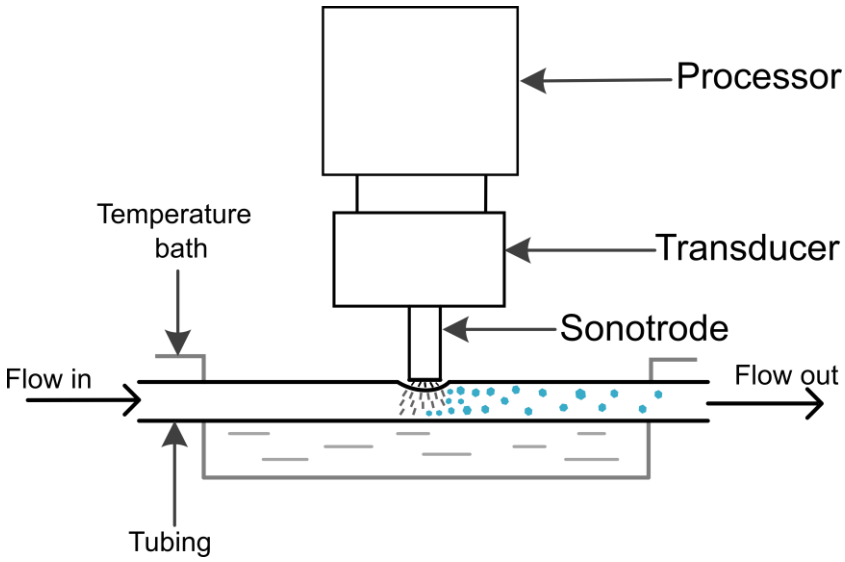

Figure 7.2 Sketch of an indirect ultrasound method for inducing nucleation of a supersaturated solution through directly pressing a probe horn on a tube. The tube is placed in a water bath for temperature control. This approach generated a spatially localized zone through maximising ultrasonication energy transferred per unit volume with the solution. From this, continuous generation of seed crystals was achieved (Jiang et al., 2015).

A typical indirect approach involves pressing an ultrasound probe on the outer part of a tube to induce nucleation through cavitation as shown in Figure 7.2 (Jiang et al., 2015, Eder et al., 2012). So whilst an indirect approach shows promise, publications surrounding the intensity and consistency of ultrasound energy from various devices to affect the crystallisation of APIs and control of critical quality attributes (CQA) is limited. Ideally, the goal is to generate a reliable target population of seeds with controlled attributes via specific ultrasound energy input whilst avoiding temperature increase and particle shedding. Demonstrating the

performance of an easy to use, indirect ultrasound process with practical applications for commercial scale use would be of great interest.

7.1.3. Aim of Case-Study

In this work, indirect ultrasound is explored as a viable and robust means for particle engineering of APIs. A semi-continuous platform which applies indirect ultrasound for inducing nucleation, particle size reduction and shape modification is investigated. The indirect process consists of an inline flow-cell generating intense ultrasonic vibrations via electrical stimulation (Figure 7.5). These mechanical vibrations are then transferred to a glass tube which in turn sonicate the incoming process stream.

Two APIs which have been found hard to nucleate with standard conditions were selected for this case-study (section 7.2.1). To establish key relationships between process parameters and product attributes, a series of isothermal desupersaturation experiments were conducted which monitored the impact of indirect power amplitude (0, 20%, 40% and 80%) on inline count profiles, chord length distributions (CLD), particle size distributions (PSD) and solution concentrations. Nucleation rates affected from ultrasound impact were then extracted through population balance modelling as a proof-of-concept demonstration. To our knowledge, this is the first study to test and implement this indirect ultrasound flow-cell strategy on APIs for nucleation acceleration and control of particle attributes. The overall platform integration and ease of operation were

additionally assessed for potential application in continuous manufacturing of pharmaceuticals.

7.2. Experimental Section

7.2.1. APIs

7.2.1.1. TAK-438

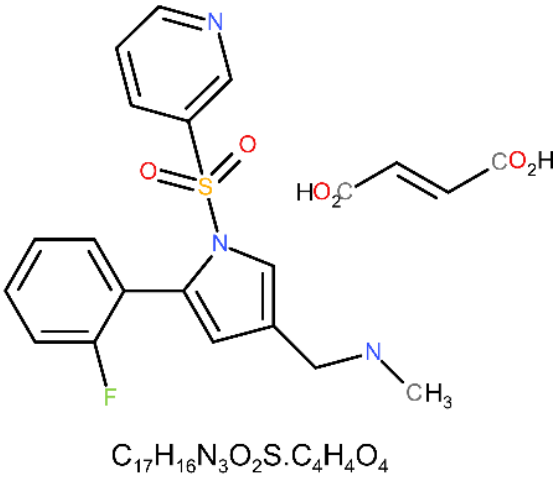

Figure 7.3 Recrystallised step affording TAK-438 with its chemical structure displayed (Li et al., 2018).

TAK-438 is a novel, orally active potassium-competitive acid blocker (P-CAB) and was synthesised by Takeda Pharmaceutical Company Ltd, Tokyo, Japan (Jenkins et al., 2015, Otake et al., 2016). It is currently in development for treatment for acid-related diseases such as gastric ulcer, duodenal ulcer and reflux esophagitis (Otake et al., 2016). The current crystallisation of TAK-438 is an unseeded batch cooling crystallisation which is dissolved in a methanol-water (70:30) solution (Figure 7.3). Upon crystallisation and isolation (filtration, washing, drying) of the crystalline

powder, offline jet milling is then employed to afford the final TAK-438 particle size

7.2.1.2. TAK-117

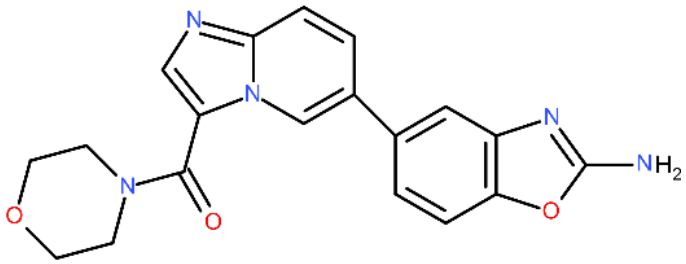

Figure 7.4 Recrystallised step affording TAK-117 with its chemical structure displayed (Durak et al., 2018).

TAK-117 is a selective PI3K*α* inhibitor. The manufacturing process relies on palladium (Pd)-catalysed Suzuki coupling reaction as the last bond-forming step (Durak et al., 2018). Recently, a revised crystallisation process for TAK-117 through temperature cycling in dimethyl sulfoxide (DMSO) was developed which greatly improved purity and recovery, physiochemical and bulk powder properties (Figure 7.4) (Durak et al., 2018).

7.2.2. Materials and Method

TAK-438 crystallisation was investigated in the solvent composition MeOH-H_20 (70:30) and TAK-117 was used in pure DMSO solvent (Figure 7.7). Both APIs were used as received from Takeda (Figure 7.3 & Figure 7.4). All solvents were purchased from Fisher-Scientific

(HPLC grade, > 99.5%). A 1 L stirred-tank glass reactor equipped with a heater-chiller unit (silicon oil as the circulating liquid) for temperature control, an overhead four-pitched blade glass agitator and an inline thermocouple for temperature monitoring was used for all experiments (Figure 7.6). A Mettler-Toledo inline FBRM probe (G400 series) for particle tracking and chord length distribution by laser back-scattering (iC FBRM V4.3) was also used.

The indirect ultrasound device consisted of a GDmini2 flow-cell (Heilscher, Teltow, Germany) with a glass tube (3.9 ml, ID: 0.15 inch) surrounded by a stainless jacket (Figure 7.5). The flow-cell is coupled with an UP200St-TD transducer (200 watts) generating intense ultrasonic vibrations with pressurized water (8 bar) for temperature control of the flow-cell. Thermocouples were inserted on the flow-cell inlet and outlet for temperature monitoring. The ultrasound was operated with continuous pulsing mode (100% cycle time) consisting of a working frequency of 26 kHz and investigated power amplitudes of 20%, 40% and 80% (Figure 7.5).

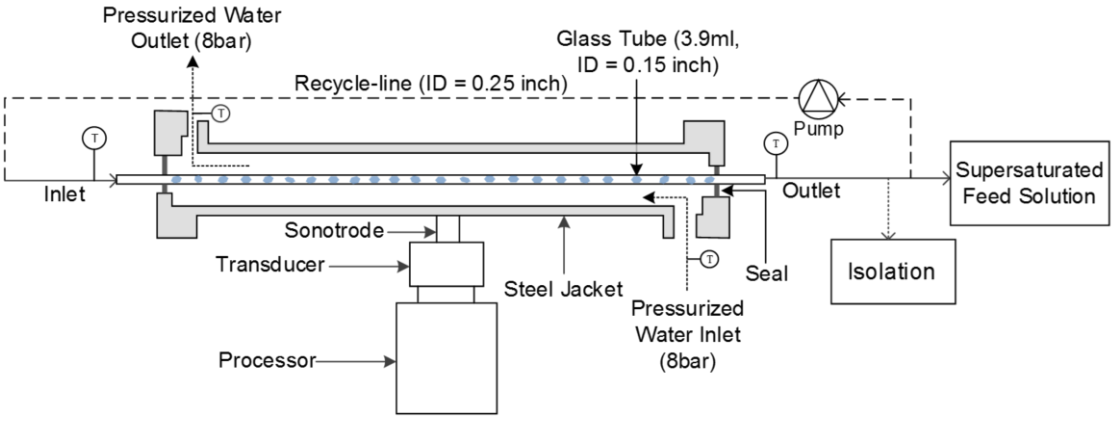

Figure 7.5 Sketch of the implemented indirect ultrasound flow-cell used in this study. Details surrounding the experimental procedure is described in section 7.2.4.

To calculate the power dissipated across the flow-cell, the following equation can be used:

$$P_{output} = \frac{P_{display}}{SA} \qquad \text{Eq 7.1}$$

From the above equation, $P_{display}$ is the observed power in watts (W) on the display unit which is a function of the set power amplitude. The surface area (SA) (m^2) was then calculated as the internal diameter and height of the flow-cell which was measured. This allowed for the ultrasound power output (KW / m^2) dissipated across the flow-cell as a function power amplitude (%) to be calculated. A list of the process parameters used in this study are shown in Table 7.1:

Table 7.1 List of investigated process parameters for the batch, recycle control and indirect ultrasound experiments.

API	Experiment type	C (mg/ml)	C_{sat} (°C)	T_{feed} (°C)	S (C/C_s)	V_{rate} (ml/min)	P_{amp} (%)	$P_{display}$ (W)	P_{output} (KW/m^2)
TAK-438	Indirect ultrasound	70	55.3	45	1.61	300	20, 40, 80	6, 15, 27	53.33, 133.1, 239.97
TAK-438	Recycle control	70	55.3	45	1.61	300	0	0	0
TAK-438	Batch control	70	55.3	45	1.61	0	0	0	0
TAK-117	Indirect ultrasound	20	76.4	35	3.09	300	40, 80	15, 27	133.1, 239.97
TAK-117	Recycle control	20	76.4	35	3.09	300	0	0	0
TAK-117	Batch control	20	76.4	35	3.09	0	0	0	0

7.2.2.1. Laser Diffraction Particle Size Method

A Malvern Mastersizer 2000 equipped with a wet dispersion unit (Hydro 2000s) was used for all particle size analysis. A manual measurement was undertaken for each sample. For TAK-438, refractive index = 1.52 and dispersant refractive index = 1.377 which was saturated 2-propanol with TAK-438. For TAK-117, refractive index = 1.52 and dispersant refractive index = 1.33 as water was used. TAK-117 was suspended in 1% w / w Triton X-100 in water to aid in particle dispersion prior to measurement. A dispersion unit speed of 1500 rpm, ultrasound 0 – 20%, sample measurement time of 10 s, 5 to 15% obscuration limit and three measurement cycles was carried out. Samples were added dropwise via transfer pipette to the wet dispersion unit to give the desired obscuration. Offline particle size distribution data was then exported from the raw files.

7.2.2.2. HPLC Concentration Method

A HPLC instrument (Agilent 1100 Series) and UPLC (Acquity, Waters) was used for all concentration measurements. All concentration measurements were carried by HPLC (Agilent 1100 Series) and UPLC (Acquity, Waters) using the method developed by Takeda. This included a UV detector at a wavelength of 230 nm and bandwidth of 4 nm. The column used was a symmetry C18.5 μm 4.5 x 75mm with the column temperature set at 25°C and a sample injection volume of 5 µL. The pump flow rate was 1 ml / min. The mobile phase consisted of a gradient of 0.1% formic acid in

H_20 (mobile phase A) and 0.1% formic acid in acetonitrile (mobile phase B). The initial ratio of mobile phase A to B was 90 / 10. This was changed to a ratio of 60 / 40 by 5 min and then increased to 90 / 10 by 6 min which was held until the end of the run. Concentration ranges for TAK-438 (0.0625, 0.125, 0.25, 0.5, 1 mg / ml, $r^2 = 0.9994$) and TAK-117 (0.03125, 0.025, 0.125, 0.25 0.5 mg / ml, $r^2 = 0.9989$) were selected for the calibration model development. Prior to HPLC analysis, MeOH-H_20 (70:30%, v / v) was used as the diluent for TAK-438 (25 ml) and pure DMSO was used as the diluent for TAK-117 (25 ml).

7.2.3. Experimental Process

The experimental apparatus used is shown in Figure 7.6. Conditions used are detailed in Table 7.1.

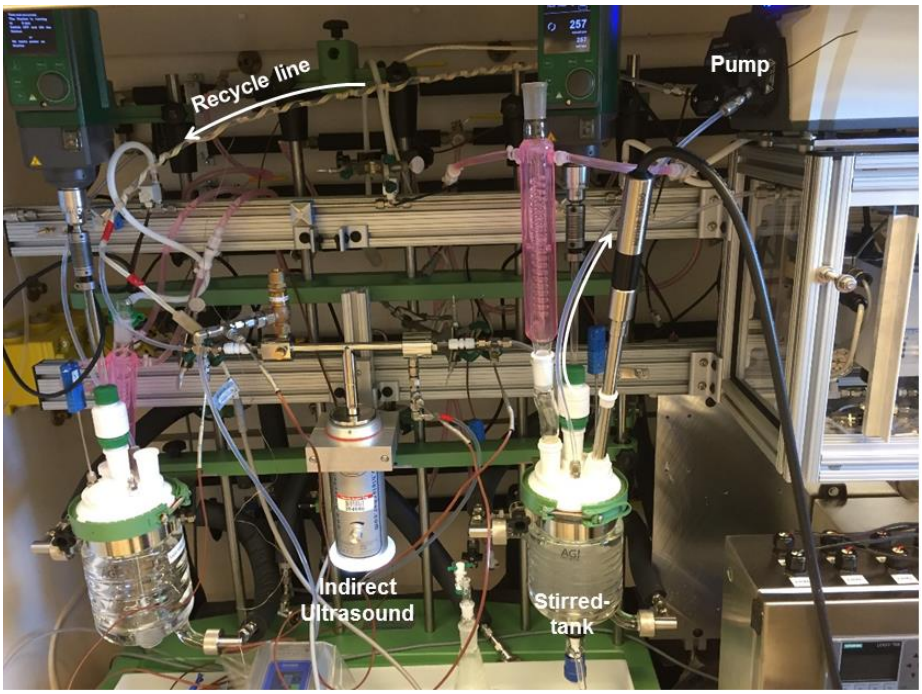

Figure 7.6 Experimental apparatus configured for this study in the process chemistry laboratory at Takeda Pharmaceuticals (Boston, USA).

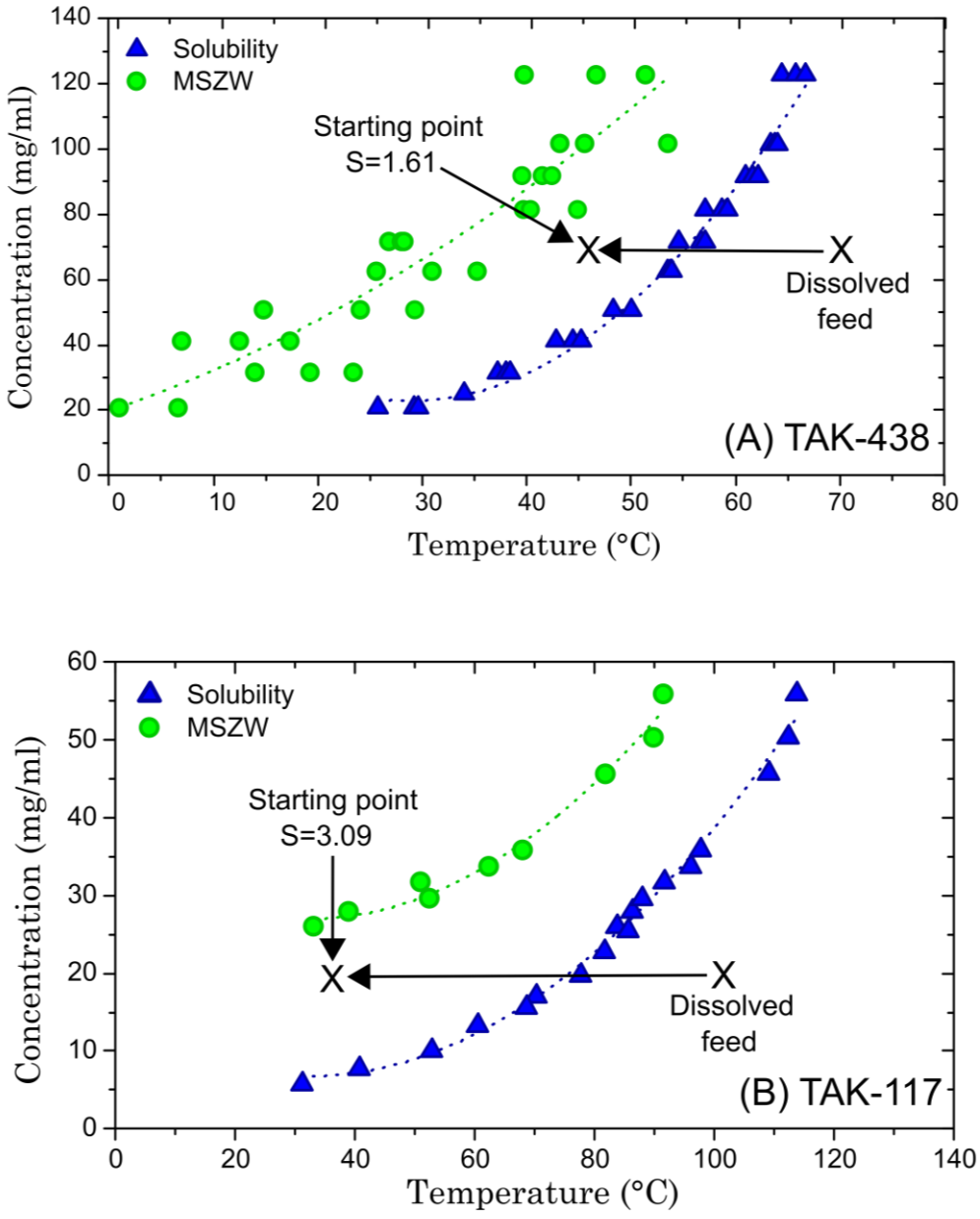

Figure 7.7 Measured solubility profiles obtained by Crystal16 instrument. TAK-438 in 70:30 (MeOH-H_20) mixture (unpublished results, (A) and TAK-117 in DMSO (Durak et al., 2018) (B) were used for each experiment.

7.2.4. Experimental Procedure

The APIs were both dissolved at their relevant compositions (TAK-438 = 70 mg / ml & TAK-117 = 20 mg / ml) and heated above their saturation point (C_{sat}) with agitation (250 rpm) to ensure rapid dissolution (Figure 7.6 & Figure 7.7). The solution was held at this temperature for up to 1 hr to ensure all particles were dissolved. FBRM was inserted in the stirred-tank vessel for particle tracking. The undersaturated solution was then slowly cooled down (20 - 30 min) to reach the desired supersaturation and held for an additional 30 min as annotated in Figure 7.7. The clear supersaturated solutions were then recirculated (T_{feed}) through a peristaltic pump (Masterflex L / S, ID = 0.25 inch, Figure 7.6) with the recycle line consisting of silicone tubing with trace-heating (Figure 7.5 & Figure 7.6). The pressurized-water jacket (8 bar, 10°C) attached to the ultrasound flow-cell (Figure 7.5) was started 30 min prior to recirculation to ensure overall equipment temperature was equilibrated.

A. Indirect Ultrasound

For the indirect ultrasound applied experiments (20%, 40%, 80%), the solutions were recirculated continuously through the flow-cell. No amplitude was applied in the initial 30 min to 1 hr of recirculation for temperature stabilisation and to confirm the absence of primary nucleation. After this initial period, the desired ultrasound power amplitude was selected (Table 7.1) and applied in continuous mode at fixed supersaturation throughout the duration of each experiment.

B. Recycle Control

For the recycle control experiments (Table 7.1) the same supersaturation and experimental procedure was followed however no ultrasound power amplitude was applied. Therefore, the solution was continuously recycled throughout the process setup (Figure 7.6) and duration of each experiment. This control was to decouple the effect of indirect ultrasound application on the crystallisation of the API.

C. Batch Control

For the batch control experiments, the same supersaturation was used and held at constant temperature within the stirred-tank vessel from 48 h to 96 h with no recirculation and application of ultrasound power amplitude (Table 7.1). This control was to decouple both the recycle control and indirect ultrasound effect on the crystallisation of the API.

7.2.4.1. Sampling Procedure

Regular sampling was implemented throughout the duration of each experiment. For concentration analysis (section 7.2.2.2), slurry samples (5 ml) were directly withdrawn from the vessel and immediately filtered via syringe filter (0.2 μm) into a pre-weighed volumetric flask (25 ml). The relevant diluents for HPLC measurement were then used. For each sampling time, triplicates were taken for a consistency check. For particle size distribution analysis (section 7.2.2.1), 25 ml to 50 ml (depending on slurry density) was directly withdrawn from the vessel by a transfer

pipette and immediately filtered via vacuum filtration, washed (TAK-438 = MeOH-H_20 (70:30), TAK-117 = H_20) and dried in a vacuum oven overnight (40°C to 45°C). Dried samples were then further subjected for microscopic analysis.

7.3. Results and Discussion

The results obtained for each of the experiments (indirect ultrasound, recycle and batch control) are presented in this section. No seeding was used in this study.

7.3.1. Analysis of TAK-438

7.3.1.1. Induction Time

Analysis of Figure 7.8 (A & B) shows clear differences in total count trends and crystallisation behaviour from the tested experimental conditions (Table 7.1). The control (batch & recycle) experiments with a supersaturation of 1.61 consisted of a slow crystallisation as there was no ultrasound effect or seeding (Figure 7.8, (A)). For the batch control, the mean induction time was 90 ± 54 min whereas the recycle control was 180 min ± 15 (Table 7.2 & Figure 7.9). Although the recycle control had an unexpected 50% increase in induction time in comparison to the batch control, in some cases through further experimentation the batch control had nucleated after several days (2 to 5). This could be due to its unpredictability as seen from the large mean induction time standard error values (Table 7.2).

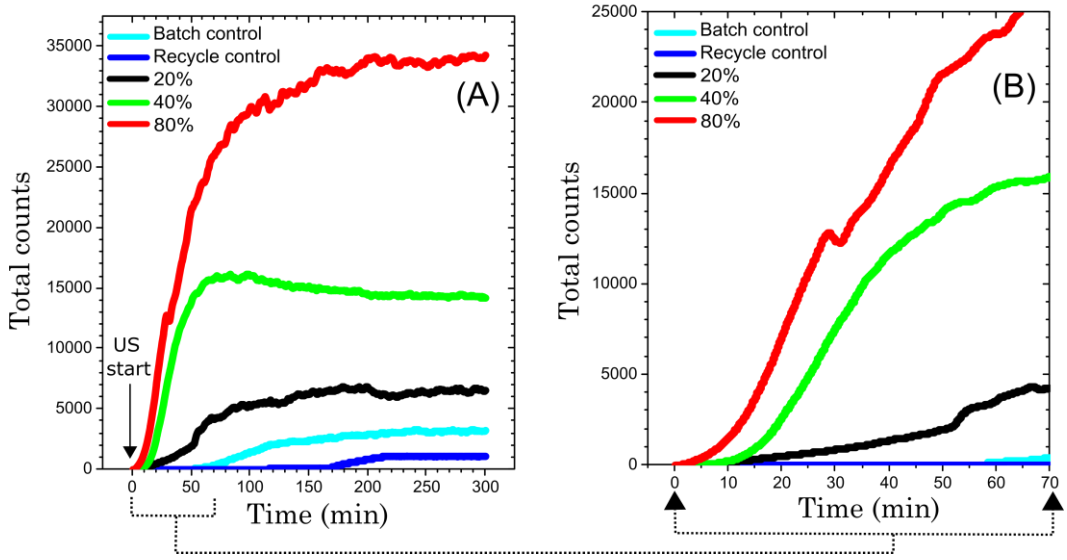

Figure 7.8 Total count profiles (macro view) obtained for TAK-438 over time. The impact of ultrasound start (20%, 40% & 80%) and control experiments (batch & recycle) without ultrasound start is shown on the same profile from 0 to 300 min (A). The early stages of total count increase (0 to 70 min) for each experiments is zoomed in (B). The onset of nucleation was defined as the induction time (T_{ind}) having more than a total counts of > 1000.

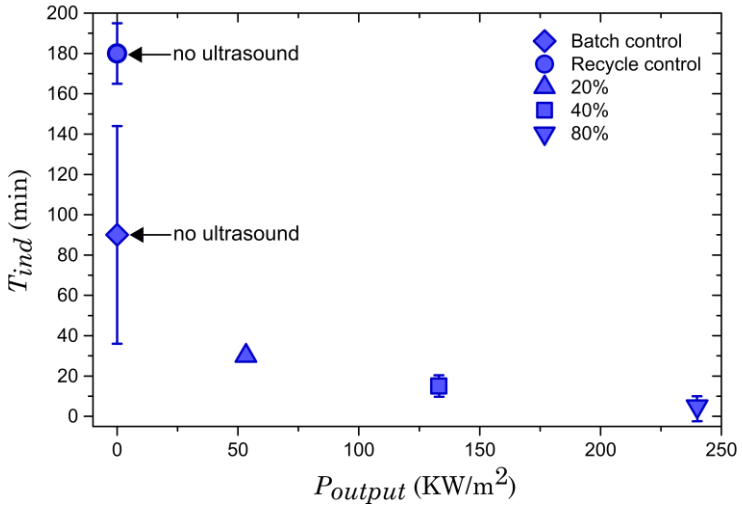

Figure 7.9 Induction time profiles for TAK-438 obtained from FBRM profiles (Figure 7.8) at different power outputs (Eqn 7.1). No power output is calculated for the control experiments as there was no ultrasound effect.

Table 7.2 Induction times for TAK-438 for each experimental condition is shown.

Experiment Type	P_{output} (KW/m^2)	T_{ind} (min)
Batch control	0	90 ± 54
Recycle control	0	180 ± 15
Ultrasound	53.33	30
Ultrasound	133.1	15 ± 2.5
Ultrasound	239.97	5 ± 5.51

When applying indirect ultrasound at the selected power amplitudes (Table 7.1) the effect of ultrasound had a considerable impact on the total count profiles in comparison to the control experiments (Figure 7.8, (A)). Increasing the power amplitude from 20% (53.33 KW / m^2) to 80% (239.97 KW / m^2) reduced the mean induction time from 30 min to 5 ± 5.51 min (Table 7.2, Figure 7.8 (B) & Figure 7.9). Selecting the highest power amplitude of 80% (239.97 KW/m^2) produced an instantaneous occurrence of nucleation within 5 min of ultrasound start (Table 7.2 & Figure 7.9). This generated a rapid increase in total counts from 0 to 200 min due to enhanced secondary nucleation which had levelled off from 200 to 300 min as supersaturation is depleted (Figure 7.8, (A)).

Similarly, whilst a rapid increase in total counts from ultrasound start is also seen for 20% and 40% (Figure 7.8, (A & B)), it was clear with increasing ultrasound power, the mean induction time decreases simultaneously (Table 7.2, Figure 7.8 (B) & Figure 7.9). The mean induction times consist of smaller standard error values (15 ± 2.5 min & 5 ± 5.51 min) with less spread in variability when applying ultrasound power

(133.1 KW/m^2 & 239.97 KW/m^2) in comparison to the control experiments (90 ± 54 min & 180 ± 15 min) (Table 7.2). This indicates that indirect ultrasound energy input facilitates and provides control over primary nucleation kinetics at fixed supersaturation for TAK-438.

7.3.1.2. Particle Size and Shape

The sampling method (described in 7.2.4.1) allowed for particle size distributions (Figure 7.10), Dv50s (Figure 7.11 & Figure 7.12) and shapes (Figure 7.13) to be tracked over time during the experimental process. As the control (batch & recycle) experiments nucleated slowly over time, final PSDs were only collected (Figure 7.10, (A)). The batch control had a final Dv50 of 116.9 ± 7.54 μm with a broad distribution (span = 2.05, Table 7.3 & Figure 7.10, (A)). The recycle control had a final Dv50 of 91.28 ± 2.31 μm with a narrow distribution (span = 1.81, Figure 7.10, (A)). As the recycle control achieved a smaller and narrower PSD in comparison to the batch control, this could be attributed to de-agglomeration of particles from the continuous recycling effect. This is illustrated in the microscopic images (Figure 7.13, (A & B)). Both control experiments maintained rod-like particle shapes (Figure 7.13, (A & B)).

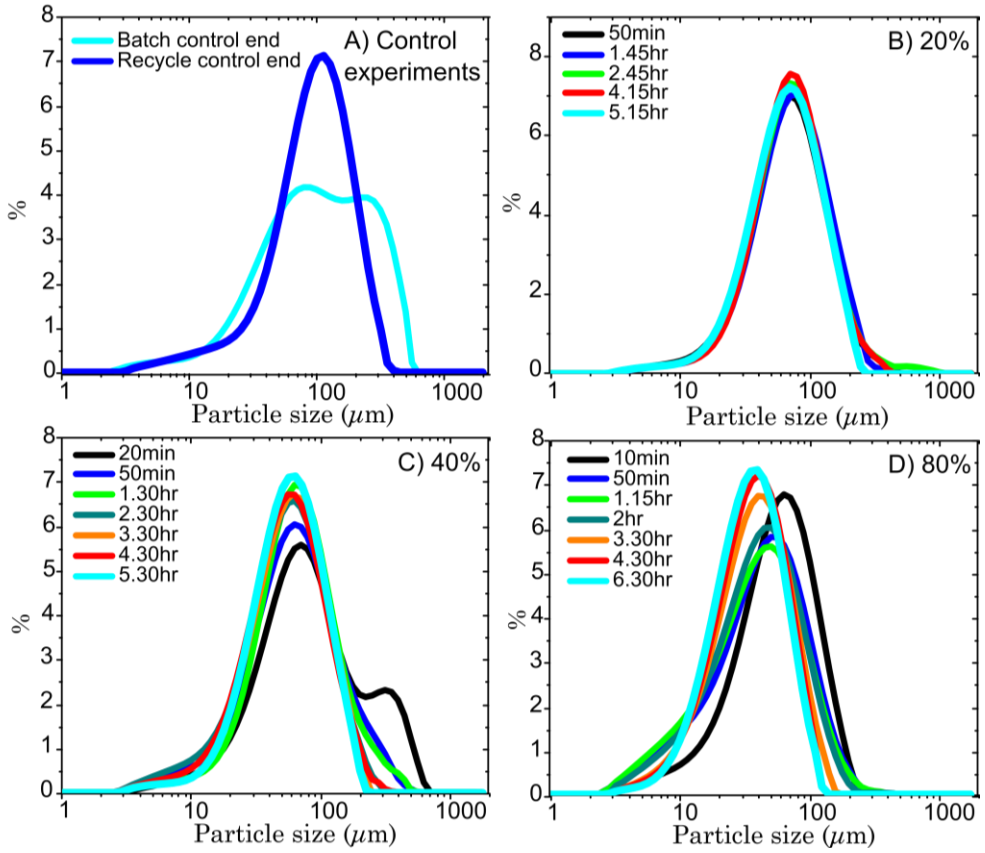

Figure 7.10 PSDs for control (batch & recycle) experiments (A) and PSDs for different ultrasound power amplitudes (20%, 40% & 80%) measured over time (B, C and D).

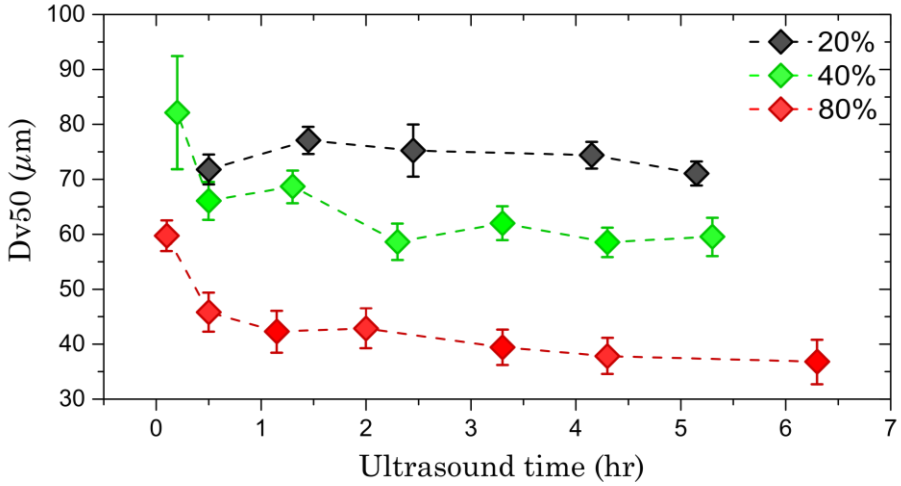

Figure 7.11 Offline Dv50 particle size measurements plotted over time for different ultrasound power amplitudes (20%, 40% & 80%).

Table 7.3 Final Dv50 and span values for each experiment is shown.

Experiment Type	Power amplitude (%)	Dv50 (μm)	StE	Span
Batch control	0	116.9	± 7.537	2.053
Recycle control	0	91.28	± 2.310	1.809
Indirect ultrasound	20	71.07	± 2.193	1.705
Indirect ultrasound	40	59.57	± 0.693	1.722
Indirect ultrasound	80	36.8	± 0.133	1.647

At 20% (53.33 KW / m^2) power amplitude, 71.80 μm (Dv50) during 50 min of ultrasound was achieved which remained constant from 50 min (71.80 μm) to 5.15 hr (71.07 μm) as seen in Figure 7.11. There was no substantial shift in PSD from 50 min to 5.15 hr (Figure 7.10, (B)). However, compared to the control experiments, a smaller final Dv50 of 71.07 μm with a tighter span (1.71) was produced for 20% power amplitude. No impact on particle shape was observed (Figure 7.13, (C & D)).

Increasing the power amplitude to 40% (133.1 KW / m^2) generated an initial Dv50 of 82.14 μm after 20 min of ultrasound which reduced to a final Dv50 of 59.57 μm after 5.30 hr (Table 7.3 & Figure 7.11). The reduction in particle size over time (reduced by 22.57 μm, Figure 7.11) is also seen from the PSD shift (right to left) in Figure 7.10 (C) which achieved a final span of 1.72. When operating at 80% (239.97 KW / m^2) power amplitude, a Dv50 of 59.74 μm after 10 min of ultrasound was produced. This reduced to a final Dv50 of 36.80 μm after 6.30 hr which was the smallest particle size

achieved from all conditions with a span of 1.65. 40% and 80% power amplitudes had also an additional effect on particle shape through the reduction in aspect ratio from rod-like to circular particles (Figure 7.13, E - H). Overall, when compared to the control experiments, increasing power amplitude produced smaller particle sizes with tighter spans (Table 7.3, Figure 7.10 & Figure 7.12) with a more pronounced effect on particle shape at high values (Figure 7.13, F & H).

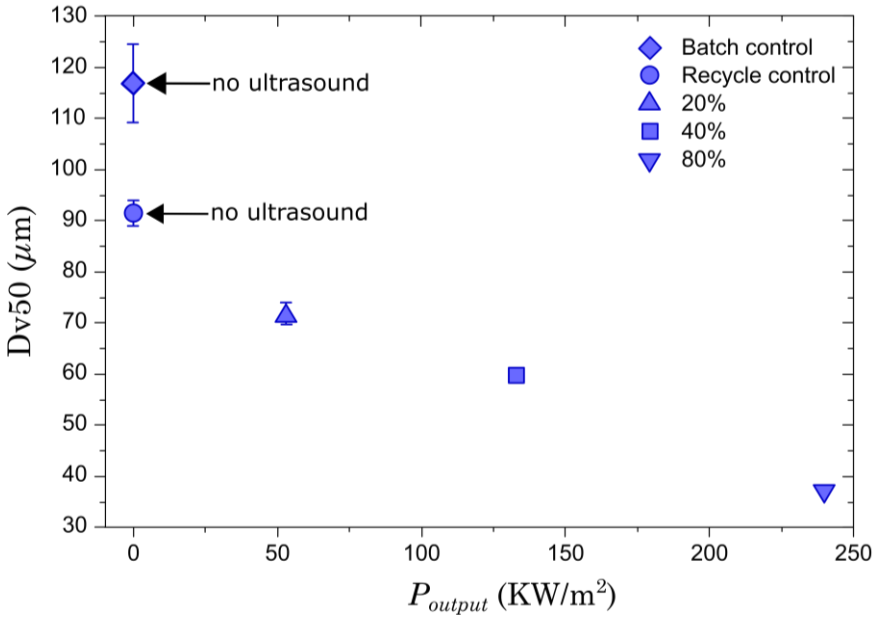

Figure 7.12 Comparison of final Dv50 particle sizes between controls (batch & recycle) and indirect ultrasound conditions (20%, 40% & 80%).

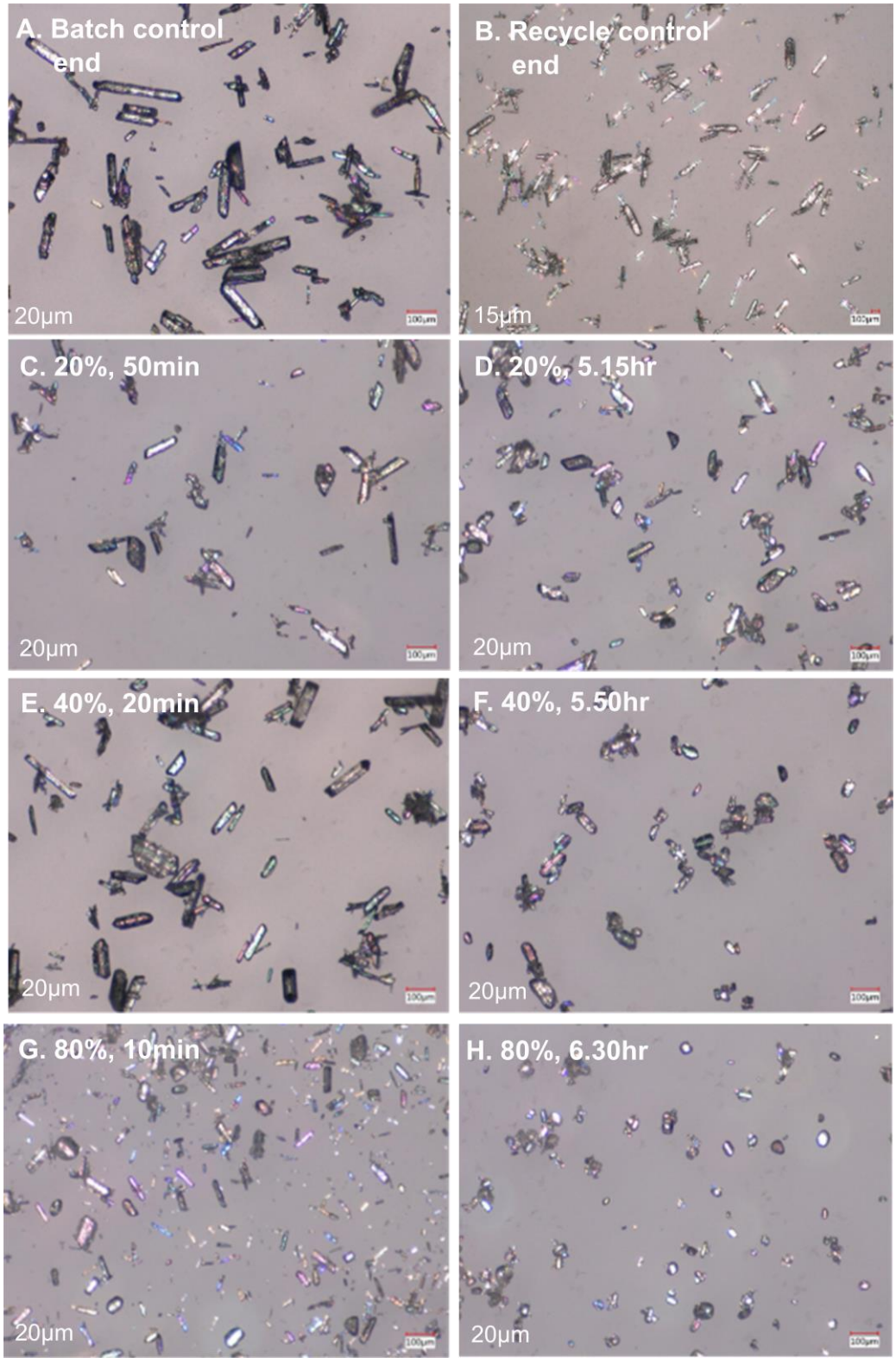

Figure 7.13 Obtained microscopic images for all experiments (A - H) at 20x magnification for majority of the analysed samples.

7.3.1.3. Concentration Profiles

The concentration profiles obtained for 20% and 80% ultrasound conditions show a rapid decline within 2 hours of continuous ultrasound after which a slow decrease from 3 to 6.30 hr is observed (Figure 7.14). For 80%, overall depletion of concentration was considerably quicker than 20% which approached the solubility at 40 mg / ml indicating desupersaturation (Figure 7.14). This was expected as 80% (239.97 KW / m^2) had a shorter mean induction time than 20% (Table 7.2) with increased nucleation kinetics (Figure 7.8, (A & B)) and the smallest final Dv50 of 36.08 μm (Table 7.3). As the experiments were conducted under isothermal conditions, supersaturation consumption is preceded upon the rapid nucleation burst at 80%. This is due to the available crystal surface area from nucleation after which supersaturation decreases as there is no available new surface area.

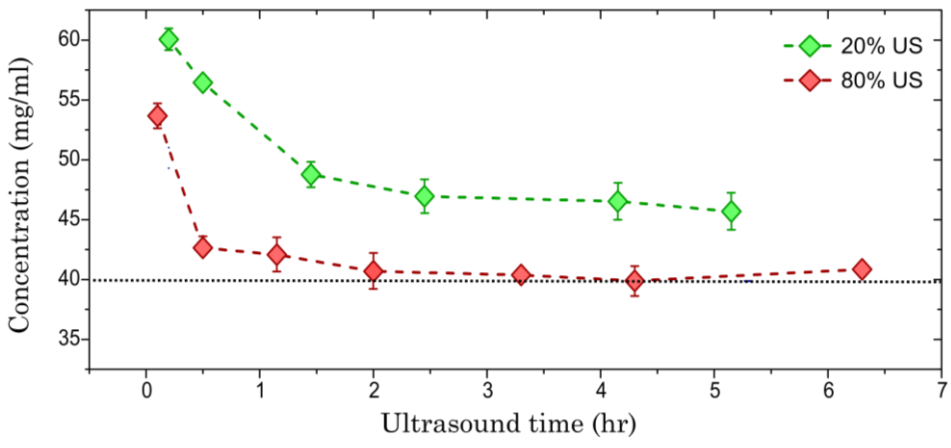

Figure 7.14 Concentration profiles obtained for indirect ultrasound conditions (20% & 80%) which was tracked over time.

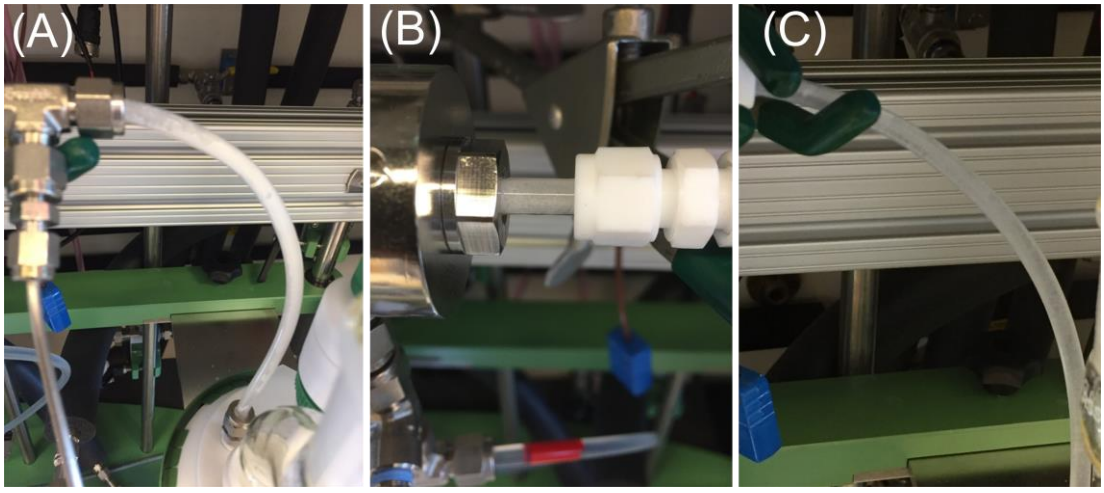

Figure 7.15 Process images of the ultrasound flow-cell outlet and tubing into the feed vessel (Figure 7.6). T°C monitoring was initially attached on the outlet which encountered excessive fouling as shown on the tubing (A). T°C monitoring was then removed on the outlet for experiments listed in Table 7.1 with a tubing changeover to minimise fouling effects (B & C).

From Figure 7.14, 20% remains above the solubility after 5 hr of ultrasound indicating a significant amount of time is required for desupersaturation. As noticed, the concentration profile for 40% was not shown due to unexpected observations which could have been due to several factors. These factors could have ranged from the error associated with the sampling method and time lag for concentration measurement via offline HPLC. Importantly, temperature gradients (5°C drop) were observed across the process setup from initial experimental tests leading to temperature losses and a strong fouling occurrence from ultrasound start shown on the flow-cell outlet (Figure 7.15, (A)). During the experiments, the flow-cell temperature was set at 10°C (vendor recommendation) which

may have added to the temperature loss effect throughout the course of the experiments.

To overcome the fouling effect (Figure 7.15, (A)), associated fittings were removed with a replacement tubing in place to enable quick tubing changeover if significant fouling had been built-up during the nucleation burst upon ultrasound start. Whilst there was no outlet temperature monitoring of the flow-cell for TAK-438, these measures enabled smooth and consistent experimental runs over a number of hours (0 to 6.30 hr) with minimal fouling (Figure 7.15, (B & C)).

7.3.2. Analysis of TAK-117

7.3.2.1. Induction Time

Analysis of Figure 7.16 (A) shows clear differences in total count trends and crystallisation behaviour from the tested conditions Table 7.1. For the control (batch & recycle) experiments, a long induction time of 360 min for the batch control is observed whereas a comparatively short mean induction time of 20 ± 5 (340 min reduction) was achieved for the recycle control (Table 7.4 & Figure 7.17). As observed (Figure 7.16, (A)), the application of indirect ultrasound at 40% (133.1 KW / m^2) and 80% (239.97 KW / m^2) had considerable impact on crystallisation kinetics in comparison to the recycle control. This is clear from the rapid total count increase from 0 – 200 min (80%) and 0 to 900 min (40%). Similar to the recycle control experiments, short induction times of 8.26 min (40%) and 14.26 min (80%) were achieved (Table 7.4 & Figure 7.17).

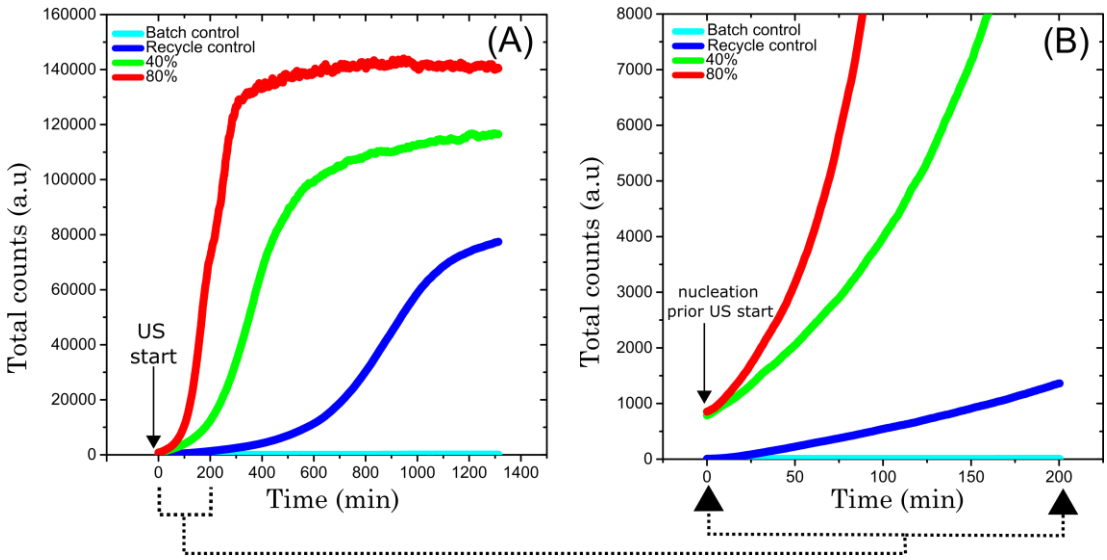

Figure 7.16 Total count profiles (macro view) obtained for TAK-117 versus time. The impact of starting ultrasound (40% & 80%) and the control experiments (batch & recycle) 0 to 1400 min (A). The early stages of total count increase (0 to 200 min) for each of the experiments is zoomed in (B). The onset of nucleation was defined as the induction time (T_{ind}) having more than a total counts of > 500.

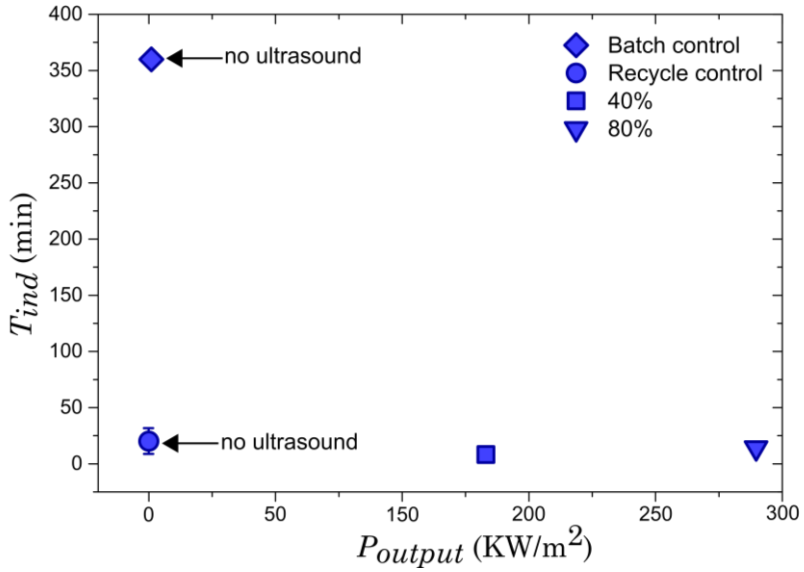

Figure 7.17 Induction time values for TAK-117 obtained from FBRM (Figure 7.16) at different applied power outputs (Eqn 7.1). No power output is calculated for the control experiments.

Table 7.4 Induction times for TAK-117 for each experimental condition is shown.

Experiment Type	P_{output} (KW/m^2)	T_{ind} (min)
Batch control	0	360
Recycle control	0	20 ± 5
Ultrasound	133.1	8.26
Ultrasound	239.97	14.26

Increasing ultrasound power amplitude from 40% (133.1 KW / m^2) to 80% (239.97 KW / m^2) did not correlate to a simultaneous decrease in induction time (Table 7.4). This was due to the occurrence of nucleation prior to starting ultrasound which was confirmed through total counts > 500 and visual checks (Figure 7.16, (B)). Indeed, the recycling effect (without ultrasound) had consistently reduced the mean induction time which could be due to a number of factors. For instance, a relatively high supersaturation of 3.09 was selected for TAK-117 compared to 1.61 for TAK-438 (Figure 7.7).

With a high supersaturation, the API is more prone to nucleate from the cooling effect of the flow-cell jacket set at 10°C or shear imposed from the fast pinching of the recycle-line via the Masterflex pump (Figure 7.6). Nevertheless, after the induction of nucleation an increase in power amplitude from 40% (133.1 KW / m^2) to 80% (239.97 KW / m^2) increased the secondary nucleation kinetics. This is seen from the rapid increase in total count profiles upon ultrasound start (Figure 7.16).

7.3.2.2. Particle Size and Shape

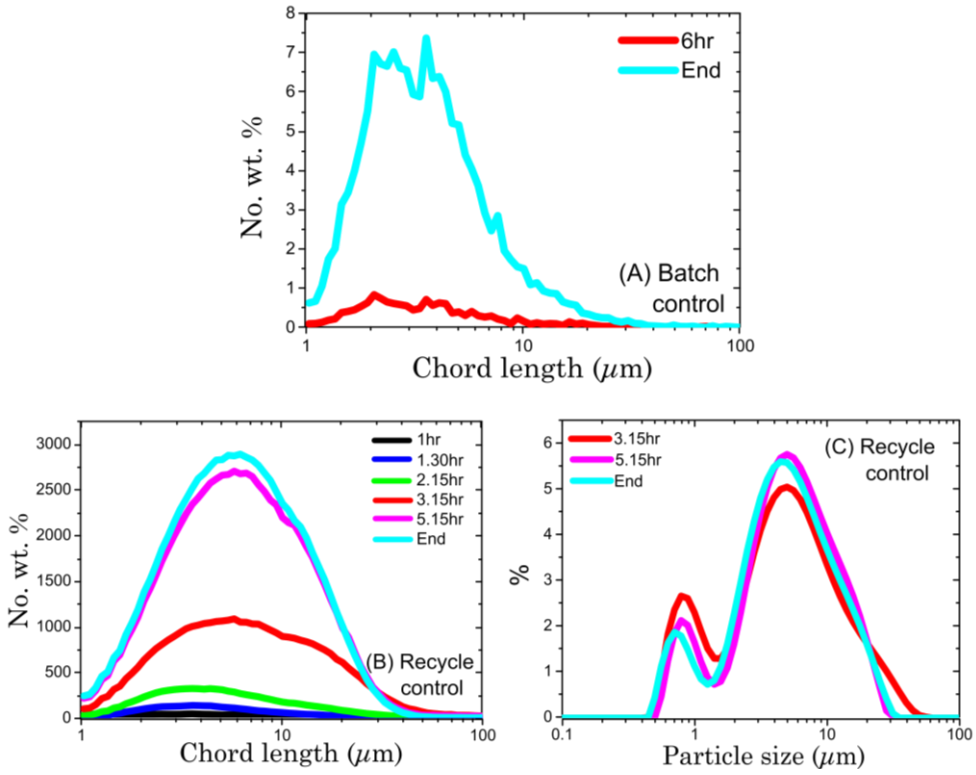

Figure 7.18 CLDs and PSDs obtained for control experiments. In situ CLDs measured at the onset of nucleation (6hr) and end for batch control is shown (A). Both CLDs and PSDs measured at frequent intervals at different times is shown for the recycle control (B & C).

The CLDs for batch control indicates nucleation with limited growth of particles generated small sizes from 5 – 10 μm (Figure 7.18, (A)) which is also seen in the microscopic images (Figure 7.20, (A)). This is further emphasised from the recycle control distributions (Figure 7.18, (B & C)) and the particle images (Figure 7.20, (B)) which produced a final Dv50 of 5.75 μm ± 0.031. A large particle span of 2.68 was measured for the recycle control most likely indicating that TAK-117 had nucleated to final small agglomerated needle-like particles with excessive fines.

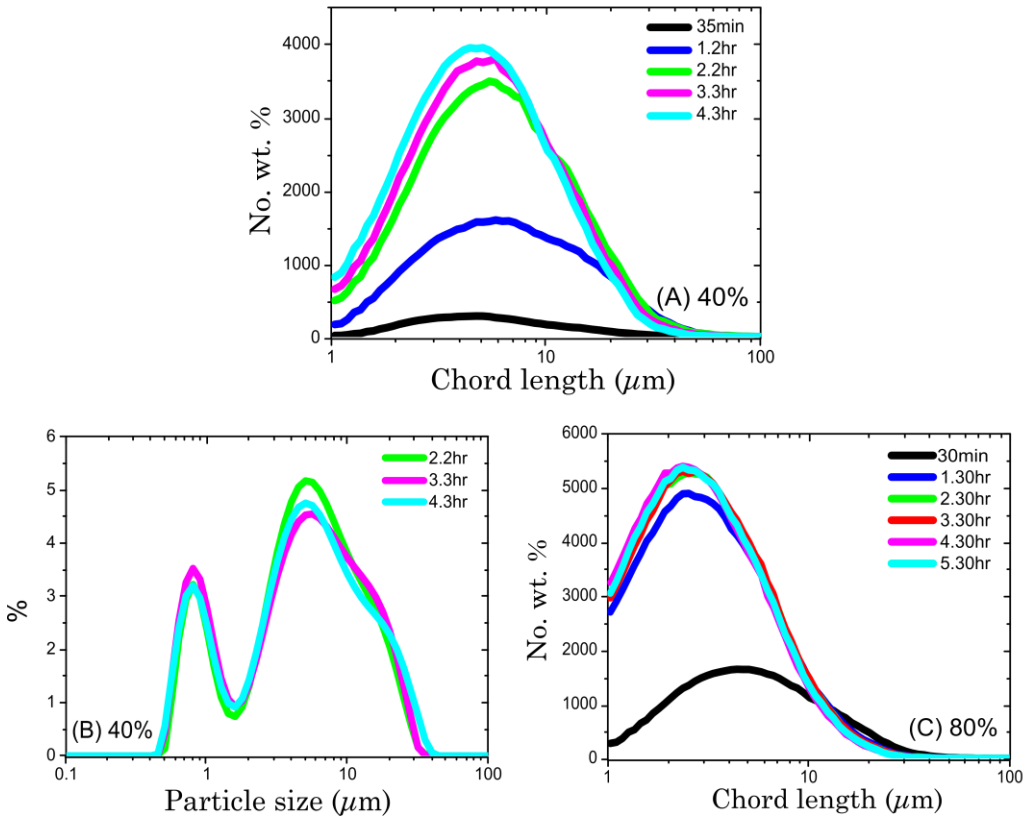

Figure 7.19 CLDs and PSDs obtained for ultrasound affected experiments. Both CLDs and PSDs measured at frequent intervals at different times is shown for 40% (A & B) as well as CLDs measured at different time intervals for 80% (C).

This could explain the small peak to the left observed in Figure 7.18 (C). Laser diffraction method applied in the mastersizer instrument is based on a spherical model for particle characterisation through Mie theory of light scattering (Malvern, 2012). Therefore when measuring needle-like or agglomerated systems, laser diffraction is unable to distinguish between different particle shapes in a sample which can lead to deficiencies and artefacts in the PSD distribution (Durak et al., 2018). Similar to the controls (batch and recycle), small particle sizes were achieved for experiments with applied 40% (133.1 KW / m^2) produced 5.22 μm ± 0.08

with a span of 2.98 (Table 7.4). Though minimal difference in Dv50s is seen between the recycle control and 40% condition (Table 7.4), the application of ultrasound imparts de-agglomeration of particles (Figure 7.19, (A & C) & Figure 7.20, (C to F)) throughout the course of each experiment. This can also be seen from the CLD distributions (Figure 7.19, (A & B)) which indicates de-agglomeration of particles over time. For instance, applying ultrasound at 40% (133.1 KW / m^2) shows a shift in CLD distributions over time from right (35 min) to left (4.3 hr) in Figure 7.19 (A). A more substantial shift from right (30 min) to left (5.30 hr) is also seen for the 80% (239.97 KW / m^2) condition. However, TAK-117 exhibited slow filterability of the particles which agglomerated upon filtration. This was encountered for the 80% experiment which displayed long filtration times (> 45 min) for each small slurry sample (~ 5 ml) being collected. Therefore, no offline PSD measurement was obtained due to long filtration times. Furthermore, whilst difficult to conclude, more circular shaped particles were produced from the 80% condition as shown from the microscopic images (Figure 7.20, (E & F)).

Table 7.5 Measured PSDs and spans for the recycle control and ultrasound affected experiments.

Experiment Type	Power amplitude (%)	Dv50 (μm)	StE	Span
Recycle control	0	5.746	± 0.031	2.684
Indirect ultrasound	40	5.222	± 0.077	2.983

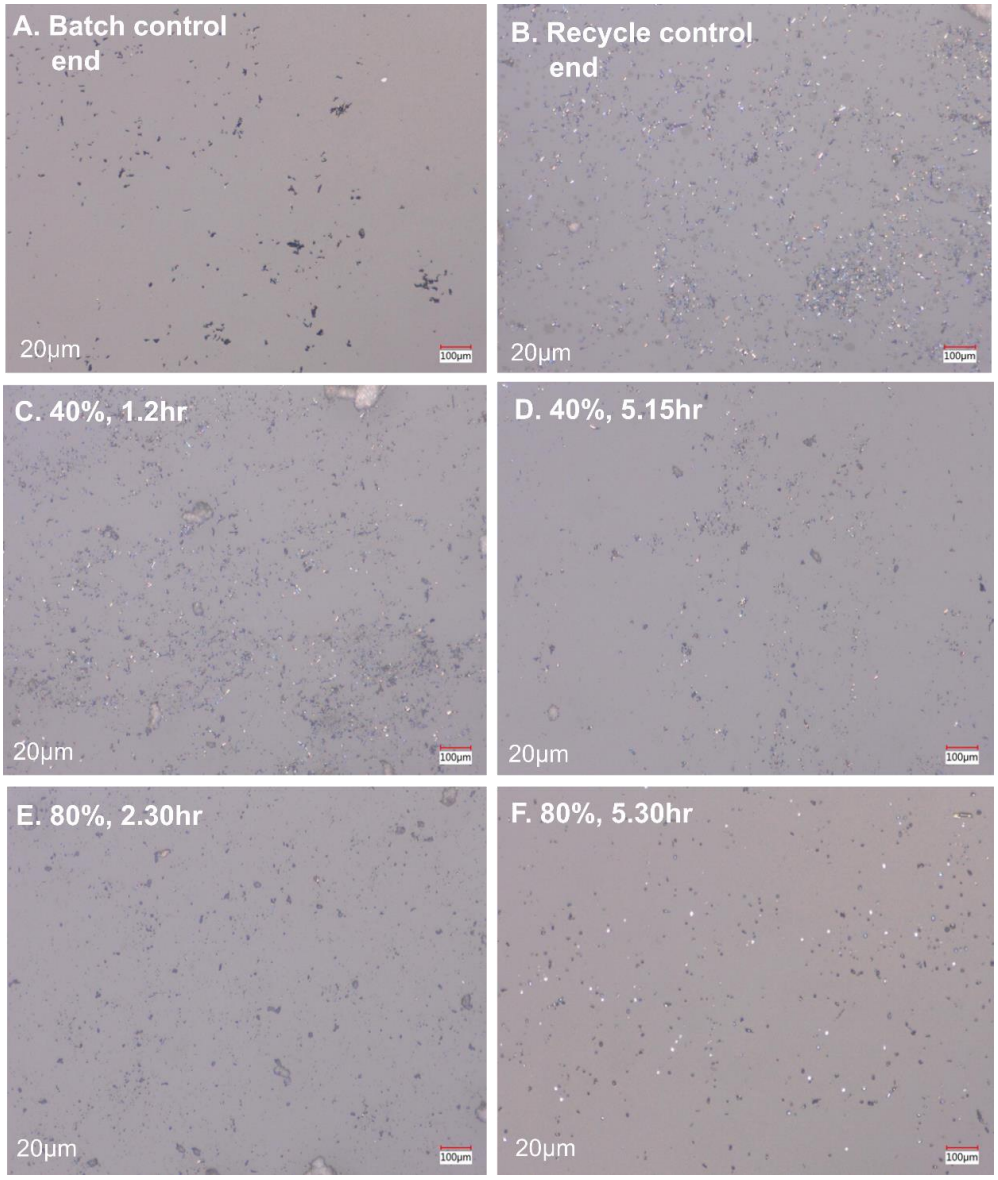

Figure 7.20 Collected microscopic images for controls (batch and recycle) and ultrasound affected (40% & 80%) experiments from A to F at 20x magnification.

7.3.2.3. Concentration Profiles

The rate of concentration depletion between the recycle control, 40% and 80% ultrasound experiments is shown (Figure 7.21). Each of these experiments consisted of a mean induction time < 30 min (Table 7.4).

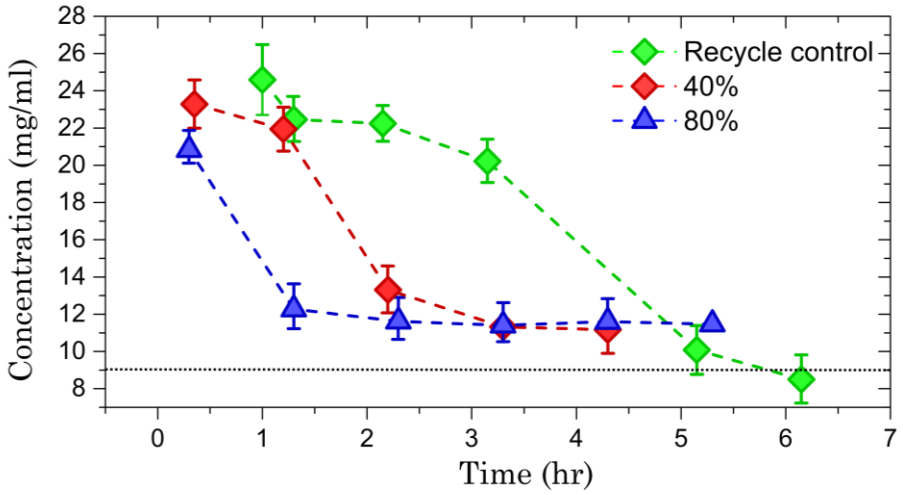

Figure 7.21 Concentration profiles obtained for the recycle control and ultrasound affected (40% & 80%) experiments is displayed over time.

As the recycle control had no ultrasound impact, desupersaturation occurred slowly over time from 1 hr (first sample collected) to 6.15 hr (Figure 7.21). Equilibrium was not reached by 6.15 hr (Figure 7.21). On the other hand, both 40% (133.1 KW / m^2) and 80% (239.97 KW / m^2) ultrasound power showed a rapid concentration decrease within 3.30 hr (Figure 7.21). Similar to TAK-117, operating at 80% power amplitude generated faster nucleation kinetics when applying ultrasound (Figure 7.16, (A & B)) and the subsequent consumption of supersaturation during the isothermal process. The equivalent total count series for these experiments are in Figure 7.16 (A).

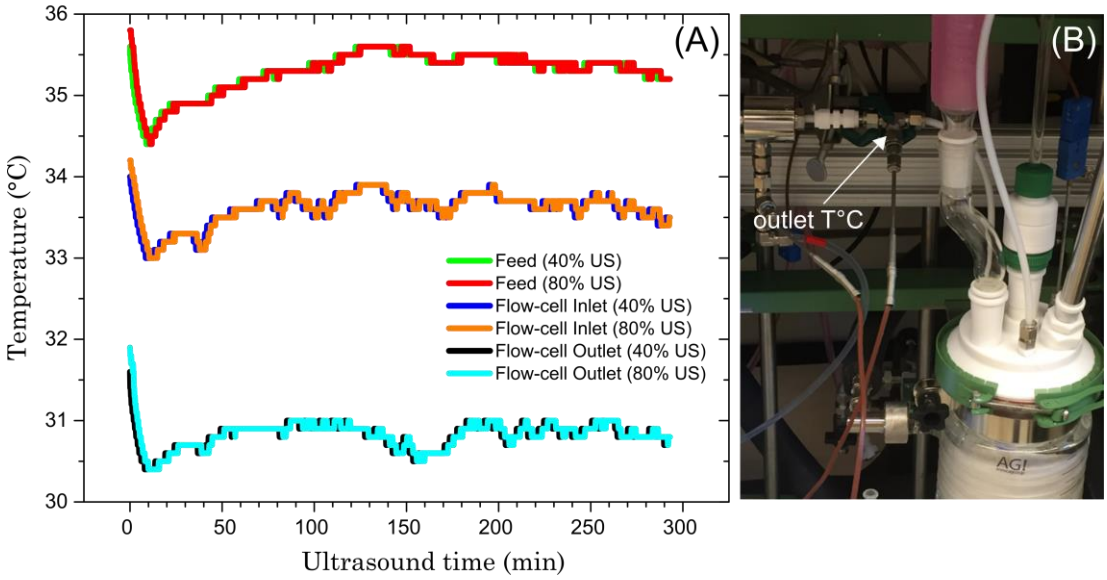

Figure 7.22 Temperature profiles for 40% & 80% ultrasound experiments. Thermocouples were placed at different positions across the process setup for TAK-117 (Figure 7.6). This allowed for temperature monitoring in the feed reactor vessel and flow-cell inlet prior to ultrasound power impact and flow-cell outlet immediately after ultrasound (A). An image displaying the positioning of the thermocouple on the flow-cell outlet is shown (B).

In comparison to TAK-438, no fouling occurred for TAK-117. Therefore, temperature profiles for the flow-cell inlet and outlet from attached thermocouples were obtained for 40% and 80% ultrasound experiments (Figure 7.5). The results in Figure 7.22, (A & B) show increasing the power amplitude from 40% to 80% resulted in no added temperature increase across the process setup as both temperature profiles (inlet and outlet) remained constant from 0 to 300 min (Figure 7.22, (A)). For both 40% and 80%, the outlet of the flow-cell (Figure 7.22, (B)) was 4°C to 5°C lower than the set feed reactor (35°C) whereas the flow-cell inlet temperature was 2°C to 3°C lower (Figure 7.22, (A)). The temperature drop (< 5°C) from the feed

to the flow-cell outlet was due to the flow-cell jacket set at 10°C (vendor recommendation) throughout each experiment (Figure 7.5) and the distance of the overall recycle-line across the process setup (Figure 7.6) leading to temperature loss.

Across all process conditions for both TAK-438 & TAK-117 there was no observed temperature increase to the processing solution from indirect ultrasound to the feed vessel. Hence, the feed vessel was able to maintain constant temperature (45°C & 35°C) throughout each experiment.

7.3.3. Estimation of Nucleation Kinetics

The results for both APIs demonstrate a considerable impact of indirect ultrasound (Figure 7.5 & Figure 7.6) on the crystallisation behaviour specifically in terms of mean induction times (Table 7.2 & Table 7.4), total count trends (Figure 7.8 & Figure 7.16) and concentration profiles (Figure 7.14 & Figure 7.21).

As the indirect ultrasound platform has the potential to be deployed as a continuous nucleator, a quantitative measure of the nucleation rate is essential. This will firstly help to give an indication of the ease and extent at which a given API will nucleate under the influence of ultrasound, the number of nuclei and subsequent seeds generated as well as providing control over the growth surface for crystallisation. Moreover, estimation of the nucleate rate can allow for the prediction of key product attributes such as the particle size distribution.

In this section, extraction of TAK-438 and TAK-117 nucleation rate values is estimated from the various experimental conditions tested with and without ultrasound (Table 7.1). Parameter estimation through the process modelling platform gCRYSTAL 4.2.0 (described in section 3.2.3.2) is used for a quantitative analysis of the primary nucleation rate when applying ultrasound power. Whilst the purpose of this section is for experimental data fitting and kinetic estimation, further work comprising of model validation, optimisation and prediction for product attributes is out with the scope of this work as well as a detailed modelling study on the indirect ultrasound mechanism.

To estimate the nucleation kinetics of TAK-438 in MeOH:H_20 (70:30) and TAK-117 in DMSO from the control and ultrasound applied experiments, physical properties such as molecular weight, density, solubility, etc., were configured in the global specifications module within the gCRYSTAL 4.2.0 user interface (Figure 7.23). A model of the reactor vessel was then built in gCRYSTAL 4.2.0 using an MSMPR unit operation configured in batch mode (Figure 7.23) to represent the experimental batch stirred-tank crystalliser. The MSMPR unit configured in the flowsheet, models the crystallisation slurry by means of a well-mixed single compartment which assumes that the mixing time is much lower than the time scales of nucleation, growth and agglomeration (Schöll et al., 2007). Under this assumption, the energy dissipation from the stirrer can be averaged over the whole crystalliser and hence the mechanism for the particle formation

can be assumed to be independent on the position within the crystalliser (Marchisio et al., 2006, Vicum et al., 2004). Other assumptions state that the liquid and solid phases in the bulk are in thermal and mechanical equilibrium, that is, same temperature and pressure.

Time invariant controls configured for the model flowsheet include mass of crystals in the slurry and solution composition which was retrieved from experimental concentration profiles via HPLC from the sampling method (described in section 7.2.4.1). PSD data from the Malvern Mastersizer 2000 (laser diffraction) captured at different experimental time points (section 7.2.4.1) was used for the PSD location parameter (characterisation of the model distribution) and PSD standard deviation. Temperature profiles (TC) were input as piecewise constant as there was no cooling in the reactor.

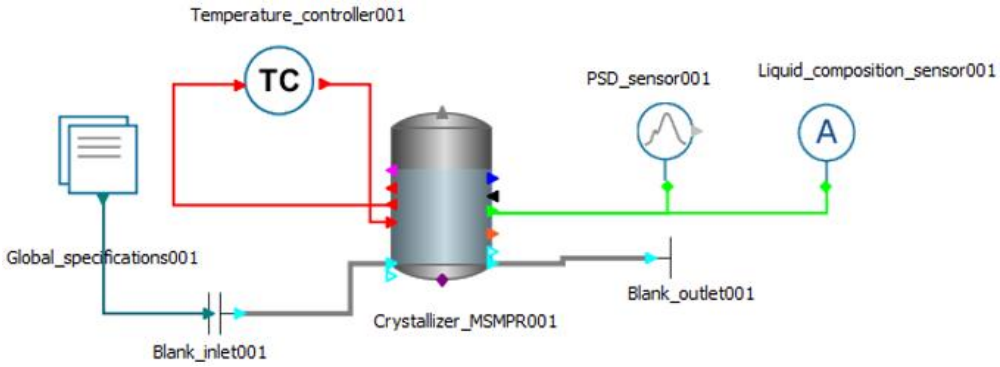

Figure 7.23 Schematic of flowsheet model used to describe the crystallisation of both APIs in their respective solutions and for parameter estimation. Typical experimental inputs include process temperature profile (TC), solution concentration (A), particle size measurements (PSD sensor) with selected models (for primary nucleation & growth) and operating conditions in the crystalliser MSMPR unit.

The model selected for the computation of the primary nucleation rate considers an Arrhenius type reaction with an energy barrier for the formation of a stable nucleus (Mullin, 1997). Primary nucleation kinetic parameters to be estimated were thus selected as power law kinetics (equation 7.2) with the driving force expressed as the absolute supersaturation (c^*) (equation 7.3):

$$J = A\, exp\left[\frac{-16\pi\gamma^3 v^2}{3k^3T^3(\ln S)^2}\right] \quad \text{Eq 7.2}$$

$$c^* = C - C(T_{sat}) \quad \text{Eq 7.3}$$

Here, the primary nucleation rate constant (J) = $m^3\ s^{-1}$ e.g. the number of nuclei formed per unit time per unit volume, temperature (T), degree of supersaturation (S) and interfacial tension (γ) are the three main variables which govern the rate of nucleation.

After model development, the performed experiments with and without ultrasound (controls) were imported into the gCRYSTAL folder of "Experiments > Performed," where the measured concentration profile retrieved from HPLC during sampling, PSD retrieved from laser diffraction also during sampling and temperature were manually inserted and saved. On the successful inputs of the experimental data, a group of kinetic parameters for TAK-438 and TAK-117 could be estimated using the "Parameter Estimations" tool in the software. Several multiple tries of initial guesses for lower and upper bounds for the crystallisation kinetic

parameters were usually necessary to obtain a good agreement between model predictions and experimental measurements. Recommended bounds for parameter estimation can be from the gCRYSTAL 4.2.0 user guide (gGCRYSTAL).

7.3.3.1. Modelling Analysis of TAK-438

For TAK-438, a nucleation rate constant (power law kinetics) of 15 log (# / m^3.s) and supersaturation order of 1 was selected for the primary nucleation model as the initial guesses. The software expresses the nucleation rate as a logarithm (log) for simplicity. The growth and dissolution model consisted of manually selected power law kinetics (Davey and Garside, 2006) with a growth rate constant of 0.00039 (m / s) and supersaturation order of 1.98. No activation energy was applied for both models. The initial guesses with appropriate lower and upper bounds for parameter estimation were informed through initial range fittings.

The estimated results in Figure 7.24 shows a good fit when applying 20% power amplitude as seen for the observed and predicted concentration (A) and Dv50 (B) values. This is evident from the resultant weighted residual of 3.47 which is significantly less than the χ^2-value (95%) of 16.919. Increasing the amplitude to 80% shows the majority of predicted concentrations to remain below the experimental values over the course of the experiments (Figure 7.24, (C)). This disagreement is further reflected in the weighted residual of 40.1687 which is greater than the χ^2-value (95%) of 21.0261.

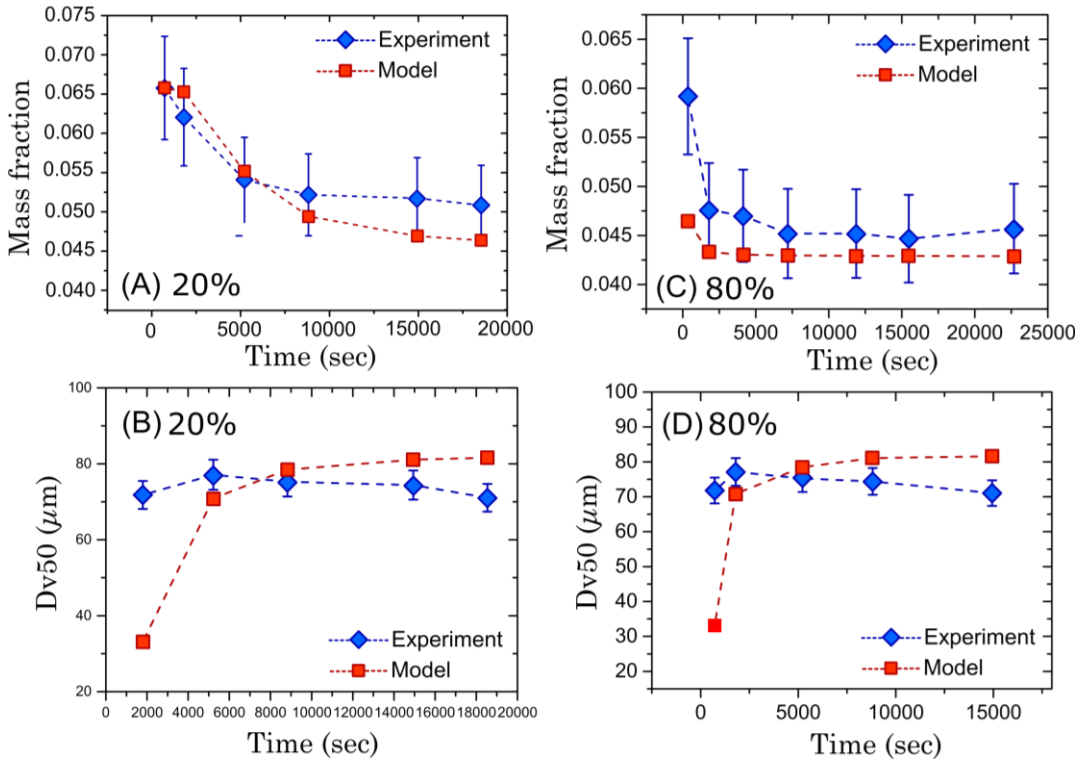

Figure 7.24 Experimental and predicted concentration and Dv50 profiles over time for 20% (A & B) and 80% (C & D) ultrasound conditions for TAK-438. Due to lack of concentration and Dv50 experimental data tracked over time for the control (batch & recycle) experiments as well as inaccurate concentration profiles for 40%, estimation of primary nucleation kinetics was not possible for these conditions.

Furthermore, for 20% power amplitude, the initial predicted Dv50 is 33.11 μm which is significantly lower than the experimental Dv50 71.8 μm at 18000 (seconds) (Figure 7.24, (C)).Similarly for 80%, a Dv50 of 39.92 μm is predicted which is lower than the experimental 59.74 μm at 360 (seconds) (Figure 7.24, (D)). The disagreement between the Dv50s during the initial phase of nucleation is attributed to the significant effect of

ultrasound on reducing the mean induction time of TAK-438 and consequently increasing the nucleation rate (Figure 7.24, (B & D)).

Therefore when compared to the calculated values, a larger experimental Dv50 is achieved at the first measurement point due to rapid nucleation upon ultrasound start. As observed in Figure 7.23, a unit operation accounting for ultrasound kinetics and application is yet to be built in a gCRYSTAL flowsheet. Furthermore from Figure 7.24, (B & D), the experimental Dv50s show a downward trend over time. For instance, at 80% power amplitude a size reduction from 59.76 μm (360 seconds) to 36.80 μm (22680 seconds) occurs. The predicted Dv50s from the model (Figure 7.24, (B & D)) are unable to follow a similar downward trend as the size reduction is a result of de-agglomeration and particle breakage from ultrasonication power that are not accounted for in the process model.

7.3.3.2. Modelling Analysis of TAK-117

For TAK-117, a range of rate constants from 25 to 40 log (# /m^3.s) and a supersaturation order of 1 were selected for the primary nucleation model as initial estimate bounds. The growth and dissolution model consisted of manually selected power law kinetics (Davey and Garside, 2006) with a rate constant of 8.8396 x 10^{-8} and 8.8396 x 10^{-8} (m / s) and supersaturation order of 1.3 and 2. No activation energy was applied for both models. The initial guesses with appropriate lower and upper bounds for parameter estimation was informed through initial range fittings and through the modelling platform suggested values (gGCRYSTAL).

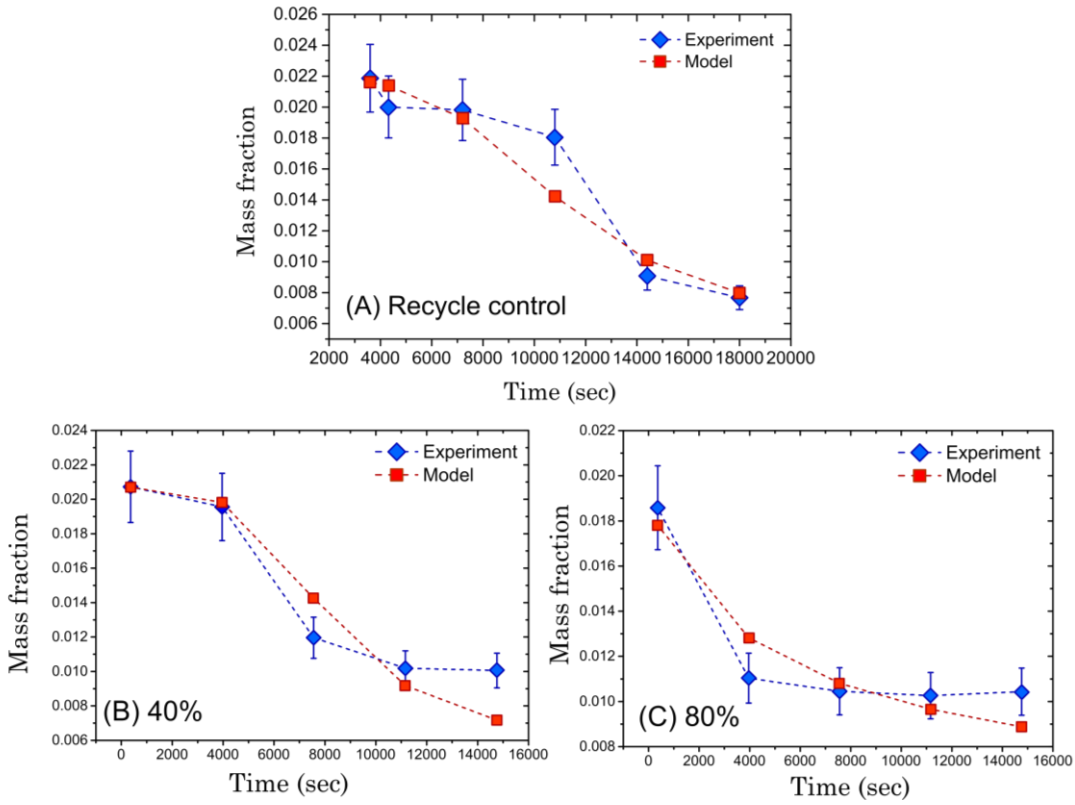

Figure 7.25 Experimental and predicted concentration profiles over time for the recycle control (A), 40% (B) and 80% (C) conditions for TAK-117. Due to lack of Dv50 experimental data tracked over time, predicted Dv50 profiles were not generated from start to end for each experiment.

The predicted recycle control concentrations (Figure 7.25, (A)) from 3600 to 18000 seconds other than at 14400 seconds display reasonable agreement with the experimental values. This is reflected in the weighted residual of 6.51 which is less than the χ^2-value (95%) of 12.60. For 40% power amplitude (Figure 7.25, (B)), the predicted concentrations (0.0143, 0.0092, 0.0072 mg / ml) are out of range with the experimental values (0.0120, 0.0101, 0.0101 mg / ml) from 7560 seconds to 14760 seconds. Hence the weighted residual was 12.9127 which was greater than the χ^2-value (95%) of 9.49 indicating the model fit is poor. For 80%

(Figure 7.25, (C)) it was difficult to obtain frequent PSD measurements over time due to poor filterability (as described in section 7.3.2.2). Nevertheless, a good fit was obtained (Figure 7.25, (C)) which had a weighted residual of 5.4784 which was less than the χ^2-value (95%) of 7.81473.

The Dv50s for the recycle control were collected at 11340 seconds and 18000 seconds (end) in addition to 40% power amplitude at 7920 seconds (mid-point) (Figure 7.26). The predicted Dv50s gave good agreement with the recycle control and 40% power amplitude experiments as nucleation occurred prior to applying ultrasound power (Figure 7.16 & Figure 7.17) whereby once applying ultrasound power, there was minimal impact on the particle size for TAK-117 (Figure 7.18 & Figure 7.19).

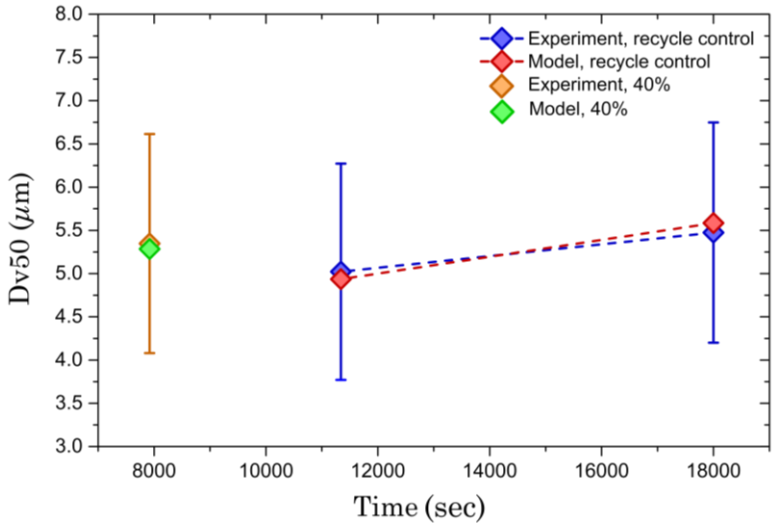

Figure 7.26 Experimental and Dv50 values for the recycle control and 40% ultrasound condition. Measured Dv50 for the 40% was obtained only at 7920 seconds whereas Dv50s for the recycle control were measured at 11340 seconds and 18000 seconds (end).

As stated earlier, model validation tests with an extensive parameter estimation study (growth and dissolution, secondary nucleation, breakage etc.,) was out with the scope of this work. However, the experimental and PBM modelling results (Figure 7.24, Figure 7.25 & Figure 7.26) provides a preliminary attempt to estimate kinetics to explore the effect of ultrasound in different systems. Whilst further work would be required to develop validated models with targeted design of experiments, extraction of primary nucleation rate values was achieved thus providing a reasonable basis for quantitative comparison between the two investigated APIs through the indirect ultrasound platform (Figure 7.27).

The effect of ultrasound power output on the primary nucleation rate is shown for both APIs (Figure 7.27). For TAK-438, increasing the power output from 53.33 KW / m^2 to 239.97 KW / m^2 increased primary nucleation kinetics from 18.89 # / m^3.s to 23.99 # / m^3.s (Figure 7.27). This observation is consistent with the induction time results as 239.97 KW / m^2 had a mean induction time of 5 ± 5.51 min which is considerably shorter than 30 min at 53.33 KW / m^2 power output (Table 7.2).

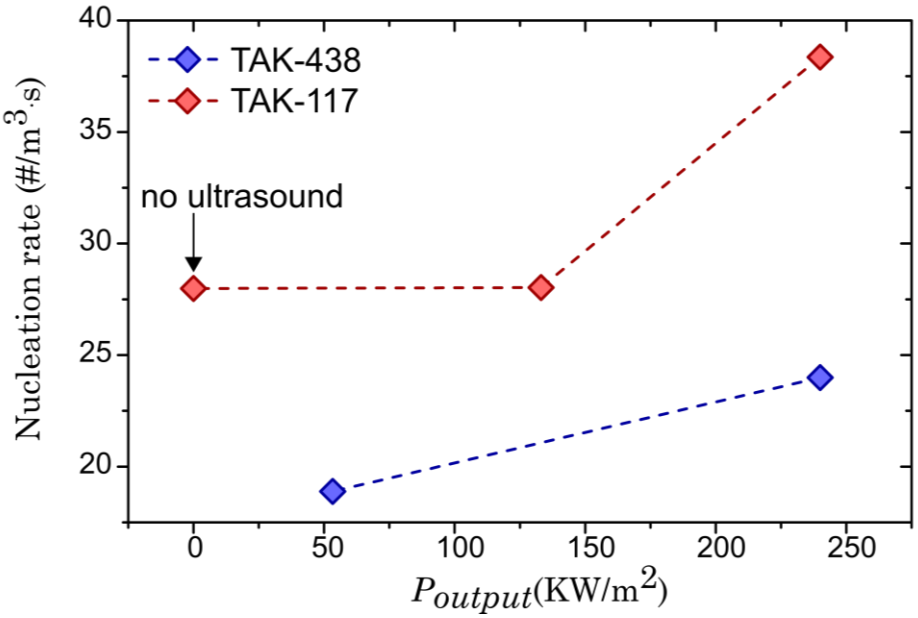

Figure 7.27 The primary nucleation rate and ultrasound power input is shown for TAK-438 & TAK-117 experiments.

For TAK-117, the recycle control yielded a nucleation rate of 27.99 # / m^3.s whereas applying a power output of 133.1 KW / m^2 produced 28.03 # / m^3.s (Figure 7.27). Similar nucleation rates for both conditions (recycle control & 133.1 KW / m^2) were observed as primary nucleation was induced from the recycling effect for all conditions (described in section 7.3.2.1). However, increasing ultrasound power to 239.97 KW / m^2 had substantial impact on nucleation kinetics with a rate value of 38.36 # / m^3.s which potentially indicates a minimum threshold is required to affect the nucleation rate using ultrasound power (Figure 7.27).

7.4. Summary

In this work, the impact of indirect ultrasound application on API nucleation behaviour is demonstrated through a semi-continuous crystallisation process. The approach successfully sonicated the process stream without direct contact through generating and transferring sufficient power efficiency to influence nucleation kinetics.

A rapid initiation of nucleation (10 min) at high power amplitudes (80%) was consistently delivered for TAK-438 compared to the slow induction times of 2 to 5 hours without the presence of ultrasound. For TAK-117, the recycling strategy without ultrasound power reduced the nucleation time. However once power amplitude was applied, the nucleation rate considerably increased from 27.99 to 38.36 # / m^3.s. TAK-117 shows the highest nucleation rate overall with increased response to ultrasound at higher energy whereas little increase at low energy is seen. TAK-438 shows a gradual increase in nucleation rate with increasing energy. Whilst further work on detailing nucleation rate dependence is required, these results highlight the potential for controlling nucleation rate as a function power amplitude.

Tight PSDs for TAK-438 of different size bands (Dv50) of 71.07 μm, 59.7 μm and 36.80 μm were achieved with increasing power amplitude. Interestingly, as sufficient power input was continuously transferred to the process stream, size reduction and de-agglomeration of particles occurred. As a result, this had an additional effect on particle shape. This is most

noticeable for TAK-438 as elongated rods became more circular shaped particles. Hence, the indirect flow-cell strategy can be used for various particle engineering applications for improving downstream particle processing e.g., de-agglomeration of seeds.

As an alternative technique to traditional direct ultrasound use, numerous advantages were seen with the indirect platform. Firstly, uniform power efficiency was continuously transferred across the configured flow-cell for prolonged periods of time across all experimental conditions (Table 7.1). Another promising feature is the potential to accurately control the supersaturation within the flow-cell through pressurized water (8 bar) for temperature control independent of power amplitude (Figure 7.2). With long enough residence times dictated by the flow-rate and length of the flow-cell as well as temperature control, this would potentially allow the platform to operate as a continuous nucleating device for crystallisation processes. Furthermore, from the conducted experiments there was no heating effects from indirect ultrasound being transferred directly back into the collecting vessel. Heating effects from direct ultrasound is a common problem which often leads to poorly controlled crystallisation processes.

In this study, we implemented an indirect ultrasound platform as a means for inducing nucleation and engineering of particle attributes. The strategy presents as an appealing method for accelerating the rate of slowly nucleating APIs as well as targeting various particle sizes, manipulating

particle shape and continuous in situ seed generation. The quantification of nucleation rate versus ultrasound energy provides a basis to deliver precise control of growth surface through size and number of seed crystals produced. Further work would be required to validate this approach and optimise the experimental method to enable parameter estimation of reliable kinetic modelling and to understand the underlining effect ultrasound is having on nucleation.

Chapter 8

Conclusions and Future Outlook

8. Conclusions and Future Outlook

8.1. Conclusions

Crystallisation is a critical operation in pharmaceutical manufacturing which ultimately dictates critical particle attributes that includes crystal size, size distribution, shape, surface area and polymorphic form. These properties can have considerable impact on downstream processing and the final drug performance characteristics such as oral bioavailability. Whilst significant research in recent years has demonstrated the ability to design well-controlled processes, delivering tight control of particle attributes by first-intent remains a considerable challenge. To meet the required product specification, typically either multiple crystallisation trials are conducted or external unit operations such as dry mechanical milling are utilised for size reducing and de-agglomerating the crystallised product.

To avoid these issues, the goal of this work was to investigate particle engineering strategies which were easy to integrate with crystallisation to achieve direct manipulation and control of particle attributes. As such, high shear rotor-stator and indirect ultrasound devices were applied and proven to provide a range of practically useful control over the process outcomes. The results potentially enable a practitioner to deploy alternative strategies in pharmaceutical manufacturing for targeting a particular attribute specification such as particle size. This would save

considerable time and cost by avoiding the need for multiple batch repeats or further post-processing unit operations.

In chapter 4, wet milling was combined with a seeded cooling crystallisation process for acetaminophen. By combining the two unit operations into a single intensified process along with tuning of wet mill process parameters, improved particle attributes (PSD & shapes) were achieved in contrast to operating a batch cooling crystallisation alone. For example, industrial batch crystallisation can often suffer from broad and bimodal particle size and size distributions with wide spans which poses issues for bulk powder processing (Kim et al., 2005). Alternatively, the combined method was shown to consistently deliver monomodal particle size and size distributions with narrow spans as well as de-agglomerated (dispersed) suspensions. Along with high particle shape circularities and low surface energies from 30 to 50 mJ / m^2, it is believed these improved attributes would facilitate downstream processing such as flowability and content uniformity. However, correlating the product attributes yielded from the combined process to wider material properties was out with the scope of this work.

Advanced real-time measurements through inline PAT (FBRM & PVM) sensors with offline analysis highlighted additional challenges associated with the combined process. The presence of wet milling during crystallisation was shown to considerably affect mechanistic processes such as breakage (mass fracture & attrition), secondary nucleation and

growth rates which, although the experimental time interval of occurrence was determined and desired product attributes were generated, numerical estimation of rate kinetics was not estimated. This is important in particular for process modelling and optimisation of the combined method which can reduce the number of experiments required in a DoE. Furthermore, whilst the energy dissipation rate (E^*) model showed promise to predict particle size for single experiments, the model was unable to correlate to size when including different speed and teeth configurations (Engstrom et al., 2013). The inability to unaccount for the multitude of mechanisms (breakage, secondary nucleation, growth) as well as the mechanical properties (Young's modulus, hardness, etc.,) of the compound were believed to be the main cause for the breakdown of the E^* model. These parameters would be important to include in future mechanistic model development for rotor-stator wet milling of APIs.

Chapter 5 applied the combination approach to an unseeded cooling crystallisation for acetaminophen which possesses a wide average metastable zone width of 28.7°C ± 0.8 (Brown et al., 2018). The effect of cooling and high shear wet milling enhanced nucleation kinetics (< 15 min) at moderate supersaturations across the process scales tested (1 L, 2 L & 10 L). However, the dependence of induction time vs high shear was not achieved in this study and would be an important aspect to determine in future work. Nevertheless, the WMC method produced desired particle attributes of small size and size distributions (< 33 – 55 μm) with tight

spans (1 – 1.4) whilst simultaneously maintaining constant supersaturation through an optimal cooling profile. It is noted, from both chapter 4 and 5, the smallest particle size threshold reached for acetaminophen was ~ 30 μm through the recirculation mode. From the range of wet mill process parameters tested, achieving lower sizes was challenging. This is assumed to be from the mechanical properties and the intermolecular framework comprising acetaminophen form 1 into a compact and rigid herringbone crystal structure influencing the particle size limit when undergoing fracturing processes such as size reduction from mechanical milling.

The combined strategy was then successfully utilised as a robust continuous seed generator by triggering nucleation which was configured as an overall 3-stage continuous MSMPR through a highly intensified approach. The proof-of-concept study mitigated the need for external seed generation and common continuous crystallisation issues such as fouling and encrustation as well as enabling the production of a stream of consistent seed particles. For longer continuous crystallisation campaigns (> 10 hr), it is recommended to develop a practical method to operate the wet mill intermittently to alleviate processing issues in the rotor-stator framework such as leakage and over-heating. Nonetheless, the combined strategy was proven to be a flexible and modular platform for seed generation which can potentially be deployed on-demand for crystallisation processes.

As shown, the integration of high shear wet milling produces instantaneous changes (~ 50% size reduction within 30 min) to particle suspensions. In chapter 6, a breakage only process was investigated with the incorporation of inline sensors (FBRM & PVM), computational tools and offline measurement techniques for quantitative estimation of size and shape distributions. The use of multi-sensor analysis revealed key insights into the performance, discrepancies and agreements between the different measurement modes which has shown to be essential for process understanding in chapters 4, 5 & 7. Situations arose where inline measurements and computational tools outperformed with regards to particle size and shape (aspect ratio) agreement in contrast to offline analysis and vice-versa for different crystalline materials (acetaminophen, benzoic acid and metformin HCL) during wet milling.

In principle, improvements are still needed for accurate measurement of PSD and shape distributions for different crystalline materials. FBRM & PVM tools proved beneficial for process characterisation such as potentially removing the need for sampling and dilution. However the results emphasised the importance and influence of mechanical properties and solvent selection when designing wet milling processes. This was evident when using benzoic acid in water leading to bubbles persisting throughout wet milling causing chord splitting and thus the accuracy of the inline CLD measurements. The use of multi-sensor measurement tools provides a significant step towards accurate solid phase characterisation

for important attributes such as size and shape when undergoing complex inline mechanical milling processes such as high shear wet milling. Efficient monitoring tools as evident in this study also show the potential application for future control strategies. For example, a recent study operated a model-free control scheme using an online monitoring technique (μ-DISCO) with wet milling (Rajagopalan et al., 2019). The control strategy successfully managed to steer three different seed populations of two different needle-like compounds to desired target average lengths.

The final experimental chapter (chapter 7) of this thesis presented indirect ultrasound as a potential technique for particle engineering of APIs with benefits compared with conventional direct ultrasound processes. The indirect ultrasound flow-cell coupled with a crystalliser provided control over the induction of nucleation and delivered the target particle size and size distribution, span and shapes for the investigated APIs. The extraction of nucleation rates using the gCRYSTAL process modelling platform for TAK-438 (23.99 # / m^3.s) and TAK-117 (38.36 # / m^3.s) at the highest power output (239.97 KW / m^2) revealed the different propensity of API's to nucleate under the influence of indirect sonication. Research studies surrounding the impact and process strategies for deploying indirect ultrasound on crystalline materials is currently neglected in the literature in comparison to direct ultrasound. However, this technique provides capabilities for generating well-conditioned seeds as there is no

direct contact with the processing stream and so avoids common issues such as particle shedding.

Furthermore, whilst continuous ultrasound pulsing (indirectly) caused no substantial heating effects or large operating sounds, it is recommended to explore the efficiency of a single-pulse and multiple-pulse mode on the induction of nucleation and particle attribute control. A key benefit of this would be the ability to reduce energy consumption which would generate great interest to industrial manufacturers for applications such as scale-up.

8.2. Future Recommendations

Particle engineering through wet milling (rotor-stator and indirect ultrasound) has shown capability for tailoring pharmaceutical compounds with the desired attributes for performance in patients. Each chapter has demonstrated a number of potential advantages from combining wet milling with crystallisation in a recycle mode. However, several limitations have also been observed and there are certain areas of interest which require further scientific investigation to enable more general application of this technology.

8.2.1. Mechanical Properties and Solvent Effects

In chapters 4 to 6, the effect of rotor-stator wet mill particle breakage was presented. Mass fracture and attrition mechanisms occurred, however only a limited range of material properties were tested. Hence further

work would be required to understand the response performance of other materials to the process conditions, for example across brittle materials and more plastic systems such as ibuprofen.

As evident in chapter 6, mechanical and solvent properties can affect particle dispersion during milling (Luner et al., 2012). Previous development work for chapter 6 (unpublished) has shown the influence of solvents to increase the propensity of particle suspensions to agglomerate, foam and form bubbles during wet milling. Therefore, establishing relationships between these solvent properties to wet milling operability is important for overall process optimisation, efficiency and predictability.

Knowledge of this would improve the milling efficiency. For instance, knowing an APIs young's modulus, elasticity, brittleness and hardness values which can be measured through nanoindentation techniques is important. This can then provide pre-determined knowledge on an APIs tendency to break or fracture which would allow pre-selection of milling parameters such as milling time and thus avoid over-milling of crystalline materials. Mechanistic correlations against particle size could also be built providing predictive capabilities of wet milling at different processing scales.

8.2.2. Population Balance Modelling

Whilst not explicitly explored in this thesis, population balance models are undoubtedly important for quantifying and describing complex rate

processes that may occur simultaneously. For PBM development, carefully designed and parametric estimation experiments need to be carried out for extraction of the specific rate parameters describing nucleation, growth and breakage. Recent advances in available commercial suites such as gPROMS with built-in PBMs enable users to model unit operations such as rotor-stator wet mills (Luciani et al., 2015). Key features of the wet mill model include batch, fed-batch and continuous operation, transient accumulation of material, breakage with equipment and operation relation parameters and crystallisation mechanisms such as growth (mass transfer and surface integration). An example of a configured flow-sheet in gPROMS (PSE Enterprise Ltd.) is shown (Figure 8.1) containing a rotor-stator wet mill attached to a crystalliser unit. Interfaces such as these, present the opportunity in particular for experimentalists, for process modelling, design and control.

Along with the mechanical and solvent property considerations, future work could look to estimate the specific breakage rate and breakage frequencies for a range of organic molecules through the recycle mode (Figure 8.1). This could inform the development of a breakage classification system which potentially, can provide essential knowledge for predicting the particle size reduction performance during wet milling. It can also be used to reveal and establish the relationship between the particle shape and breakage characteristics.

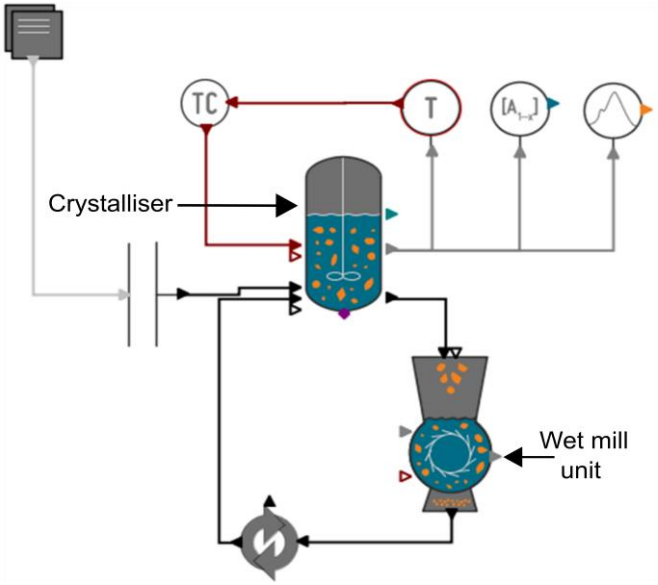

Figure 8.1 Example of a process flowsheet for modelling and simulation of combining wet milling via the recycle-loop mode.

8.2.3. Continuous Single-Pass Milling

The single-pass mode is a promising approach for pharmaceutical applications however only a few publications have been reported (Yang et al., 2015). Establishing relationships between process parameters and product attributes as well as recommended standardised process configurations would provide the potential to enable an alternative continuous seed generation strategy. Although this thesis has focused primarily on the recycle-loop mode, proof-of-concept studies were investigated (unpublished) using the single-pass approach for continuous in situ seed generation. Seeds were then directly transferred to continuous crystallisers for crystal growth to assess the performance (Figure 8.2 and Figure 8.3).

The process was tested on acetaminophen, lovastatin and metformin HCL, which involved feeding through a saturated / supersaturated solution through the high shear wet mill. An advantage of this approach over the recycle-loop mode is the ability to generate smaller seed sizes. For example, a size limit threshold of ~ 30 μm was achieved for acetaminophen through the recycle-loop mode whereas the single-pass mode generated < 15 μm seed particles. Therefore to reach even smaller seed sizes such as 1 μm for providing optimum surface area for crystal growth, the single-pass mode would require significant process optimisation and selection of parameters such milling speed and configuration, mill temperature, flow-rate and feed concentration which can be investigated in future work.

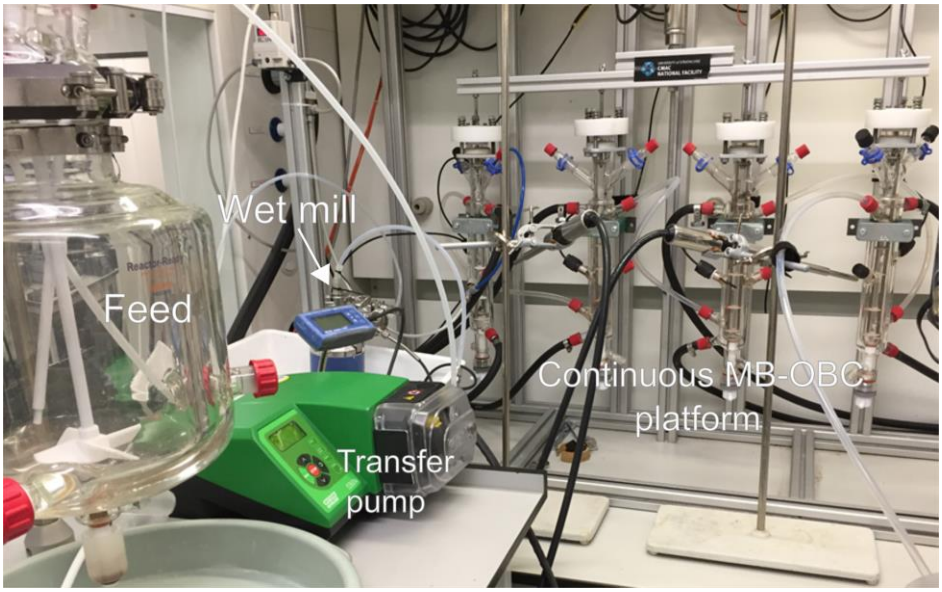

Figure 8.2 Process configuration of a proof-of-concept demonstration for a continuously seeded crystallisation of lovastatin in a moving baffled oscillatory baffled crystalliser (MB-OBC). The rotor-stator wet mill generated seeds through a single-pass of the feed solution which was then subjected for growth in the MB-OBC platform.

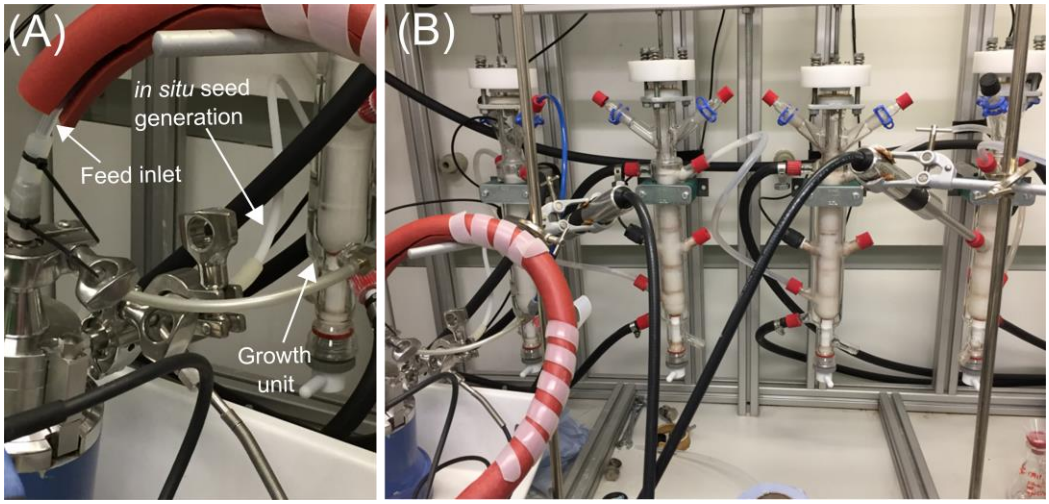

Figure 8.3. Images of the same proof-of-concept study shown in Figure 8.2. A zoomed in view of the direct seed transfer for growth is seen from the wet mill (A) and continuous crystallisation across the baffled reactors (B).

From the explored proof-of-concept studies, it would be desirable to firstly enable a workflow development on the susceptibility of APIs with different MSZWs to nucleate under a high shear environment. This could then inform the range of seed masses (loading) and seed sizes that can be achieved from a single-pass. Secondly, upon devising a standardised process configuration for a single-pass strategy, feedback control measures could be implemented to provide control over the supersaturation generation inside the wet mill as a function of temperature and the rotation speed (rpm) both of which can be controlled independent of each other. These control strategies could be used in conjunction with continuous crystallisation strategies for instance for targeting and dialling different particle sizes in the same continuous campaign simply by tuning the seed generation stage. Ultimately, it is the seed generation stage which controls the crystallisable product and thus the product particle size.

References

AAMIR, E., NAGY, Z. & RIELLY, C. 2010. Evaluation of the effect of seed preparation method on the product crystal size distribution for batch cooling crystallization processes. *Crystal Growth & Design,* 10**,** 4728-4740.

ABU BAKAR, M. R., NAGY, Z. K., SALEEMI, A. N. & RIELLY, C. D. 2009. The impact of direct nucleation control on crystal size distribution in pharmaceutical crystallization processes. *Crystal Growth and Design,* 9**,** 1378-1384.

ACEVEDO, D., KAMARAJU, V. K., GLENNON, B. & NAGY, Z. K. 2017. Modeling and Characterization of an in Situ Wet Mill Operation. *Organic Process Research & Development,* 21**,** 1069-1079.

AGIMELEN, O. S., HAMILTON, P., HALEY, I., NORDON, A., VASILE, M., SEFCIK, J. & MULHOLLAND, A. J. 2015. Estimation of particle size distribution and aspect ratio of non-spherical particles from chord length distribution. *Chemical Engineering Science,* 123**,** 629-640. https://doi.org/10.1016/j.ces.2014.11.014

AGIMELEN, O. S., JAWOR-BACZYNSKA, A., MCGINTY, J., DZIEWIERZ, J., TACHTATZIS, C., CLEARY, A., HALEY, I., MICHIE, C., ANDONOVIC, I., SEFCIK, J & MULHOLLAND, A.D. 2016. Integration of in situ imaging and chord length distribution measurements for estimation of particle size and shape. *Chemical Engineering Science,* 144**,** 87-100. https://doi.org/10.1016/j.ces.2016.01.007

AGIMELEN, O. S., MULHOLLAND, A. J. & SEFCIK, J. 2018a. Software for transforming measured chord length distribution data to particle size distribution. https://doi.org/10.15129/c147b4c4-6e2e-43bd-bdfd-fd889ef2d5ee

AGIMELEN, O. S., SVOBODA, V., AHMED, B., CARDONA, J., DZIEWIERZ, J., BROWN, C. J., MCGLONE, T., CLEARY, A., TACHTATZIS, C., MICHIE, C., FLORENCE, A. J., ANDONOVIC, I., MULHOLLAND, A. J. & SEFCIK, J. 2018b. Multi-sensor inline measurements of crystal size and shape distributions during high shear wet milling of crystal slurries. *Advanced Powder Technology*, 29, 2987-2995. https://doi.org/10.1016/j.apt.2018.09.003

AGRAWAL, S. & PATERSON, A. 2015. Secondary Nucleation: Mechanisms and Models. *Chemical Engineering Communications,* 202**,** 698-706.

ALVAREZ, A. J., SINGH, A. & MYERSON, A. S. 2011. Crystallization of Cyclosporine in a Multistage Continuous MSMPR Crystallizer. *Crystal Growth & Design,* 11**,** 4392-4400.

ATIEMO-OBENG, V. A. & CALABRESE, R. V. 2004. Rotor-stator mixing devices. John Wiley & Sons, Inc.: Hoboken, NJ.

AUSTIN, L., SHOJI, K., BHATIA, V., JINDAL, V., SAVAGE, K. & KLIMPEL, R. 1976. Some results on the description of size reduction as a rate process in various mills. *Industrial & Engineering Chemistry Process Design and Development,* 15**,** 187-196.

BADMAN, C. & TROUT, B. L. 2015. Achieving continuous manufacturing. May 20–21, 2014 continuous manufacturing symposium. *Journal of pharmaceutical sciences,* 104**,** 779-780.

BAKEEV, K. A. 2010. *Process analytical technology: spectroscopic tools and implementation strategies for the chemical and pharmaceutical industries*, John Wiley & Sons.

BALÁŽ, P. 2008. High-energy milling. *Mechanochemistry in Nanoscience and Minerals Engineering*. Springer.

BAŁDYGA, J., MAKOWSKI, Ł., ORCIUCH, W., SAUTER, C. & SCHUCHMANN, H. P. 2008. Deagglomeration processes in high-shear devices. *Chemical Engineering Research and Design,* 86**,** 1369-1381.

BARRETT, M., MCNAMARA, M., HAO, H., BARRETT, P. & GLENNON, B. 2010. Supersaturation tracking for the development, optimization and control of crystallization processes. *Chemical Engineering Research and Design,* 88**,** 1108-1119.

BARRETT, P. & GLENNON, B. 1999. In-line FBRM monitoring of particle size in dilute agitated suspensions. *Particle & Particle Systems Characterization: Measurement and Description of Particle Properties and Behavior in Powders and Other Disperse Systems,* 16**,** 207-211.

BARRETT, P. & GLENNON, B. 2002. Characterizing the metastable zone width and solubility curve using Lasentec FBRM and PVM. *Chemical Engineering Research and Design,* 80**,** 799-805.

BAUER, J. F. 2009. Pharmaceutical solids: size, shape, and surface area. *Journal of Validation Technology,* 15**,** 37-45.

BAXENDALE, I. R., BRAATZ, R. D., HODNETT, B. K., JENSEN, K. F., JOHNSON, M. D., SHARRATT, P., SHERLOCK, J.-P. & FLORENCE, A. J. 2015. Achieving Continuous Manufacturing: Technologies and Approaches for Synthesis, Workup, and Isolation of Drug Substance. May 20–21, 2014 Continuous Manufacturing Symposium. *Journal of Pharmaceutical Sciences,* 104**,** 781-791.

BECKMANN, W. 2000. Seeding the desired polymorph: background, possibilities, limitations, and case studies. *Organic process research & development,* 4**,** 372-383.

BECKMANN, W. 2013. *Crystallization: Basic concepts and industrial applications*, John Wiley & Sons.

BEEBE, R. A., BECKWITH, J. B. & HONIG, J. M. 1945. The determination of small surface areas by krypton adsorption at low temperatures. *Journal of the American Chemical Society,* 67**,** 1554-1558.

BERNOTAT, S. & SCHÖNERT, K. 2000. Size reduction. *Ullmann's encyclopedia of industrial chemistry*.

BILLOT, P., COUTY, M. & HOSEK, P. 2010. Application of ATR-UV spectroscopy for monitoring the crystallisation of UV absorbing and nonabsorbing molecules. *Organic Process Research & Development,* 14**,** 511-523.

BORN, M. & LANDE, A. 1981. The calculation of the compressibility of regular crystals from the lattice theory. *The calculation of the compressibility of regular crystals from the lattice theory Transl. into ENGLISH from Devt. Physik, Ges.(Germany),* 20, 21-24, 1918 210-216.

BOTSARIS, G. D. & DENK JR, E. G. 1970. Growth rates of aluminum potassium sulfate crystals in aqueous solutions. *Industrial & Engineering Chemistry Fundamentals,* 9**,** 276-283.

BRAATZ, R. D. 2002. Advanced control of crystallization processes. *Annual Reviews in Control,* 26**,** 87-99.

BRIGGS, N. E., SCHACHT, U., RAVAL, V., MCGLONE, T., SEFCIK, J. & FLORENCE, A. J. 2015. Seeded Crystallization of β-l-Glutamic Acid in a Continuous Oscillatory Baffled Crystallizer. *Organic Process Research & Development,* 19**,** 1903-1911.

BRIUGLIA, M. L., SEFCIK, J. & TER HORST, J. H. 2018. Measuring secondary nucleation through single crystal seeding. *Crystal Growth & Design,* 19**,** 421-429.

BROWN, C., MCGLONE, T., FLORENCE, A., KHINAST, J. & RANTANEN, J. 2017. Continuous Crystallisation. *Continuous Manufacturing of Pharmaceuticals*. John Wiley & Sons, Ltd.

BROWN, C. J., MCGLONE, T., YERDELEN, S., SRIRAMBHATLA, V., MABBOTT, F., GURUNG, R., L. BRIUGLIA, M., AHMED, B., POLYZOIS, H., MCGINTY, J., PERCIBALLI, F., FYSIKOPOULOS, D., MACFHIONNGHAILE, P., SIDDIQUE, H., RAVAL, V., HARRINGTON, T. S., VASSILEIOU, A. D., ROBERTSON, M., PRASAD, E., JOHNSTON, A., JOHNSTON, B., NORDON, A., SRAI, J. S., HALBERT, G., TER HORST, J. H., PRICE, C. J., RIELLY, C. D., SEFCIK, J. & FLORENCE, A. J. 2018. Enabling precision manufacturing of active pharmaceutical ingredients: workflow for seeded cooling continuous crystallisations. *Molecular Systems Design & Engineering*, 3, 518-549. DOI: 10.1039/c7me00096k

BROWN, C. J. & NI, X.-W. 2012. Determination of metastable zone width, mean particle size and detectable number density using video imaging in an oscillatory baffled crystallizer. *CrystEngComm,* 14**,** 2944-2949.

BURCHAM, C. L., COLLINS, P. C., JARMER, D. J. & SEIBERT, K. D. 2009. Reduction of particle size of drug substance for low-dose drug products. *Formulation and Analytical Development for Low-Dose Oral Drug Products***,** 205.

CALABRESE, R., FRANCIS, M., KEVALA, K., MISHRA, V., PADRON, G. & PHONGIKAROON, S. Fluid dynamics and emulsification in high shear mixers. Proc. 3rd World Congress on Emulsions, 2002. 1-10.

CAO, Z., GROEN, H., HAMMOND, R., LAI, X., LIANG, K., MOUGIN, P., ROBERTS, K., SAVELLI, N., THOMAS, A. & WHITE, G. Monitoring the crystallisation of organic speciality chemical products via on-line analytical techniques. 14th Industrial Symposium on Industrial Crystallisation, IChemE, 1999.

CAPELO-MARTÍNEZ, J.-L. 2009. *Ultrasound in chemistry: analytical applications*, John Wiley & Sons.

CARDONA, J., FERREIRA, C., MCGINTY, J., HAMILTON, A., AGIMELEN, O. S., CLEARY, A., ATKINSON, R., MICHIE, C., MARSHALL, S., CHEN, Y.-C., SEFCIK, J., ANDONOVIC, I., TACHTATZIS, C. 2018. Image analysis framework with focus evaluation for in situ characterisation of particle size and shape attributes. *Chemical Engineering Science*, 191, 208-231. https://doi.org/10.1016/j.ces.2018.06.067

CARDONA, J. & TACHTATZIS, C. 2018. ImagingApp: image analysis framework for particle size and shape characterisation. https://doi.org/10.15129/99c4558f-f59e-4be8-80e2-b0425178332b

CHALLENER, C. A. 2018. FDA Drug Approvals Hit Record Levels in 2017. *Gene,* 2018.

CHATTERJEE, S. FDA perspective on continuous manufacturing. IFPAC Annual Meeting, Baltimore, MD, 2012.

CLONTZ, N. A., JOHNSON, R. T., MCCABE, W. L. & ROUSSEAU, R. W. 1972. Growth of magnesium sulfate heptahydrate crystals from solution. *Industrial & Engineering Chemistry Fundamentals,* 11**,** 368-373.

COLE, K. P., GROH, J. M., JOHNSON, M. D., BURCHAM, C. L., CAMPBELL, B. M., DISEROAD, W. D., HELLER, M. R., HOWELL, J. R., KALLMAN, N. J., KOENIG, T. M., MAY, S. A., MILLER, R. D., MITCHELL, D., MYERS, D. P., MYERS, S. S., PHILLIPS, J. L., POLSTER, C. S., WHITE, T. D., CASHMAN, J., HURLEY, D., MOYLAN, R., SHEEHAN, P., SPENCER, R. D., DESMOND, K.,

DESMOND, P. & GOWRAN, O. 2017. Kilogram-scale prexasertib monolactate monohydrate synthesis under continuous-flow CGMP conditions. *Science,* 356**,** 1144-1150.

COTE, A. & SIROTA, E. 2010. CRYSTALLIZATION: The Pursuit of a Robust Approach for Growing Crystals Directly to Target Size. *American Pharmaceutical Review,* 13**,** 46.

DAVEY, R. & GARSIDE, J. 2006. *From Molecules to Crystallizers - An Introduction to Crystallization,* Oxford, Oxford University Press.

DE ANDA, J. C., WANG, X. & ROBERTS, K. 2005. Multi-scale segmentation image analysis for the in-process monitoring of particle shape with batch crystallisers. *Chemical Engineering Science,* 60**,** 1053-1065.

DENEAU, E. & STEELE, G. 2005. An in-line study of oiling out and crystallization. *Organic Process Research & Development,* 9**,** 943-950.

DEVARAKONDA, S., EVANS, J. M. & MYERSON, A. S. 2003. Impact of ultrasonic energy on the crystallization of dextrose monohydrate. *Crystal Growth & Design,* 3**,** 741-746.

DORIS, G. & GRAY, D. 1980. Adsorption of n-alkanes at zero surface coverage on cellulose paper and wood fibers [J]. *J Colloid Interface Sci,* 77**,** 353-362.

DORRIS, G. M. & GRAY, D. G. 1980. Adsorption of n-alkanes at zero surface coverage on cellulose paper and wood fibers. *Journal of Colloid and Interface Science,* 77**,** 353-362.

DUNUWILA, D. D. 1997. An investigation of the feasibility of using in situ ATR FTIR spectroscopy in the measurement of crystallization phenomena for research and development of batch crystallization processes. Michigan State University. Ph.D. Thesis.

DUNUWILA, D. D. & BERGLUND, K. A. 1997. ATR FTIR spectroscopy for in situ measurement of supersaturation. *Journal of Crystal Growth,* 179**,** 185-193.

DURAK, L., KENNEDY, M., LANGSTON, M., MITCHELL, C., MORRIS, G., PERLMAN, M. E., WENDL, K., HICKS, F. & PAPAGEORGIOU, C. D. 2018. Development and Scale-Up of a Crystallization Process To Improve an API's Physiochemical and Bulk Powder Properties. *Organic Process Research & Development,* 22**,** 296-305.

EDER, R. J. P., SCHRANK, S., BESENHARD, M. O., ROBLEGG, E., GRUBER-WOELFLER, H. & KHINAST, J. G. 2012. Continuous Sonocrystallization of Acetylsalicylic Acid (ASA): Control of Crystal Size. *Crystal Growth & Design,* 12**,** 4733-4738.

ENGSTROM, J., WANG, C. C., LAI, C. J. & SWEENEY, J. 2013. Introduction of a new scaling approach for particle size reduction in toothed rotor-stator wet mills. *International Journal of Pharmaceutics,* 456**,** 261-268.

ERDEMIR, D., LEE, A. Y. & MYERSON, A. S. 2009. Nucleation of crystals from solution: classical and two-step models. *Accounts of Chemical Research,* 42**,** 621-629.

FORSYTH, C., BURNS, I. S., MULHERAN, P. A. & SEFCIK, J. 2015. Scaling of glycine nucleation kinetics with shear rate and glass–liquid interfacial area. *Crystal Growth & Design,* 16**,** 136-144.

FORSYTH, C., MULHERAN, P. A., FORSYTH, C., HAW, M. D., BURNS, I. S. & SEFCIK, J. 2014. Influence of controlled fluid shear on nucleation rates in glycine aqueous solutions. *Crystal Growth & Design,* 15**,** 94-102.

GARSIDE, J. 1982. Nucleation. *Biological mineralization and demineralization.* Springer.

GARSIDE, J. & DAVEY, R. J. 1980. Invited review secondary contact nucleation: kinetics, growth and scale-up. *Chemical Engineering Communications,* 4**,** 393-424.

GCRYSTAL Parameter estimation Initial Guesses and Suggested Bounds - A gCRYSTAL User Guide. Process Systems Enterprise (PSE) Ltd. London, UK.

GIBBS, G. 1928. Collected Works. Thermodynamics.

GRACIN, S., BRINCK, T. & RASMUSON, Å. C. 2002. Prediction of Solubility of Solid Organic Compounds in Solvents by UNIFAC. *Industrial & Engineering Chemistry Research,* 41**,** 5114-5124.

GRACIN, S., UUSI-PENTTILÄ, M. & RASMUSON, Å. C. 2005. Influence of ultrasound on the nucleation of polymorphs of p-aminobenzoic acid. *Crystal Growth & Design,* 5**,** 1787-1794.

GRÖN, H., BORISSOVA, A. & ROBERTS, K. J. 2003. In-process ATR-FTIR spectroscopy for closed-loop supersaturation control of a batch crystallizer producing monosodium glutamate crystals of defined size. *Industrial & Engineering Chemistry Research,* 42**,** 198-206.

GUO, Z., ZHANG, M., LI, H., WANG, J. & KOUGOULOS, E. 2005. Effect of ultrasound on anti-solvent crystallization process. *Journal of Crystal Growth,* 273**,** 555-563.

HARTER, A., SCHENCK, L., LEE, I. & COTE, A. 2013. High-Shear Rotor–Stator Wet Milling for Drug Substances: Expanding Capability with Improved Scalability. *Organic Process Research & Development,* 17**,** 1335-1344.

HEINRICH, J. & ULRICH, J. 2012. Application of Laser-Backscattering Instruments for In Situ Monitoring of Crystallization Processes–A Review. *Chemical Engineering & Technology,* 35**,** 967-979.

HENG, J. Y., THIELMANN, F. & WILLIAMS, D. R. 2006. The effects of milling on the surface properties of form I paracetamol crystals. *Pharmaceutical Research,* 23**,** 1918-1927.

HO, R., NADERI, M., HENG, J. Y., WILLIAMS, D. R., THIELMANN, F., BOUZA, P., KEITH, A. R., THIELE, G. & BURNETT, D. J. 2012. Effect of milling on particle shape and surface energy heterogeneity of needle-shaped crystals. *Pharmaceutical Research,* 29**,** 2806-2816.

HOGG, R. 1999. Breakage mechanisms and mill performance in ultrafine grinding. *Powder Technology,* 105**,** 135-140.

HOJJATI, H. & ROHANI, S. 2006. Measurement and prediction of solubility of paracetamol in water-isopropanol solution. Part 1. Measurement and data analysis. *Organic Process Research & Development,* 10**,** 1101-1109.

HUKKI, R. 1961. Proposal for a solomonic settlement between the theories of von Rittinger, Kick and Bond. *Trans. AIME,* 220**,** 403-408.

IRIZARRY, R., CHEN, A., CRAWFORD, R., CODAN, L. & SCHOELL, J. 2017. Data-driven model and model paradigm to predict 1D and 2D particle size distribution from measured chord-length distribution. *Chemical Engineering Science,* 164**,** 202-218.

JENKINS, H., SAKURAI, Y., NISHIMURA, A., OKAMOTO, H., HIBBERD, M., JENKINS, R., YONEYAMA, T., ASHIDA, K., OGAMA, Y. & WARRINGTON, S. 2015. Randomised clinical trial: safety, tolerability, pharmacokinetics and pharmacodynamics of repeated doses of TAK-438 (vonoprazan), a novel potassium-competitive acid blocker, in healthy male subjects. *Alimentary Pharmacology & Therapeutics,* 41**,** 636-648.

JIANG, M. & NI, X. 2019. Reactive Crystallization of Paracetamol in a Continuous Oscillatory Baffled Reactor. *Organic Process Research & Development*, 23, 882-890.

JIANG, M., PAPAGEORGIOU, C. D., WAETZIG, J., HARDY, A., LANGSTON, M. & BRAATZ, R. D. 2015. Indirect Ultrasonication in Continuous Slug-Flow Crystallization. *Crystal Growth & Design,* 15**,** 2486-2492.

JIANG, M., ZHU, Z., JIMENEZ, E., PAPAGEORGIOU, C. D., WAETZIG, J., HARDY, A., LANGSTON, M. & BRAATZ, R. D. 2014. Continuous-flow tubular crystallization in slugs spontaneously induced by hydrodynamics. *Crystal Growth & Design,* 14**,** 851-860.

JONES, A. G. 2002. *Crystallization process systems*, Elsevier.

JUHÁSZ, A. Z. & OPOCZKY, L. 1990. Mechanical activation of minerals by grinding pulverizing and morphology of particles.

KADAM, S. S., MESBAH, A., VAN DER WINDT, E. & KRAMER, H. J. 2011. Rapid online calibration for ATR-FTIR spectroscopy during batch crystallization of ammonium sulphate in a semi-industrial scale crystallizer. *Chemical Engineering Research and Design,* 89**,** 995-1005.

KAIL, N., BRIESEN, H. & MARQUARDT, W. 2007. Advanced geometrical modeling of focused beam reflectance measurements (FBRM). *Particle & Particle Systems Characterization,* 24**,** 184-192.

KAIL, N., MARQUARDT, W. & BRIESEN, H. 2009. Estimation of particle size distributions from focused beam reflectance measurements based on an optical model. *Chemical Engineering Science,* 64**,** 984-1000.

KAMAHARA, T., TAKASUGA, M., TUNG, H., HANAKI, K., FUKUNAKA, T., IZZO, B., NAKADA, J., YABUKI, Y. & KATO, Y. 2007. Generation of Fine Pharmaceutical Particles via Controlled Secondary Nucleation under High Shear Environment during Crystallization-Process Development and Scale-up. *Organic Process Research & Development,* 11**,** 699-703.

KEMPKES, M., EGGERS, J. & MAZZOTTI, M. 2008. Measurement of particle size and shape by FBRM and in situ microscopy. *Chemical Engineering Science,* 63**,** 4656-4675.

KIM, S., LOTZ, B., LINDRUD, M., GIRARD, K., MOORE, T., NAGARAJAN, K., ALVAREZ, M., LEE, T., NIKFAR, F. & DAVIDOVICH, M. 2005. Control of the particle properties of a drug substance by crystallization engineering and the effect on drug product formulation. *Organic Process Research & Development,* 9**,** 894-901.

KIM, S., WEI, C. & KIANG, S. 2003. Crystallization Process Development of an Active Pharmaceutical Ingredient and Particle Engineering via the Use of Ultrasonics and Temperature Cycling. *Organic Process Research & Development,* 7**,** 997-1001.

KLEINEBUDDE, P., KHINAST, J. & RANTANEN, J. 2017. *Continuous manufacturing of pharmaceuticals*, John Wiley & Sons.

KÖLLGES, T. & VETTER, T. 2017. Model-Based Analysis of Continuous Crystallization/Reaction Processes Separating Conglomerate Forming Enantiomers. *Crystal Growth & Design,* 17**,** 233-247. https://doi.org/10.1021/acs.cgd.6b01487

KÖLLGES, T. & VETTER, T. 2018. Design and Performance Assessment of Continuous Crystallization Processes Resolving Racemic Conglomerates. *Crystal Growth & Design,* 18**,** 1686-1696. https://doi.org/10.1021/acs.cgd.7b01618

KÖLLGES, T. & VETTER, T. 2019. Polymorph selection and process intensification in a continuous crystallization-milling process: A case study on L-glutamic acid crystallized from water. *Organic Process Research & Development*. 23, 361-374. https://doi.org/10.1021/acs.oprd.8b00420

KONDOR, A., QUELLET, C. & DALLOS, A. 2015. Surface characterization of standard cotton fibres and determination of adsorption isotherms of fragrances by IGC. *Surface and Interface Analysis,* 47**,** 1040-1050.

KOUGOULOS, E., SMALES, I. & VERRIER, H. M. 2011. Towards integrated drug substance and drug product design for an active pharmaceutical ingredient using particle engineering. *Aaps Pharmscitech,* 12**,** 287-294.

KUEHN, S. 2018. Pharmaceutical Manufacturing: Current Trends and What's Next. *AIChE Journal,* 114**,** 23 - 29.

LAWTON, S., STEELE, G., SHERING, P., ZHAO, L., LAIRD, I. & NI, X.-W. 2009. Continuous Crystallization of Pharmaceuticals Using a Continuous Oscillatory Baffled Crystallizer. *Organic Process Research & Development,* 13**,** 1357-1363.

LEANE, M., PITT, K., REYNOLDS, G. & GROUP, M. C. S. W. 2015. A proposal for a drug product Manufacturing Classification System (MCS) for oral solid dosage forms. *Pharmaceutical Development and Technology,* 20**,** 12-21.

LEANE, M., PITT, K., REYNOLDS, G. K., DAWSON, N., ZIEGLER, I., SZEPES, A., CREAN, A. M., DALL AGNOL, R. & THE MANUFACTURING CLASSIFICATION SYSTEM WORKING, G. 2018. Manufacturing classification system in the real world: factors influencing manufacturing process choices for filed commercial oral solid dosage formulations, case studies from industry and considerations for continuous processing. *Pharmaceutical Development and Technology,* 23**,** 964-977.

LEE, I., VARIANKAVAL, N., LINDEMANN, C. & STARBUCK, C. 2004. Rotor-stator milling of APis-empirical scale-up parameters and theoretical relationships between the morphology and breakage of crystals. *American Pharmaceutical Review,* 7**,** 120-123.

LEGRAS, A., KONDOR, A., HEITZMANN, M. & TRUSS, R. 2015. Inverse gas chromatography for natural fibre characterisation: Identification of the critical parameters to determine the Brunauer–Emmett–Teller specific surface area. *Journal of Chromatography A,* 1425**,** 273-279.

LEWINER, F., KLEIN, J., PUEL, F. & FEVOTTE, G. 2001. On-line ATR FTIR measurement of supersaturation during solution crystallization processes. Calibration and applications on three solute/solvent systems. *Chemical Engineering Science,* 56**,** 2069-2084.

LI, M., OSHIMA, T., HORIKAWA, T., TOZAWA, K., TOMITA, T., FUKUI, H., WATARI, J. & MIWA, H. 2018. Systematic review with meta-analysis: Vonoprazan, a potent acid blocker, is superior to proton-pump inhibitors for eradication of clarithromycin-resistant strains of Helicobacter pylori. *Helicobacter***,** e12495.

LI, M. & WILKINSON, D. 2005. Determination of non-spherical particle size distribution from chord length measurements. Part 1: Theoretical analysis. *Chemical Engineering Science,* 60**,** 3251-3265.

LI, Y., O'SHEA, S., YIN, Q. & VETTER, T. 2019. Polymorph selection by continuous crystallization in the presence of wet milling. *Crystal Growth & Design*. 19, 2259-2271. https://doi.org/10.1021/acs.cgd.8b01894

LIU, J. & RASMUSON, Å. C. 2013. Influence of agitation and fluid shear on primary nucleation in solution. *Crystal Growth & Design,* 13**,** 4385-4394.

LIU, L., MARZIANO, I., BENTHAM, A., LITSTER, J., WHITE, E. & HOWES, T. 2013. Influence of particle size on the direct compression of ibuprofen and its binary mixtures. *Powder technology,* 240**,** 66-73.

LIU, L., RASHID, A., MARZIANO, I., WHITE, E., HOWES, T. & LITSTER, J. 2012. Flowability of binary mixtures of commercial and reprocessed ibuprofen through high shear wet milling (HSWM) with lactose. *Advanced Powder Technology,* 23**,** 454-458.

LIVINGSTON, H. 1949. The cross-sectional areas of molecules adsorbed on solid surfaces. *Journal of Colloid Science,* 4**,** 447-458.

LO, E., MATTAS, E., WEI, C., KACSUR, D. & CHEN, C.-K. 2012. Simultaneous API particle size reduction and polymorph transformation using high shear. *Organic Process Research & Development,* 16**,** 102-108.

LUCIANI, C. V. 2018. Impact of Process Parameters on the Grinding Limit in High-Shear Wet Milling. *Organic Process Research & Development*. 22, 1328-1333.

LUCIANI, C. V., CONDER, E. W. & SEIBERT, K. D. 2015. Modeling-Aided Scale-Up of High-Shear Rotor–Stator Wet Milling for Pharmaceutical Applications. *Organic Process Research & Development,* 19**,** 582-589.

LUNER, P. E., ZHANG, Y., ABRAMOV, Y. A. & CARVAJAL, M. T. 2012. Evaluation of Milling Method on the Surface Energetics of Molecular Crystals Using Inverse Gas Chromatography. *Crystal Growth & Design,* 12**,** 5271-5282.

LYCZKO, N., ESPITALIER, F., LOUISNARD, O. & SCHWARTZENTRUBER, J. 2002. Effect of ultrasound on the induction time and the metastable zone widths of potassium sulphate. *Chemical Engineering Journal,* 86**,** 233-241.

MALVERN, I. 2012. A basic guide to particle characterization. *MRK1806-01***,** 24. https://www.malvernpanalytical.com/en/learn/knowledge-center/whitepapers/WP120620BasicGuidePartChar

MARCHISIO, D. L., SOOS, M., SEFCIK, J., MORBIDELLI, M., BARRESI, A. A. & BALDI, G. 2006. Effect of fluid dynamics on particle size distribution in particulate processes. *Chemical Engineering & Technology: Industrial Chemistry-Plant Equipment-Process Engineering-Biotechnology,* 29**,** 191-199.

MASCIA, S., HEIDER, P. L., ZHANG, H., LAKERVELD, R., BENYAHIA, B., BARTON, P. I., BRAATZ, R. D., COONEY, C. L., EVANS, J. M. B., JAMISON, T. F., JENSEN, K. F., MYERSON, A. S. & TROUT, B. L. 2013. End-to-End Continuous Manufacturing of Pharmaceuticals: Integrated Synthesis, Purification, and Final Dosage Formation. *Angewandte Chemie International Edition,* 52**,** 12359-12363.

MASON, T. J., RIERA, E., VERCET, A. & LOPEZ-BUESA, P. 2005. Application of ultrasound. *Emerging Technologies For Food Processing*. Elsevier.

MAZZOTTI, M., OCHSENBEIN, D. R., SALVATORI, F. & ALBUQUERQUE, D. I. 2015. Characterization and Modelling Crystallization Processes - 1D PBEs. *ETH Zurich Crystal Shape Summer School*.

MCGINTY, J. 2017. *Batch to continuous organic salt crystallisation: model based design.* University of Strathclyde. Ph.D. Thesis. http://digitool.lib.strath.ac.uk/R/?func=dbin-jump-full&object_id=28764

MCGLONE, T., BRIGGS, N. E. B., CLARK, C. A., BROWN, C. J., SEFCIK, J. & FLORENCE, A. J. 2015. Oscillatory Flow Reactors (OFRs) for Continuous Manufacturing and Crystallization. *Organic Process Research & Development,* 19**,** 1186-1202.

MERSMANN, A. 2001. *Crystallization technology handbook*, CRC Press.

MESBAH, A., HUESMAN, A. E., KRAMER, H. J. & VAN DEN HOF, P. M. 2011. A comparison of nonlinear observers for output feedback model-based control of seeded batch crystallization processes. *Journal of Process Control,* 21**,** 652-666.

MITCHELL, N. A., Ó'CIARDHÁ, C. T. & FRAWLEY, P. J. 2011. Estimation of the growth kinetics for the cooling crystallisation of paracetamol and ethanol solutions. *Journal of Crystal Growth,* 328**,** 39-49.

MULLIN, J. W. 1997. *Crystallization*, Butterworth-Heinemann.

MYERSON, A. 2002. *Handbook of industrial crystallization*, Butterworth-Heinemann.

MYERSON, A. S. & GINDE, R. 2002. Crystals, crystal growth, and nucleation. *Handbook of Industrial Crystallization (Second Edition).* Elsevier.

NAGY, Z. K. & BRAATZ, R. D. 2012. Advances and new directions in crystallization control. *Annual Review of Chemical and Biomolecular Engineering,* 3**,** 55-75.

NASR, M. M., KRUMME, M., MATSUDA, Y., TROUT, B. L., BADMAN, C., MASCIA, S., COONEY, C. L., JENSEN, K. D., FLORENCE, A. & JOHNSTON, C. 2017. Regulatory Perspectives on Continuous Pharmaceutical Manufacturing: Moving From Theory to Practice: September 26-27, 2016, International Symposium on the Continuous Manufacturing of Pharmaceuticals. *Journal of Pharmaceutical Sciences,* 106**,** 3199-3206.

NEWELL, H. E., BUCKTON, G., BUTLER, D. A., THIELMANN, F. & WILLIAMS, D. R. 2001. The use of inverse phase gas chromatography to measure the surface energy of crystalline, amorphous, and recently milled lactose. *Pharmaceutical Research,* 18**,** 662-666.

OMAR, H. M. & ROHANI, S. 2017. Crystal population balance formulation and solution methods: A review. *Crystal Growth & Design,* 17**,** 4028-4041.

OTAKE, K., SAKURAI, Y., NISHIDA, H., FUKUI, H., TAGAWA, Y., YAMASAKI, H., KARASHIMA, M., OTSUKA, K. & INATOMI, N. 2016. Characteristics of the novel potassium-competitive acid blocker vonoprazan fumarate (TAK-438). *Advances in Therapy,* 33**,** 1140-1157.

OTTOBONI, S., PRICE, C. J., STEVEN, C., MEEHAN, E., BARTON, A., FIRTH, P., MITCHELL, A. & TAHIR, F. 2019. Development of a novel continuous filtration unit for pharmaceutical process development and manufacturing. *Journal of Pharmaceutical Sciences,* 108**,** 372-381.

PÉREZ-CALVO, J.-F., KADAM, S. S. & KRAMER, H. J. M. 2016. Determination of kinetics in batch cooling crystallization processes—A sequential parameter estimation approach. *AIChE Journal,* 62**,** 3992-4012.

POWELL, K. A., BARTOLINI, G., WITTERING, K. E., SALEEMI, A. N., WILSON, C. C., RIELLY, C. D. & NAGY, Z. K. 2015. Toward Continuous Crystallization of Urea-Barbituric Acid: A Polymorphic Co-Crystal System. *Crystal Growth & Design,* 15**,** 4821-4836.

PRICE, C. J. 2017. Application of Ultrasound in Crystallization (Sonocrystallization). *Engineering Crystallography: From Molecule to Crystal to Functional Form*. Springer.

QAMAR, S. & WARNECKE, G. 2007. Numerical solution of population balance equations for nucleation, growth and aggregation processes. *Computers & Chemical Engineering,* 31**,** 1576-1589.

QAMAR, S., WARNECKE, G. & ELSNER, M. P. 2009. On the solution of population balances for nucleation, growth, aggregation and breakage processes. *Chemical Engineering Science,* 64**,** 2088-2095.

QIU, Y. & RASMUSON, Å. C. 1994. Estimation of crystallization kinetics from batch cooling experiments. *AIChE Journal,* 40**,** 799-812.

QUON, J. L., ZHANG, H., ALVAREZ, A., EVANS, J., MYERSON, A. S. & TROUT, B. L. 2012. Continuous crystallization of aliskiren hemifumarate. *Crystal Growth & Design,* 12**,** 3036-3044.

R WILLIAMS, D. 2015. Particle engineering in pharmaceutical solids processing: surface energy considerations. *Current Pharmaceutical Design,* 21**,** 2677-2694.

RAHMAN, M. S. 2009. MECHANICAL PROPERTIES OF FOODS. *Food Engineering-Volume I***,** 143.

RAJAGOPALAN, A. K., BOTSCHI, S., MORARI, M. & MAZZOTTI, M. 2019. Feedback Control for the Size and Shape Evolution of Needle-like Crystals in Suspension. III. Wet Milling. *Crystal Growth & Design*. 19, 2845-2861.

RAMISETTY, K. A. & RASMUSON, Å. C. 2018. Controlling the Product Crystal Size Distribution by Strategic Application of Ultrasonication. *Crystal Growth & Design,* 18**,** 1697-1709.

RAMKRISHNA, D. & SINGH, M. R. 2014. Population balance modeling: current status and future prospects. *Annual Review of Chemical and Biomolecular Engineering,* 5**,** 123-146.

RANDOLPH, A. & LARSON, M. 1962. Transient and steady state size distributions in continuous mixed suspension crystallizers. *AIChE Journal,* 8**,** 639-645.

RANDOLPH, A. D. & LARSON, M. A. 1988. *Theory of particulate process: analysis and techniques of continuous crystallization*, Academic Press.

RANODOLPH, A. 2012. *Theory of particulate processes: analysis and techniques of continuous crystallization*, Elsevier.

RASHID, A., WHITE, E., HOWES, T., LITSTER, J. & MARZIANO, I. 2017. From Raw Data to Process: The Path to a Batch or a Continuous Crystallizer Design for Ibuprofen. *Organic Process Research & Development,* 21**,** 187-194.

ROBERTS, K. J., DOCHERTY, R. & TAMURA, R. 2017. *Engineering crystallography: from molecule to crystal to functional form*, Springer.

ROBERTSON, K., FLANDRIN, P.-B., KLAPWIJK, A. R. & WILSON, C. C. 2016. Design and Evaluation of a Mesoscale Segmented Flow Reactor (KRAIC). *Crystal Growth & Design,* 16**,** 4759-4764.

RUECROFT, G., HIPKISS, D., LY, T., MAXTED, N. & CAINS, P. W. 2005. Sonocrystallization: The Use of Ultrasound for Improved Industrial Crystallization. *Organic Process Research & Development,* 9**,** 923-932.

SALEEMI, A. N., RIELLY, C. D. & NAGY, Z. K. 2012. Comparative Investigation of Supersaturation and Automated Direct Nucleation Control of Crystal Size Distributions using ATR-UV/vis Spectroscopy and FBRM. *Crystal Growth & Design,* 12**,** 1792-1807.

SALVATORI, F. & MAZZOTTI, M. 2017. Manipulation of Particle Morphology by Crystallization, Milling, and Heating Cycles—A Mathematical Modeling Approach. *Industrial & Engineering Chemistry Research,* 56**,** 9188-9201.

SALVATORI, F. & MAZZOTTI, M. 2018. Experimental Characterization and Mathematical Modeling of Breakage of Needle-like Crystals in a Continuous Rotor-Stator Wet Mill. *Crystal Growth & Design*. 18, 5957-5972.

SANDER, J. R., ZEIGER, B. W. & SUSLICK, K. S. 2014. Sonocrystallization and sonofragmentation. *Ultrasonics Sonochemistry,* 21**,** 1908-1915.

SCHOELL, J., IRIZARRY, R., SIROTA, E., MENGEL, C., CODAN, L. & COTE, A. 2019. Determining particle-size distributions from chord length measurements for different particle morphologies. *AIChE Journal,* 65.

SCHÖLL, J., LINDENBERG, C., VICUM, L., BROZIO, J. & MAZZOTTI, M. 2007. Precipitation of α L-glutamic acid: determination of growth kinetics. *Faraday Discussions,* 136**,** 247-264.

SCHORSCH, S., OCHSENBEIN, D. R., VETTER, T., MORARI, M. & MAZZOTTI, M. 2014. High accuracy online measurement of multidimensional particle size distributions during crystallization. *Chemical Engineering Science,* 105**,** 155-168.

SCHORSCH, S., VETTER, T. & MAZZOTTI, M. 2012. Measuring multidimensional particle size distributions during crystallization. *Chemical Engineering Science,* 77**,** 130-142.

SCHULTZ, J., LAVIELLE, L. & MARTIN, C. 1987. The role of the interface in carbon fibre-epoxy composites. *The Journal of Adhesion,* 23**,** 45-60.

SHAH, U. V., OLUSANMI, D., NARANG, A. S., HUSSAIN, M. A., TOBYN, M. J., HINDER, S. J. & HENG, J. Y. 2015. Decoupling the contribution of surface energy and surface area on the cohesion of pharmaceutical powders. *Pharm Res,* 32**,** 248-59.

SIDDIQUE, H., BROWN, C. J., HOUSON, I. & FLORENCE, A. J. 2015. Establishment of a Continuous Sonocrystallization Process for Lactose in an Oscillatory Baffled Crystallizer. *Organic Process Research & Development,* 19**,** 1871-1881.

SIMONE, E., SALEEMI, A. N. & NAGY, Z. 2014a. Application of quantitative Raman spectroscopy for the monitoring of polymorphic transformation in crystallization processes using a good calibration practice procedure. *Chemical Engineering Research and Design,* 92**,** 594-611.

SIMONE, E., SALEEMI, A. N. & NAGY, Z. K. 2014b. Raman, UV, NIR, and Mid-IR Spectroscopy with Focused Beam Reflectance Measurement in Monitoring Polymorphic Transformations. *Chemical Engineering & Technology,* 37**,** 1305-1313.

SIMONE, E., ZHANG, W. & NAGY, Z. K. 2015. Application of process analytical technology-based feedback control strategies to improve purity and size distribution in biopharmaceutical crystallization. *Crystal Growth & Design,* 15**,** 2908-2919.

SRAI, J. S., BADMAN, C., KRUMME, M., FUTRAN, M. & JOHNSTON, C. 2015. Future supply chains enabled by continuous processing—Opportunities and challenges. May 20–21, 2014 Continuous Manufacturing Symposium. *Journal of pharmaceutical sciences,* 104**,** 840-849.

STANKIEWICZ, A. I. & MOULIJN, J. A. 2000. Process intensification: transforming chemical engineering. *Chemical Engineering Progress,* 96**,** 22-34.

STEENDAM, R. R., KESHAVARZ, L., BLIJLEVENS, M. A., DE SOUZA, B., CROKER, D. M. & FRAWLEY, P. J. 2018. Effects of scale-up on the mechanism and kinetics of crystal nucleation. *Crystal Growth & Design,* 18**,** 5547-5555.

SUSLICK, K. S. 1990. Sonochemistry. *Science,* 247**,** 1439-1445.

SVOBODA, V., MACFHIONNGHAILE, P., MCGINTY, J., CONNOR, L. E., OSWALD, I. D. H. & SEFCIK, J. 2017. Continuous Cocrystallization of Benzoic Acid and Isonicotinamide by Mixing-Induced Supersaturation: Exploring Opportunities between Reactive and Antisolvent Crystallization Concepts. *Crystal Growth & Design,* 17**,** 1902-1909.

SWARTZ, M. E. 2005. UPLC™: an introduction and review. *Journal of Liquid Chromatography & Related Technologies,* 28**,** 1253-1263.

TICEHURST, M. D. & MARZIANO, I. 2015. Integration of active pharmaceutical ingredient solid form selection and particle engineering into drug product design. *Journal of Pharmacy and Pharmacology,* 67**,** 782-802.

TROWBRIDGE, L., GRIMSEY, I. & YORK, P. 1998. Influence of milling on the surface properties of acetaminophen. *Pharm Sci (Suppl),* 1**,** 310.

TUNG, H.-H., PAUL, E. L., MIDLER, M. & MCCAULEY, J. A. 2009. *Crystallization of organic compounds: an industrial perspective*, John Wiley & Sons.

VACCARO, A., ŠEFČÍK, J. & MORBIDELLI, M. 2006. Modeling focused beam reflectance measurement and its application to sizing of particles of variable shape. *Particle & Particle Systems Characterization,* 23**,** 360-373.

VARIANKAVAL, N., COTE, A. S. & DOHERTY, M. F. 2008. From form to function: crystallization of active pharmaceutical ingredients. *AIChE Journal,* 54**,** 1682-1688.

VEKILOV, P. G. 2010. Nucleation. *Crystal Growth & Design,* 10**,** 5007-5019.

VETTER, T., BURCHAM, C. L. & DOHERTY, M. F. 2014. Regions of attainable particle sizes in continuous and batch crystallization processes. *Chemical Engineering Science,* 106**,** 167-180.

VETTER, T., IGGLAND, M., OCHSENBEIN, D. R., HANSELER, F. S. & MAZZOTTI, M. 2013. Modeling nucleation, growth, and Ostwald ripening in crystallization processes: a comparison between population balance and kinetic rate equation. *Crystal Growth & Design,* 13**,** 4890-4905.

VETTER, T., MAZZOTTI, M. & BROZIO, J. R. 2011. Slowing the growth rate of ibuprofen crystals using the polymeric additive Pluronic F127. *Crystal Growth & Design,* 11**,** 3813-3821.

VICUM, L., OTTIGER, S., MAZZOTTI, M., MAKOWSKI, Ł. & BAŁDYGA, J. 2004. Multi-scale modeling of a reactive mixing process in a semibatch stirred tank. *Chemical Engineering Science,* 59**,** 1767-1781.

WARD, J. D., MELLICHAMP, D. A. & DOHERTY, M. F. 2006. Choosing an operating policy for seeded batch crystallization. *AIChE Journal,* 52**,** 2046-2054.

WARZECHA, M., GUO, R., M. BHARDWAJ, R., REUTZEL-EDENS, S. M., PRICE, S. L., LAMPROU, D. A. & FLORENCE, A. J. 2017. Direct observation of templated two-step nucleation mechanism during olanzapine hydrate formation. *Crystal Growth & Design,* 17**,** 6382-6393.

WILSON, D., BUNKER, M., MILNE, D., JAWOR-BACZYNSKA, A., POWELL, K., BLYTH, J. & STREATHER, D. 2018. Particle engineering of needle shaped crystals by wet milling and temperature cycling: Optimisation for roller compaction. *Powder Technology*. 339, 641-650.

WONG, S. Y., TATUSKO, A. P., TROUT, B. L. & MYERSON, A. S. 2012. Development of continuous crystallization processes using a single-stage mixed-suspension, mixed-product removal crystallizer with recycle. *Crystal Growth & Design,* 12**,** 5701-5707.

WOOD, B., GIRARD, K., POLSTER, C. & CROKER, D. M. 2019. Progress to date in the design and operation of continuous crystallization processes for pharmaceutical applications. *Organic Process Research & Development*. 23, 122-144.

WU, H., DONG, Z., LI, H. & KHAN, M. 2014. An integrated process analytical technology (PAT) approach for pharmaceutical crystallization process understanding to ensure product quality and safety: FDA scientist's perspective. *Organic Process Research & Development,* 19**,** 89-101.

WYNN, E. 2003. Relationship between particle-size and chord-length distributions in focused beam reflectance measurement: stability of direct inversion and weighting. *Powder Technology,* 133**,** 125-133.

YANG, M. 2011. CFD simulations for scale up of wet milling in high shear mixers. University of Maryland. Ph.D. Thesis. http://hdl.handle.net/1903/11595

YANG, Y., PAL, K., KOSWARA, A., SUN, Q., ZHANG, Y., QUON, J., MCKEOWN, R., GOSS, C. & NAGY, Z. K. 2017. Application of feedback control and in situ milling to improve particle size and shape in the crystallization of a slow growing needle-like active pharmaceutical ingredient. *International Journal of Pharmaceutics,* 533**,** 49-61.

YANG, Y., SONG, L., GAO, T. & NAGY, Z. K. 2015. Integrated Upstream and Downstream Application of Wet Milling with Continuous Mixed Suspension Mixed Product Removal Crystallization. *Crystal Growth & Design,* 15**,** 5879-5885.

YANG, Y., SONG, L., ZHANG, Y. & NAGY, Z. K. 2016a. Application of Wet Milling-Based Automated Direct Nucleation Control in Continuous Cooling Crystallization Processes. *Industrial & Engineering Chemistry Research,* 55**,** 4987-4996.

YANG, Y., ZHANG, C., PAL, K., KOSWARA, A., QUON, J., MCKEOWN, R., GOSS, C. & NAGY, Z. K. 2016b. Application of ultra-performance liquid chromatography as an online process analytical technology tool in pharmaceutical crystallization. *Crystal Growth & Design,* 16**,** 7074-7082.

YLÄ-MAIHANIEMI, P. P., HENG, J. Y., THIELMANN, F. & WILLIAMS, D. R. 2008. Inverse gas chromatographic method for measuring the dispersive surface energy distribution for particulates. *Langmuir,* 24**,** 9551-9557.

ZEIGER, B. W. & SUSLICK, K. S. 2011. Sonofragmentation of molecular crystals. *Journal of the American Chemical Society,* 133**,** 14530-14533.

ZHANG, J., XU, S. & LI, W. 2012. High shear mixers: A review of typical applications and studies on power draw, flow pattern, energy dissipation and transfer properties. *Chemical Engineering and Processing: Process Intensification,* 57-58**,** 25-41.

ZHANG, Z., SUN, D. W., ZHU, Z. & CHENG, L. 2015. Enhancement of crystallization processes by power ultrasound: current state-of-the-art and research advances. *Comprehensive Reviews in Food Science and Food Safety,* 14**,** 303-316.

ZHAO, L., RAVAL, V., BRIGGS, N. E. B., BHARDWAJ, R. M., MCGLONE, T., OSWALD, I. D. H. & FLORENCE, A. J. 2014. From discovery to scale-up: [small alpha]-lipoic acid : nicotinamide co-crystals in a continuous oscillatory baffled crystalliser. *CrystEngComm,* 16**,** 5769-5780.

ZHOU, D. & QIU, Y. 2010. Understanding material properties in pharmaceutical product development and manufacturing: powder flow and mechanical properties. *Journal of Validation Technology,* 16**,** 65.